Application of HPGR and X-Ray CT to investigate the potential of Witwatersrand gold ore for heap leaching: A process mineralogy approach

---

by

Glen Nwaila

A thesis submitted at the University of Cape Town in fulfilment of the requirements for the degree of

Master of Science

Department of Chemical Engineering

University of Cape Town

May 2014

SYNOPSIS

Auriferous conglomerates of the Archaean Witwatersrand Basin in South Africa host one of the largest known gold resources and rate as the world's most outstanding example of a fossil megaplacer deposit. For the past 40 years, Witwatersrand gold production in South Africa has been progressively declining due to problems related to high energy costs, decreasing grade, accessibility to greater depths, health and safety issues, labour union unrest and economic uncertainties: thus the overall viability of current gold production is questionable. Ultimately, the future of Witwatersrand gold mining relies on devising smarter strategies across the entire industry, but in particular critical areas such as comminution and extraction.

With the continuous increase in mining depth, dominance of low-grade gold ores and strict safety regulations, metallurgical processing options have become limited. Heap leaching is a well-established technology which continues to grow in use and provides several benefits to solve some of these problems. High pressure grinding rolls (HPGR) is another technology with significant potential, especially for its application in coarse particle heap leaching due to its ability to induce micro-cracks as well as its high grinding efficiency and low energy requirements. This study explores the use of these two technologies in a process mineralogical framework using novel 3D X-ray computed tomography mineralogical analysis in order to assess a potential of the Witwatersrand gold ore for heap leaching.

In this study, a composite bulk sample comprising Ventersdorp contact reef (VCR) and the Elsburg reefs (ER) was collected from Harmony gold mine, Carletonville and comminuted using HPGR at three different pressure settings (120, 90 and 60 bar). Large (-16/+11.2 mm) and small (-5.6/+4 mm) particles of the HPGR product were then mineralogically characterised using a combination of laboratory techniques including conventional optical microscopy, Quantitative Scanning Electron Microscopy (QEMSCAN), X-Ray and Neutron Computed Tomography (X-ray CT/XRCT and NCT), Quantitative X-Ray Diffraction (QXRD) and X-Ray Fluorescence (XRF). The samples were then packed in laboratory leach columns and treated with cyanide solution operated in continuous mode in order to investigate the potential for heap leaching.

The first phase of the work focused on the development of an ore characterisation method using 3D X-ray CT together with appropriate reconstruction algorithms to describe the HPGR induced crack network and mineralogy of the samples. Comparisons of the results from 2D QEMSCAN and 3D X-ray CT showed similar bulk mineralogy (>80 % silicates), crack network (<1 vol. %), gold grain size distribution (mean size < 200 μm) and gold grain shape (moderate sphericity with sub to rounded grains) within the limitations of each technique. The biggest challenge faced was in overcoming partial volume effects observed at a voxel size of 17 μm resulting in the overestimation of gold grain size.

It was clear that the HPGR pressure settings strongly influenced the development and distribution of fractures within the particles produced, which in turn governs the efficacy of the cyanide leaching. Particle populations produced by the different HPGR pressure settings were ranked in order of predicted leachability based on quantifying fracture properties such as width (or dilation) and density. These features govern porosity and permeability within particles and thus their response to cyanidation. Small particles showed slightly wider HPGR induced cracks (0.04-0.15 mm) compared to larger particles (0.02-0.67 mm). Porosity and crack volume were found to be between 0.12 to 0.87 volume percentages. Particle fracture patterns showed that crack connectivity was the lowest on the 60 bar HPGR product, and increased on the 90 bar and 120 bar HPGR product. In terms of these parameters (crack and porosity volume percent together with the crack width), the smaller particles range of the 90 bar HPGR pressure product were ranked as the optimal particle type for the leach tests.

Gold dominantly occurs as fine (<50 μm in QEMSCAN and <200 μm in X-ray CT) native gold with a strong association to iron sulphides (pyrite and pyrrhotite). A minor proportion of gold occurs in alloys (Au-Ag-Hg). The host assemblage is dominated by cyanide insoluble minerals (i.e. >80 wt. % silicate gangue), but the presence of sulphide minerals (~4 wt. %) in the form of pyrite, arsenopyrite, pyrrhotite, chalcopyrite and galena, will influence the consumption of cyanide. Less than 10 % of the gold was found to be liberated with the majority of the gold found to be associated with sulphide (pyrite and non-magnetic pyrrhotite) and silicate minerals. Three main generations of pyrite (compact, porous and euhedral pyrite) were found in the ore and interpreted to have different reaction rates. Porous pyrite was interpreted to be the most reactive form of pyrite followed by compact pyrite whereas euhedral pyrite is classified as the least reactive. Gold occurs as micro-inclusions in porous and compact pyrite. Sulphide minerals (i.e. pyrite) need to be decomposed to release the ubiquitous micro-inclusions of gold, but those present in the VCR are likely to be more reactive than those in the ER, thus having a more favourable influence on gold cyanidation.

Complementary column leach studies showed the importance of feed preparation in optimising gold recovery. Dissolution of the gold and sulphide minerals by cyanide penetrating along the HPGR induced fractures essentially played the role of particle size reduction and continued reaction. The pH progressively dropped while gold extraction was occurring slowly from the start of the leach cycle until the first 220 hours due to oxidation of sulphide minerals. A rapid gold extract phase was observed after 220 hours until termination of the leach cycle at 334 hours. The smaller particles produced with the HPGR yield the highest gold recovery reaching 60.7 % within 334 hours leach cycle and large particles yield the lowest gold extraction (~30 %) when compared to small particles. Small particles show wider crack width and crack-porosity Overall, the results show amenability of the Witwatersrand gold ores to the process of heap leaching when prepared using HPGR, and demonstrate the value of a multi-disciplinary approach.

DECLARATION

I declare that this thesis is my own work. It is being submitted for the degree of Master of Science (MSc) in the University of Cape Town. This thesis has not been submitted before for any degree or examination in any other university.

Glen Nwaila

31st Day of May **2014**

ACKNOWLEDGEMENTS

I would like to express my gratitude to my supervisor, Dr. Megan Becker, whose expertise, understanding and patience added considerably to my graduate experience. I appreciate her vast knowledge and skills in many areas (e.g. mineralogy, automated SEM, ethics, interaction with participants and writing skills), and her assistance in writing reports and preparation of presentations (i.e. grant proposals, scholarship applications and this thesis). I would also like to thank A/Prof. Jochen Petersen for sharing his knowledge on heap leaching, design of experiments, editorial work and his co-supervision from proposal writing to the final thesis.

A very special thank you goes to Emeritus Prof. David Louis Reid for introducing me to the best research team: without his motivation and encouragement I would not have considered a graduate career. I would like to extend my appreciation to Dr. Yousef Ghorbani for his assistance during setup of leaching experiments, research design and his column leaching schematic and creative design. Prof. Hartwig Frimmel is thanked for sharing his knowledge and advice on the Witwatersrand mineralogy and genesis. Necsa team (Mr. Frikkie de Beer and Lunga Bam) is acknowledged for their expert advice, analysing samples using neutron tomography in Switzerland, participation and providing micro-focus X-ray CT access, Harmony gold mining company (Messrs. Manie Keyser, Sias Le Roux and Aubrey de Wet) for supplying samples and access to their mine, Mintek for ore preparation (Dr. Johnny Kalala), Stellenbosch University (Ms Madelaine Frazenburg) for SEM-EDX work and Exxaro for QEMSCAN pre-main study analysis (Solly Theron).

I recognize that this research would not have been possible without the assistance of Aubrey Mainza, Kirsten Corin and James Mwase for their assistance with various technical aspects of the research. Appreciation goes to Johan van Eeden of Sibanye Gold for arranging funding of the project and the company for their continued support of this project. This work is based on research supported by the South African Research Chairs Initiative of the Department of Science and Technology and the National Research Foundation of South Africa. This work is also based on National Research Foundation grants UID 85533 (MB) and 85453 (J-PF). The grant holder acknowledges that opinions, findings and conclusions or recommendations expressed in any publication generated by the NRF supported research are that of the authors and that the NRF accepts no liability whatsoever in this regard. A special thank you goes to various members of the Centre for Minerals Research (CMR): Bismark Donkor for screening of the ore, Lorraine Nkemba for QEMSCAN sample preparations and Gaynor Yorath for her assistance throughout all the aspects of gold

deportment studies using QEMSCAN. In conclusion, I would also like to thank my parents (Daniel and Catherine Nwaila) for the support they provided me with through my entire life and in particular I must acknowledge my wife Phumzile Nwaila, without whose love, encouragement and editing assistance, I would not have finished this thesis.

LIST OF PUBLICATIONS AND PRESENTATIONS

1. **Nwaila, G**., Becker, M., Petersen, J., Reid, D. L., Ghorbani, Y., Franzidis, J-P., de Beer, F.C and Bam, L., 2013. Investigation into the potential of Witwatersrand gold ore for heap leaching using X-ray CT and process mineralogy, Minerals to Metals Research day, 7 November 2013, Cape Town.

2. Nwaila, G., **Bam, L** and De Beer, F.C., 2013. Radiography of Dense Minerals in Rocks Using Micro-CT, 1st International Conference on Tomography of Materials and Structures, 1 July 2013, Ghent University, Belgium.

3. **Nwaila, G**., Becker, M., Petersen, J., Reid, D. L., Ghorbani, Y., Franzidis, J-P., de Beer, F.C and Bam, L., 2013. A Process mineralogical study of the Witwatersrand gold ore in Carletonville, South Africa, SAIMM Mineral Processing Conference, 6-8 August 2013, Cape Town.

4. Nwaila, G., **Becker, M**., Ghorbani, Y., Petersen, J., Reid, D. L., Bam, L. C., De Beer, F. C and Franzidis, J.-P., 2013. A geometallurgical study of the Witwatersrand gold ore at Carletonville, South Africa. AusIMM GEOMET Conference 2013. Brisbane: AusIMM, 75-83.

5. **Nwaila, G**., Becker, M., Petersen, J., Reid, D. L., Ghorbani, Y., Franzidis, J-P., de Beer, F.C and Bam, L., 2013. Application of X-ray CT and QEMSCAN in Process mineralogical study of gold: A Case study of the Witwatersrand gold ore, Radiography with Radiation conference, 23-24 September 2013, NECSA.

6. **Nwaila, G**., Becker, M., Petersen, J., Reid, D. L., Ghorbani, Y., Franzidis, J-P., de Beer, F.C and Aubrey, A.N., 2012. A process mineralogical study of gold at Kusasalethu mine, Carletonville goldfield, Mineral Processing Conference, 1-3 August 2012, Southern African Institute of Mining & Metallurgy Western Cape Branch.

7. **Nwaila, G**., Becker, M and Reid, D. L., 2011. Mineralogical characterisation of the VCR and Elsburg gold reefs at Kusasalethu Mine, Carletonville. 8th annual International Geo-synthesis conference, 28 August-02 September 2011, Cape Town, South Africa.

TABLE OF CONTENTS

List of abbreviations and acronyms ..... **i**

Chemical formulas ..... **ii**

Mineral names and formulas ..... **iii**

Glossary ..... **iv**

CHAPTER 1: INTRODUCTION **1**

1.1 BACKGROUND 1

1.2 PROBLEM STATEMENT 6

1.3 OBJECTIVES OF THIS STUDY 7

1.4 KEY QUESTIONS 7

1.5 SCOPE OF RESEARCH 7

1.6 ORGANISATION OF THE THESIS 9

CHAPTER 2: LITERATURE REVIEW **10**

2.1 CHEMICAL AND PHYSICAL CHARACTERISTICS OF GOLD 10

2.2 OVERVIEW OF GOLD ORE DEPOSITS 11

2.3 GOLD CYANIDATION 12

2.3.1 Principles of gold cyanidation 12

2.3.2 Chemistry of cyanide and gold dissolution 12

2.3.3 Application of gold cyanidation 14

2.4 CHEMICAL HEAP LEACHING 15

2.4.1 Chemical heap leach dissolution kinetics 17

2.4.2 Advantages and disadvantages of heap leaching 19

2.4.3 Effect of sulphide minerals during gold cyanidation 20

2.4.4 Mineral exposure in crushed particles 21

2.5 COMMINUTION 22

2.5.1 High pressure grinding rolls 23

2.6 PROCESS MINERALOGY 27

2.6.1 Representative sampling 28

2.6.2 Analytical tools used in process mineralogy studies 30

2.7 CRITICAL REVIEW OF THE LITERATURE 38

CHAPTER 3: GEOLOGICAL SETTING 40

3.1 REGIONAL GEOLOGY 40

3.1.1 The Kaapvaal Craton 40

3.1.2 The Witwatersrand Basin 41

3.1.3 The Ventersdorp and Transvaal Supergroup 44

3.1.4 Stratigraphy and mineralogical features of the Witwatersrand ores 45

3.2 LOCAL GEOLOGICAL SETTING 46

3.2.1 Elsburg reefs (ER) 47

3.2.2 The Ventersdorp Contact Reef (VCR) 48

CHAPTER 4: MATERIALS AND METHODS 50

4.1 INTRODUCTION 50

4.2 REPRESENTATIVE SAMPLING AND SPLITTING 50

4.2.2. Sample splitting 51

4.3 HPGR TEST WORK PROCEDURE 52

4.3.1 Particle size distribution analysis 55

4.3.2 Ore preparation for mineralogical studies 55

4.3.3 Fire Assay 55

4.3.4 X-ray Fluorescence (XRF) 56

4.3.5 Optical microscopy 56

4.3.6 Quantitative X-ray diffraction (QXRD) 56

4.3.7 Scanning electron microscopy (SEM) 57

4.3.8 QEMSCAN 57

4.3.9 Micro-focus X-ray CT 60

4.3.10 Micro-focus Cold neutron tomography 61

4.4 COLUMN LEACHING EXPERIMENTS 62

4.4.1 Equipment used and measurements performed 63

CHAPTER 5: DEVELOPING THE ORE CHARACTERISATION METHOD USING MICRO-FOCUS X-RAY CT 65

5.1 INTRODUCTION 65

5.2 MINERALOGICAL COMPOSITION OF THE WITWATERSRAND GOLD ORE 65

5.3 MEASUREMENT PARAMETERS 66

5.4 RECONSTRUCTION PROCESS 69

5.5 VISUALISATION AND DATA MANIPULATION 70

5.5.1 Phase segmentation 70

5.5.2 Data Validation 72

5.5.3 Ore porosity and crack analysis 74

5.5.4 Gold characterisation 75

5.6 ALTERNATIVE SOURCES OF TOMOGRAPHY: COLD NEUTRON TOMOGRAPHY 80

5.7 CHALLENGES ENCOUNTERED DURING DEVELOPMENT OF THE METHOD 81

CHAPTER 6: INVESTIGATION INTO THE POTENTIAL OF WITWATERSRAND GOLD ORE FOR HEAP LEACHING 84

6.1 INTRODUCTION 84

6.2 COMMINUTION 84

6.2.1 HPGR specific energy and grinding force 84

6.2.2 Particle size distribution 85

6.2.3 Quantitative analysis of cracks 86

6.3 MINERALOGICAL CHARACTERISATION AND GOLD DEPORTMENT 90

6.3.1 Petrography of the Witwatersrand gold ore 90

6.3.2 Gold grain size distribution and morphology 94

6.3.3 Mineralogical association and gold liberation status 102

6.3.4 Summary of gold deportment studies in the prediction of metallurgical behaviour 105

6.4 CYANIDE LEACHING EXPERIMENTS 106

6.4.1 The pH behaviour 107

6.4.2 Gold extraction curves 107

6.4.3 Crack density and mineral dissolution potential 109

6.4.4 Laboratory cyanide-leaching performance discussion 110

CHAPTER 7: CONCLUDING DISCUSSION AND RECOMMENDATIONS FOR FUTURE WORK 112

7.1 CONCLUDING DISCUSSION 112

7.2 RECOMMENDATIONS FOR FUTURE WORK 116

REFERENCES 117

APPENDICES..... 129

Appendix I: Chemical assay of different HPGR pressure setting and size fractions using XRF (%). 129

Appendix II: Size by size bulk mineralogy obtained using QEMSCAN in wt. % 129

Appendix III: Witwatersrand gold ore Sulphur concentration 130

Appendix IV: Photographs of hand specimens obtained from underground channel mapping and sampling 130

Appendix V: The VCR and ER Channel sampling gold distribution 131

Appendix VI: Overview of different litho-facies uranium distribution trends 132

Appendix VII: Overview of different litho-facies gold distribution trends 132

Appendix VIII: HPGR prepared Witwatersrand gold ore 133

Appendix IX: QEMSCAN field images 134

Appendix X: Selected QEMSCAN trace mineral search 135

Appendix XI: X-ray CT 3D gold distribution and image classification 136

Appendix XII: Laboratory leaching experiments procedure 141

Appendix XIII: Laboratory leaching Results 147

Appendix XIV: Harmony Gold: Kusasalethu mine recovery grade and tons milled 149

Appendix XV: Harmony Gold: Kusasalethu mine operating cost per kg and gold production per annum 150

LIST OF FIGURES

Figure 1-1: West Rand gold mines with special reference to Kusasalethu gold mine (Harmony Gold, 2013). 1

Figure 1-2: History of Witwatersrand Basin gold production rate (p, in kilograms per year (kg yr–1)), divided into four stages: 1) beginning, 1884–1910; 2) early, 1911–1951; 3) transition, 1952–1965; 4) late, 1966–2007. Data from Chamber of Mines of South Africa website, http://www.bullion.org.za. Best-fitting Gaussian (normal) distribution curves to the early-stage (blue curve) and the late-stage (red curve) data correspond to ultimate recoverable resource (URR) totals of 27 550 and 53 825 metric tonnes, respectively (Hartnady, 2009). 2

Figure 1-3: Gold crystal structure illustrating research scope and limitation (red text and lines indicate aspects covered in this study). 8

Figure 2-1: Structure of gold: (a) Atomic structure of gold; b) Crystal arrangement for metallic gold (http://www.chemicalelements.com/elements/au.html). 10

Figure 2-2: Eh-pH diagram for the Fe-S-CN-H_2O system at 25^oC (Marsden and House, 1992). 14

Figure 2-3: Gold cyanidation process flow sheet (http://dcsengineer.com/app_mining.html). 15

Figure 2-4: Schematic diagram of chemical heap leaching (wiki.biomine.skelleftea.se). 16

Figure 2-5: Simulation of heap leach production model (Robertson, 2008). 17

Figure 2-6: Comparative leach kinetics of oxide, transitional and sulphide gold ores in heap leaching (Tuprag Gold Co., Kisladag Mine Heap Leach Unit, Turkey). 18

Figure 2-7: The concept of exposure and liberation of mineral by hydrometallurgy and that by physical separation process (Hsih et al., 1995). 22

Figure 2-8: Specific Energy per Mill Type (Wang and Forssberg, 2007). 23

Figure 2-9: Schematic diagram of the HPGR (Napier-Munn et al., 1996). 24

Figure 2-10: HPGR breakage mechanism (Daniel, 2007). 27

Figure 2-11: Analytical resolution verses detection limit (www.eaglabs.com). 31

Figure 2-12: Nikon XTH 225 ST micro-focus X-ray tomography at Necsa MIXRAD facility (Hoffman and de Beer, 2012). 33

Figure 2-13: Three most common X-ray CT beam configurations (http://serc.carleton.edu). 35

Figure 2-14: The potential roles of X-ray CT in an integrated heap leach system (Dhawan et al., 2012). 37

Figure 3-1: Main Archaean stratigraphic units of the Kaapvaal Craton. The West Rand and Central Rand Groups constitute the Witwatersrand Supergroup. Bold dashed line

outlines the boundary of the Kaapvaal Craton as inferred from aeromagnetic data. The crustal blocks (amalgamated by 2.8 Ga) are separated by major lineaments (Frimmel et al., 2009). 41

Figure 3-2: The Witwatersrand Basin: a) Location of Witwatersrand gold Province showing distribution of Goldfields regions, Witwatersrand Supergroup, Dominion Group, Mesoarchaean granitoid domes and Archaean; b) Stratigraphic column of Carletonville Goldfield showing location of the VCR, ER and subsequent Witwatersrand Reefs (Frimmel et al., 2009; Koglin et al., 2010). 42

Figure 3-3: Oligomictic pebbly quartz arenite (reef), Vaal Reef, Stilfontein mine, Klerksdorp gold field; note the veneer of bitumen on the basal unconformity and 3 cm above the *base* on a bedding plane defining the top of pebbly layer; cross-bedding (so) in hanging wall, and an in *situ* ventifact; scale bar=1 cm. (B) same as A, but highlighting the position of fine- to coarse-grained rounded pyrite (Frimmel, 2005). 45

Figure 3-4: Photomicrographs illustrating morphological and textural features of Witwatersrand gold orebodies (combined transmitted and reflected light, scale bars=0.2 mm: (A) Contrasting morphological types of gold particles occurring together on a mm-scale. (B) Gold micro-nugget (Au) with overfolded rims next to rounded pyrite (Py) from same sample as shown in A (Frimmel, 2005). 46

Figure 3-5: The classification of Elandsrand Reef Zone (Mambane, 2009). 47

Figure 4-1: Schematic diagram showing sequential coning and quartering method. 52

Figure 4-2: Side view an HPGR pilot plant with a capacity of 650 tonnes per hour showing main components (www.goldenqueen.com/gall07.htm). 53

Figure 4-3: Comminution using HPGR and screening of particles with special reference to experimented two-size fraction (-16 mm/+11.2mm and -5.6 mm/+4mm). 54

Figure 4-4: Major elements correlation using ICP-MS actual assays against QEMSCAN calculated assays 60

Figure 4-5: (a) Schematic of the leach reactors; (b) Set up of leach reactors with stand and 8-channel pump head in a fume hood; (c) designed frame inside the leach reactor loosely holding stacked particles. 63

Figure 5-1: Summary of the modal mineralogy (in weight percent) of the Witwatersrand gold ore as determined by QEMSCAN (Others include uraniferous minerals). 66

Figure 5-2: Linear attenuation coefficients as a function of X-ray energy for gold ores. Values used are based on end-member compositions and average densities and were calculated using XCOM Photon Cross-Section database (Berger et al., 1998). 68

Figure 5-3: Conversion of the 2D projections into a 3D volume (tomography) using the CT-Pro software 69

Figure 5-4: An illustration of the Witwatersrand gild ore 3D volume produced through reconstruction (-16+11.2 mm). 70
Figure 5-5: Segmentation and region of interest (ROI) extraction of Witwatersrand gold ore particles using VG-Studio Max 2.2. 71
Figure 5-6: 2D X-ray CT and QEMSCAN false colour image illustrating crack propagation (crack region= red dotted line). 72
Figure 5-7: Summary of the modal mineralogy (in weight percent) of the Witwatersrand gold ore as determined by X-ray CT. 73
Figure 5-8: Crack and porosity volume percentage acquisition using volume analyser. 74
Figure 5-9: Sample volume analyser showing quantification of gold in a sample..... 76
Figure 5-10: Visualisation of defect analysis on Witwatersrand gold ore particle map. 77
Figure 5-11: Ore characterisation using X-ray CT: a) 2D X-ray CT false colour image (grey represent silicates, golden yellow represent Fe sulphide bearing minerals and red represent gold); b) 3D image showing gold and its association with sulphide-bearing minerals; c) A 3D view of sulphide minerals; d) Rotated view of gold particles in partially coded transparent gangue minerals, and e) Rotated 3D distribution of gold particles (gangue minerals virtually stripped)..... 78
Figure 5-12: Gold grain size distribution and shape of 120 bar large particle: a) Gold grain size distribution verses frequency percentage obtained using X-ray CT; b) Gold grain sphericity determined using X-ray CT; c) Gold grain size distribution obtained using QEMSCAN; d) Gold grain shape factor determined by QEMSCAN. 79
Figure 5-13: Correlation between 2D ICON and X-ray CT characterisation: (a) ICON tomography and (b) X-ray CT slice showing gold and host gangue minerals. 80
Figure 5-14: The concept of grain overestimation of X-ray CT data due to limited voxel size resulting in partial volume effect. 82
Figure 6-1: Cumulative particle size distribution of the Witwatersrand gold ore prepared by HPGR with different pressure settings. 86
Figure 6-2: X-ray CT illustration of Witwatersrand ore HPGR-induced cracks: 4 to 6 mm represent small particles and 11 to 16 mm represent large particles (dotted line highlights some of the most pronounced cracks in particles)..... 87
Figure 6-3: Quantification of crack network width using X-ray CT (green= small particles and red= large particles). 88
Figure 6-4: Quantification of HPGR induced cracks and ore porosity using X-ray CT (left green filled bar) and QEMSCAN (right red bar). 89
Figure 6-5: 2D SEM images illustrating the morphology of the three generations of pyrite: (a) VCR-semi rounded compact pyrite (Py-1) and porous pyrite (Py-2) associated with

quartz (Qtz) and uraniferous minerals (UR); (b) VCR-porous pyrite filled with quartz inclusions surrounded by muscovite-chlorite matrix; (c) ER- euhedral pyrite (Py-3) interlocked with compact pyrite; (d) ER- euhedral pyrite associated with re-crystallised quartz and compact pyrite. 91
Figure 6-6: Schematic representations of three different generations of pyrite. 92
Figure 6-7: Reflected light photomicrographs of the Witwatersrand gold ore (a) Gold (Au) associated with quartz (Qtz) and Pyrrhotite (Po); (b) Coarse to fine gold particles associated with Pyrrhotite; (c) Coarse gold grain in poly-mineral boundary; (d) Pyrrhotite and compact pyrite (Py-1); (e) Semi-rounded porous pyrite (Py-2) filled with fine gold inclusions and compact pyrite surrounded by re-crystallised quartz; (f) Euhedral pyrite surrounded by quartz pebbles. 93
Figure 6-8: QEMSCAN trace mineral search showing particle mappings of gold. 94
Figure 6-9: QEMSCAN gold grain size distribution against frequency 95
Figure 6-10: QEMSCAN gold morphology inspection using shape factor functionality. 96
Figure 6-11: X-ray CT small particles gold grain size distribution against frequency percentage (the Gaussian dotted line fit represent the distribution trend. 98
Figure 6-12: X-ray CT small particles gold sphericity distribution against frequency percentage. 99
Figure 6-13: X-ray CT large particles gold grain size distribution against frequency percentage (the Gaussian fit represent the distribution trend). 100
Figure 6-14: X-ray CT large particles gold sphericity distribution against frequency percentage. 101
Figure 6-15: QEMSCAN mineralogical association of gold with gangue mineralogy 102
Figure 6-16: Liberation characteristics of the Witwatersrand gold ore (legend for liberation status can be found in Table 6-3). 104
Figure 6-17: 2D X-ray CT false colour images illustrating the Witwatersrand gold ore based on comminution and their expected leaching behaviour. 105
Figure 6-18: Change in pH over time for large particles (-16/+11.2 mm) and small particles (-5.6/+4 mm) from leaching experiments. Error bars represent the standard deviation of every sampling interval. 107
Figure 6-19: Cumulative gold recovery percentage verses time for large particles (-16/+11.2 mm) and small particles (-5.6/+4 mm) from leaching experiments. Error bars represent the standard deviation of every sampling interval. 109
Figure 6-20: X-ray CT false colour images showing crack network distribution and exposure of valuable mineral. 110

LIST OF TABLES

Table 1-1: The top ten deepest mines in the world (Mining Technology, 2013). 3
Table 2-1: Classification of gold deposits (Zhou et al., 2004). 11
Table 2-2: Comparison between HPGR and AG/SAG Mills (Koenig and Hudson, 2006)..... 26
Table 4-1: Feed samples used in the HPGR tests..... 53
Table 4-2: Measurement condition and information obtained using QEMSCAN. 58
Table 4-3: Comparison between QEMSCAN calculated and ICP-MS actual assays 59
Table 4-4: Summary of measurement parameters using Nikon XTH 225 ST micro-focus X-ray tomography. 61
Table 4-5: Summary of the Witwatersrand gold ore investigated. 62
Table 4-6: Correlation between pump gear number and flow rate. 63
Table 5-1: QEMSCAN Modal mineralogy grouped to mineral groups. 73
Table 6-1: Specific energy and grinding force at the different pressure of HPGR 85
Table 6-2: Summary of gold grains size distribution (mm) statistics generated using X-ray CT..... 97
Table 6-3: Description of liberation status classification scheme 103

List of abbreviations and acronyms

2D	Two-dimensional space
3D	Three-dimensional space
BMA	Bulk modal analysis
BSE	Back-scattered electron
Chl	Chlorite
CT	Computed Tomography
DRZ	Deelkraal Reef Zone
EDX	Energy Dispersive X-rays
EMPA	Electron Microprobe Analysis
ERZ	Elandsrand Reef Zone
FEG	Field emission gun
g/t	Grams per metric ton
GDP	Gross Domestic Product
HPGR	High Pressure Grinding Rolls
ICP	Inductively Coupled Plasma
IGRZ	Intermediate Glassy Reef Zone
MLA	Mineral Liberation Analyser
Ms	Muscovite
MSE	Mean squared error
Mt	Metric ton
OES	Optical Emission Spectrometer
PLS	Pregnant leach solution
PMA	Particle Mineralogical Analyses
Po	Pyrrhotite
PSD	Particle size distribution
Py	Pyrite
QEMSCAN	Quantitative Evaluation of Minerals by Scanning Electron Microscopy
QXRD	Quantitative X-ray Diffraction
Re-Os	Rhenium-Osmium Radiometric Dating
ROI	Region of Interest
ROM	Run-of-mine ore
SAG	Semi-Autogenous Mill

SEM/EDS	Scanning Electron Microscope and Energy Dispersive Spectrometry
SHRIMP	Sensitive high-resolution ion microprobe
TIMA	TESCAN Integrated Mineral Analyzer
Tons	Metric tonne
UBRZ	Uranium Band Reef Zone
U-Pb	Uranium–Lead Radiometric Dating
VCR	Ventersdorp Contact Reef
Wt. %	Weight percentage
WDXRF	Wavelength dispersive X-ray Fluorescence
X-ray CT	X-ray Computer Tomography
XRD	X-ray Diffraction
XRF	X-ray Fluorescence
ρl	Liquid density (g/cm3)
ρs	Ore density (g/cm3)

Chemical formulas

$CaCO_3$	Calcium carbonate
CN^-	Cyanide
Cu	Copper
Fe	Iron
Fe^{2+}	Ferrous iron
Fe^{3+}	Ferric iron
H^+	Hydrogen ions
H_2	Molecular hydrogen
H_2S	Hydrogen sulphide
K^+	Potassium ion
KCN	Potassium Cyanide
Na^+	Sodium ion
NaCN	Sodium Cyanide
$NaHCO_3$	Sodium bicarbonate or sodium hydrogen carbonate
Pb	Lead
S	Sulphur
S^{2-}	Sulphide ion

SO_2	Sulphur dioxide
SO_4^{2-}	Sulphate ion

Mineral names and formulas

Apatite	$Ca_5 (PO_4)_3(OH)$
Arsenopyrite	FeAsS
Biotite	$K (Mg, Fe_3^{2+}) (Al, Fe^{3+}) Si_3O_{10} (OH, F)_2$
Calcite	$CaCO_3$
Chalcopyrite	$CuFeS_2$
Chlorite	$(Mg,Fe)_3(Si,Al)_4O_{10}(OH)_2.(Mg,Fe)_3(OH)_6$
Electrum	Au± (Ag, Hg)
Fe oxides / hydroxides	$FeO - Fe_2O_3$
Galena	PbS
Gold	Au
K-Feldspar	$KAlSi_3O_8$
Muscovite	$KAl_2 (AlSi_3O_{10}) (OH)_2$
Plagioclase Feldspar	$NaAlSi_3O_8 - CaAl_2Si_2O_8$
Pyrite	FeS_2
Pyrophyllite	$Al_2Si_4O_{10} (OH)_2$
Pyrrhotite	$Fe_{1-x}S$
Quartz	SiO_2
Rutile/Ilmenite	$TiO_2 - FeTiO_3$
Sphene	$CaTiO (SiO_4)$
Uraniferous Minerals	$\pm UO_2$ (Ce, La, Y, Yh) PO_4
Zircon	$ZrSiO_4$

Glossary

Area %: A mineral quantification based on surface areas, i.e. 2D measurement as opposed to a 3D volumetric quantification.

Average Grain Size: The average size of a specific mineral type, measured as the average intercept length in x-direction.

Average Particle Size: The average size of a particle, measured as the average intercept length in x-direction across the particle (regardless of the mineral type).

Barren: A particle is considered barren if it contains 0 area % of the mineral of interest.

Binary particles: Particle consisting of 2 phases.

ECD: The size of particles or grains is expressed in Equivalent Circular Diameter (ECD), which is the diameter of a circle with the same area as that of the object.

Grain: A mineral grain that consists of a single mineral type. Several grains can make a particle. In the case of a liberated grain, the terms ‘grain’ and ‘particle’ are equivalent.

Liberated: In the context of this study a particle containing >70 area % of the mineral of interest is considered “liberated”. The set limit might vary depending on the mineral or process used to treat it. Gold only has to be in contact with the leach medium and thus only needs to be exposed.

Locked: In the context of this study, a mineral of interest is considered locked when the mineral exposure is less than 30 %.

Mineral association %: The number of pixels of a mineral type adjacent to the mineral of interest expressed as a percentage of all the pixels associated with the mineral of interest.

Mineral of Interest: This term is equivalent to a ‘sort-category’. If one would like to determine the liberation characteristics of, for example, gold, the dataset will be sorted according to the characteristic ‘particle contains gold’.

Particle: Several grains make up a particle. A particle usually refers to a fragment of a rock or ore, the size of which is dependent on crushing and milling conditions as well as the size class it deports to.

Ternary+ particle: Two or more phases are associated with the mineral of interest (whether enclosed or attached).

Weighted Average Grain Size: Due to stereological effects, the sectional size of the gold grains will always be smaller than the actual grain-size. It is therefore necessary to calculate a ‘weighted average grain-size’ in order to obtain a more realistic average gold grain-size; this is done by giving each grain a weight proportional to the volume fraction of that grain, i.e. a large grain will have a bigger weight than a small grain.

CHAPTER 1: INTRODUCTION

1.1 BACKGROUND

Gold (Au) is generally found in two main forms: the first as pure native gold and the second as an alloy with other elements such as silver and mercury (referred to as electrum). The former is generally more common and is hosted by a variety of minerals in diverse geological environments. Gold belongs to the same group of elements as copper and silver in the periodic table and it is commonly found to be associated with these elements in ore assemblages (Juvonen, 1999). Some of the main minerals groups commonly associated with gold are the sulphides, silicates, oxides and carbonates. Sulphide ores contain variable quantities of electrum and native gold, whereas silicate ores are dominated by native gold. South Africa's gold deposits are predominantly located in the Witwatersrand Basin with some limited occurrences in greenstone belts such as the Barberton greenstone belt. The focus in this project was on gold found in the Witwatersrand Basin, which is commonly associated with quartz and sulphide minerals. Figure 1-1 shows a map of South Africa and the location of the study area.

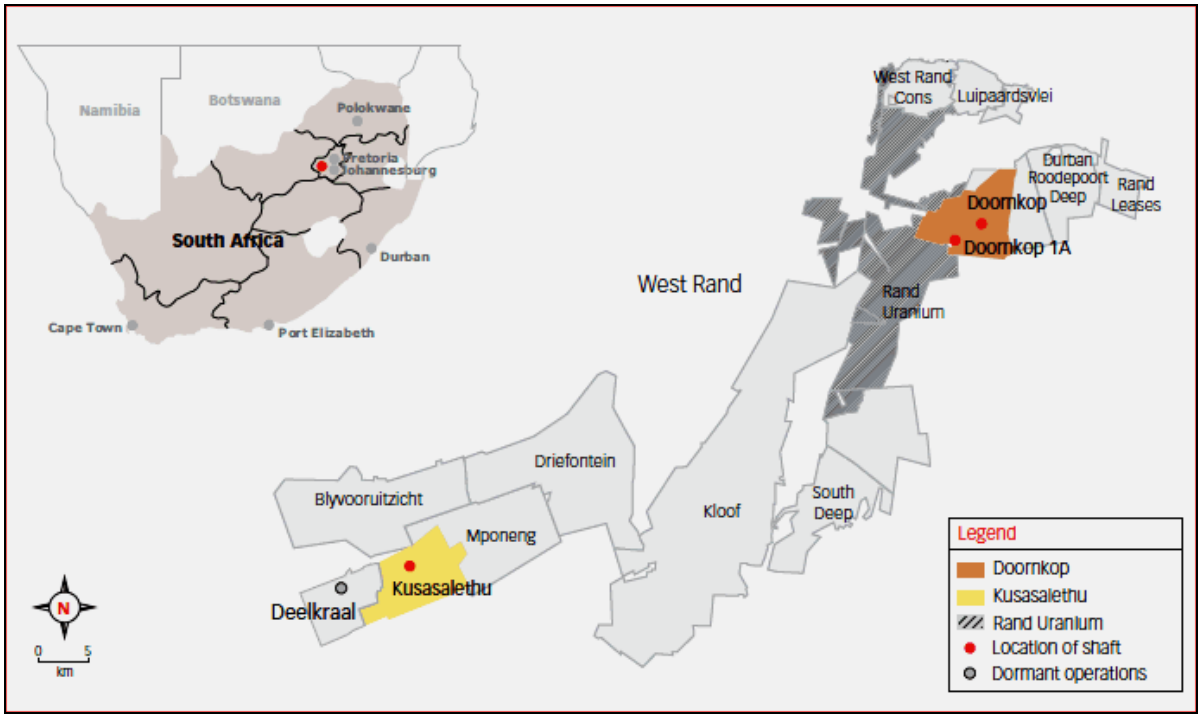

Figure 1-1: West Rand gold mines with special reference to Kusasalethu gold mine (Harmony Gold, 2013).

In terms of the South African economy, gold is one of the main natural resources. Based on 2011 figures, South Africa contributes 6.8 % (191 tons) to the global gold production. Regardless of the significant contribution from platinum group elements (PGE), diamond, coal, iron ore and a diversity of other small-scale mining activities, gold mining remains a key contributor to South Africa's economy (Chamber of Mines of South Africa, 2012). In 2011, it accounted for 10.7 % (R68.9 billion) in foreign currency earnings and 2 % of the gross domestic product (GDP). For the past 40 years, gold production in South Africa has progressively declined due to problems related to: (a) high energy costs; (b) decreasing gold ore grade; (c) accessibility difficulties; (d) safety issues; (d) labour unions' unrest and (e) economic uncertainties. Figure 1-2 illustrates South Africa's declining gold production rate over time (Chaize, 2009; Chamber of Mines of South Africa, 2012; Hartnady, 2009).

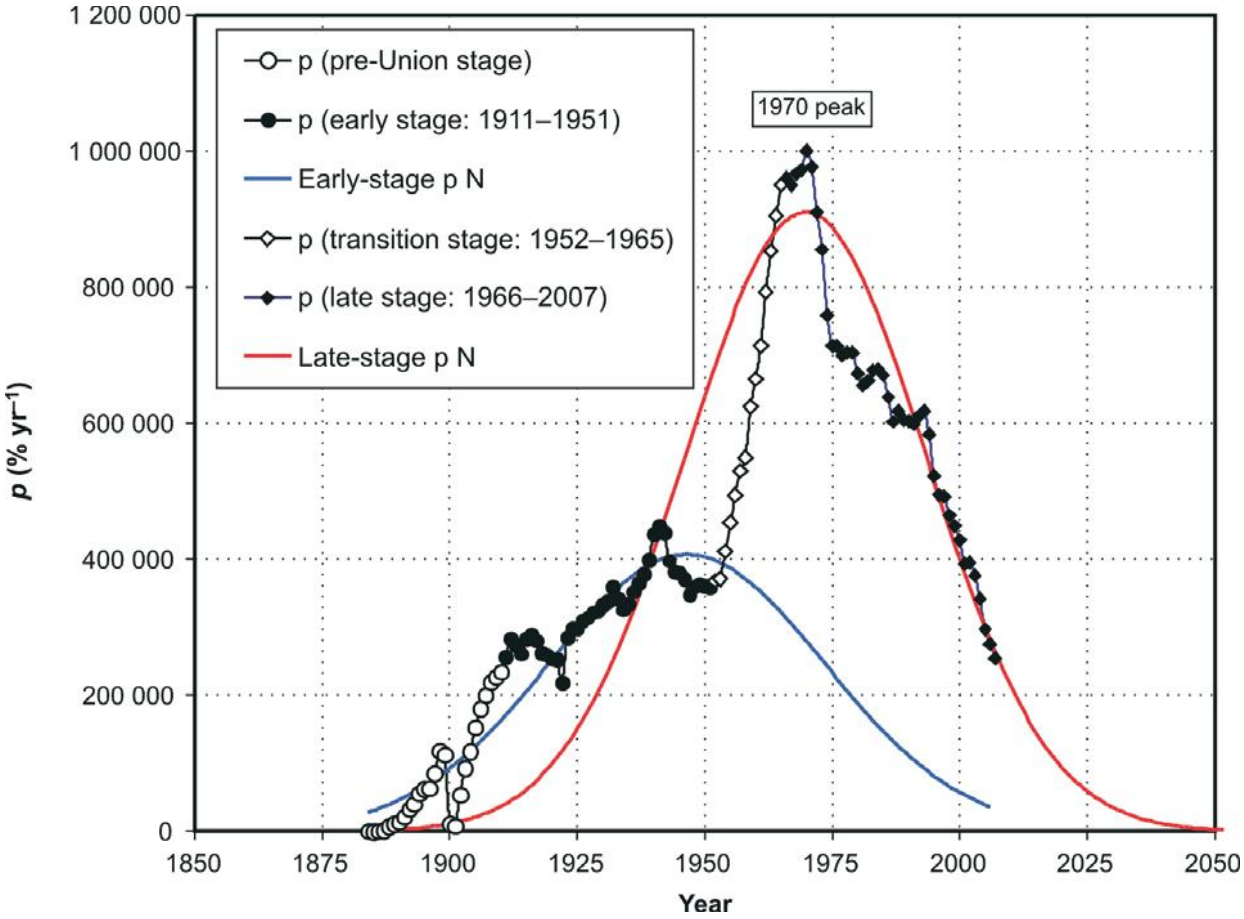

Figure 1-2: History of Witwatersrand Basin gold production rate (p, in kilograms per year (kg yr–1)), divided into four stages: 1) beginning, 1884–1910; 2) early, 1911–1951; 3) transition, 1952–1965; 4) late, 1966–2007. Data from Chamber of Mines of South Africa website, http://www.bullion.org.za. Best-fitting Gaussian (normal) distribution curves to the early-stage (blue curve) and the late-stage (red curve) data correspond to ultimate recoverable resource (URR) totals of 27 550 and 53 825 metric tonnes, respectively (Hartnady, 2009).

Conventional methods (such as ball mills for comminution and cyanide tank leaching for gold extraction) used to process gold are continuously being re-evaluated (Longley et al., 2002). This re-evaluation is due to the increasing mining depth, especially in what are the world's deepest mines, and the decreasing ore grade (Hartnady, 2009). Table 1-1 shows the top ten deepest mines in the world, of which eight are South African gold mines. If the obvious safety factors (for example, fall of ground due to seismicity, methane intersections and elevated temperatures) and market uncertainties (for example, low confidence from investors) are not enough, cost-effective solutions to the problems of mineral processing are crucial to the future of these historic deposits (Chamber of Mines of South Africa, 2012). Metallurgical costs principally arise from the energy requirements, particularly for comminution as fine particles (-75 µm) are necessary for efficient extraction of the quartz and pyrite-hosted gold by cyanide leaching. Since the gold head grades in the Witwatersrand ROM ores are only a few grams per metric ton (1.9 to 7 g/t), smart comminution practice needs to focus on the behaviour of the major rock forming minerals that make up the host.

Table 1-1: The top ten deepest mines in the world (Mining Technology, 2013).

Location	Name of mine	Depth (km)	Commodity
South Africa	Mponeng	2.4-3.9	Gold
South Africa	Tau Tona	3.9	Gold
South Africa	Savuka	3.7	Gold
South Africa	Driefontein	3.4	Gold
South Africa	Kusasalethu	3.3	Gold
South Africa	Moab Khotsong	2.6-3.054	Gold
South Africa	South Deep	2.95	Gold
Canada	Kidd Creek	2.93	Copper and Zinc
South Africa	Great Noligwa	2.6	Gold
Canada	Creighton	2.5	Copper and Nickel

Different comminution devices exist in gold processing (for example, stirred, autogenous and semi-autogenous mills), but they are all associated with high energy costs (Longley et al., 2002; Roufail, 2011). Comminution with high-pressure grinding rolls (HPGR) involves the more energy-efficient process of particle-bed breakage (compression breakage) and 10–50 % energy savings have been claimed on coarse particle (>2 mm) reduction when compared with other equipment (Patzelt et al., 1995; Rosario et al., 2009; Wipf, 2005). One of the important benefits of the HPGR is the production of numerous intra-particle fractures as a consequence of the compressive stresses that build up between the rollers. For harder ores such as the Witwatersrand quartzites, conventional comminution does not offer any major improvement options on crushing size fractions that are >2 mm in terms of energy and valuable mineral exposure (Dhawan et al., 2012). Although HPGR capital costs are higher, an operation would require several tertiary conventional crushers to provide the same crushing power contributed by one HPGR for the same size fraction (Baum and Ausburn, 2011). Structural weakening of this sort has resulted in facilitated size reduction, and of particular significance in this study, the creation of navigable pathways for leach solutions (Dunne et al., 1996; Ghorbani et al., 2013). Fracture patterns induced throughout the ore particles during various pressures of HPGR coarse comminution may be exploited by the leach solutions and promote further size reduction and continued gold dissolution (Kodali et al., 2011).

Traditional gold extraction routes such as cyanide tank leaching involve several stages that require high operating costs. Heap leaching as an alternative method of conventional gold cyanidation has been applied extensively to process low-grade copper, gold, silver and uranium ores. It has gained much popularity from the late 1970s (Petersen and Dixon, 2007). The process of heap leaching is generally considered as economically viable and less complex due to its design simplicity and low energy cost of processing low-grade ores (Dhawan et al., 2012). Its success is defined by complex factors such as: (a) the amenability of the ore; (b) particle size; (c) particle morphology; (d) ore porosity and permeability; (e) liquid and gas flow and (f) temperature distribution (Dixon and Petersen, 2003; Ghorbani et al., 2011; Leahy et al., 2007; Moreno et al., 1999). There are many successful heap leaching operations around the world amongst them are the Çöpler gold mine (Turkey) operated by Alacer Gold Corporation, Cripple Creek in Colorado (USA) operated by AngloGold Ashanti, and many more in Australia, North and South America (Alacer Gold, 2011; AngloGold, 2008). Comminution also plays a major role in the process of heap leaching as it is the most energy-intensive stage during metallurgical processing. Apart from the energy savings

achieved by avoiding fine grinding (-75 µm); heap leaching could become an alternative to traditional tank-based circuits. Furthermore, part of the leach extraction could conceivably be carried out underground, thereby avoiding the need to transport some of the mine feed to the surface and make use of the geothermal gradient in heating the cyanide leach solution. Active underground heap leaching technology has been implemented to process different low-grade deposits such as selected copper ores in the case of the Zambian Copper Belt and uranium in Australia (Steven, 2009; van der Lee, 2008).

Successful gold extraction methods are directly related to the intrinsic mineralogical features of the gold ore being processed (Jansen and Taylor, 2003; Chryssoulis and McMullen, 2005; Coetzee et al., 2011). Given that gold extraction is related to mineralogy, there is a need to have a good understanding of the mineralogy and its variation throughout the ore body. Representative samples extracted from variable domains, or composite samples of the ore body, must be utilised when conducting studies on the process mineralogy of gold (Coetzee et al., 2011; Lotter, 2011). Process mineralogy studies aim to cover aspects such as the nature and mode of occurrence of the gold within any sample (ore, metallurgical product, panned concentrate and tailings). These further characterise its speciation, grain size and shape, mineral association, chemistry and liberation characteristics.

Carbonaceous material, graphite and clays are known to adsorb dissolved gold-cyanide complexes leading to gold losses and this process is known as ‘preg-robbing’ (Zhou et al., 2004). Fe-bearing minerals such as pyrite and pyrrhotite are known to present a variety of challenges during gold extraction: reaction passivation, consumption of free cyanide and oxygen). Compared to pyrite, pyrrhotite is even more susceptible to oxidation (Becker et al., 2010; Belzile et al., 2004; Rand, 1977).

In the past, traditional mineralogical studies focused on the use of optical microscopy. In the last two decades, 2D automated scanning electron microscopes such as MLA, QEMSCAN and TIMA have revolutionised process mineralogy by being able to provide relatively rapid (compared to traditional methods) information on all aspects of the ore mineralogy (Benvie, 2007; Goodall et al., 2005). The more recent application of the state of the art X-ray computed tomography (X-ray CT) into process mineralogy has provided the capacity for non-destructive 3D imaging down to 500 nm with little or no sample preparation required. Although X-ray CT is well known in the medical industry, it has recently gained significant attention from the mining, mineral processing, oil and gas industries (Chetty et al., 2012; Ghorbani et al., 2011; Ketcham and Carlson, 2001; Kyle et al., 2008; Miller and Lin 2009).

There is limited literature in the public domain on the application of X-ray CT for gold characterisation.

In the case of Witwatersrand gold ores, more economically viable methods of gold liberation and extraction are desired if these gold deposits are to continue contributing to the future of the South African economy. Various process mineralogical studies on a range of operations have shown the benefit (overall energy savings, cost savings and improved metal recoveries) achieved in heap leach operations (Coetzee et al., 2011; Lotter, 2011). In order to achieve these benefits, a complete characterisation of the ore must be undertaken in conjunction with experimental tests to determine the ore metallurgical performance (Taylor, 2011; Kodali et al., 2011). A comprehensive understanding of HPGR technology in comminution, mineralogy and its relationship to heap leach behaviour is needed to successfully optimise or control the behaviour of an ore during heap leaching. The benefits derived by a multidisciplinary approach, such as process mineralogy, not only result in process efficiency but, also contribute to sustainable development strategies: mining of low grade ores, improving safety, conservation of water and reduction of energy consumption , which are key themes of the UCT Minerals to Metals Initiative.

1.2 PROBLEM STATEMENT

The gold mines in South Africa are well known to be some of the deepest mines in the world sometimes reaching up to approximately 4 km depth below surface. It is not surprising that the mining related costs of gold in South Africa may result in questions about the economic viability. Traditional methods of gold production involve comminution (size reduction using ball mills) and processing via cyanide tank leaching (gold extraction) which are associated with their own energy, cost and environmental implications. Consequently, numerous opportunities for novel improvement and optimisation strategies in gold mining and processing exist in South Africa. One such strategy involves the use of the more energy efficient HPGR for comminution coupled with cyanide heap leaching compared to tank leaching. A suitable approach to investigate the potential of these novel strategies requires an integrated approach of the ore mineralogy and the application of 3D imaging using micro-focus 3D X-ray CT.

1.3 OBJECTIVES OF THIS STUDY

The objective of this study is to investigate the potential of Witwatersrand gold ore for heap leaching as a contribution to evaluating alternative cyanide leaching strategies in a process mineralogical framework. A composite sample prepared using HPGR, comprising the Ventersdorp Contact Reef (VCR) and Elsburg Reefs (ER) will be characterised using state-of-the-art micro-focus X-ray CT together with other complementary analytical tools and process mineralogy techniques prior to a set of laboratory scale column leach tests.

1.4 KEY QUESTIONS

The objectives of this research will be addressed by exploring the following key questions:

(i) What information can be obtained on a Witwatersrand gold ore using micro-focus X-ray CT?
(ii) What are the effects of HPGR feed pressure, crack volume, crack width and distribution on comminution of the Witwatersrand gold ore?
(iii) What are the mineralogical features of the Witwatersrand gold ore affecting cyanide leaching and heap leaching?
(iv) Is there potential for heap leaching the Witwatersrand gold ore?

1.5 SCOPE OF RESEARCH

Aspects of comminution, hydrometallurgy and mineralogy will be covered in this study. The scope and limitations of this study are illustrated in Figure 1-3. Mineralogical aspects focused on in this study are petrography, mineral chemistry and deportment (mineral liberation, gold grain size, association and morphology). This will be measured using QEMSCAN, X-ray CT, optical microscopy, XRF, ICP-MS and QXRD techniques. Specific mineral relativities (pyrite and pyrrhotite) were only investigated to predict their behaviour during gold cyanidation by consideration of mineral morphology and theoretical galvanic interactions and not by dedicated electrochemical techniques. The focus of this study was on gold process mineralogy and therefore excluded additional metals (U, Ag and Pt) associated with the Witwatersrand gold ores.

The only beneficiation components that are considered here are comminution and gold cyanidation. Comminution in this study focused on assessing different HPGR crushing pressures and the induced crack network. The cyanidation component of the beneficiation process investigated the dissolution of gold from Witwatersrand ore in a set of laboratory scale cyanide column leaching experiments by monitoring pH and gold recovery over a period of two weeks. Gold processing and refinery processes such as carbon-in-pulp (CIP), carbon-in-leach (CIL), electrowinning (EW) and smelting fall beyond the scope of this study.

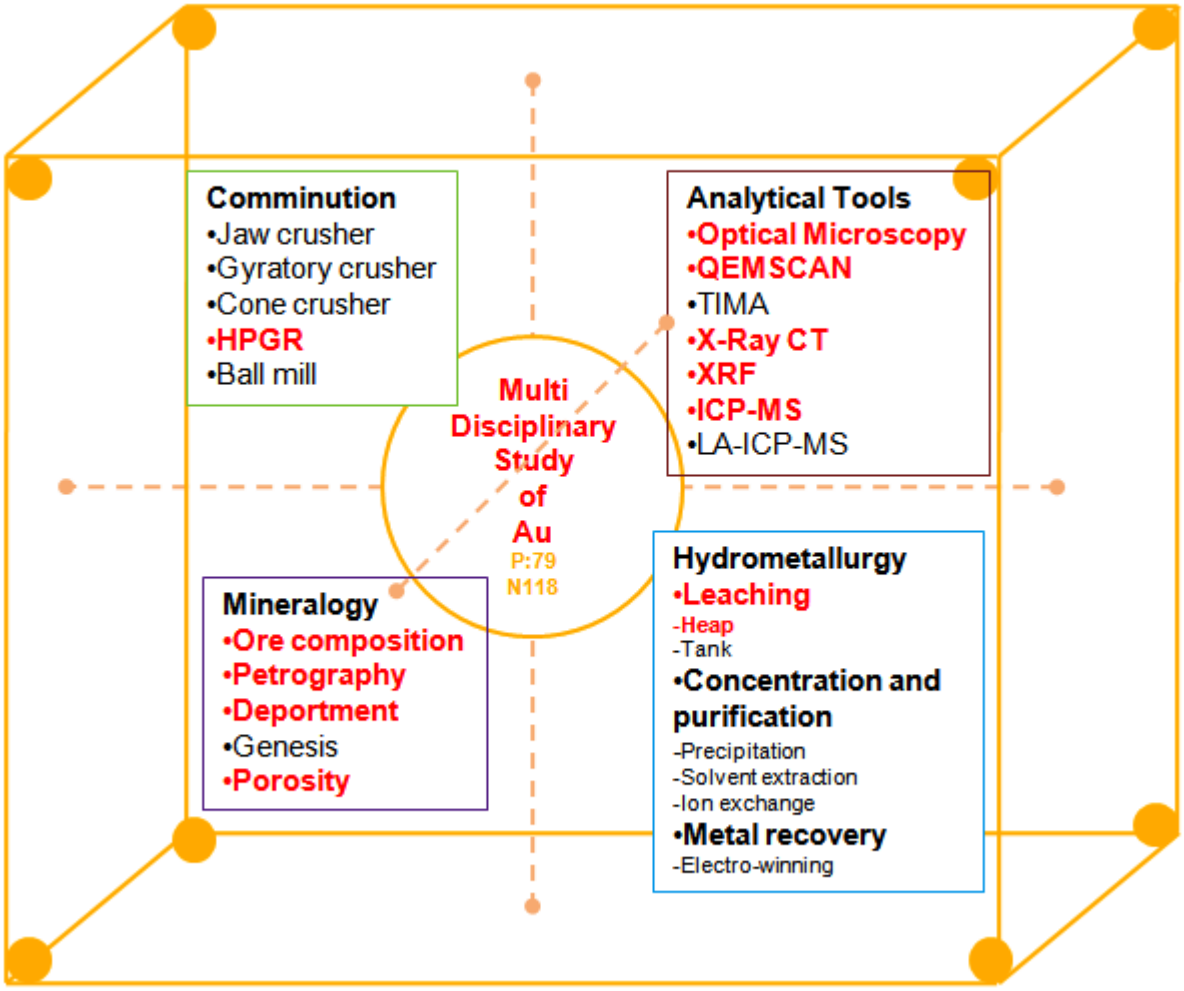

Figure 1-3: Gold crystal structure illustrating research scope and limitation (red text and lines indicate aspects covered in this study).

1.6 ORGANISATION OF THE THESIS

The body of this thesis is divided into seven chapters, starting with the Introduction in Chapter 1, in which the background, scope of the thesis and key questions are presented. This is followed by a critical review of the literature in Chapter 2, focusing on gold ore deposits, gold mineralogy, electrochemical properties of gold, gold heap leaching and the field of process mineralogy. A summary of the regional and local geological setting of Witwatersrand ore is given in Chapter 3. Chapter 4 provides details of the techniques and experimental methods used for ore characterisation and cyanide leaching experiments. Chapter 5 details the specific development of the X-ray CT ore characterisation method in conjunction with more routine process mineralogy tools. Chapter 6 presents the results from the experimental tests investigating the potential of Witwatersrand ore for heap leaching. A concluding discussion summarising the findings as well as several recommendations for further research are given in Chapter 7. The complete set of results from the various analyses and experiments are presented in the appendices.

CHAPTER 2: LITERATURE REVIEW

2.1 CHEMICAL AND PHYSICAL CHARACTERISTICS OF GOLD

Gold is a precious metal due to its relatively low abundance and its unique physical and chemical characteristics. It is defined as a heavy metal that is: (a) soft – can be scratched with a finger nail; (b) malleable – can be hammered into sheets; (d) ductile and (e) bright sun yellow in colour when pure. The most familiar unit of weight for gold is the troy ounce which is equivalent to 31.10 g (McKibben, 2005). Gold occurs in two known oxidation states: the first one is as Au^{+} (aurous) and the second is as Au^{3+} (auric). Its chemical symbol, Au is derived from the ancient Latin word *aurum* meaning 'shining dawn'. It has atomic number of 79 in the periodic table of elements (Figure 2-1). The average concentration of gold in the earth's crust is 0.005 g/t and it is much lower than most other valuable metals, such as 0.007 g/t for silver and 50 g/t for copper (Wong Wai and Arun, 2009).

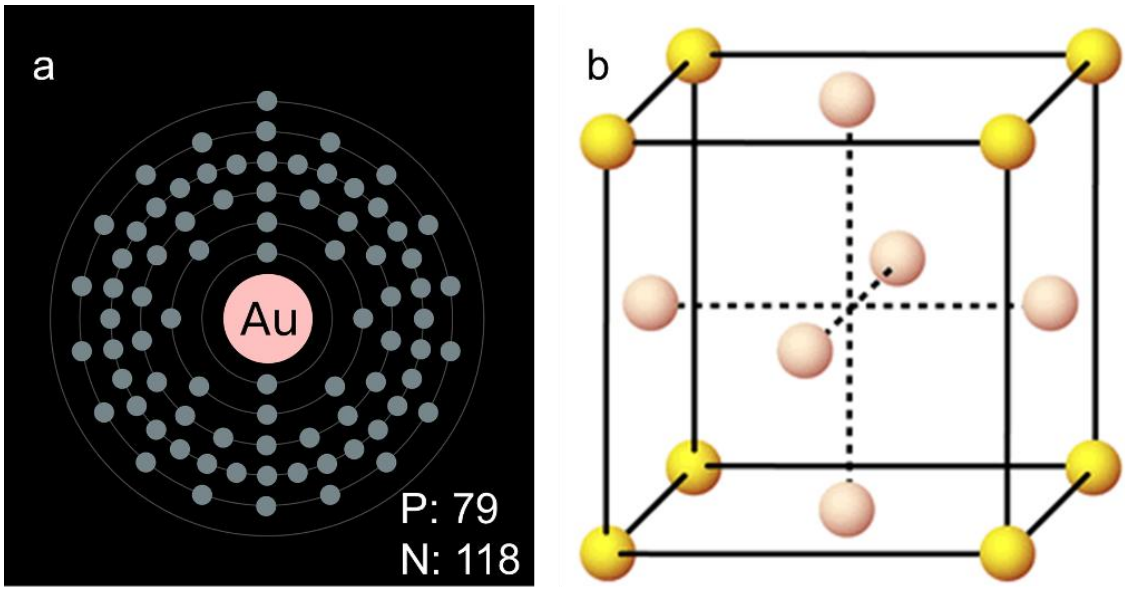

Figure 2-1: Structure of gold: (a) Atomic structure of gold; b) Crystal arrangement for metallic gold (http://www.chemicalelements.com/elements/au.html).

2.2 OVERVIEW OF GOLD ORE DEPOSITS

Gold predominantly forms via precipitation from hydrothermal fluids and thus has been exploited from ore deposits formed by this important mineralising process (Frimmel and Minter, 2002; Robert et al.,1997). Gold ore deposits can be classified based on mineralogy and texture which influence their extraction. Ores containing discrete gold particles distributed along the margins of the host assemblages are described as *free milling gold*. *Refractory ores* contain gold enclosed in host minerals which may need to be processed further to liberate the precious metal. Using combinations of gold mineralogy and mineral processing techniques, gold bearing ores are classified into seven categories (Table 2-1):

Table 2-1: Classification of gold deposits (Zhou et al., 2004).

Deposit Type	Characteristics
Placers	Gold is easily liberated or has been liberated prior to processing, for example, Witwatersrand (RSA).
Quartz vein-lode ores	Gold occurs mainly as native gold in quartz veins, lodes or stock works, for example, Homestake (USA).
Oxidised ores	Gold usually occurs as either liberated or in the alteration products of sulphide minerals, and the degree of gold liberation is generally increased by oxidation, for example, Pierina (Peru).
Iron sulphide ores	Gold occurs as liberated particles, attachments to and inclusions in sulphide (commonly in pyrite, and less commonly in marcasite and pyrrhotite, and as sub-microscopic gold in sulphide minerals, for example, Carlin-type (USA).
Arsenic sulphide ores	Gold occurs as liberated particles and inclusions, and sub-microscopic gold in arsenopyrite and oxidised products, for example, Sao Bento (Brazil).
Telluride ores	Gold occurs as native gold and gold tellurides, either liberated or locked in sulphides, for example, Cripple Creek (USA).
Carbonaceous-sulphidic ores	Gold occurs mainly as fine-grained particles, sub-microscopic gold in sulphides, and surface gold absorbed onto the surface of carbonaceous matter and iron hydroxides, for example, Meikle (USA).

2.3 GOLD CYANIDATION

2.3.1 Principles of gold cyanidation

The most common method of processing gold is the process of *cyanidation* which was first introduced in 1887 by McArthur and Forrester. For the past century, several studies have been conducted with the aim to optimise the efficiency of the cyanidation process (Fivaz, 1988 and references therein). Cyanide is universally used due to its relatively low cost and great effectiveness for gold dissolution. Variables affecting gold cyanidation involve mineralogy of the ore, available free cyanide concentration, pH and temperature. Cyanide (CN^-) is a single carbon atom with a triple bond to a nitrogen atom that is useful in extracting gold from the ore through a process of gold cyanidation (Fivaz, 1988). While cyanide is both economically viable and effective, the use and transportation poses a significant environmental and human risk due to its toxicity (ICMC, 2013). Despite the toxic nature of cyanide, most hydrometallurgical operations take place in open reactor vessels (open heaps, tanks and vats).

2.3.2 Chemistry of cyanide and gold dissolution

The most widely used sources of cyanide in gold extraction are sodium cyanide (NaCN), Potassium Cyanide (KCN) and Calcium Cyanide (Ca (CN_2)). These compounds easily dissolve and ionise in water to form a metal cation (i.e. Na^+) and free cyanide ions (CN^-) illustrated in equation 2.1. Cyanide leaching is effective at a pH of 9.5 to 11. When cyanide ions associate with water, they form HCN and OH^- ions which increase the pH (equation 2.2). At a high pH, the total dissolved cyanide exists as free cyanide. Half of the total cyanide exists as HCN and the other half as free cyanide at pH region of 9. Undesirable reactions (equation 2.3 and 2.4) might occur during cyanide leaching. This can happen because hydrogen cyanide and free cyanide can be oxidised by oxygen to form cyanate (CNO^-). Cyanate does not dissolve gold. The overall effect of cyanate is that it reduces the available free cyanide concentration consequently slowing down the reaction (Marsden and House, 1992).

$$NaCN \leftrightarrow Na^+ + CN^- \qquad \text{Eq. (2.1)}$$

$$CN^- + H_2O \leftrightarrow HCN + OH^- \qquad \text{Eq. (2.2)}$$

$$4HCN+3O_2 \leftrightarrow 4CNO^-+2H_2O \quad \text{Eq. (2.3)}$$

$$3CN^-+2O_2+H_2O \leftrightarrow 3CNO^-+ 2OH^- \quad \text{Eq. (2.4)}$$

Oxidation of gold is a prerequisite for its dissolution in alkaline cyanide solution. The cyanidation process involves dissolution of gold ore in a dilute cyanide solution in the presence of lime and oxygen of which the resultant reaction is referred to as the *Elsner's equation*. During the reaction series, oxygen is reduced and hydrogen peroxide is formed as an intermediate product: equation 2.5 (Bodlander, 1896). Hydrogen peroxide becomes the oxidising agent in the second reaction (see equation 2.6) of which the balanced reaction is presented in equation 2.7 (Elsner, 1846).

$$2Au+4NaCN+O_2+2H_2O \rightarrow 2Au\ (CN)_2^-+2NaOH+H_2O_2 \quad \text{Eq. (2.5)}$$

$$2Au+4CN^-+ H_2O_2=2Au\ (CN)_2^-+2OH^- \quad \text{Eq. (2.6)}$$

$$4Au+8NaCN^-+O_2+2H_2O \rightarrow 4NaAu\ (CN)_2+4NaOH \quad \text{Eq. (2.7)}$$

The reaction series depends strongly on oxygen which is added by bubbling air through the solution or by spraying the solution onto the leach heaps. Elsner's equation (equation 2.7) is stoichiometrically correct, but it does not cater for the cathodic reaction associated with gold dissolution since the dissolution involves an electrochemical process in which the anodic reaction is gold dissolution and the cathodic reaction is oxygen reduction. Anodic reaction takes place at the reacting particle surface which is constantly reduced as the process proceeds (Wong Wai and Arun, 2009). Several theories exist describing the dissolution mechanism under both acidic and alkaline condition (Marsden and House, 2006). It is important to understand the rate controlling factors of gold cyanidation which will allow the selection of correct operating conditions. These conditions are explained through the use of the electrochemical nature of the gold cyanidation reaction. The reaction is determined by the rate of diffusion of cyanide or dissolved oxygen to the gold surface depending on their relative concentrations (Kudryk and Kellogg, 1954).

Redox potential during gold cyanidation is one of the most important factors used to explain the stability of gold and other species in aqueous solutions. Redox potential is related to the potential-pH diagrams (Eh-pH diagrams) or Pourbaix diagrams (Figure 2-2) described using the *Nernst equation* (equation 2.8).

Nernst Equation: $E = E^o - \frac{RT}{nF} \ln K$ Eq. (2.8)

In which,

E = potential for reduction-oxidation reaction

E^o =standard potential for reduction-oxidation reaction

n = number of electron involved in the electrochemical reaction,

F = Faraday constant = 96485 Coulomb/mole of electron

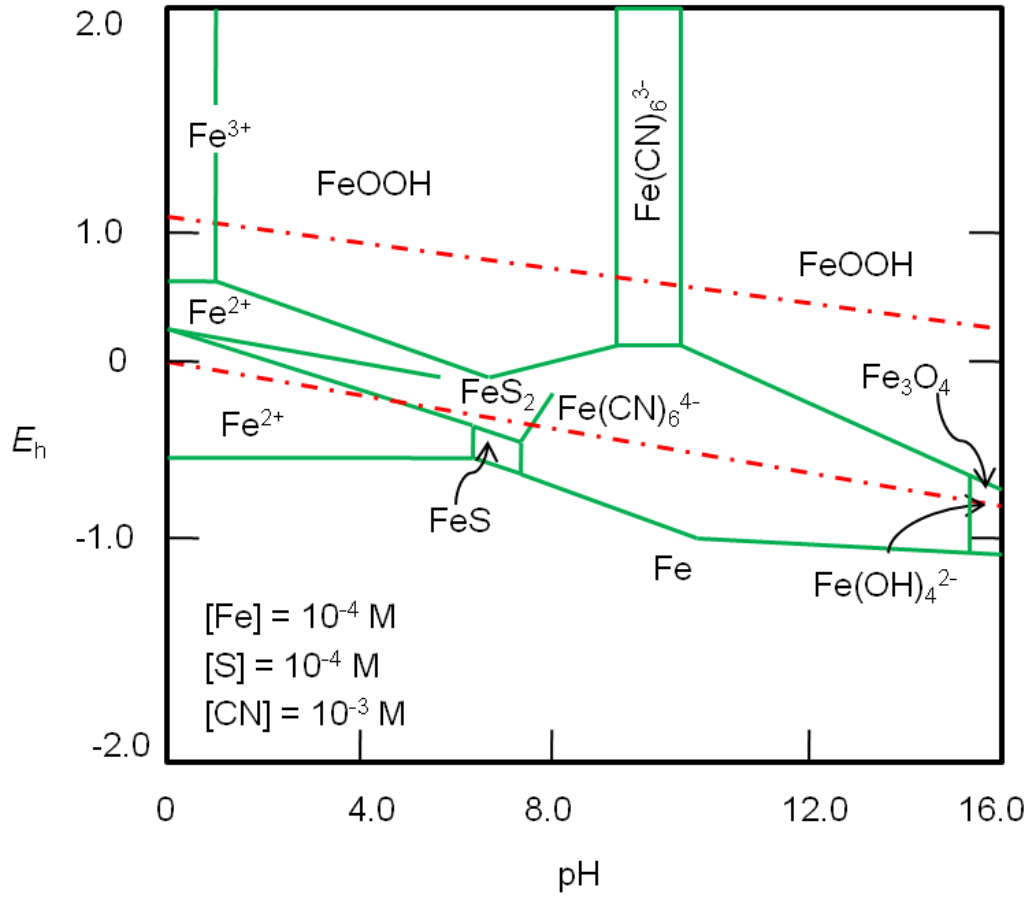

Figure 2-2: Eh-pH diagram for the Fe-S-CN-H_2O system at 25°C (Marsden and House, 1992).

2.3.3 Application of gold cyanidation

The application of gold cyanidation is detailed in Figure 2-3 which shows the process flow sheet. The process begins with crushing of ROM ore, followed by grinding and classification. The milled ore is then fed to a series of tanks for cyanidation. Lime is added to the cyanide pulp to prevent hydrolysis and neutralise any acidic bicarbonate in the mill water. Gold in

solution is then loaded onto activated carbon by adsorption. When the loading is complete, the gold is eluted, or desorbed from the carbon and recovered by electrowinning or zinc precipitation prior to smelting. Several other stages such as cyanide reduction and destruction, reagent mixing, water recovered and re-used, storage, tailings pump and disposal to tailings storage facility are site specific (Aghamirian and Yen, 2005; Sánchez-Chacón and Lapidus, 1997a; Vorster and Flatman, 2001).

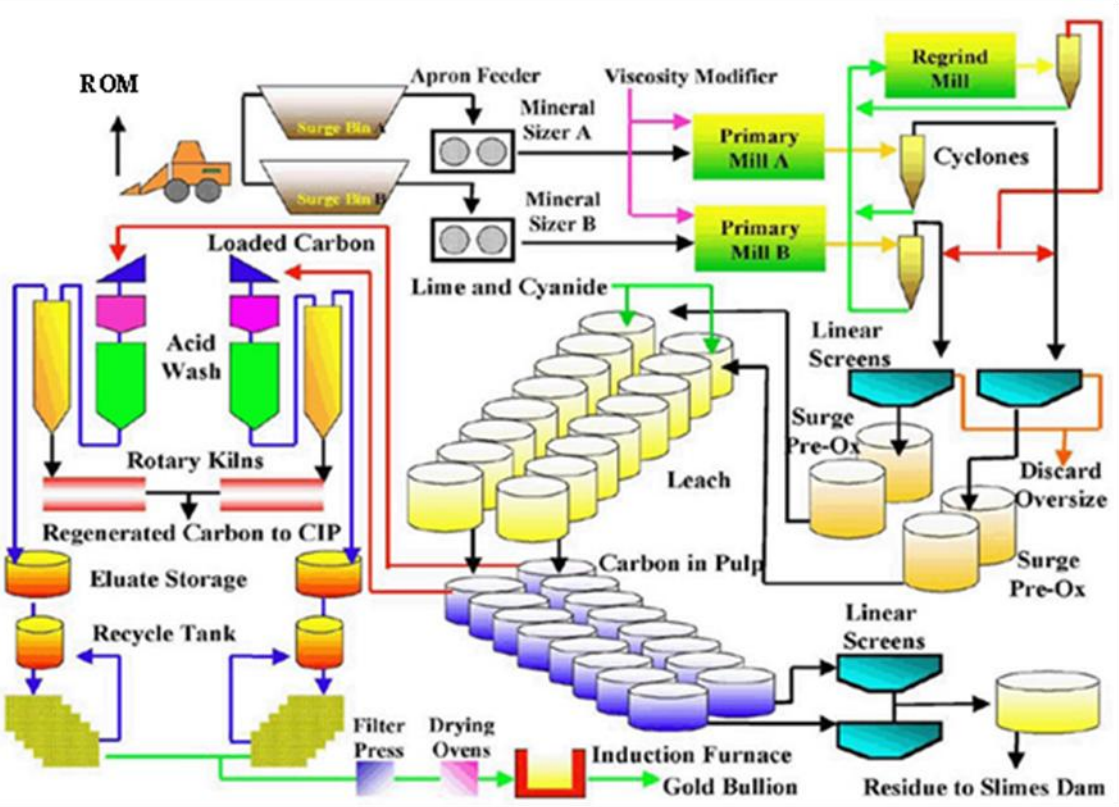

Figure 2-3: Gold cyanidation process flow sheet (http://dcsengineer.com/app_mining.html).

2.4 CHEMICAL HEAP LEACHING

Since its large-scale application to gold processing in the 1970s at Carlin (Nevada, USA), heap leaching has been applied extensively over the past four decades (Figure 2-4). It has been used mostly to process low grade gold, silver, uranium, copper and zinc ores (Petersen and Dixon, 2007; Trexler et al., 1990; Trexler et al., 1987). Copper bearing ores are the largest installations in terms of land area and annual tonnage processed. In the USA, heap leaching accounts for approximately 30 % of their copper production.

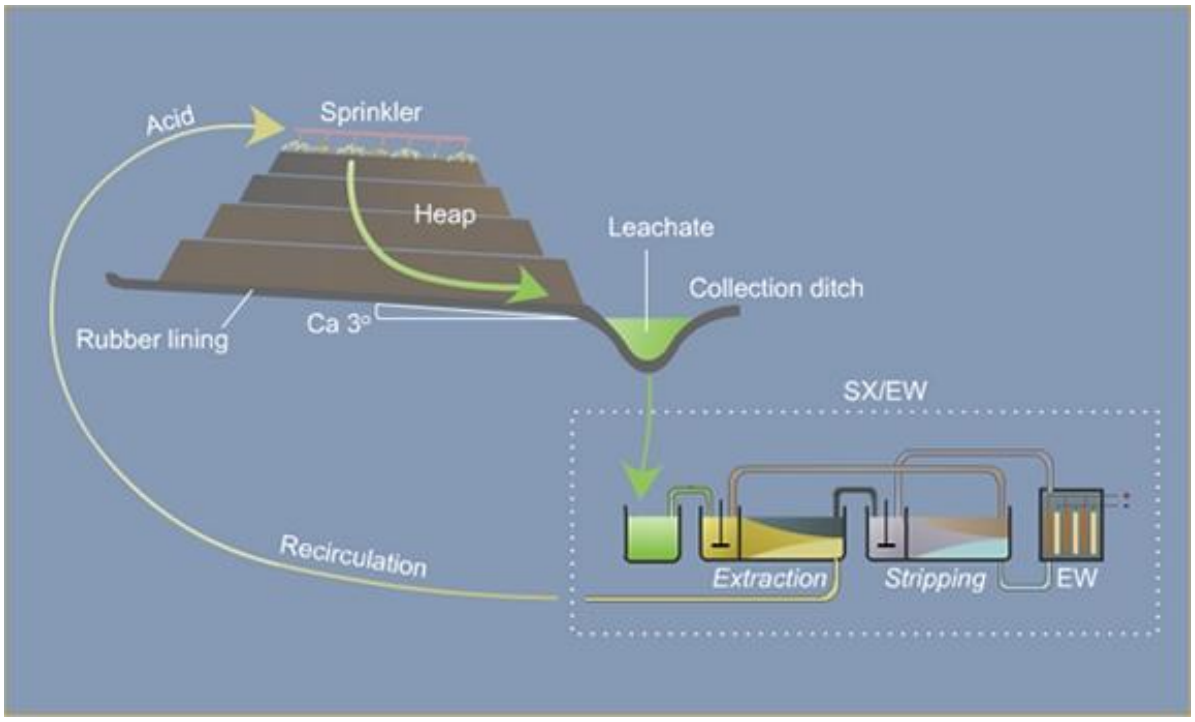

Figure 2-4: Schematic diagram of chemical heap leaching (wiki.biomine.skelleftea.se).

The heap leaching process entails drip irrigation or sprinkling of a lixiviant (cyanide solution in gold ores) over a stacked pile of crushed ore on an impervious pad (Figure 2-4). Cyanide solution dissolves the gold from the host gangue minerals and the *pregnant leach solution* (PLS) passes down through the ore pile. The pregnant leach solution is recovered at the bottom of leach pad which usually consists of a geo-membrane liner and sometimes clay (either to create a true composite liner or more commonly as good quality bedding layer for the geo-membrane). Permeable crushed rock drainage system called an over liner with a drainage pipe network is also used (Thiel and Smith, 2003). The pregnant solution is then pumped through tanks containing activated charcoal at the process plant which absorbs the gold. Gold-bearing charcoal is chemically treated to release the gold and is reactivated by heating for future use. The resultant gold-bearing strip solution with high concentration is treated at the process plant to produce a bar of impure gold. The impure bar is sent to a smelter for refining.

2.4.1 Chemical heap leach dissolution kinetics

Various mathematical and production models of heap leaching have been proposed describing gold leaching as a function of mass transport steps and kinetic expressions (Sánchez-Chacón and Lapidus, 1997). Figure 2-5 illustrate the heap production model and input parameters. The degree of gold liberation or exposure is one of the controlling mechanisms in heap leaching. Adequate solution residence time is required thus the percolation rate of the fluids should also be slow enough to provide sufficiently long contact of the lixiviant with the ore particle. This is done to dissolve the metal of interest. Compound measures are frequently adopted during ore preparation (comminution) of which primary crushing is applied to reduce particle size down to approximately 15 mm. Secondary and tertiary crushing are applied to reduce particle size to the required size fraction generally >2 mm for heap leaching. Run-of-mine ore material requires minimal breakage following normal production related blasting. During comminution a certain amount of fines are generated. These may lead to decreased permeability and in extreme cases resulting in heap clogging (Robertson, 2008).

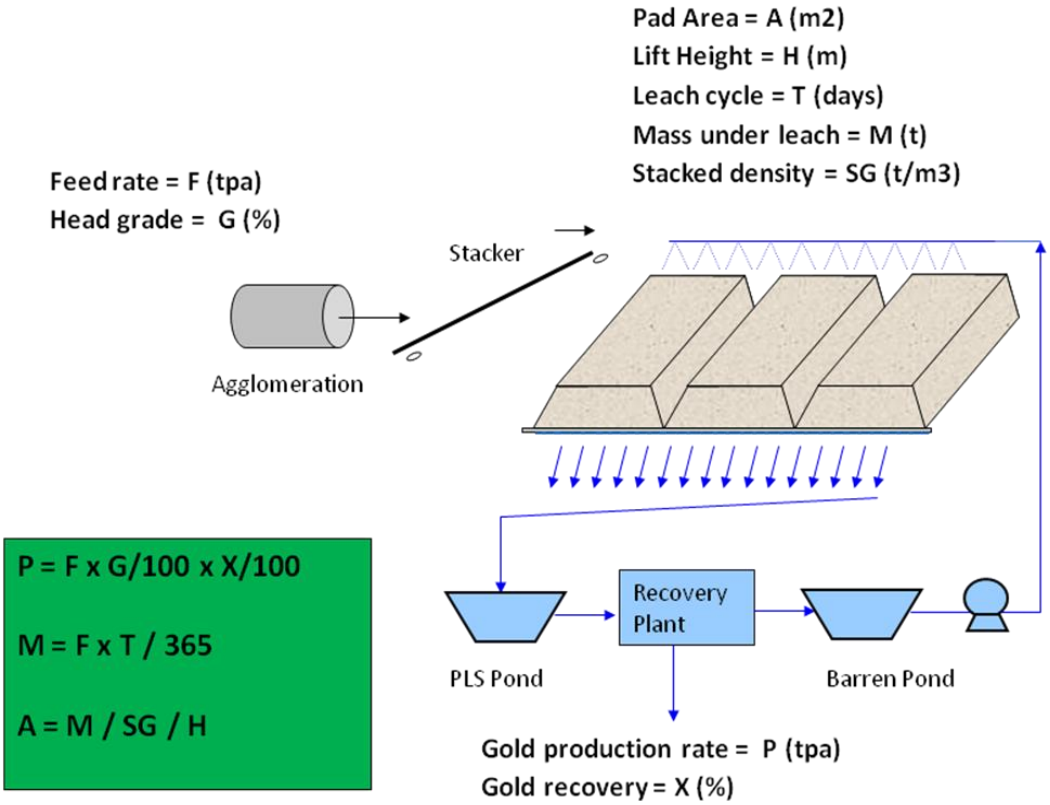

Figure 2-5: Simulation of heap leach production model (Robertson, 2008).

Leach recovery rates generally increase under higher lixiviant concentrations, temperature, dissolved oxygen and pH (>9.5) for cyanide leach and lower pH (<2) for acid leach conditions (Robertson et al., 2005). Metal extraction rates in comparative leach kinetics of oxide, transitional and sulphide gold ores from the Kisladag mine heap leach unit in Turkey are shown in Figure 2.6. Results show an initially fast leaching rate reaching up to 60 % extraction over the first 10 days of leaching. This is followed by an intermediate rate period reaching up to 70 % which occurs between the first 10 to 30 days. Lastly, a steady phase reaching up to 90 % gold extraction over a period of 90 days follows. The initial fast leaching rate period during leaching is a function of liberation degree and accessibly of valuable mineral. Minerals that are liberated will leach first and the encapsulated minerals require pathways through cracks and pores for the leach solution to percolate (Ogbonna et al., 2006). The highest gold recovery reaching up to 90 % can be achieved in typical oxide gold ore over 90 days leach cycle whereas sulphide gold ores will yield an average of 60 % over the same period. Transition gold ores can recover an average of 70 % gold on the same duration and this is controlled by mineral dissolution potential amongst other factors (Robertson et al., 2005; Zanbak, 2012).

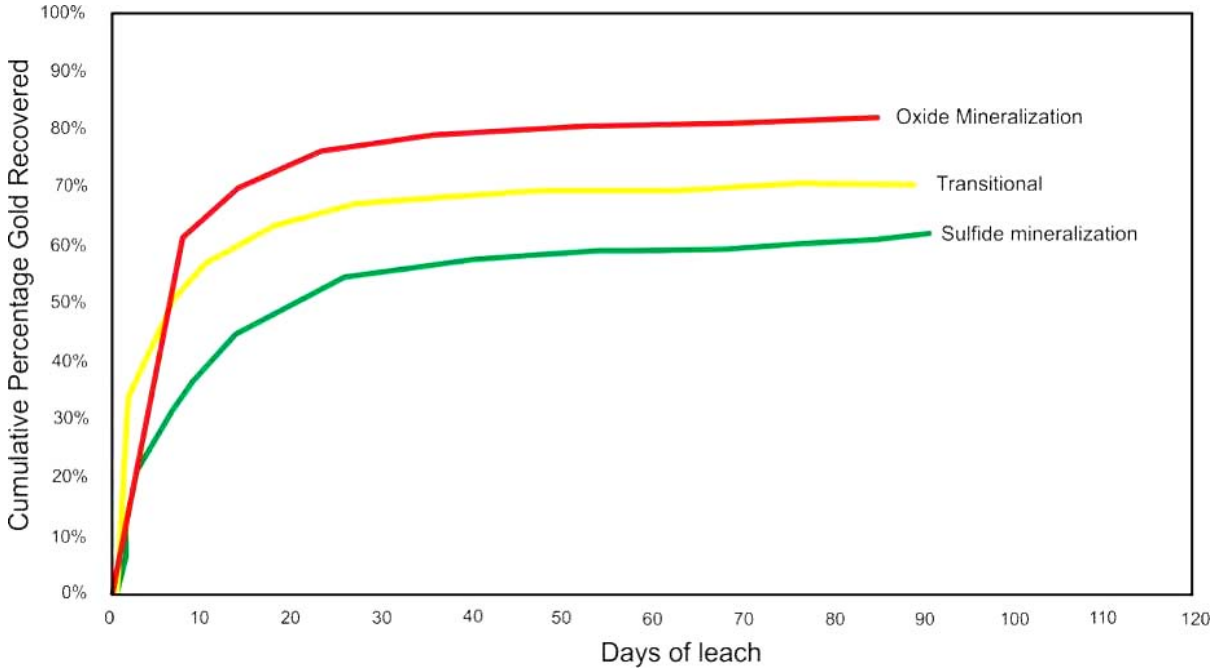

Figure 2-6: Comparative leach kinetics of oxide, transitional and sulphide gold ores in heap leaching (Tuprag Gold Co., Kisladag Mine Heap Leach Unit, Turkey).

2.4.2 Advantages and disadvantages of heap leaching

Typical chemical heap leaching requires 60 to 90 days for processing ore that could be leached in 24 hours in a conventional agitated leach plant; but it has the following *operational advantages compared to tank leaching*:

i) Comminution: agitated leaching requires finely milled (-75 µm) ore whereas heap leaching is done on coarse crushed particles. A reduction in cost and energy input in the heap leaching technology is one of the benefits compared to conventional leaching which is associated with high energy cost and complex designs. Nevertheless, in almost all heap leaching operations, ore is crushed and agglomerated prior to placement on the heap to increase permeability of the heap and maintain the high pH needed for leaching to occur (Robertson, 2008).
ii) Solids-liquid separation steps are not required for heap leaching.
iii) Tailings disposal costs are very high for conventional agitated leaching and are associated with liquid containment dams whereas heap leach pads can be left in place for reclamation.

Disadvantages of heap leaching:

i) The stacked ore must be porous enough to allow the solution to percolate through the heap.
ii) High clay content results in heap clogging
iii) Solution concentration is affected in places with high rainfall
iv) Long leach cycles and hold-up
v) Lengthy experimental programmes
vi) Large footprint
vii) Acid-mine drainage wastes

The above mentioned disadvantages usually result in mining companies using agitated leaching for high grade ores and heap leaching for low grade material and surface dumps.

2.4.3 Effect of sulphide minerals during gold cyanidation

There are two most common mechanisms through which sulphide minerals can interfere with gold cyanide leaching namely: (a) galvanic interaction between gold and the conducting mineral in contact with gold and (b) through dissolution of the mineral which influences solution speciation (Marsden and House, 2006). Most metal sulphides decompose readily in aerated alkaline cyanide solution and commonly get oxidised to form thiocyanate. This results in the formation of sulphate and sulphide complexes. These newly formed complexes are adsorbed onto gold surfaces resulting in a slow gold dissolution rates (Aghamirian, 1997). The behaviour of gold dissolution in the presence of sulphide minerals depends strongly on the solubility of sulphides and the oxygen concentration in the solution. Sulphide minerals are to some extent soluble in cyanide solution and tend to dissociate in the leaching solution. Kinetic studies indicated that sulphur species also directly affect the gold leaching reaction due to their ability to form passive film of sulphur (Aghamirian and Yen, 2005; Deschênes et al., 2009). Below are some of the most common sulphides and their effect on cyanidation:

i) Pyrite

The effect of pyrite during gold leaching depends on the morphology, concentration and distribution of pyrite mineral. When the gold ore contains less than 10 % of pyrite, leaching rates are barely affected. Kinetic leaching studies have indicated that gold extraction rates get reduced to approximately 80 % where the concentration is > 20 % (Liu and Yen, 1995; Guo et al., 2004).

ii) Pyrrhotite

The effect of pyrrhotite is largely determined by its form and concentration. Pyrrhotite exists in two main forms (i.e. magnetic and non-magnetic) of which both forms are problematic when compared to pyrite. Magnetic pyrrhotite is well known to be the oxygen consumer (Becker et al., 2010). Oxidation and non-oxidation dissolution studies of pyrrhotite identified that oxidative dissolution character is acid-producing and non-oxidative dissolution is acid-consuming (Thomas et al., 2000).

iii) Galena

Galena is usually converted to lead hydroxide via the oxidation of sulphide during gold cyanide leaching. Lead catalyses the oxidation of soluble sulphide to thiocyanate through

the precipitation of lead sulphide. Galena is oxidised to thiocyanate producing lead ions which precipitate to form lead hydroxide. This reduces cyanide efficiency leading to prolonged extraction rates (Guo et al., 2004; Marsden and House, 1992).

iv) Chalcopyrite

$CuFeS_2$ dissolves rapidly during gold cyanidation, forming soluble copper cyanide complexes. Copper dissolution is undesirable since it consumes cyanide and oxygen. Continuous addition of fresh free cyanide solution in the reactor can prevent the effect of copper (Dai and Jeffrey, 2006; Marsden and House, 2006).

2.4.4 Mineral exposure in crushed particles

It is important to understand the liberation and exposure of minerals during size reduction. This has a significant influence on the advancement of physical or chemical mineral dressing. Several parameters on liberation status have been proposed to solve mineral concentration and extraction problems (Austin and Luckie, 1988). Mineral grains do not necessarily need to be completely liberated for hydrometallurgical extraction of metals. Surface front for solution attack during leaching can be provided by partial exposure of mineral grains (Hsih et al., 1995). Figure 2-7 illustrates the concept of exposure and liberation of a particular mineral in an ore feed. Research indicated the importance of comminution media (i.e. HPGR) partial exposure of valuable mineral through creation of micro-cracks which assist with solution-valuable mineral interaction during leaching resulting in improved metal extraction (Kodali et al., 2011).

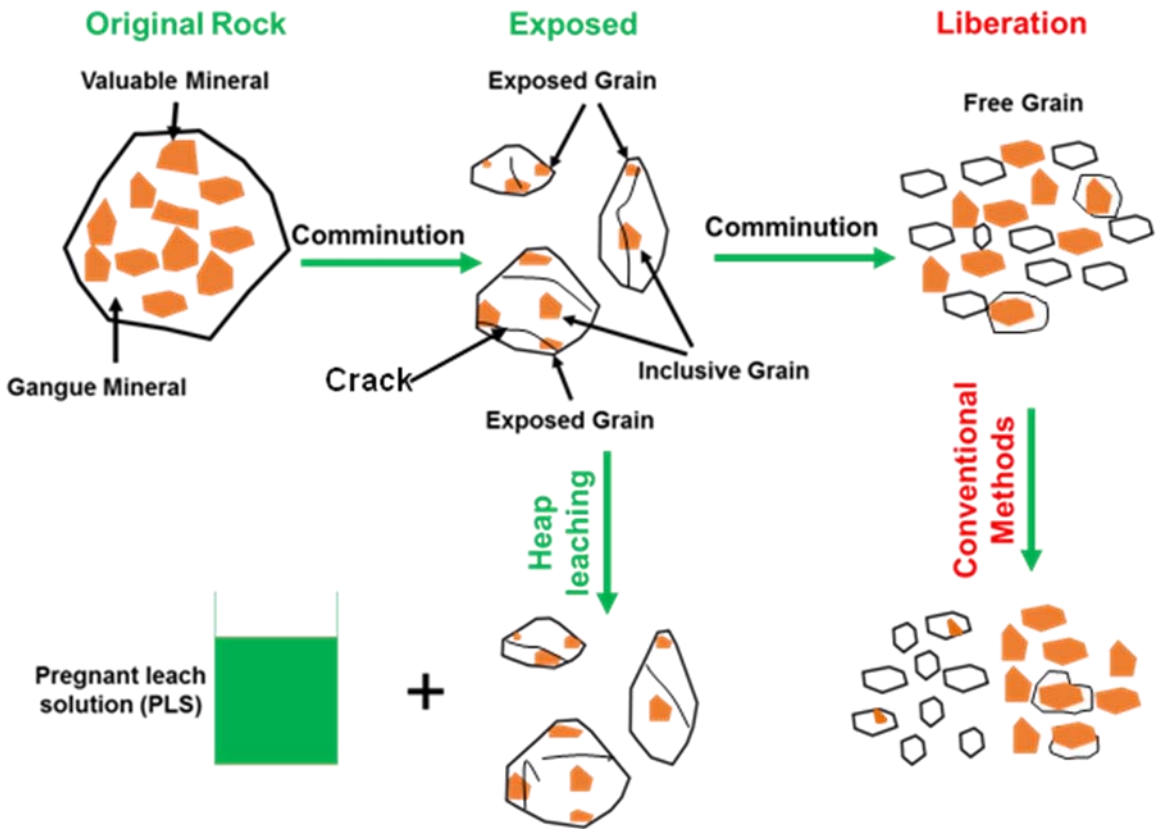

Figure 2-7: The concept of exposure and liberation of mineral by hydrometallurgy and that by physical separation process (Hsih et al., 1995).

2.5 COMMINUTION

Comminution involves particle size reduction of the ore to a size suitable for processing. A primary crusher, such as a jaw-crusher, is used to reduce ore into particles less than 150 mm in diameter. In most instances, crushing continues using a cone crusher and an internal sizing screen until the ore is less than 19 mm. Comminution in jaw and cone-crushers is a dry process, with water spray applied only to control dust. From the cone-crusher, the ore is fed to the grinding circuit where wet milling occur using autogenous or semi-autogenous mills (SAG). Gold grade and mineralogy, ore hardness and economics play a significant role in determining the degree of grinding or crushing performed to prepare the ore (Stanford, 1987; Weiss, 1985). Figure 2-8 illustrate the increase in energy requirements (specific energy input) with finer grinding.

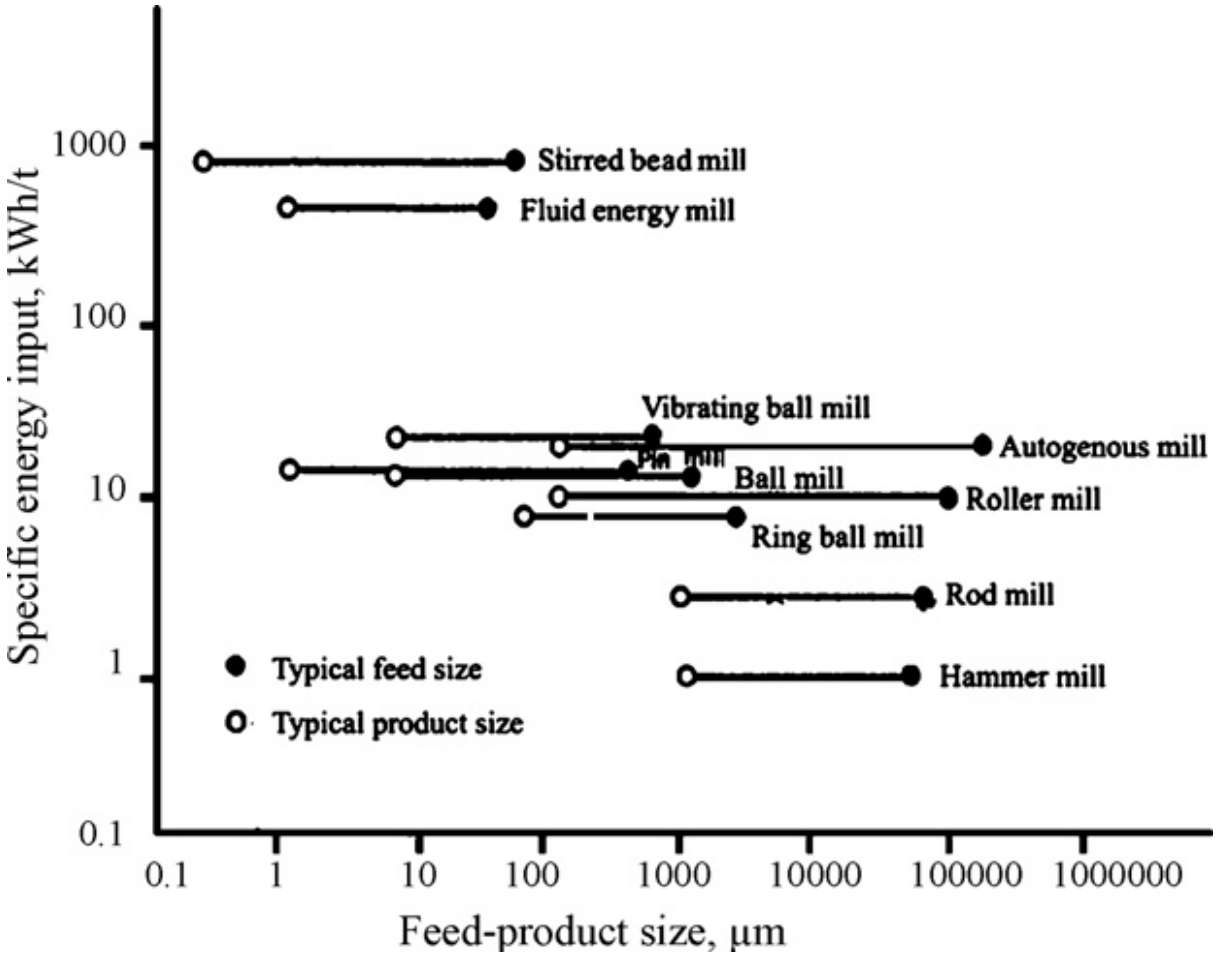

Figure 2-8: Specific Energy per Mill Type (Wang and Forssberg, 2007).

2.5.1 High pressure grinding rolls

Since the 1970's the use of high pressure grinding roll (HPGR) technology has become more common. HPGR was developed in the early 1970s and originally used in the cement industry. It is one of the most energy efficient technology of breaking particles is to compress such particles between two plates (Schonert, 1988). It has become more common in many other commodities such as diamonds, base metals and iron ore following the development of more resistant liner wear technology (Lim et al., 1996; Lim et al., 1997). Although several HPGR installations occur on gold process plants (for example, Africa, Australia, Chile, Brazil, Peru and New Zealand), this technology is not yet implemented in South Africa's gold mining operations. Several installations of the HPGR in the mining industry were as a result of improvements in the roll design (Daniel and Morrell, 2004).

HPGR consists of two counter rotating rolls; one is fixed while the other known as the floating roll is movable as illustrated in Figure 2-9 (Napier-Munn et al., 1996). The floating roll is connected to a hydro-pneumatic spring system which applies a force on the roll which in turn applies a force on the ore being ground. The feed is choke-fed into the HPGR through a hopper situated above the rolls. The feeding mechanism and the rotating rolls allow for continuous rather than batch processing of the ore (Ntsele and Sauermann, 2007; Napier-Munn et al., 1996).

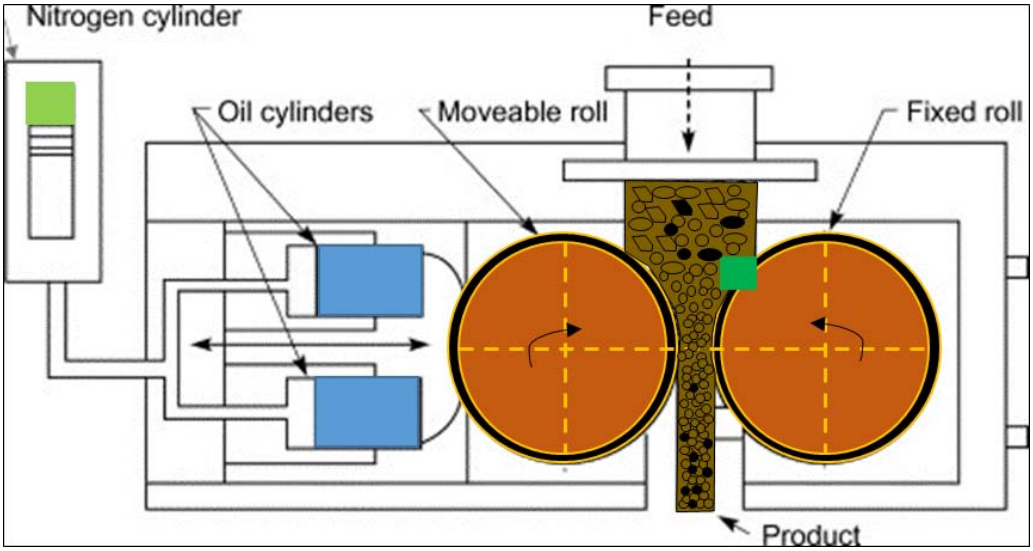

Figure 2-9: Schematic diagram of the HPGR (Napier-Munn et al., 1996).

The application of HPGR is approximately 25 to 40 % more efficient than conventional crushers and mills when it comes to coarse particle ore preparation (Daniel, 2007). Typical energy savings of 10–50 % can be expected when installing HPGR compared to other comminution equipment and the reduction in energy is due to the particle-bed breakage (compression breakage) that occurs in an HPGR as compared to impact breakage in SAG/AG mills (Patzelt et al., 1995; Wipf, 2005; Rosario et al., 2011).

To compare different grinding sizes and energy requirements, the following example was used: Grinding an ore with a bond work index of 20 kWhr/t, P_{80} -5 mm coarse particles requires only ~7.7 kWhr/t whereas grinding to a P_{80} -75 µm requires 21.8 kWhr/t. Therefore the 5 mm coarse grind power requirement in the milling circuit is only approximately one third of what is generally taken as the industry standard of 75 µm. In this example there is a saving of 14.1 kWhr/t in power cost alone, thus HPGRs are more effective in power savings (Longley et al., 2002).

There is some consensus that preferential weakening of the particles occurs due to application of HPGR (Thompsen et al., 1996; Rosario et al., 2011; Morley, 2010). Particle breakage in the HPGR is the result of high inter-particle stresses produced when a bed of solids is compressed moving through the narrow gap, created between two pressurised rolls. Large quantities of fines are usually created in the HPGR product as a result of higher inter-particle stresses when compared to the product from conventional crushing.

Research has indicated that not only the reduction in energy consumption but also the selective liberation and the improvement in leaching performance have been achieved (Esna-Ashari and Kellerwessel, 1998; Dunne et al., 1996). The presences of these inter-particle fractures are likely to encourage the percolation of the leach fluid. This occurs through the particles without the need for further energy to break the ore to a particle size where gold is liberated. HPGR does not only improve percolation through crack network but also improved mineral recovery (Ghorbani et al., 2013).

Assuming that the preferential weakening of the particles prepared by HPGR occurs along grain boundaries or cleavage planes, it suggests that there may be some gold ore types or process mineralogical domains for which this type of breakage mechanism may be favourable (i.e. free gold on sulphide grain boundaries vs. locked gold). It will be important to study mineralogy of the ore in detail in order to compare the textural differences of the target gold ores.

Besides the benefits that come with the application of HPGR technology in the minerals industry, HPGR still presents various inadequacies which currently restrain broader application. Similar to other crushers, HPGR is challenged by ore with a high proportion of very fine material (Morley, 2010). Cushion crushing action causing a major decrease in process efficiency. Wet feed material causes slippage of the material on the roll surface accelerating wear. The feed is likely to contain tramp metal which can damage the roll surface creating serious maintenance issues. Other disadvantages of HPGR when compared to SAG mills are: (a) high capital cost; (b) high maintenance cost; (c) low availability–long down time and (d) required ancillary equipment–feed preparation, dry processing, dust extraction, de-agglomeration and screening. Because of these disadvantages, HPGR is perceived high risk for short-term usage. Certain gold ores and majority of base metals usually contain a mixture of very hard rock (i.e. quartzite, softer material (i.e. conglomerates), and clays (i.e. shale), which can greatly affect the throughput of HPGR (Saramak and Kleiv, 2013).

Efficiency of comminution ranking includes the sum of strain energy and the surface energy required. The baseline for assessing this is energy determined from single-particle fracture experiments. Based on several ranking schemes, HPGR are more energy efficient than SAG mills at low reduction ratios, but they lose their advantage at high reduction ratios (Valery et al., 2010; Koenig and Hudson, 2006). The magnitude of efficiencies also varies depending on the desired product size. Table 2-1 present the comparison of HPGR and AG/SAG mills.

Table 2-2: Comparison between HPGR and AG/SAG Mills (Koenig and Hudson, 2006).

Aspect	**HPGR**	**AG/SAG**
Grinding Mechanism	Inter-particle compression	Impact, attrition and compression
Residence Time	Low-single pass	High (feed migrates through length of mill)
Availability	>90 % -2-4 change outs pa	>90 % -1-2 change outs pa
Size regulated feed Required	Yes – strongly affects stud breakage	AG-No, SAG – Sometimes
Product particle micro-cracking	Yes (beneficial for downstream processes	Negligible
Maximum Throughput	2000 tph	4000 tph
Footprint	Small	Large
Specific power	1-5 kWh/t	5-12 kWh/t
Delivery time	Substantially faster	Substantially longer
Variation in feed hardness	Single parameter variable	High losses
Delivery time	Substantially faster	Substantially longer

In particle bed compression, not only particles in direct contact with the device get subjected to energy transfer (Tavares, 2007). Random impact breakage is energy-inefficient due to the uncertainty of a particle experiencing an impact force from the grinding media. HPGR

particle breakage mechanisms are characterised based on the end products which are (Daniel, 2007): (a) Inter-granular breakage: Cracks propagate within a particular mineral causing structural weakening of the mineral; (b) Trans-granular breakage: Cracks propagate across different phases of minerals, resulting in breakage across grain boundaries; and (c) Preferential breakage: Breakage occurs along grain boundaries, resulting in the separation of different mineral phases resulting in potentially improved mineral liberation. Figure 2-10 presents the three main HPGR breakage mechanisms.

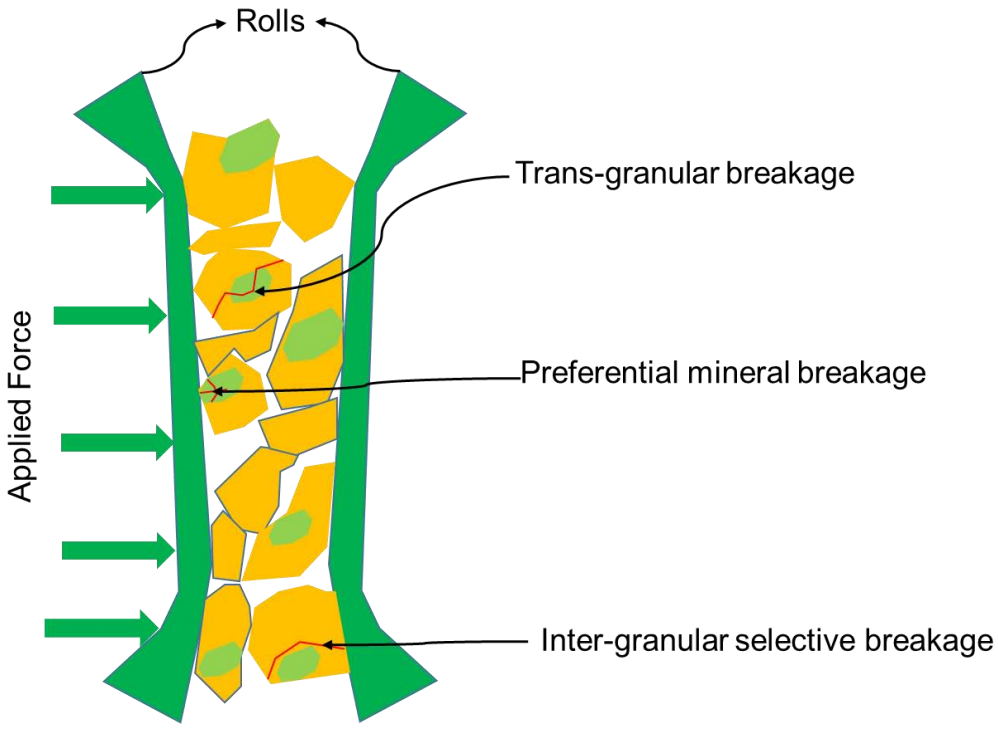

Figure 2-10: HPGR breakage mechanism (Daniel, 2007).

2.6 PROCESS MINERALOGY

Process mineralogy aims to identify and diagnose processing characteristics. It provides a basis for understanding process efficiencies and limitations posed by mineralogical attributes and variations (Gu, 2003; Lotter et al., 2010; McKay et al., 2007; Zhou et al., 2004). It is used for predictive metallurgy, troubleshooting, process control and plant optimisation. Process mineralogy was designed using geology, sampling, mineralogy and mineral processing. The addition of applied statistics to the interpretation of flotation tests and plant scale trials further enhanced this development (Fragomeni et al., 2009; Triffett et al., 2008). Modern process mineralogy has been advanced to a more powerful, integrated practice as a

hybrid discipline. The Montcalm nickel-copper ore (Northern Ontario, Canada) is just one example of a documented case study that used modern process mineralogy, to demonstrate the diagnostic power and accurate scale-up characteristics of this integrated modern practice (Charland et al., 2006; Lotter, 2011).

2.6.1 Representative sampling

In process mineralogy studies, representative sampling plays the most important role and controls the outcomes of the study (Gy, 1979; Lotter, 2011). Statistics and sampling are significant in this study due to the inhomogeneous spatial distribution of coarse gold (nugget-effect) and higher density of sulphide minerals. In order to acquire a representative sample, a large sample mass is usually taken from underground stopes, tailings, ROM which are then are crushed/milled to reduce the particle size (Coetzee et al., 2011). Sample splits are taken from the crushed products for mineralogical characterisation and to conduct laboratory experiments. The biggest errors always creep in during sampling. Inaccuracies also occur in the final assay and characterisation in the lab (Bartlett and Viljoen, 2002). This brings the question of how large a gold ore sample should be and what sampling procedure should be used for it to be statistically representable in a process mineralogy investigation.

The key approach to solving sampling errors of gold ore has been modelled based on variance (quantitative measure of how representative a sample is). It is considered that samples with large particle sizes have a high variance. It is necessary to take large samples to obtain what are loosely called 'representative samples'. The most accepted method for estimating the variances of samples with different particle sizes involves a theoretical consideration of the fundamentals of sampling (Bartlett and Viljoen, 2002). This is quantified using the 'Gy' formula (equation 2.9). It is applied after appropriate calibration by sampling experiments to establish the parameters for particular ores (Gy, 1979). These methods have been used extensively to determine the variance size relationships for sampling the Witwatersrand gold ores (Bartlett and Viljoen, 2002; Assibey-Bonsu, 1996). The Gy model is based upon the equi-probable sampling model and assumes the random distribution of mineral particles in the host rock matrix of a specific particle size:

$$\sigma^2_R = f.g.c.l.d^3_n/M \qquad \text{Eq. (2.9)}$$

Where:

σ^2_R=Relative variance of sample

d_n = Nominal size of the fragments in the sample. This is the maximum particle size in the lot to be sampled. In practice, d_n is taken as the mesh size that retains 5 % of the lot being sampled and is measured in centimeters.

M = Mass of the sample

f = particle shape factor which is an index varying in most cases between 0 and 1. For most ores a value of 0.5 is used.

g = granulometric factor (or grain size distribution factor) and takes the values between 0 and 1. For most ores g is taken as 0.25.

c = mineralogical composition factor and is the volume proportion of the gold in the host matrix. It is calculated from the grade of ore in the sample and the density of gold.

l = liberation factor. In the original Gy formula the liberation factor was the ratio of the liberation size of the mineral and the nominal size of the fragments in the sample. Gy made an empirical adjustment whereby the liberation factor was taken as the square root of this ratio.

L = (do/dn) 0.5.

d_o = The liberation size for the mineral particles, i.e. the maximum particle diameter that ensures complete liberation of the mineral. It equates to the particle size of the minerals.

In the case of gold ores from the Witwatersrand gold ores which consist of complex mineralogy, the Gy formula is usually calibrated by taking logs and substituting the exponent 3, or 2.5 in a modification to the original formula (equation 2.10). Nominal particle size in the sample comprises exponent ‘α’. The equation then becomes:

$$\text{Log}\,(M^* \sigma^2_R) = \text{Log}\,K + \alpha\,\text{Log}\,(d_n) \qquad \text{Eq. (2.10)}$$

The constant K covers all the factors which affect the relationships. K may include the factors, l, c, g and f in the original Gy equation but could also incorporate others and possibly

different terms which are not known (Francois-Bongarcon, 1993; Francois-Bongarcon, 1995; Afewu and Lewis, 1998).

2.6.2 Analytical tools used in process mineralogy studies

Traditional ore characterisation was conducted using optical microscopy as a starting point providing the first level of information on the mineralogy of the valuable and gangue minerals. The method is subject to the shortcomings of human error and lack of statistically reliable data, which in turn has led to the development of more sophisticated methods of analysis. Modern process mineralogy involves the application of qualitative and quantitative mineralogy tools such: (a) automated electron microprobe (EPMA); (b) secondary ionisation mass spectrometry (SIMS); (c) proton induced X-ray emission (micro-PIXE); (d) automated scanning electron microscopes (MLA, TIMA and QEMSCAN) (e) micro-beam tomography (neutron and X-ray tomography) and (f) laser ablation inductively coupled plasma mass spectrometry (LA-ICP-MS). These tools are more reliable, faster, more quantitative data and on-site instruments provide data within one shift when compared to conventional optical microscopes (Oosthuyzen, 1985; Weller et al., 1998; Gottlieb et al., 2000; Goodall et al. 2005; Kyle et al., 2008; Dhawan et al., 2012; Godel, 2013). Figure 2-11 present comparison of detection limit verses resolution between various analytical tools used in process mineralogy. Depending on the level of details required and ore investigated, a specific technique is used (i.e. LA-ICP-MS and SIMS are used to study invisible gold and for depth profiling whereas QEMSCAN is preferred for visible gold). Here, only methods relevant to this study will be discussed.

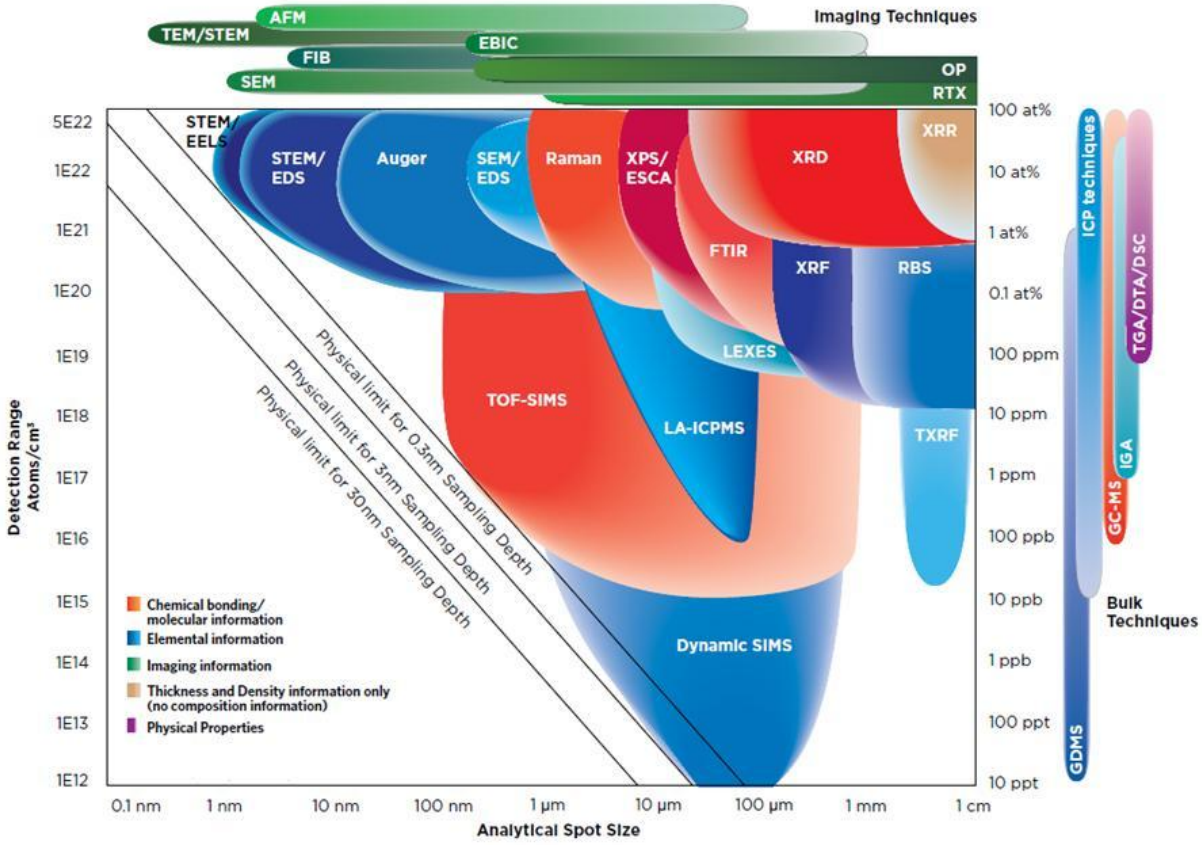

Figure 2-11: Analytical resolution verses detection limit (www.eaglabs.com).

a) Automated-SEM (MLA, QEMSCAN and TIMA)

Automated SEM techniques allows quantitative chemical analysis of materials and generation of high-resolution mineral maps and images as well as porosity structure (Gottlieb et al., 2000; Fandrich et al., 2007). They use a scanning electron microscopy platform (SEM) with an electron beam source in combination with one to two energy-dispersive X-ray spectrometers (EDS). The instruments brought good progresses in speed and accuracy and have become the leading mineralogical systems used today in the mining industry (Andersen et al., 2009; Rollinson et al., 2011; Ayling et al., 2012). They comprise several modes of measurements such as trace mineral search (TMS), which searches the back-scattered electron (BSE) images for phases of interest. Bulk mineralogical analyses and composite ore assays are quantified with certainty when compare to qualitative determination ore composition. This information then offers good mineralogical foundation for diagnosing performance (Ayling et al,, 2012; Hunt et al., 2011;

Lotter, 2011). Mineralogical characterisations which include liberation status, association, grain size distribution and texture are now easy to study on a wide range of sample types using automated-SEM.

b) X-ray fluorescence spectrometry

XRF is used to determine both major and minor elements chemistry. Instrumental analysis methods including X-ray fluorescence were introduced to mining and process industries in the 1960's (Bernstein, 1963). XRF spectrometers can be divided into two main groups: wavelength dispersive XRF spectrometer (WDXRF) and energy dispersive X-ray spectrometer (EDXRF). The elements that can be analysed as well as the detection levels depend on the type of spectrometer used. The WDXRF has an elemental range from beryllium to uranium while the EDXRF has a range from sodium to uranium. WDXRF utilises an analysing crystal to disperse the different energies form the sample. The EDXRF has a detector, which is able to differentiate the energies of the characteristic radiation directly from the sample (Enzweiler and Webb, 1996; Engelbrecht, 2011).

c) X-ray Diffraction

XRD analysis is used to identify the major minerals present. XRD is a quick and inexpensive way to identify and quantify minerals, particularly those not easily distinguishable by other analytical techniques (i.e. identification of clay minerals and l phyllosilicates). In the case of gold ores, data collection is done using an X-ray diffractometer employing Co-radiation, since most gold ores are iron-rich and this causes X-ray fluorescence (resulting in a high background) when Cu-radiation is used (Coetzee et al., 2011). Phase quantification is done using the *Rietveld method*. The Rietveld method creates a virtual separation of overlapping peaks, thereby allowing an accurate determination of the structure.

d) X-ray computed tomography (X-ray CT)

X-ray computed tomography is a non-destructive technique for visualizing interior features within solid objects, and for obtaining digital information on their 3-D geometries and properties (Ketcham and Carlson, 2001). The word *tomos* is the Greek word for 'cut' or

'section'. An X-ray CT image is referred to as a slice which is comprised of *voxels* making the volume elements. The grey scale levels or values in X-ray CT slice correspond to the X-ray attenuation coefficient which reflects the quantity of X-rays scattered or absorbed as they pass through each voxel. X-ray attenuation is primarily a function of X-ray energy and the density and atomic number of the material being imaged (Lovea et al., 2009; UCTC, 2013; Godel and Barnes, 2010). Figure 2-12 illustrates the external components of a micro-focus X-ray CT.

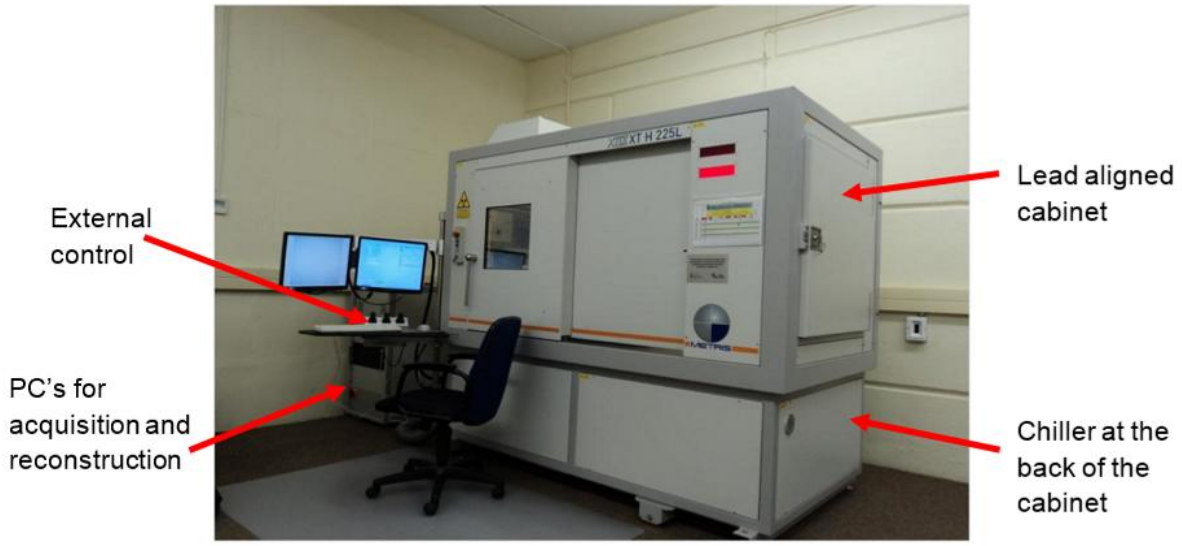

Figure 2-12: Nikon XTH 225 ST micro-focus X-ray tomography at Necsa MIXRAD facility (Hoffman and de Beer, 2012).

Tomographic imaging consists of directing X-rays at an object from multiple orientations and measuring the decrease in intensity along a series of linear paths. Beer's law characterises this decrease. This law describes the intensity reduction as a function of X-ray energy, path length, and material linear attenuation coefficient. Three equations have been proposed based on the fundamentals of Beer's law and the nature of material (Godel, 2013; UCTC, 2013):

$$I = I_0 \exp[-\mu x] \qquad \text{Eq. (2.11)}$$

$$I = I_0 \exp\left[\sum_i (-\mu_i x_i)\right] \qquad \text{Eq. (2.12)}$$

$$I = \int I_0(E) \exp\left[\sum_i \left(-\mu_i(E) x_i\right)\right] dE \qquad \text{Eq. (2.13)}$$

Where: I_0: X-ray intensity

I: final X-ray intensity

μ: material's linear attenuation coefficient (unit 1/length)

x: length of the X-ray path

i: increment

E: X-ray energy

Equation 1 is referred to as the simplest form of Beer's Law for a monochromatic X-ray beam through a homogeneous material. If there are multiple materials, equation one is modified to form equation two where each increment mirrors a single material with attenuation coefficient μ_i with linear extent x_i. This equation can be solved directly in a well-calibrated system using a monochromatic X-ray source (i.e. synchrotron or gamma-ray emitter). Polychromatic X-ray source takes into account the fact that the attenuation coefficient is a strong function of X-ray energy when used. The complete solution would require solving the equation over the range of the X-ray energy spectrum utilised represented by equation 3 (Ketcham and Carlson 2001; UCTC, 2013).

The majority of reconstruction strategies solve for a single attenuation value at each spatial position, therefore this calculation is usually not solved properly. In such cases, attenuation is taken as an effective linear attenuation coefficient, rather than an absolute. This complicates absolute calibration, as effective attenuation is a function of both the X-ray spectrum and the properties of the scan object. It also leads to beam-hardening artifacts which consequently result in changes in image grey values caused by preferential attenuation of low-energy X-rays (Hoffman and De Beer, 2012). A detailed description of the physical processes responsible for X-ray attenuation are presented in Withjack, (1988); ASTM, (1992); Silver, (1994).

X-ray CT instrument elements are comprised of a: (a) X-ray source; (b) a series of detectors that measure X-ray intensity attenuation along multiple beam paths, and (c) a rotational geometry with respect to the object being imaged. Different configurations (Figure 2-13) of these components can be used to create X-ray CT scanners optimised for imaging objects of

various sizes and compositions. The great majority of CT systems use X-ray tubes, although tomography can also be done using a synchrotron or gamma-ray emitter as a monochromatic X-ray source. Important tube characteristics are the target material and peak X-ray energy, which ultimately determines the X-ray spectrum that is generated; current, which determines X-ray intensity; and the focal spot size, which impacts spatial resolution (Godel, 2013).

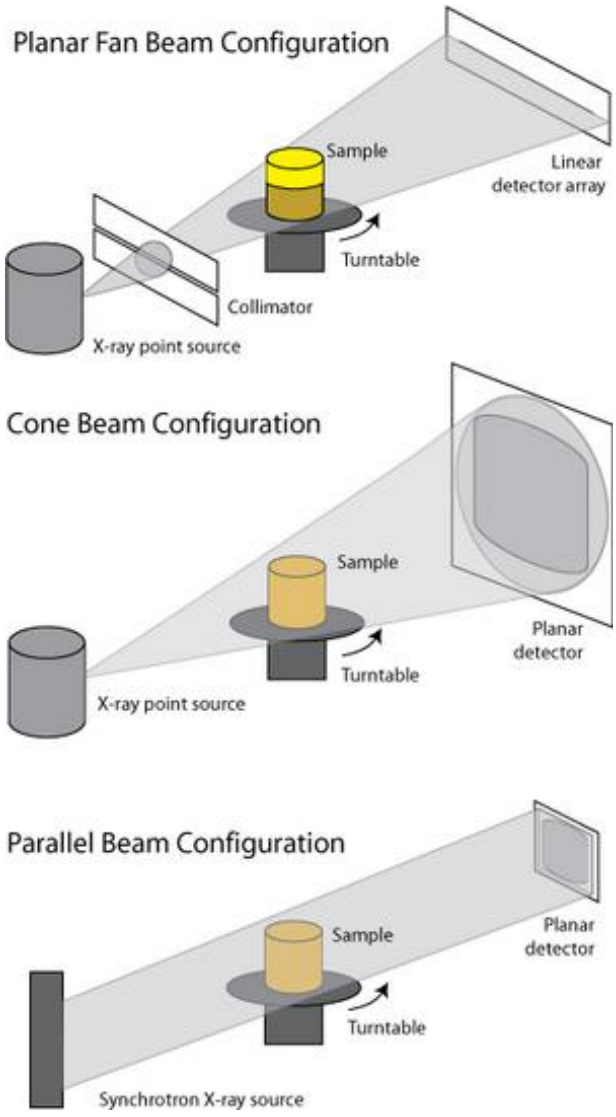

Figure 2-13: Three most common X-ray CT beam configurations (http://serc.carleton.edu).

The ability of X-ray CT's reconstructed sequential topographies to show information of the ore textural variation makes it an appropriate useful tool in ore characterisation. Proficiencies of X-ray CT to permit rapid evaluation of economic minerals bring an innovative technology to the minerals industry. It minimises ore characterisation time, cost and assists in ore

mineral distribution interpretation. Although X-ray CT comes with state of the art imaging technique, the following limitations have been recognised through application in process mineralogy over the past decade (UCTC, 2013; Boin and Haibel, 2006):

i. Lack of direct mineralogical information

ii. Complex analysis software (not adapted for process mineralogy application)

iii. High resolution requires small objects

iv. Finite resolution causes some blurring of material boundaries

v. Calibration of grey levels to attenuation coefficients complicated by polychromatic X-rays

vi. Large (dm-scale) geological specimens cannot be penetrated by low-energy X-rays, reducing resolving capability

vii. Not all features have sufficiently large attenuation contrasts for useful imaging (carbonate fossils in carbonate matrix; quartz vs. muscovite)

viii. Image artefacts (beam hardening) can complicate data acquisition and interpretation

ix. Large data volumes (gigabytes+) require considerable computer resources for visualisation and analysis

Overall, X-Ray CT shows potential improvement in traditional metallurgical test work and can be applied during heap leaching studies as detailed in Figure 2-14. Its application as a characterisation method recently has introduced a new prediction tool for 3D analysis of multiphase particles and packed particle beds (Dhawan et al., 2012).

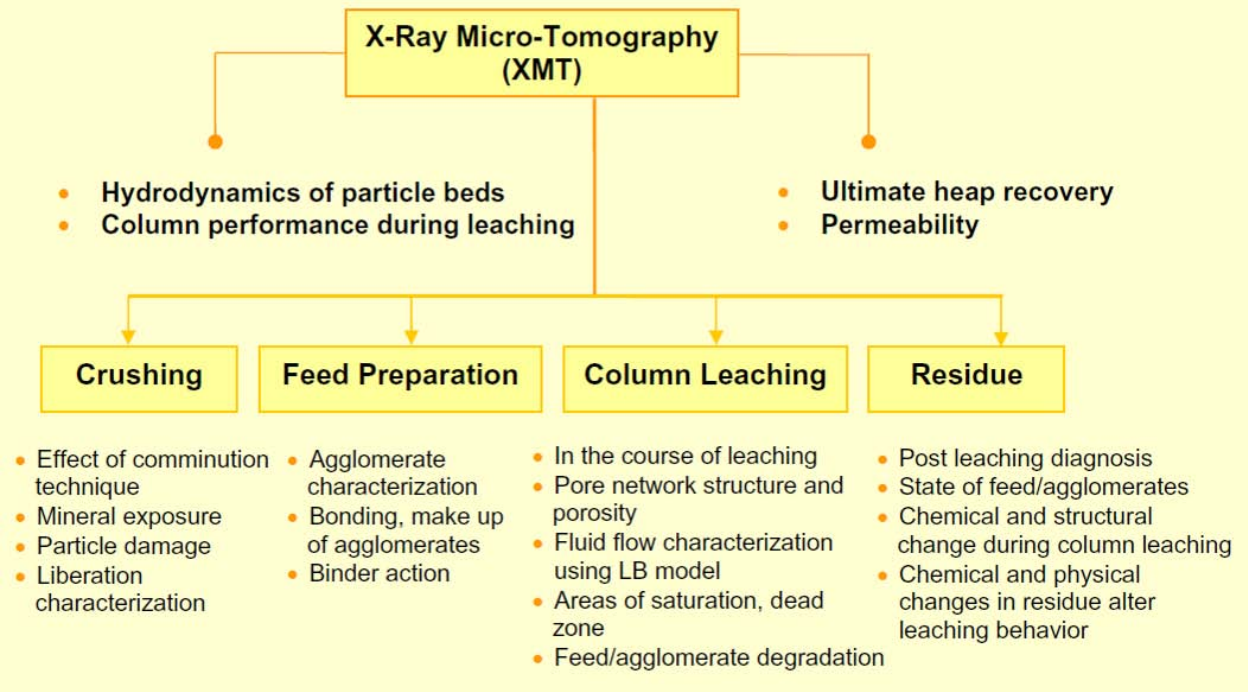

Figure 2-14: The potential roles of X-ray CT in an integrated heap leach system (Dhawan et al., 2012).

e) Micro-focus Cold neutron tomography

Neutron radiography is the process by which film is exposed by first passing neutrons through an object to produce a visible image of the materials that make up the object. This technique allows for studies of the physical properties of material that complement X-ray radiography (IAEA, 2013). Neutrons have deeper penetration capabilities through denser materials. Incorporation of digital radiography (2D), computed tomography (3D), energy-selective neutron radiography or dynamic (real-time) adds value to neutron radiography. Elimination of the need for consumables such as films and other potentially hazardous chemical compounds used in film-based radiography is another advantage of neutron technology (IAEA, 2013). The introduction of radiography with Cold Neutrons beam line facilities (ICON at Paul Sherrer Institute, Switzerland; CONRAD at Helmholtz Institute-Berlin, Germany and ANTARES at TUM, Garching, Germany) is one of the most recognised advancements in radiography. This neutron system has been in operation for users since late 2005 (Sowerby et al., 2009; Roels and Carmeliet, 2006; Kaestner et al., 2011).

2.7 CRITICAL REVIEW OF THE LITERATURE

The occurrence of gold in various forms and geological environments results in its complex mineralogy. This calls for a need to understand gold mineralogy prior to any stage of mineral processing. The literature review on process mineralogy has shown that an innovative technology such as the application of micro-focus X-ray CT offers the opportunity to study mineralogy in 2D and 3D. Complimentary techniques such as automated SEM offer the advantage of quality control and assurance on X-ray CT results. As a result, X-ray CT as a modern analytical technique can be used to improve our understanding of heap leaching operations together with process mineralogy. Alternatives of X-ray tomography such as Neutron radiography gives deep penetration abilities allowing the study of dense material, but this might hinder with imaging of less dense minerals.

This implies that it is from carefully conducted process mineralogy and X-ray CT studies that a valuable interpretation of gold cyanidation during heap leaching can be derived. In the case of less porous deposits such as the Witwatersrand gold ores, the comminution method plays a significant role. The review of the literature showed that the lower energy consumption with high- efficiency of HPGR may offer a solution with regards to solution migration through induced cracks during heap leaching and save most of the energy at the same time. Even though HPGR offers various advantages, this technology has not been applied in any of the South African gold mines. It is recognised that comminution plays a vital role as one of the prerequisites for the gold cyanidation process.

Gold cyanidation processes are governed by different factors. These are: ore composition, gold deportment, comminution method, pH, free cyanide, temperature, oxygen and sulphide minerals. When cyanide solution is added in a gold ore that contains sulphide minerals, a passive film of sulphur which forms on the surface of gold during gold cyanidation will reduce gold extraction rates. Certain minerals such as pyrrhotite will consume most of the oxygen during gold cyanidation thus retarding the cyanidation process. This makes the traditional methods of processing gold to be associated with high operational costs due to several stages of processing that need to be followed. In a country such as South Africa where gold production is in a continuous decline and which is dominated by the production of low grade ore and market uncertainties, a novel gold extraction alternative is required. The process of coarse particle leaching technology offers an alternative of processing gold at lower costs. This is due to its simplicity of design (less complicated as compared to tank leaching) and

lower operating cost. The success of heap leaching technology requires a detailed mineralogical understating of the gold, lixiviant diffusion at a particle scale and particle size. These imply that only certain ores are amenable to the process of heap leaching. From the literature reviewed, it was recognised that the success of heap leaching depends on a series of factors of which ore preparation, mineralogy and hydrometallurgy are the key aspects.

The key questions generated from the literature review and presented in the introduction (section 1.4) are repeated here:

(i) What information can be obtained on a Witwatersrand gold ore using micro-focus X-ray CT?
(ii) What are the effects of HPGR feed pressure, crack volume, crack width and distribution on comminution of the Witwatersrand gold ore?
(iii) What are the mineralogical features of the Witwatersrand gold ore affecting cyanide leaching and heap leaching?
(iv) Is there potential for heap leaching the Witwatersrand gold ore?

CHAPTER 3: GEOLOGICAL SETTING

3.1 REGIONAL GEOLOGY

This section presents a summary of the regional geologic setting of the Archaean Witwatersrand Basin and the remarkable geological history that pre- and post-dated basin development, together with the controls and influences that lead to what is the largest gold deposit on Earth. In this study, understanding of ore petrogenesis forms the framework of deciphering mineralogical assemblage of the ore and also assists in predicting possible reactions that can take place during processing.

3.1.1 The Kaapvaal Craton

The Kaapvaal Craton (Figure 3-1) in South Africa formed over a period from approximately 3600 to 2500 Ma and can be subdivided into four main domains, namely (a) Eastern - started with the development of the Barberton Greenstone Belt at approximately 3550 to 3200 Ma, (b) Central - the basement was constructed by granitoid domes such as Johannesburg and the Vredefort dome and later the deposition of the Witwatersrand Supergroup, (c) Northern – Murchison (3230 to 3090 ma), Pietersburg (2949 Ma) and Giyani (3203 Ma) Greenstone Belts and (d) Western domain - lies to the west of Colesberg magnetic anomaly and consist of the Amalia (2754 Ma), Kraaipan (3080 Ma) and Madibe (3097 Ma) Greenstone Belts; the Gaborone granite complex and the granitoid terrane in the Kimberly region (3250 Ma). Various episodic magmatic activities in the form of a series of granitic plutons continued until 2690 Ma (Eglington and Armstrong, 2004; Lowe and Byerly, 2007; De Wit et al., 1992; Bumby et al., 2012). The Kimberley and Witwatersrand blocks are joined along the Colesberg magnetic lineament, a prominent marker that may represent the near surface expression of an Archaean suture zone (De Wit et al., 1992; Doucouré and de Wit, 2002). By 3.0–2.9 Ga, the craton was part of a relatively stable continent with a well-formed 30–50 km thick continental crust underlain by approximately 250–300 km thick lithospheric mantle, but which was subsequently affected by the collision of the neighbouring Zimbabwe Craton (Tinker et al., 2002). Near- and far-field tectonic deformation driven by the collision led to basin development and the deposition of the Dominion, Witwatersrand and

Pongola Basins. Continued basin development followed with the deposition of the Ventersdorp, Transvaal – Griqualand West and Waterberg – Soutpansberg sediments.

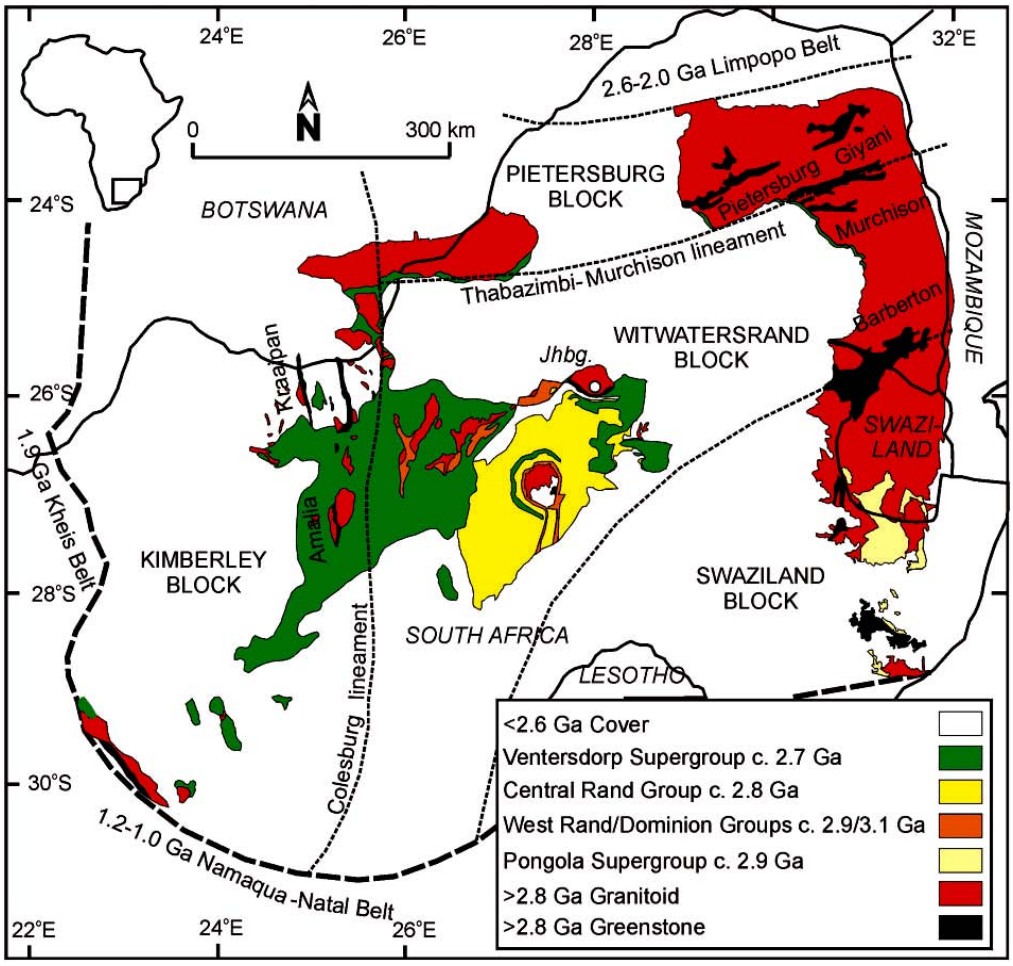

Figure 3-1: Main Archaean stratigraphic units of the Kaapvaal Craton. The West Rand and Central Rand Groups constitute the Witwatersrand Supergroup. Bold dashed line outlines the boundary of the Kaapvaal Craton as inferred from aeromagnetic data. The crustal blocks (amalgamated by 2.8 Ga) are separated by major lineaments (Frimmel et al., 2009).

3.1.2 The Witwatersrand Basin

Although widely cited in the international literature, the term 'Witwatersrand Basin' is deceptive because it traditionally encompasses the West Rand and the overlying Central Rand litho-stratigraphic Groups which were most likely deposited under very different tectonic and palaeo-environmental regimes (Frimmel et al., 2009). Several of the other post-cratonic "basins" listed above have now been interpreted as composite, sharing only their

depocentres. With a total thickness of approximately 7000 m, the Witwatersrand Supergroup can be subdivided into the basal West Rand Group (depositional age <2.98 to 2.91 Ga) and the younger Central Rand Group (<2.90 to 2.78 Ga). The West Rand Group contributes less than 5 % of Witwatersrand gold production while the Central Rand contains greater than 80 (Frimmel et al., 2005; Frimmel and Müller, 2011). The remainder occurs in post-Witwatersrand reefs in the overlying Ventersdorp Group (Ventersdorp Contact Reef or VCR) and Transvaal Supergroup (Black Reef). The Central Rand Group and overlying VCR are the most outstanding examples of fossil placer deposits and together represent the largest gold resource known (Kositcin and Krapež, 2004).

This study focuses on the Central Rand Group with special reference to the West Wits line section located in the town of Carletonville. The auriferous conglomerates (reefs) of the Witwatersrand Basin occur within seven separate goldfields located along the eastern, northern and western margins of the basin. These goldfields are known as Evander, East Rand, Central Rand, West Rand, Far West Rand, Klerksdorp and Free State (Figure 3-2). Typically within each goldfield there are one or sometimes two major reef units present, which may be interbedded with one or more secondary reef units. As a result of faulting and other primary controls on mineralisation, the goldfields are not continuous and are characterised by the presence or dominance of different reef units (Robb and Meyer, 1995; Frimmel and Minter, 2002).

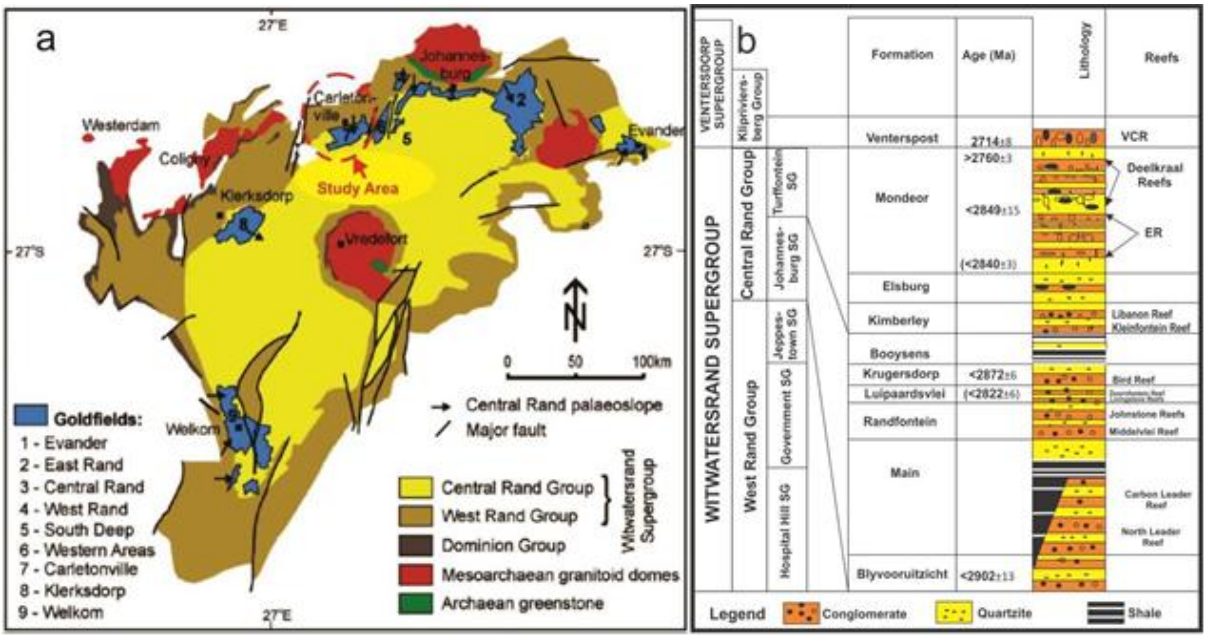

Figure 3-2: The Witwatersrand Basin: a) Location of Witwatersrand gold Province showing distribution of Goldfields regions, Witwatersrand Supergroup, Dominion Group, Mesoarchaean granitoid domes and Archaean; b) Stratigraphic column of Carletonville Goldfield showing location of the VCR, ER and subsequent Witwatersrand Reefs (Frimmel et al., 2009; Koglin et al., 2010).

There are at least two important gold-bearing reefs in overlying successions, namely the Ventersdorp Contact Reef (VCR) and the Black Reef (BLR) which unconformably overlies the Witwatersrand Supergroup. The Central Group of the Witwatersrand Supergroup is a terrigenous sequence with mainly arenaceous and argillaceous and some rudaceous lithology which was deposited in a fluvio-deltaic environment(Robb and Meyer, 1995). Deposition of auriferous conglomerates within the Central Rand Group has been documented as having been in the form of fluvial sands (now quartzites), interlaid with coarse gravels. Heavy minerals were deposited at the proximal end of streams after flowing down uplifted basin edges as well as in the proximal edges of submarine fans that formed at the entrance to the shallow inland sea (Engelbrecht et al., 1986; Boyle, 1987; Els, 1987).

Different gold mineralisation models have been proposed in the Witwatersrand Basin for over a century, but the most dominant models are the placer, hydrothermal and modified placer model (Frimmel et al., 2005; Frimmel and Minter, 2002; Jolley et al., 2004; Schaefer et al., 2010). The placer model describes gold association with unconformity surfaces. The hydrothermal model claims that, the gold was transported as bi-sulphide complexes and precipitated when the fluid was reduced by hydrocarbons, as shown by the pyro-bitumen association. The hydrothermal model also describes the uraninite overgrowing post-depositional phyllosilicates as evidence. On the other hand, the modified placer model shows that the silver and mercury concentrations are not uniform in the reefs as it would be expected from precipitation that comes from a fluid, and the phyllosilicates disappear closer to the reefs (Frimmel and Gartz,1997; Gartz and Frimmel, 1999; Frimmel et al., 2005). Evidence in support for the modified placer theory is further supported by the dating of gold formation at 3010 Ma and rounded pyrite at 2990 Ma (using Re-Os dating methods), thereby showing that gold genesis predated sediment deposition (Kirk et al., 2001). A detailed review and summary of the Witwatersrand gold mineralisation arguments is presented in Frimmel et al.,(2005). Despite these different schools of thought, the most primary control to the gold distribution remains the association with quartz-pebble conglomerates on intra-basinal unconformities.

3.1.3 The Ventersdorp and Transvaal Supergroup

The Neoarchaean Ventersdorp Supergroup is unconformably overlain by the Transvaal Supergroup. The dominantly volcanic Ventersdorp Supergroup overlies the Witwatersrand Supergroup conformably on the Central Rand in certain localities but unconformably along the north-west margin of the Witwatersrand Basin. A 2714 ±16 and 2709 ±8 Ma age determined for samples from the Klipriviersberg Group (near the base of the Supergroup) and of a porphyry from the overlying Makwassie Formation of the Platberg Group has been interpreted as the onset of deposition of the Ventersdorp volcanics (Armstrong et al., 1991).The Ventersdorp Supergroup was deposited in a large elliptical basin. It is commonly believed that towards the end of the Witwatersrand deposition the thick sediment pile deposited on the 'young' craton resulted in stress overload and subsequent tensional faulting of the crust. These faults acted as conduits for the lava of the Ventersdorp Supergroup, and the start of a continental rifting event. A mantle plume model has been applied to interpret the Ventersdorp Supergroup and suggests that the plume head may have been marginal to the Kaapvaal Craton (Eriksson et al., 2002; Hatton, 1995). It should be noted that as much as the Ventersdorp lavas extruded almost immediately after Witwatersrand deposition, there is a long gap of some approximately 70 Ma in between the two Supergroups. The Klipriviersberg Group makes up the base of the Ventersdorp Supergroup, and consists of five formations, namely; the Westonaria, Alberton, Orkney, Jeannette, and Edenville formations. The Alberton and Westonaria Formation of the Klipriviersberg Group form the hanging wall lithology of the VCR in the study area (Armstrong et al., 1991).

The Transvaal Supergroup (2.65–2.05 Ga) is made of two geographically separate basins which are separated by a broad basement high, referred to as the Vryburg arch. The basins have been named following their geographic distribution, namely, the Transvaal basin (located in the former Transvaal region) where it circumscribes the Bushveld Complex and the Griqualand West Basin (located in the former Griqualand region) that extends into southern Botswana. It is late Archaean–earliest Proterozoic platform succession developed on the Kaapvaal Craton (Cheney, 1996). The Transvaal basin conformably overlies the Ventersdorp Supergroup. Two Groups of the Transvaal Supergroup occur in the study area, that is, the Chuniespoort Group and the lower part of the Pretoria group. The Pretoria group outcrops are visible in the study area and the Timeball hill Quartzite (50 – 90 m thick) forms

the Gatsrand Ridge and the shales of this formation form the southern slopes to the ridge (Eriksson and Reczko, 1995; Eriksson et al., 1993).

3.1.4 Stratigraphy and mineralogical features of the Witwatersrand ores

Several comprehensive reviews of Witwatersrand ore mineralogy have been published, the most recent being Frimmel (2007); Frimmel and Minter, (2002); Frimmel et al.,(2005); Koglin et al.,(2010), and the numerous references therein. Gold-bearing quartz pebble conglomerates of the Witwatersrand gold province are characterised by small-medium-large (variable size fraction), well-rounded vein quartz pebbles which are surrounded by smaller-grained pyrite (Figure 3-3). The matrix is quartzitic and extremely indurated by recrystallisation, contains abundant euhedral pyrite and a phyllosilicate assemblage indicative of a lower greenschist-facies grade of metamorphism (chlorite, chloritoid, pyrophyllite and muscovite).

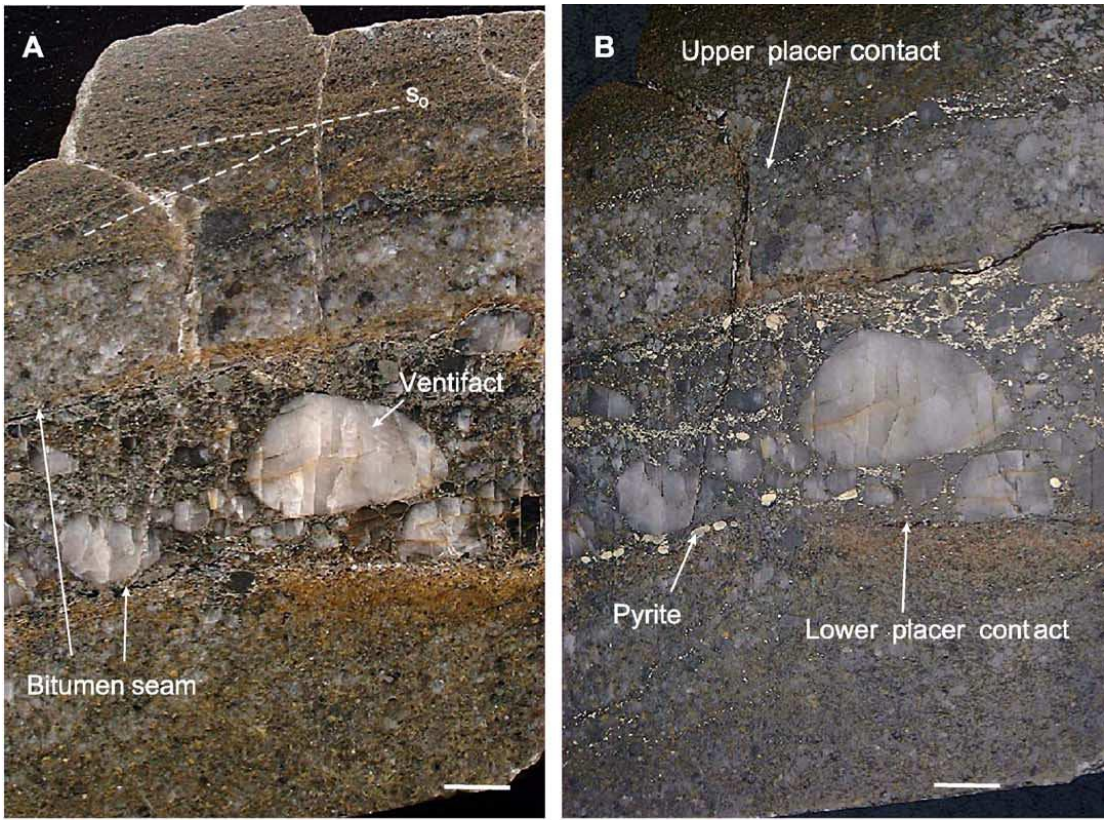

Figure 3-3: Oligomictic pebbly quartz arenite (reef), Vaal Reef, Stilfontein mine, Klerksdorp gold field; note the veneer of bitumen on the basal unconformity and 3 cm above the *base* on a bedding plane defining the top of pebbly layer; cross-bedding (so) in hanging wall, and an in *situ* ventifact; scale bar=1 cm. (B) same as A, but highlighting the position of fine- to coarse-grained rounded pyrite (Frimmel, 2005).

Gold occurs in the matrix as finely divided particles with a general grain size range of 5 µm to 1.2 mm (Figure 3-4) which varies from reef to reef (Hallbauer and Joughin, 1972; Barton and Hallbauer, 1996). There is a strong association between gold and pyrite (Koglin et al., 2010). Radioactive minerals such as uraninite and brannerite also occur in these auriferous conglomerates and they are usually associated with muscovite, zircon, sphene and pyrite (Ramdohr, 1957; Ramdohr, 1969; Ramdohr, 1958; Mngoma, 2012). However, this mineral association is not diagnostic of uranium-minerals; more important is the spatial relationship with other evidently detrital phases and with 'carbon seams'. Pyrite is the most common heavy mineral in all of the fluvial deposits of the Witwatersrand. Fe-oxides (predominantly magnetite) are found instead of pyrite only in marine sedimentary rocks, such as shales in the West Rand Group (Frimmel, 2005).

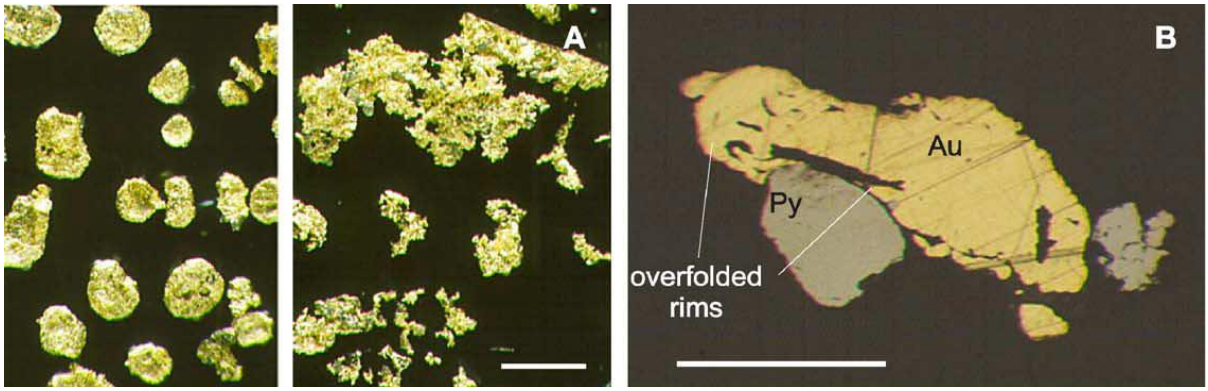

Figure 3-4: Photomicrographs illustrating morphological and textural features of Witwatersrand gold orebodies (combined transmitted and reflected light, scale bars=0.2 mm: (A) Contrasting morphological types of gold particles occurring together on a mm-scale. (B) Gold micro-nugget (Au) with overfolded rims next to rounded pyrite (Py) from same sample as shown in A (Frimmel, 2005).

3.2 LOCAL GEOLOGICAL SETTING

This section presents a summary of the local geologic setting of the Elsburg and the Ventersdorp contact reefs. It provides their stratigraphic position, gold distribution controls and mineralogical composition.

3.2.1 Elsburg reefs (ER)

The stratigraphy and the sedimentology of the Elsburg reef at West Wits line has been extensively described by Rose (1983) and has been subdivided in to four reef zones, namely: a) The Elandsrand reef zone; b) Intermediate Glassy Reef Zone; c) The Uranium Band Reef Zone; d) The Deelkraal Reef Zone. The Elsburg Reefs build a series of thin conglomerate bands developed over a relatively thin stratigraphic interval, separated from the overlying VCR by a barren quartzite. The individual bands carry highly variable amounts of gold together with uranium. In contrast to the VCR, the ER contains abundant detrital gold that shows a strong positive spatial correlation with the coarse conglomerate units and is dominantly located within detrital pyrite grains (Rose, 1983).

a) The Elandsrand Reef Zone (ERZ)

The Elandsrand Reef Zone is divided into six sub-units as illustrated in Figure 3-5:

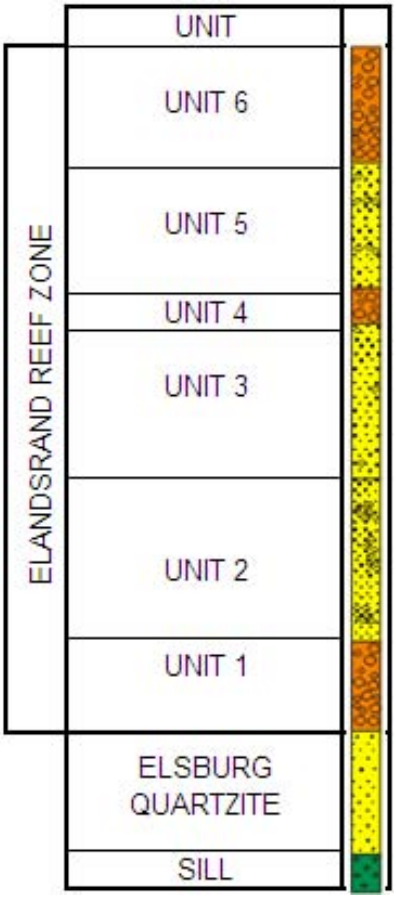

Figure 3-5: The classification of Elandsrand Reef Zone (Mambane, 2009).

The sub-units of the Elandsrand Reef Zone consist of matrix to clast supported conglomerates with lenses of internal quartzite. The conglomerate grades laterally to pebbly quartzite with variable amount of gold.

b) Intermediate Glassy and Reef Zone

This consists of polymictic conglomerate bands that alternate with quartzite units. A well mineralised small pebble conglomerate band with shale partings occurs at the base of the unit. This band is overlain by green-grey, siliceous or pebbly quartzite which is interbedded with a small pebble conglomerate.

c) *The Uranium Band Reef Zone*

The unit is made up of upward grading, matrix and clast-supported conglomerate bands. The conglomerate bands alternate with gritty and pebbly quartzite. A high gold content is associated with areas where the conglomerate is clast-supported. This unit is superficially similar to the VCR except for the absence of chlorite granules often seen in the VCR. Gold and uranium values are expected to pick up in places where the unit occurs as footwall to the VCR (Mambane, 2009).

d) The Deelkraal Reef Zone

This is the topmost unit of the Mondeor Conglomerate Formation in the Elandsrand-Deelkraal area. The unit has been described in the Deelkraal area as a polymictic matrix-supported conglomerate that alternates with gritty to pebbly yellow-green quartzite.

3.2.2 The Ventersdorp Contact Reef (VCR)

The VCR unconformably overlies and truncates the Witwatersrand Supergroup, and forms part of the Venterspost formation which has the maximum age of 2729 ±19 Ma based on U–Pb detrital zircon SHRIMP date (Kositcin and Krapež, 2004). The VCR unconformity depth extends to the region of 3000–4200 m below surface (Manzi et al., 2013). It is usually exploited as the primary reef in the Western deep level mines located in the West Wits line. Generally, the VCR is a clast supported conglomerate of small and medium-sized, sub-angular to sub-rounded (predominantly) milky quartz clasts. The matrix thereof mostly comprises a mid-to-dark grey medium-grained quartzite. The medium to dark grey colour is ascribed to the presence of phyllosilicates (i.e. chlorite).

The VCR is characterised by mineralogical variability that extends to very erratic gold grades as well as structural complexities displayed by rapid changes in dip and thickness (Everard, 1988), resulting in the incorporation of footwall and hanging wall lithology that possess very different properties. Gold is associated with approximately equal proportions of euhedral pyrite, chlorite and multiple generations of quartz. Rounded gold particles with spheroidal, disc-like or torroidal forms of evidently detrital origin are absent, thus the gold is distributed throughout the recrystallised matrix as complex intergrowths, micro-veinlets and micro-inclusions in gangue minerals (Frimmel and Gartz, 1997; Gartz and Frimmel, 1999). Five main lithofacies of the VCR occur in the study area (Everard, 1988):

CHAPTER 4: MATERIALS AND METHODS

4.1 INTRODUCTION

This chapter is subdivided into four sections describing the experimental methods and analytical equipment used in this study. Section 4.2 provides details of the methodology used for representative sampling of ore from underground active stopes and surface stockpiles, as well as the subsequent blending and splitting of the ore into smaller samples for the experimental work. Section 4.3 describes the HPGR test work procedure. Section 4.4 provides details on the analytical equipment used for mineralogical investigations. Section 4.5 describes the apparatus and procedure used for the laboratory scale column leaching experiments.

4.2 REPRESENTATIVE SAMPLING AND SPLITTING

4.2.1 Sampling

Sampling is the most important aspect of mineralogical and metallurgical studies, but it is also a very commonly underrated part of these studies. As part of this research project, sampling is one of the most essential aspects of all the methodologies undertaken to achieve the objectives. Errors introduced into the final results by using poor, biased sampling techniques cannot be offset by carrying out statistical manipulations of those data. In this study, precautions were taken when sampling the ore due to the fact that gold occurs in minute amounts that are most likely to suffer from nugget effects. Given that each sampling step carries a statistical error and that these errors are cumulative (equation 4.1), an appropriate strategy to obtain a representative sample was decided upon prior to the sampling campaign.

$$\sigma^2_{total} = \Sigma\sigma_1^2 + \sigma_2^2 + \sigma_3^2 \ldots + \sigma_n^2 \qquad \text{Eq. (4.1)}$$

σ^2 -represent the error.

A bulk composite sample of ROM ore used for this project was obtained from the Harmony gold mine located 15 km south of Carletonville, South Africa. The bulk sample comprised 80% stock pile ore and 20 % underground channel sampling gold ore. Channel samples were included to boost (blend) the grade of the stockpile ore. Based on the 2011 mining mix used at Harmony gold mine as well as the location of the sampling points, and the existing Harmony Gold geozone model, it is estimated that approximately 95 % of the ore stockpile sample is from the VCR (the primary reef mined) and 5 % of the stockpile sample is from the ER (secondary reef mined). Underground sampling was done using the Harmony Gold stope sampling standards. Stockpiles were sampled at regular distances starting with bottom edge load circumference in a general counter-wind direction. The following procedure was followed when sampling the stockpile ore:

i) Area of the stockpile from which hauling will begin was located. Using a shovel to dig into the stockpile, material was loaded inside a bucket/container.

ii) The loaded buckets were kept at heights below 1m relative to stockpiles while rolled forward during loading, thus producing a smooth mixing of the material.

iii) Point sampling was used while rotating with the stockpile to get a representative sample. Striking off the stockpile top was avoided during sampling. Each sample point filled up one bucket taken at equal increments around the pile.

iv) The shovel was inserted full-depth horizontally into the material and elicited vertically. Care was taken to retain as much of the material as possible on the blade of the shovel.

4.2.2. Sample splitting

The bulk sample weighing 570 kg was transported to MINTEK (Randburg, South Africa) for ore preparation and HPGR experimental test work. The ore sample was first crushed using a jaw crusher to a top size of 40 mm. After crushing, the ore was blended and then split into five portions of approximately 114 ±3 kg lots using the coning and quartering method. To obtain a representative sample from the coning and quartering method requires multiple combinations of sequential splitting the portions of interest into quarters and then mixing the two opposite quarters until the desired mass of each lot is achieved. The schematic in Figure 4-1 shows the flow chart followed when splitting the feed for this test work. To obtain the final

lots for the HPGR tests, more than nine sequential stages of coning and quartering were employed.

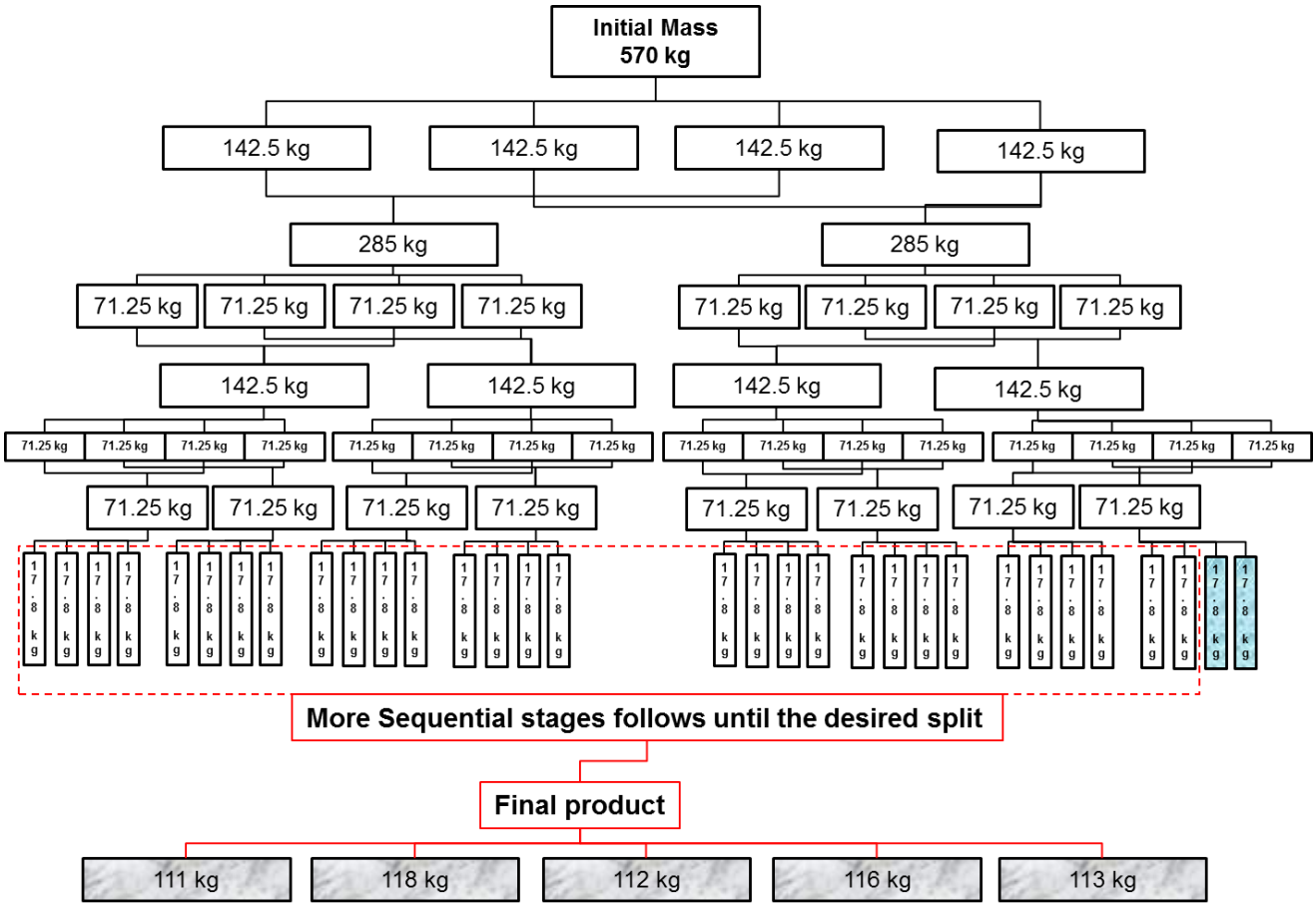

Figure 4-1: Schematic diagram showing sequential coning and quartering method.

4.3 HPGR TEST WORK PROCEDURE

After splitting the sample into five representative lots of approximately 114 ±3 kg each, HPGR tests were performed at three different pressures (60, 90, 120 bar). A repeat of the 20 bar test was conducted to determine the repeatability. One of the lots was kept aside to determine the feed particle size distribution. All comminution tests were conducted using a Köppern HPGR with single pass grinding tests performed on a 250 cm diameter by 100 cm wide HPGR unit manufactured by Köppern as shown in Figure 4-2. The desired pressure on the HPGR was set using Nitrogen gas in the accumulators and the initial gap was adjusted. The movable roll speed was also adjusted. The HPGR pilot plant was then started up by splitting the product conveyor belt first followed by the HPGR and then the feed belt. After

ensuring that it was running at the desired speed, the feed hopper was opened and immediately all the material was crushed and deposited on the belt. Table 4-1 summarises details of the samples used in the HPGR test work. Two particle-size fractions of the HPGR product were then selected from each pressure (Figure 4-3) for mineralogical characterisation and cyanide leach experiments, henceforth known as '*large particles*' (+11.2 mm/-16 mm) and '*small particle'* (+4 mm/-5.6 mm).

Table 4-1: Feed samples used in the HPGR tests.

Test	Pressure (bar)	Mass of feed sample (kg)
1	120	111
2	90	118
3	60	112
4 (Repeat)	120	116

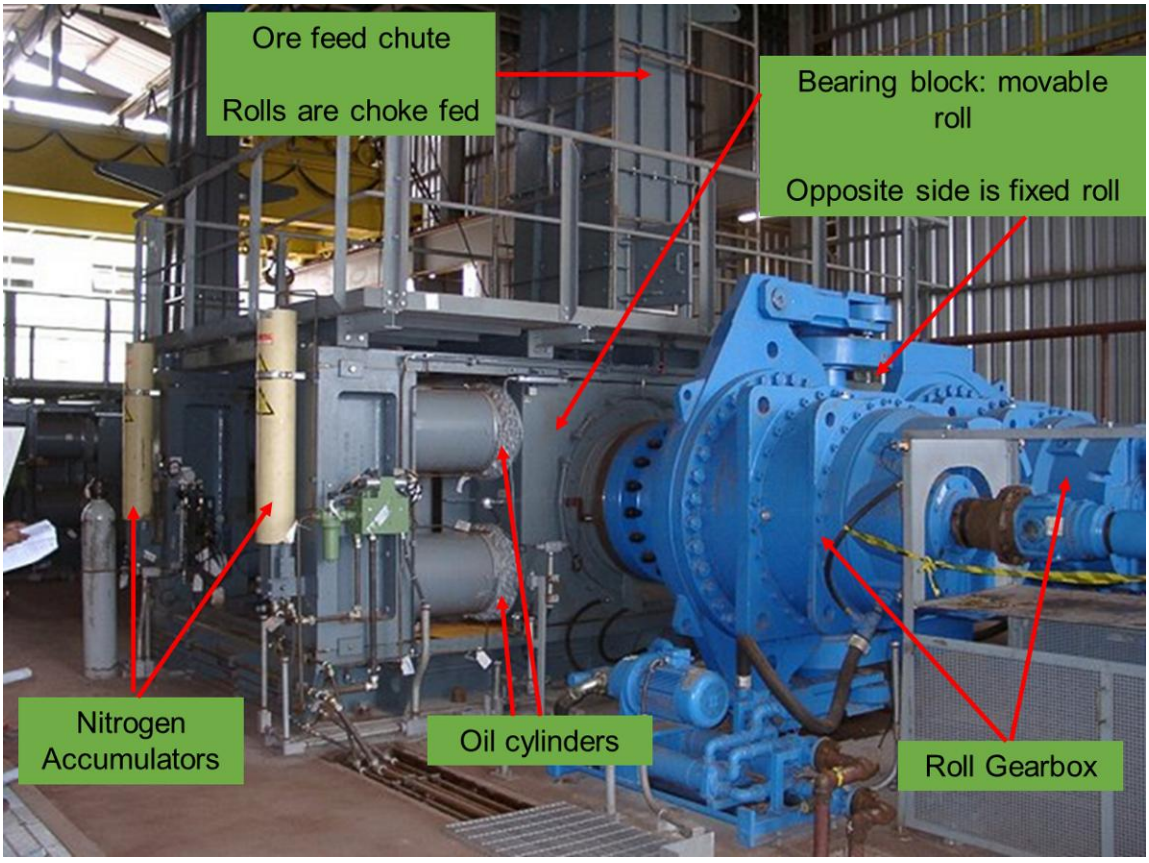

Figure 4-2: Side view an HPGR pilot plant with a capacity of 650 tonnes per hour showing main components (www.goldenqueen.com/gall07.htm).

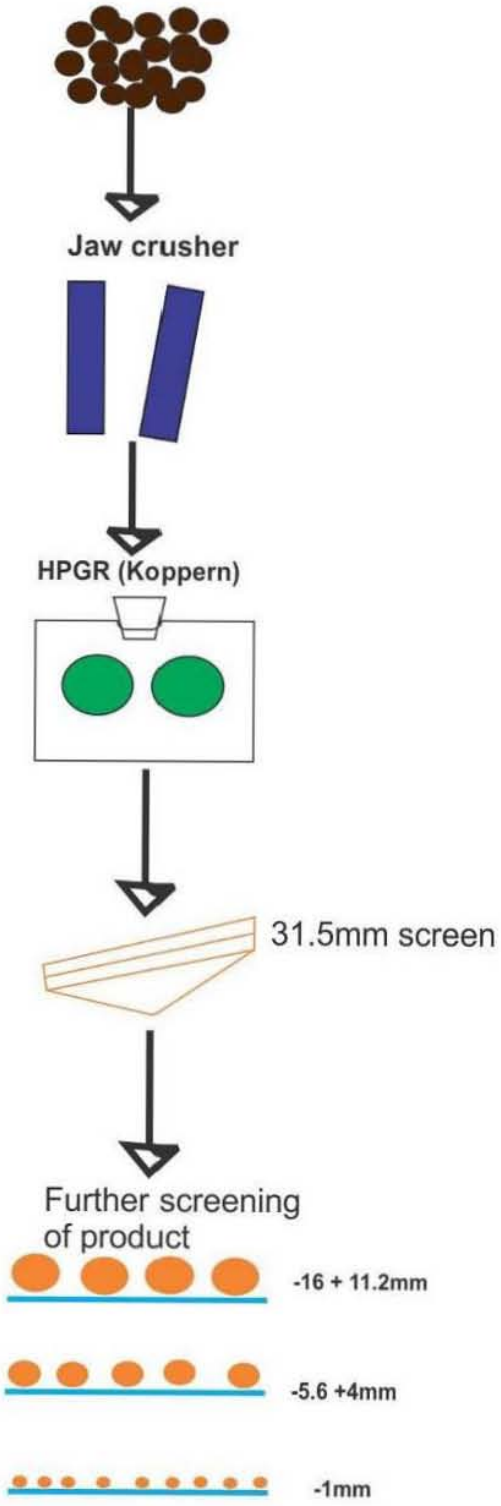

Figure 4-3: Comminution using HPGR and screening of particles with special reference to experimented two-size fraction (-16 mm/+11.2mm and -5.6 mm/+4mm).

4.3.1 Particle size distribution analysis

After performing the HPGR test work, the particle size distribution for both the feed and product were determined using a series of dry and wet screening steps. The sample was dry-screened at 1 mm, and the +1 mm and -1 mm fractions individually reweighed and compared to the initial dry mass. The + 1mm fraction was then further dry-screened on a set of root 2 series screens from the top size down to 1 mm. Each fraction was again weighed and the composite sample mass compared to the initial mass of the +1 mm sample to ensure the integrity of the sampling procedure. Using a rotary splitter, 300 g aliquots of the sub 1mm sample were obtained for wet screening at 38 µm. Both the +38 µm and -38 µm fractions were then filtered, dried and weighed.

4.3.2 Ore preparation for mineralogical studies

Preparation process was conducted in an enclosed area to avoid contamination. Equipment and tools used for preparation such as riffle, rotary splitter screens and brushes, were cleaned thoroughly after each use. The 60, 90 and 120 Bar (-16 mm/+11.2 mm and -5.6/+4mm) HPGR products were analysed using XRF, QXRD, fire assay, ICP-MS, Optical microscopy, QEMSCAN and X-ray CT. The -1 mm HPGR products were analysed using XRF, fire assay, ICP-MS and QEMSCAN.

4.3.3 Fire Assay

Fire assay was used to pre-concentrate samples to determine gold grade (Hoffman et al., 1998). Approximately 15-20 drops of silver as a collector were injected. The sample was mixed in a flux and smelted. The mixture was then tipped into a mould (i.e. iron) where the slag floats to the top, and the lead, now alloyed with the precious metals, sinks to the bottom, forming a *'button'.* After cooling, the lead button was separated from the slag and cupelled at 950°C to recover the Ag (doré bead) + Au. The Ag doré bead was digested in hot (95°C) HNO_3 + HCl. After cooling for 2 hours, the sample solution was analysed for Au by ICP-OES using a Varian 735 ICP. A blank and a digested standard were run every 15 samples. The Instrument was recalibrated after every 45 samples. One duplicate was run on every 10 samples. During the course of this study, fire assays were run at three different

analytical laboratories using the standard method described above: SGS, Performance laboratories and Goldfields assay laboratory.

4.3.4 X-ray Fluorescence (XRF)

The chemical assays were determined using Philips PW1480 wavelength dispersive X-ray fluorescence spectrometry with a dual target Mo/Sc x-ray tube. Selected samples were prepared into fusion discs for major element analysis using the fused bead method (Engelbrecht, 2011). Intensity peaks were corrected for background separation. Matrix corrections were made on all elements and theoretical coefficients were calculated using the de Jongh model in the X40 software and on-line ALPHAS programme.

4.3.5 Optical microscopy

Coarse and fine particles were mounted in resin and polished according to the QEMSCAN sample preparation procedure (see QEMSCAN section). Care was taken to ensure that gold grains were not destroyed and polished away during the preparation of the QEMSCAN blocks. A Nikon microscope was used to investigate the petrography (identify gold and other minerals by reflectivity, colour, hardness, cleavage and other mineralogical characteristics) of the Witwatersrand gold ore. Discrimination of pyrrhotite mineralogy was achieved by using the magnetic colloid method of Craig and Vaughan (1981); the magnetic colloid adheres to the magnetic pyrrhotite, thus differentiating magnetic pyrrhotite from non-magnetic pyrrhotite. The colloid was prepared by mixing $FeCl_2$ and $FeCl_3$ particles to form an insoluble black magnetite precipitate which was stored in a solution of sodium oleate. The colloid was placed over the surface of the ore mount and given a few seconds to interact and adhere to the magnetic pyrrhotite without letting the colloid dry. The samples were observed under the microscope and images were captured using a digital camera.

4.3.6 Quantitative X-ray diffraction (QXRD)

Quantitative X-ray diffraction was used to determine the concentration of the major mineral phases in the ore samples. The HPGR sub samples were prepared for QXRD by milling with a McCrone micronizing mill. A Bruker D8 X-ray Diffractometer equipped with a radiation

source and a Bruker Vantec detector (position sensitive detector) housed in the Department of Chemical Engineering at UCT was used to analyse the samples. Operation parameters included locked 2Th/Th; rotation: Start 5.000^{o}, step 0.017^{o} and end at 90.007^{o}. The Bruker Topas Rietveld software was used for mineral identification and quantification.

4.3.7 Scanning electron microscopy (SEM)

In the early stages of this study, scanning electron microscopy was used to obtain preliminary high quality images of particle textures, such as surface morphology, pore structure, permeability and coatings coupled with energy dispersive X-ray spectrometry (EDX). Six gold ore samples (comprising three VCR and three ER) were submitted to the Central Analytical Facility at the University of Stellenbosch for analysis to identify the chemical and mineralogical composition of the samples. The samples were cut into polished sections; three sections of each sample were used labelled A, B and C, respectively, and polished to ensure a flat polished surface. Analyses were performed on a Zeiss EVO® MA15 Scanning Electron Microscope fitted with an Oxford Instruments® X-Max 20 mm^2 detectors and Oxford INCA software. Beam conditions during the quantitative analyses were 20 kV and approximately 1.0 A, with a working distance of 8.5 mm and a specimen beam current of -20.00 nA. For mineral analyses counting time was 10 seconds live-time. Natural mineral standards were used for standardization and verification of the analyses.

4.3.8 QEMSCAN

The LEO SEM based QEMSCAN platform equipped with two Bruker 4010 SDD detectors at the University of Cape Town together with a Zeiss Evo QEMSCAN machine at EXXARO were an integral part of the process mineralogy study used to determine (a) the bulk modal mineralogy (BMA); (b) field images for petrography and HPGR induced crack and ore porosity analysis; and (c) trace mineral search (TMS) measurements for gold deportment.

HPGR prepared samples (small particles: -16/+11.2 mm and large particles: -5.6/+4mm) were split to the right amount for each size fraction. Graphite was added and mixed with a sample through a screen bigger than the sample size. Moulds were greased with lubricator to prevent the resin from sticking to the moulds. The moulds were labeled with the sample name, size and number. The mixture of sample and graphite was then added into the

greased mould. This was followed by calculation of the amount of resin required to pot the sample and addition of the hardener. A sufficient number of resins per mould was weighed and carefully mixed into the sample in a figure of eight patterns. Sample moulds (30 mm diameter) were then placed into the mould holder of the Citovac. These samples were placed in a vacuum for a total of 10 minutes which was broken after 5 minutes and restarted again. This helps to release trapped air bubbles. The samples were later placed in the pressure pot overnight to cure. This was followed by addition of a printed label and a further resin to the mould which was allowed to cure in the oven until dry. Once completely cured the blocks were removed from the moulds for polishing.

Polishing was done with the object to obtain a mirror-like, topographically relief-free, scratch-free surface. Polishing was conducted using different polishing pads, by leveling the back of the sample using a quick grind. The samples were carefully rinsed and lightly soaped between each grinding and polishing step. The grinding/polishing discs were rinse and lightly scrubbed with a nail-brush after each grinding/polishing step. After all of the polishing steps were completed and the samples have been rinsed and soaped, they were placed in the ultrasonic bath for approximately 10 minutes. They were then cleaned again with a generous squirt of ethanol being very careful not to scratch the surface. The samples were dried in the oven for at least an hour. Carbon coating was the final stage in the preparation of polished sections. Carbon coating is necessary to diffuse electrons off the surface of samples when they are in the microscopy. Table 4-2 presents measurement conditions and information obtained using QEMSCAN.

Table 4-2: Measurement condition and information obtained using QEMSCAN.

Measurement	Sample type	Conditions (pixel size)	Information obtained
Field image	HPGR products: Small and large particles	20 µm pixel size, 5 nA beam current	Crack and porosity volume percentage
Bulk modal analysis	-150 µm feed sample analysed in 4 fractions	1 -3 µm pixel size, 5 nA beam current	Modal mineralogical composition of the ore
Trace mineral search	-16/+11.2 mm and -5.6/+4mm HPGR products	1 µm pixel size, 2 nA beam current	Gold mineralogy

Data processing was done using QEMSCAN iExplorer software. Field images of particles acquired using QEMSCAN were stitched together using "*field stitch*" in order to obtain a complete image. The area occupied by internal cracks was calculated using the "*injector*" functionality. A simple mineral list was created through classification of minerals based on their groups and abundances. This was followed by different analyses such as particle count, liberation status, shape factor, mineral association and grain size distribution.

Data validation was performed by comparison of QEMSCAN calculated assays against XRF and assays (Table 4-3) and presented graphically in Figure 4-4. Acceptable data correlations were obtained for the major elements of the Witwatersrand gold ore. This is shown by most of the points which lie on the line with a gradient of close 1. Minor deviations from the linear correlation were observed (Figure 4-4).

Table 4-3: Comparison between QEMSCAN calculated and ICP-MS actual assays

Element	Entity	Combined	-150/+106 µm	-106/+75 µm	-75/+38 µm	-38/+0 µm
Al	QEMSCAN	4.1	2.3	2.1	2.0	5.5
	XRF	4.4	2.7	2.7	2.9	5.8
Ca	QEMSCAN	0.6	0.5	0.4	0.6	0.6
	XRF	0.6	0.6	0.6	0.6	0.7
Fe	QEMSCAN	4.2	3.7	3.3	4.1	4.6
	XRF	3.0	3.0	2.9	2.9	3.1
K	QEMSCAN	1.2	0.8	0.7	0.6	1.6
	XRF	1.5	0.8	0.9	0.9	2.0
Mg	QEMSCAN	0.5	0.4	0.3	0.4	0.6
	XRF	0.5	0.6	0.4	0.4	0.6
Na	QEMSCAN	0.1	0.1	0.1	0.1	0.2
	XRF	0.3	0.3	0.3	0.3	0.4
S	QEMSCAN	2.2	2.2	1.9	2.5	2.3
	XRF	2.4	1.1	1.4	1.7	3.2
Si	QEMSCAN	36.8	39.4	40.3	39.4	34.5
	XRF	37.1	39.2	39.6	39.4	35.3

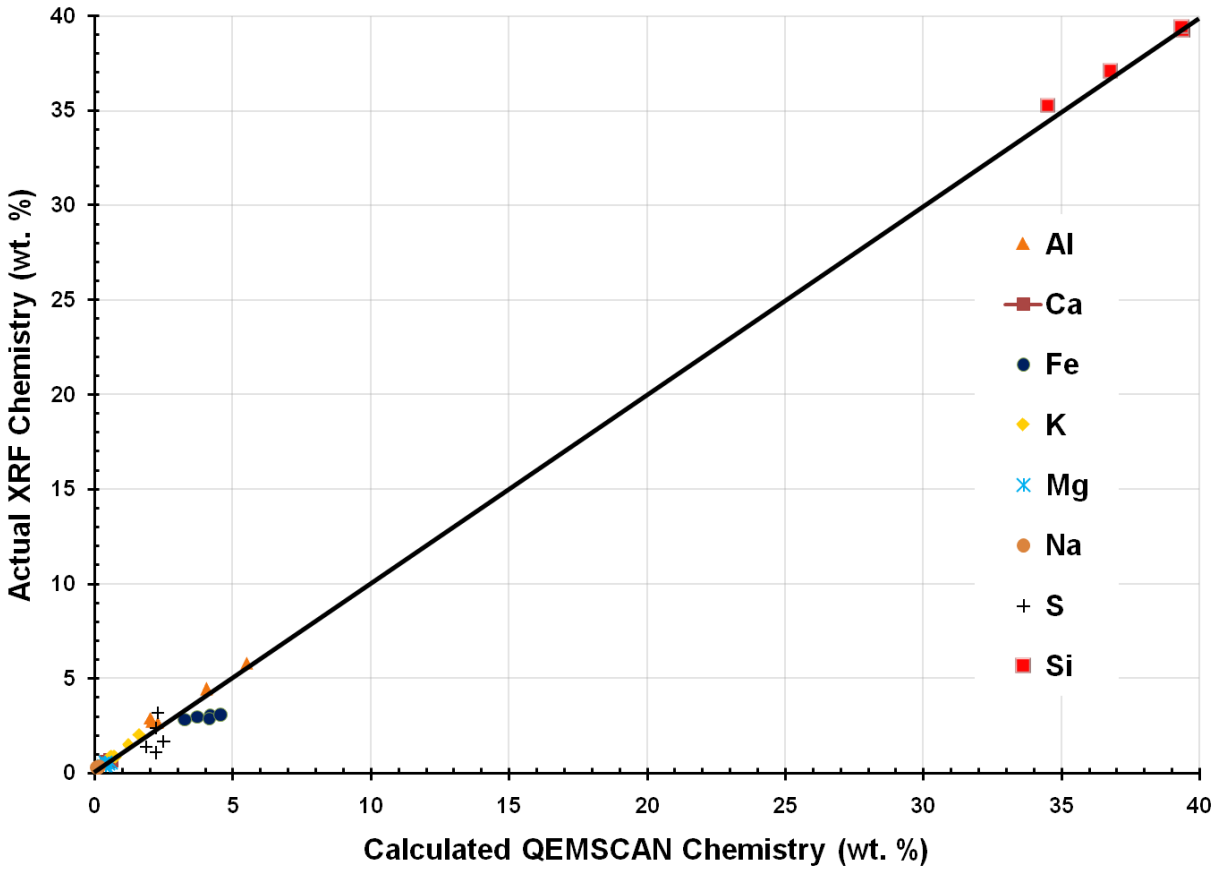

Figure 4-4: Major elements correlation using ICP-MS actual assays against QEMSCAN calculated assays.

4.3.9 Micro-focus X-ray CT

Selected particles were analysed using micro-focus X-ray computed tomography using NIKON Micro-focus X-ray CT at the MIXRAD facility hosted by the National Energy Corporation of South Africa (Necsa), in order to characterise the HPGR induced crack network and gold deportment. A full description of the MIXRAD system can be found in Hoffman and De Beer (2012). The scanning parameters for all samples in this study are detailed in Table 4-4. A high resolution (~50 nm) versa X-radia CT machine from Technikon University of Munich (TUM), Physics department in Germany was used for quality assurance and to identify minerals that were less distinct in the Necsa X-ray CT.

Table 4-4: Summary of measurement parameters using Nikon XTH 225 ST micro-focus X-ray tomography.

System Characteristic		**Value**
X-ray source	Potential	180 KV
	Current	60 (μA)
	Voxel size	~17 μm
	Beam Angle	25^{o}
	Filter	0.25 mm Cu
Translation table	Axis movement (directions)	5
	Sample Movement in Horizontal Plane (mm)	200
	Sample Movement in Vertical Plane (mm)	300
	Sample Movement in Beam Direction (mm)	610
	Rotation accuracy	1/1000th of a degree
	Tilt	0º
	Number of projections	1000
Detector	Type	Perkin Elmer
	Dynamic Range	16 bit
	Physical Size (mm)	400 x 400
	Pixel Size (Micron)	200 x 200

4.3.10 Micro-focus Cold neutron tomography

Selected particles from the X-ray CT study were then further used for cold neutrons radiography at the ICON beamline, Spallation Neutron Source (SINQ) at the Paul Scherrer Institute (PSI) in Switzerland. This Swiss ICON has a flexible design to meet the requests from a wide user community and to date; this is the strongest stationary spallation source in the world operating in continuous mode. Full details of the instrument and experimental methods are given in Kaestner et al. (2011). The micro lens system setup was used with 100 μm thick 6 Li based neutron sensitive scintillator screen. The transmitted beam intensity was

registered with the high resolution micro tomography detection device installed at the middle position of ICON facility. Multiple neutron projections were taken and later reconstructed to build a 3D image of the Witwatersrand HPGR comminuted particle. More details on X-ray CT are given in Chapter 5.

4.4 COLUMN LEACHING EXPERIMENTS

A set of laboratory scale cyanide leaching experiments were conducted in the Department of Chemical Engineering at the University of Cape Town with the aim to investigate of Witwatersrand gold ore to the process of heap leaching. The emphasis was on determining the effect of particle size on gold extraction and HPGR pressure effectiveness relative to gold recovery. The second objective of the same experiments is to investigate the extraction behaviour of HPGR products relative to time. The column leach reactors were all run in a suitable designed fume cupboard with appropriate safety protocol in place to deal with cyanide usage (Appendix XII). Table 4-5 presents feed size fraction, grade and mass of the Witwatersrand gold ore used in this study.

Table 4-5: Summary of the Witwatersrand gold ore investigated.

Reactor	Size fraction	Ore grade (g/t)	Ore mass (kg)
1	120 Bar: Large particles	1.17	3.15
2	120 Bar: Small particles	1.43	1.24
3	60 Bar: Large particles	0.80	4.60
4	60 Bar: Small particles	1.29	1.42
5	90 Bar: Small particles	0.57	1.50
6	120 Bar: Large particles	1.17	3.15
7	120 Bar: Small particles	1.43	1.24
8	60 Bar: Large particles	0.80	4.60

4.4.1 Equipment used and measurements performed

Figure 4-5a shows a schematic drawing of the leach reactor. Samples were packed into leach reactors as indicated in Figure 4-5b. The cyanide solution was continuously circulated around stacked baskets containing ore particles (Figure 4-5c). The particles were fully immersed in the leach solution and the reactor was operated in continuous mode. Internal circulation of the leach solution was achieved through a central draft tube into which air was bubbled at approximately 2700 mL/min (0.27 vvm).

The eight leach reactors were first run with water to test for any leakage for a period of 24 hours. During this test, the eight-channel pump head was tested for suitable flow rate and pump gear dial setting that was able to supply the solution equally to eight leach reactors. This was done by changing the flow rate every four hours while monitoring the supply of water into the columns and relation between water flow rate and aeration rate. Table 4-6 shows the pump dial setting relative to flow rate. For this project, a dial setting of 30 (flow rate of 0.10 L/hour/m^2) was used to run the actual leach reactors.

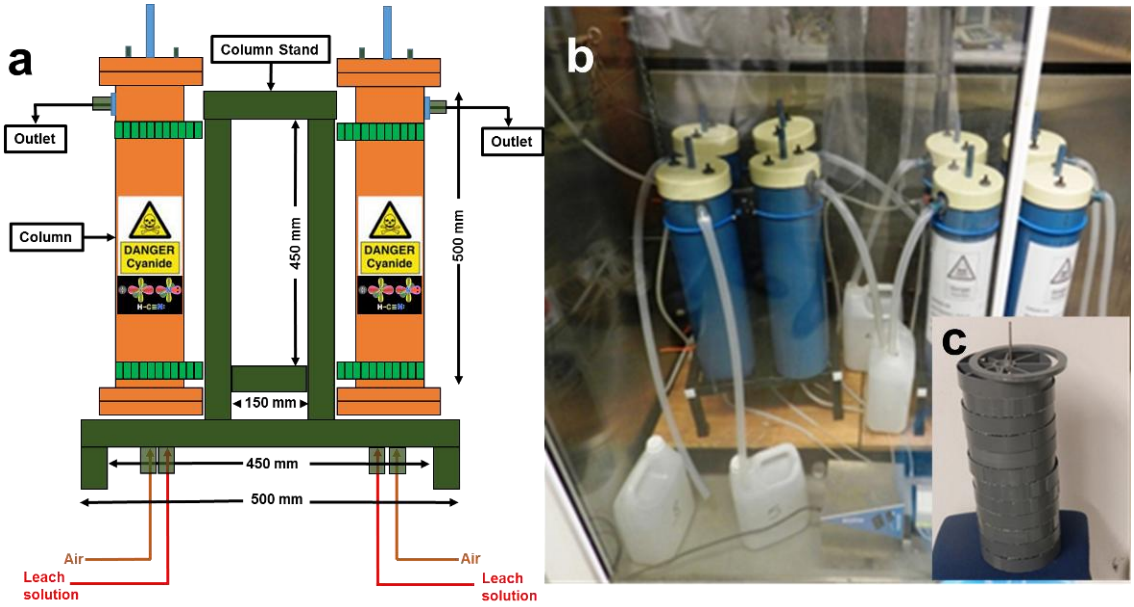

Figure 4-5: (a) Schematic of the leach reactors; (b) Set up of leach reactors with stand and 8-channel pump head in a fume hood; (c) designed frame inside the leach reactor loosely holding stacked particles.

Table 4-6: Correlation between pump gear number and flow rate.

Pump number	**Flow rate (*L*/Hour/m^2)**	**Flow rate (*L*/Day/Column)**
10	0.03	0.83
20	0.07	1.67
30	0.10	2.50
40	0.14	3.33
50	0.17	4.17
Estimated effective aeration rate range		**2700 ml/minute**

Experiments were conducted in a small laboratory scale using Erlenmeyer columns with a working volume of 7 L. Concentration of solution used was 200 ppm at a pH of approximately 11. Operating temperatures were room temperature. All pH measurements were performed using a Crison alkaline pH meter which was calibrated each time before use. Temperature was also constantly monitored using Crison pH meter. Gold concentrations were determined by inductively coupled plasma mass spectrometry (ICP-MS). The instrument used was a Thermo Fisher XSeries2. Samples were diluted 100 times with a 5 % HNO3 solution (containing 10 ppb of Bismuth, used as an internal standard).

CHAPTER 5: DEVELOPING THE ORE CHARACTERISATION METHOD USING MICRO-FOCUS X-RAY CT

5.1 INTRODUCTION

This chapter presents the development of an ore characterisation method using X-ray CT as a contribution to the investigation into the potential for heap leaching of Witwatersrand gold ore. X-ray CT provides grey level information, which needs to be "*calibrated*" to provide useful mineralogical information. The development of the method for extraction of specific process mineralogical information in this study using micro-focus X-ray CT comprises: grain segmentation, region of interest extraction, volume percent quantification of gold grain and HPGR induced crack network studies. These parameters will be used to assess the potential of X-ray CT as a tool in process mineralogy of the Witwatersrand gold ore. X-ray CT data was validated with existing process mineralogy instrumentation of which in this study was QEMSCAN, QXRD, SEM, and optical microscopy QEMSCAN. Limitations of X-ray CT in developing the methods are also presented.

5.2 MINERALOGICAL COMPOSITION OF THE WITWATERSRAND GOLD ORE

The successful application of X-ray CT in mineralogical studies is based upon a prior knowledge of the ore characteristics. Using a combination of chemical assays, optical microscopy, QXRD and QEMSCAN (refer to Chapter 4); composition of the mineralogy of the ore sample used in this study was obtained. The major minerals present in the Witwatersrand gold ore composite sample identified by QEMSCAN (Figure 5-1) analysis of the feed sample are quartz (73 wt. %), muscovite (11.6 wt. %) and chlorite (5.4 wt. %) with minor feldspar, biotite and sphene. Most of the carbonates are from calcite related to veinlets in the VCR. Pyrite and pyrrhotite are the two most common sulphides present, with traces of chalcopyrite and galena. The sulphide content accounts ~4 wt. % of the total composition. These compositions indicate that the ore is dominated by minerals with variable densities.

The gold grade of the ore investigated is in the region of 1 g/t due to a high volume of waste material dilution.

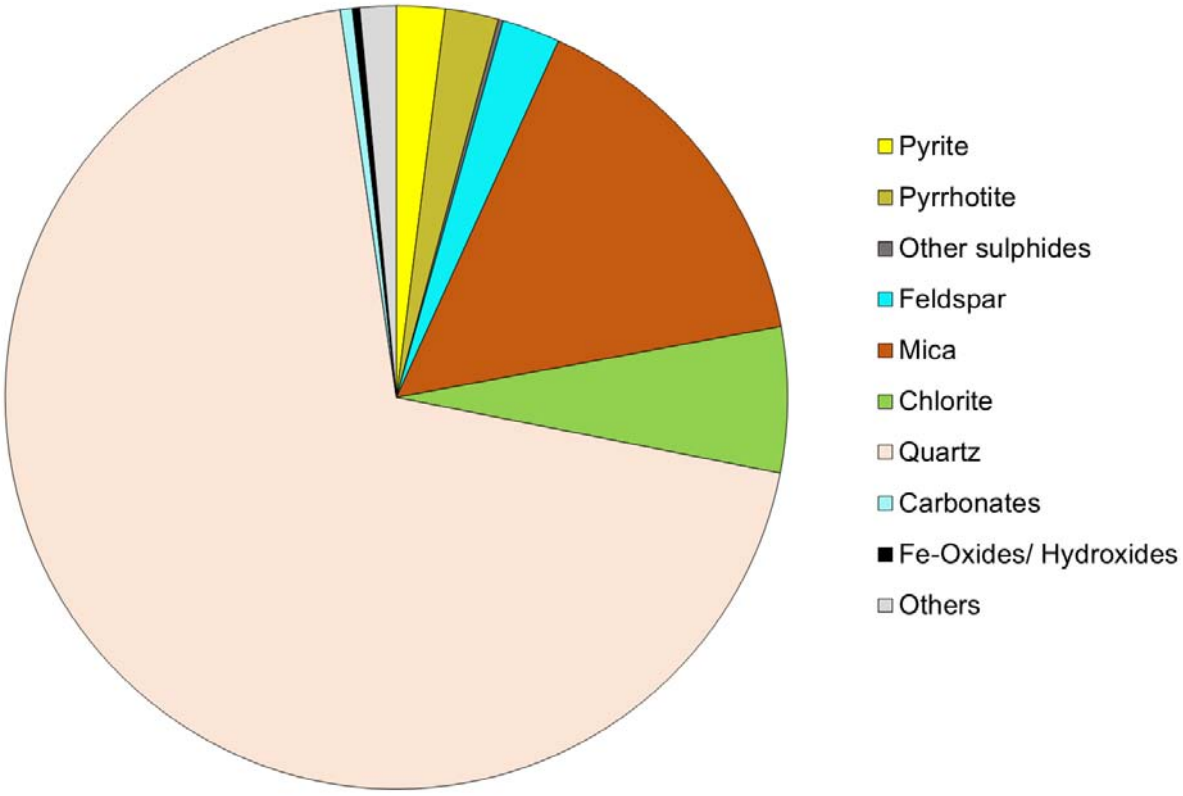

Figure 5-1: Summary of the modal mineralogy (in weight percent) of the Witwatersrand gold ore as determined by QEMSCAN (Others include uraniferous minerals).

5.3 MEASUREMENT PARAMETERS

Rock samples are often heterogeneous since they contain various minerals of different grain sizes. Measurement parameters have to be done using specific algorithms in order to discriminate different mineral phases (Godel, 2013). Individual minerals in the ore investigated also vary in size but they are all less than 5 mm. The sample size fraction plays an important role in X-ray CT studies and is governed by the amount of detail required. Larger size fractions (> 20 mm) are used in studies where the amount of detail does not require discrete statistics whereas smaller samples are used where high resolution reaching to a micro-meter scale is required. The sample size can be reduced down to -1 mm for particular studies where the source has to be as close as possible to the material scanned (for example, cracks within minerals). In the case of the Witwatersrand, gold is encapsulated in larger host material (quartz-pebble conglomerates), details are of

significance, and thus the material to be studied should be in size fractions of less than 20 mm.

Given the heterogeneous nature of Witwatersrand ore, each pixel in the radiograph taken at a specific angle (α) is a record of the total attenuation along the X-ray path (L) with local attenuation μ varying as a function of the pixel position (x) and the angle (α), defined by I (the intensity measured by the detector), I° (the intensity of the incident X-ray beam) and is given by the equation 5.1. The theoretical X-ray attenuation coefficient (μC) for a specific phase, at a given energy (ε), can be calculated using the mass attenuation coefficient (Berger et al., 1998) and mineral density (equation 5.2 where ρ is the density (g/cm^3) of the mineral/alloy and μTot(ε) is the total attenuation with coherent scattering (cm^2/g)):

$$ln\ I(L, x) / I°(\alpha) = -\int_{L_0} \mu(x, \alpha)\, dx \qquad \text{Eq. (5.1)}$$

$$\mu C(\varepsilon) = \rho .\ \mu Tot(\varepsilon) \qquad \text{Eq. (5.2)}$$

Linear attenuation coefficients of minerals associated with the Witwatersrand gold ore were calculated for the energy spectrum 0 to 500 KeV (Figure 5-2). Based on the attenuation coefficients and instrument capabilities, X-ray energy of 180 KeV was selected in this study to minimize beam-hardening effects and to provide a good contrast between the minerals of interest. Several minerals were found to have similar attenuation behaviour over a range of different X-ray energies and they were grouped together according to their classes to simplify results. These minerals are the silicates (i.e. quartz and muscovite) and sulphides (i.e. pyrite, pyrrhotite, sphalerite and chalcopyrite). If the main research interested was looking at silicates, a lower energy (<100 KeV) would used, but because the interest is on gold which is so dense, a higher energy is required.

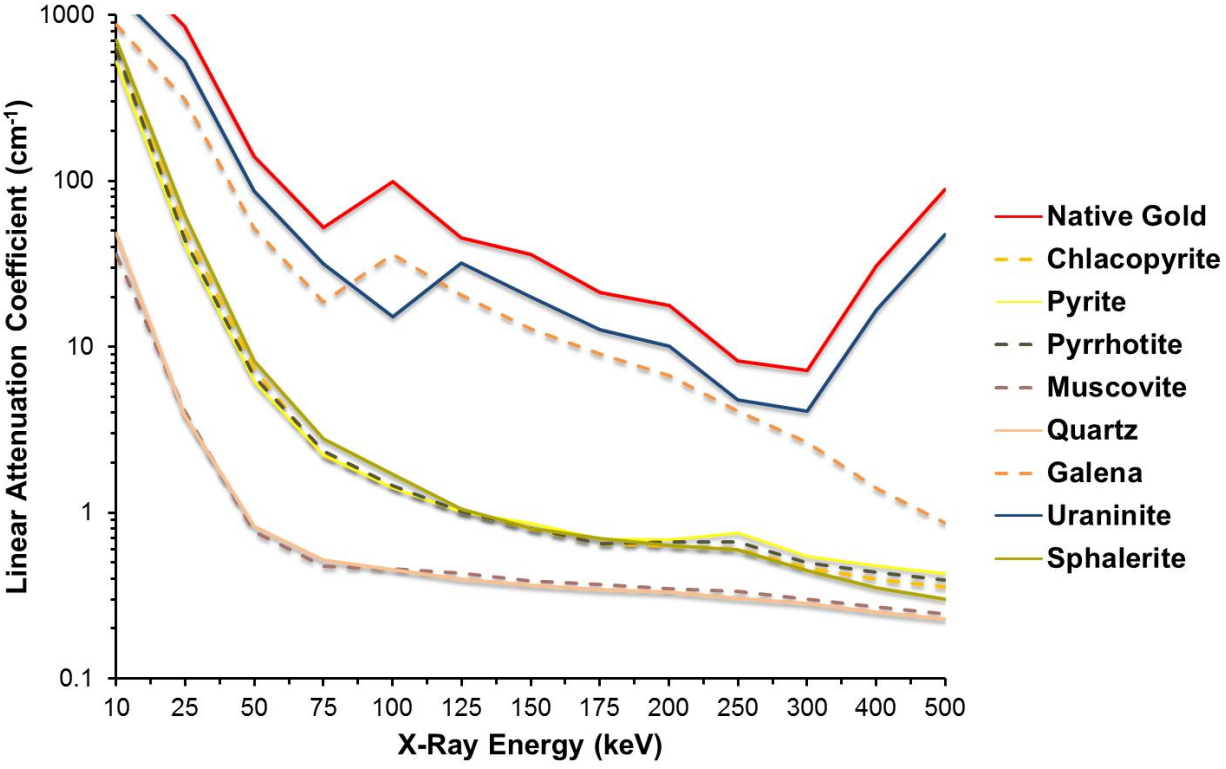

Figure 5-2: Linear attenuation coefficients as a function of X-ray energy for gold ores. Values used are based on end-member compositions and average densities and were calculated using XCOM Photon Cross-Section database (Berger et al., 1998).

Two size fractions of crushed ore were used in this study (-16+11.2 mm and -5.6+4 mm). Although each X-ray CT system is different, all scanning parameters are governed by the size of the host material (Witwatersrand gold sample), the X-ray target material and the filter material. The filter material (i.e. copper filter) absorbs the low energy X-rays and in the process hardening the X-ray beam to improve X-ray penetration through the sample. For this gold study, the sample sizes used are in the good size range of CT scanning parameters. They allow placement close to the X-ray source so as to provide optimal spatial resolution through magnification of the fine minerals (in the order of 17 µm), but also to avoid image cropping during acquisition. This is not ideal since one would expected a voxel size of close to 1 micron, but was the best that could be achieved in this study, using the instrument at Necsa. In order to improve the signal/noise ratio (S/N), a 1 second exposure time per radiograph was applied. Shading correction is applied automatically by the X-Ray system to normalise the acquired radiographs. During this phase, the sample was removed from the field of view under the exact same conditions as the sample images to acquire a dark and flat field images. The field images are used by the shading correction algorithm for normalisation.

5.4 RECONSTRUCTION PROCESS

A set of radiographs were reconstructed using the CT-PRO reconstruction software package developed by NIKON, into a virtual 3D volume. Since the X-ray images are in a 2D shadow format (radiographs), CT-Pro reconstruction software was used to transform the 2D projections into a 3D volume using a Fourier Transform method (Figure 5-3). The CT-Pro software allows for rapid (<2 minutes) reconstruction with limited input from the operator. Each projection gives the information of the beam attenuated by the sample at a particular angle. However, this requires a computer with large memory (~48 GB RAM) and processor (>2.5 GHz). Reconstruction parameters are optimised automatically so that the quality of a scan does not depend on a qualitative opinion of the operator. The final product from the reconstruction in CT-Pro is a 3D volume file (Figure 5-4).

Figure 5-3: Conversion of the 2D projections into a 3D volume (tomography) using the CT-Pro software.

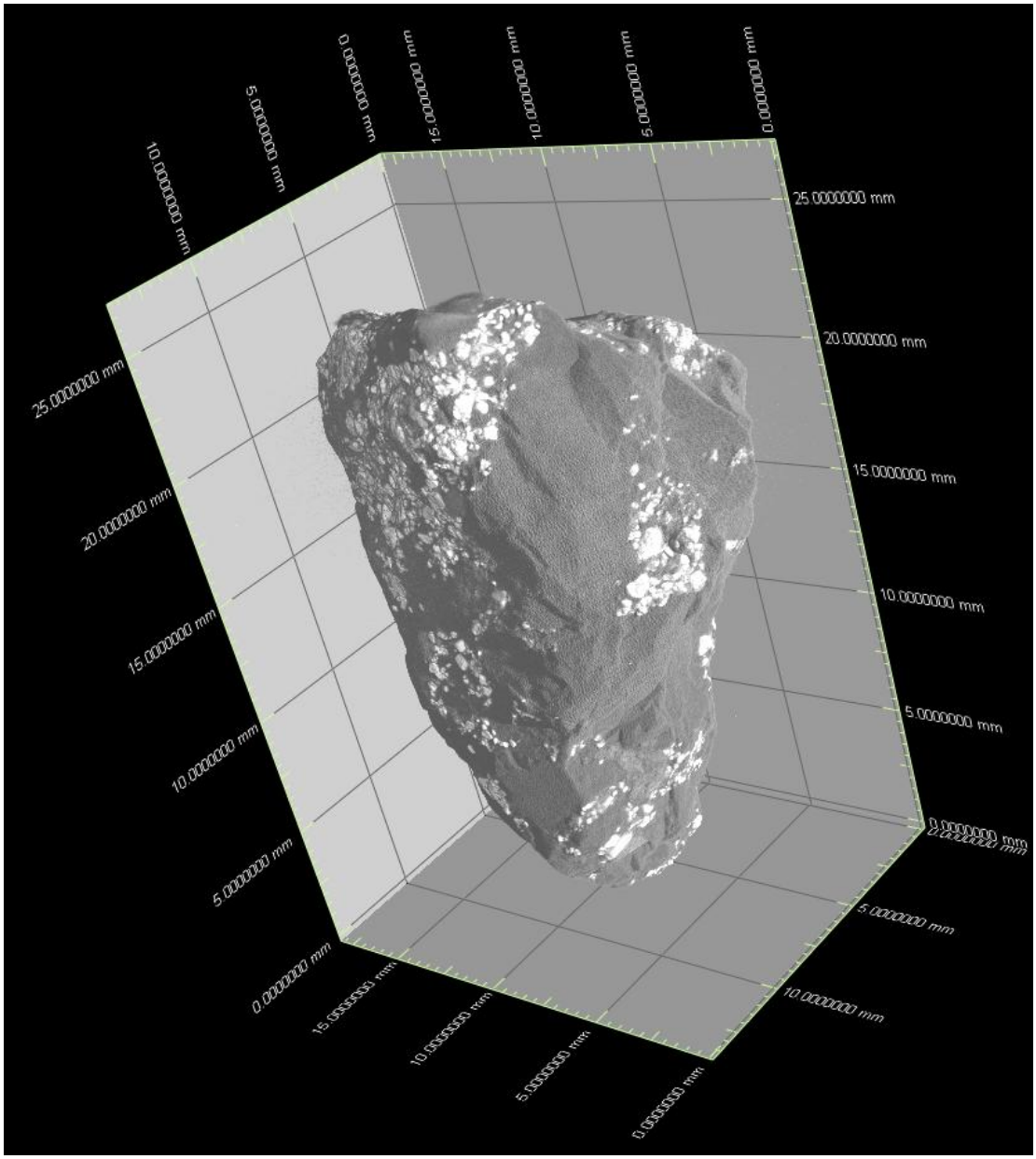

Figure 5-4: An illustration of the Witwatersrand gild ore 3D volume produced through reconstruction (-16+11.2 mm).

5.5 VISUALISATION AND DATA MANIPULATION

5.5.1 Phase segmentation

Visualization software, VG Studio MAX (2.2), was used to investigate and visualize minerals and subsequently quantify gold grains, HPGR induced cracks and ore porosity analyses. For

ease of use, different grey level categories were given false colours. Figure 5-5 illustrates how gold grains were colour coded by segmenting grey values that represent minerals of interest and extracting the volume based on those voxel values. Gold grains and associated minerals were coded with a variety of colours and these shadings were used to classify gold grains of which association characteristics and grain size distribution were obtained. When the yellow grain surface hides the phase colours, it gives the operator an opportunity to know that the segmented grey value belongs to a specific mineral.

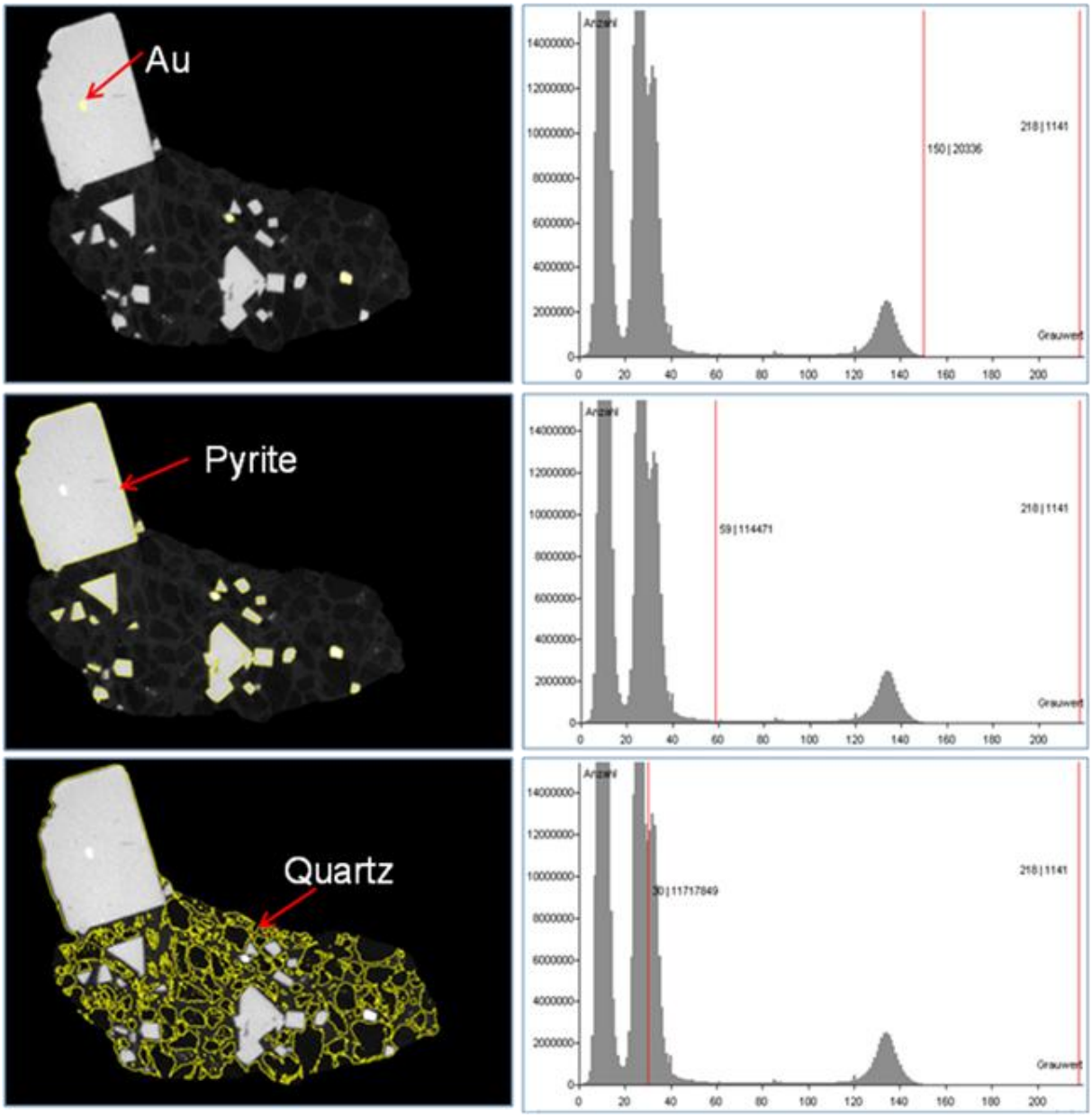

Figure 5-5: Segmentation and region of interest (ROI) extraction of Witwatersrand gold ore particles using VG-Studio Max 2.2.

5.5.2 Data Validation

Several X-ray CT scans were validated for mineral identification using QEMSCAN. No mineral calibration (i.e. pre-configuration of the system to identify minerals based on their exact attenuation) was done due to limited availability of pure mineral specimens, especially of gold and uraninite (radioactivity) therefore, QEMSCAN was used as the main direct data validation technique. The data validation process involved comparison of 2D X-ray CT slices with 2D QEMSCAN field images as indicated in Figure 5-6. Results correlation showed that individual mineral phases are easily identified using QEMSCAN whereas only minerals with high density differences can be differentiated using X-ray CT.

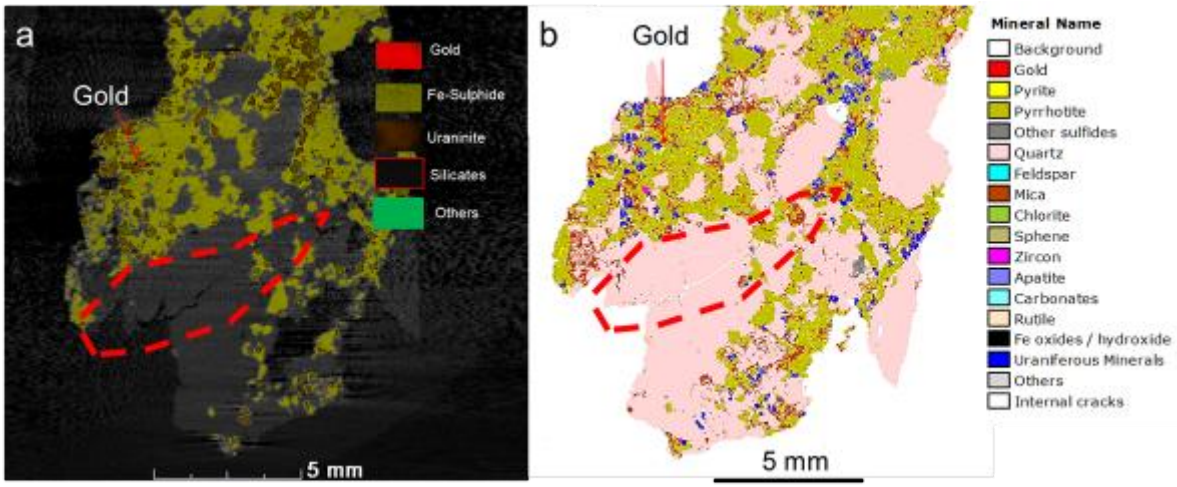

Figure 5-6: 2D X-ray CT and QEMSCAN false colour image illustrating crack propagation (crack region= red dotted line).

Mineral grouping was done on the X-ray CT due to a resolution limitation which does not allow clear distinction of minerals with relatively similar attenuation-coefficients. Figure 5-7 presents the bulk mineralogical analysis of the feed determined using X-ray CT. The X-ray CT mineralogical composition was found to be similar when compared to a simplified QEMSCAN modal mineralogy of the Witwatersrand gold ore (Table 5-1).

Table 5-1: QEMSCAN Modal mineralogy grouped to mineral groups.

Mineral	Composition (Wt. %)
Pyrite	2.1
Pyrrhotite	2.5
Other sulphides	0.2
Carbonates	0.5
Quartz	71.1
Feldspar	3.2
Mica	12.3
Chlorite	5
Sphene	0.9
Fe oxides/ hydroxides	1.6
Others	0.6

Mineral Group	Composition (Wt. %)
Sulphides	4.9
Silicates	92.4
Oxides	1.6
Other	1.1

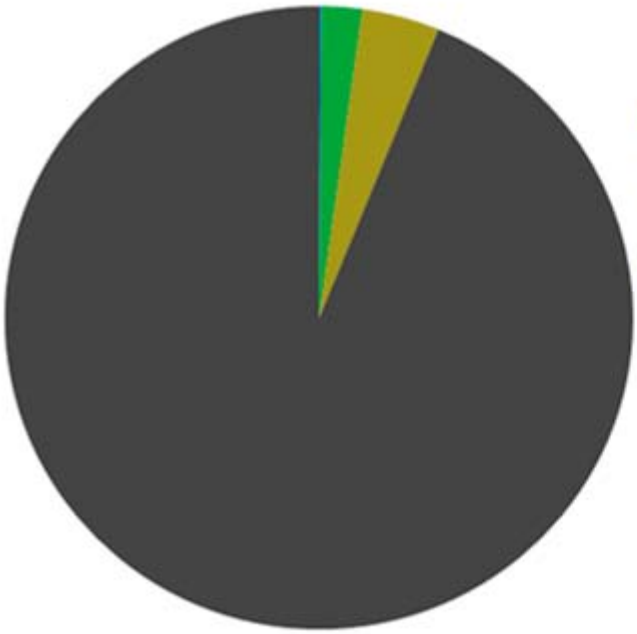

X-ray CT Mineral Group

Mineral Group	Composition (Wt. %)
Sulphides	4.0
Silicates	93.8
Oxides	0.1
Other	2.1

Figure 5-7: Summary of the modal mineralogy (in weight percent) of the Witwatersrand gold ore as determined by X-ray CT.

5.5.3 Ore porosity and crack analysis

Particle assemblages were first extracted from a predefined region of interest in order to avoid overlapping of the background with internal cracks and pores because they shared the same grey value. The cracks found in the isolated particles were mapped and quantified in terms of their percentage-based particle volumes, maximum particle widths and crack volumes. Determination of the crack volume percentage involved segmenting the cracks and porosity grey scale values. The cracks and porosity greyscale value ranges were captured in the VG-Studio Max volume analyser in order to obtain the volume percentage. Figure 5-8 demonstrates the process of crack volume quantification using the volume analyser. Four particles were analysed per size fraction in all HPGR pressure. In both the X-ray CT and QEMSCAN data, internal porosity has been included as part of crack percentage, given the petrogenetic history of the ore where most of the primary porosity has been destroyed by metamorphism (thus considered negligible) and the majority of the remaining micro pores are likely to be submicron. Details of Witwatersrand ore porosity and permeability are explained in detail in Steven (2009).

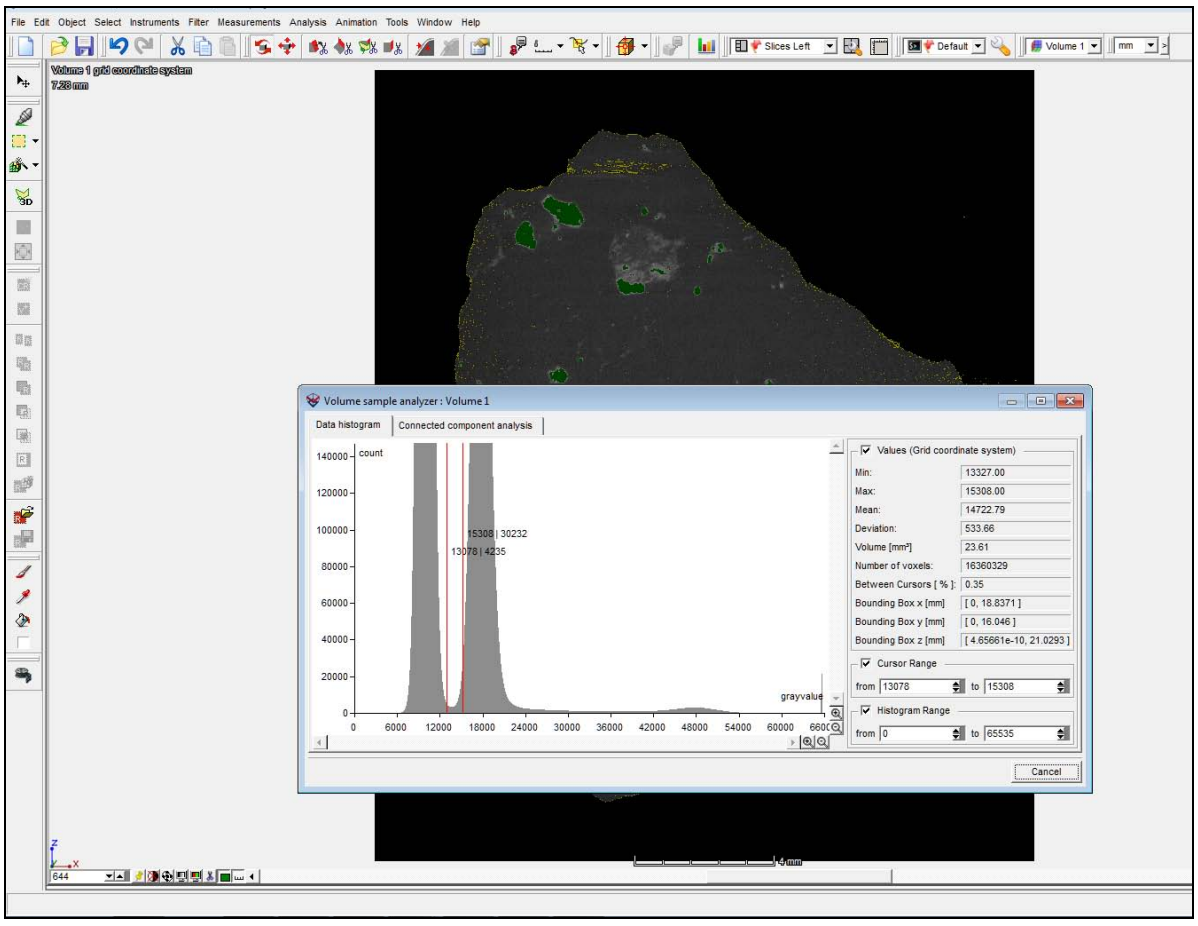

Figure 5-8: Crack and porosity volume percentage acquisition using volume analyser.

After obtaining the HPGR induced cracks and porosity volume percentage, defect analysis was run and the input parameters included voids measurements and selection of an appropriate greyscale value. The minimum crack volume considered was 0.001 mm^3 for both the large and small particles. Quantification of cracks in defect analyses allows for accurate delineation of crack and porosity due to the fact that the data comes with sphericity which can be used to characterise the degree of roundness and linear material. The micro-crack will have a large equivalent diameter but small maximum opening (sphericity <<1), while the pores will be more spherical (sphericity ≤ 1). All linear material (sphericity of 0 to 0.3) on segmented materials from defect analysis was treated as cracks. The Recalculation of the volume percentage obtained from the volume analyser was also done manually (on Microsoft excel) as a measure to validate the percentage cracks and porosity. Cracks that are smaller than the voxel size of 17 µm were not included in the calculation due to resolution limitations.

5.5.4 Gold characterisation

A region of interest was first defined followed by phase quantification. Phase quantification involved the calculation of the amount of gold based on grey values using the volume analyser in the VG studio Max software. The volume analyser tool aids the operator in selecting the appropriate greyscale interval to fit an iso-surface that will cover only the grains within that selected interval for defect analysis (Jardine, 2013). Figure 5-9 illustrates the process of phase quantification with special reference to a gold grain.

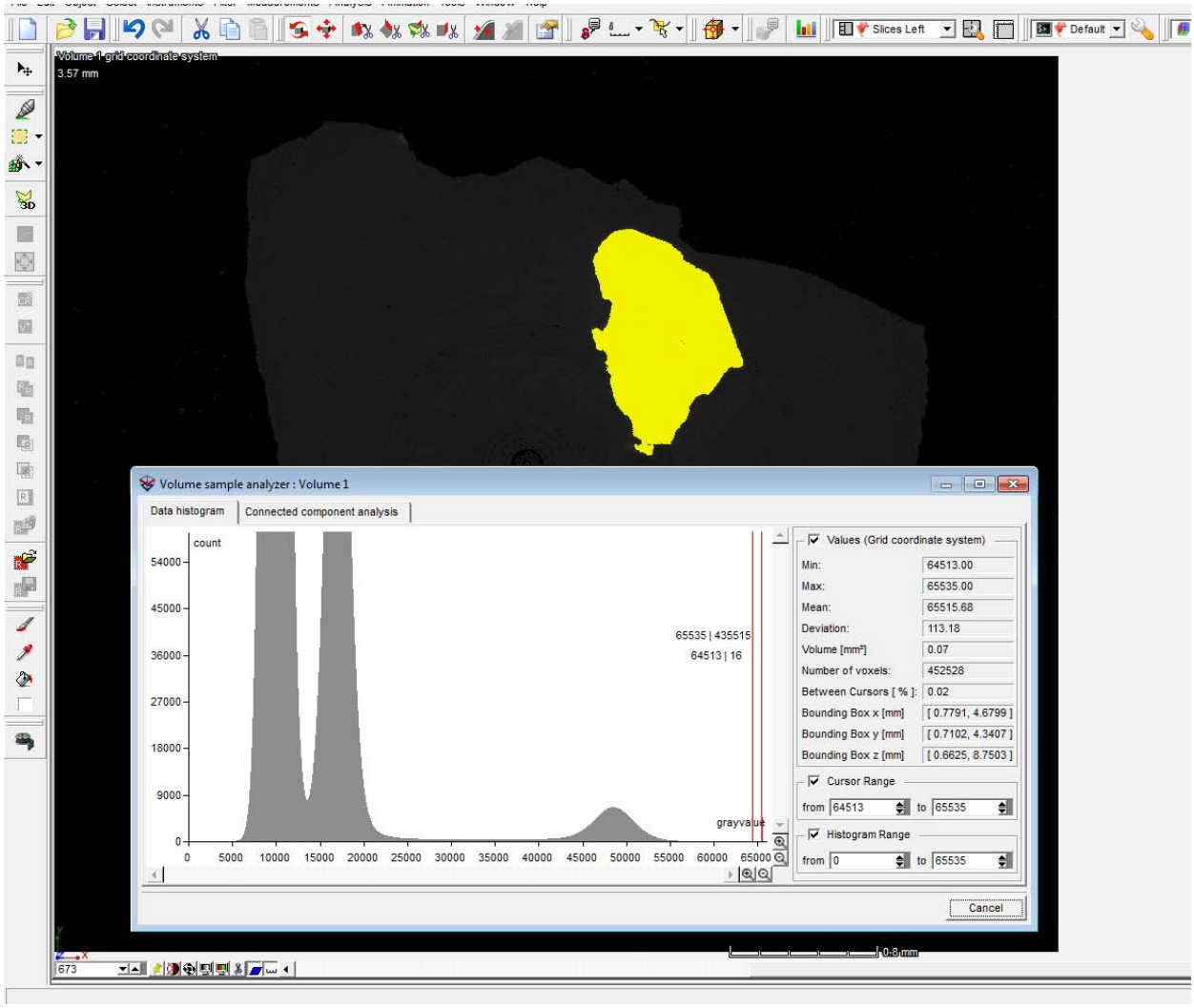

Figure 5-9: Sample volume analyser showing quantification of gold in a sample.

This was followed by running the defect analysis functionality which also uses grey values in order to obtain data on individual gold grains. A defect analysis fits a surface around clusters of voxels that contain grey values selected in a greyscale interval. Defect analysis produces its own coloured scale indicating the variation in gold grains. Data from the defect analysis contains grain diameter, sphericity, surface area, grey scale value and volume. Each gold grain is assigned a grain number which is not displayed on the colour scale and xyz co-ordinates for spatial location. Figure 5-10 shows a volume colour scale indicating the variation in gold grain size, but one gold grain is exposed at this particular slice with other grains located in various slices.

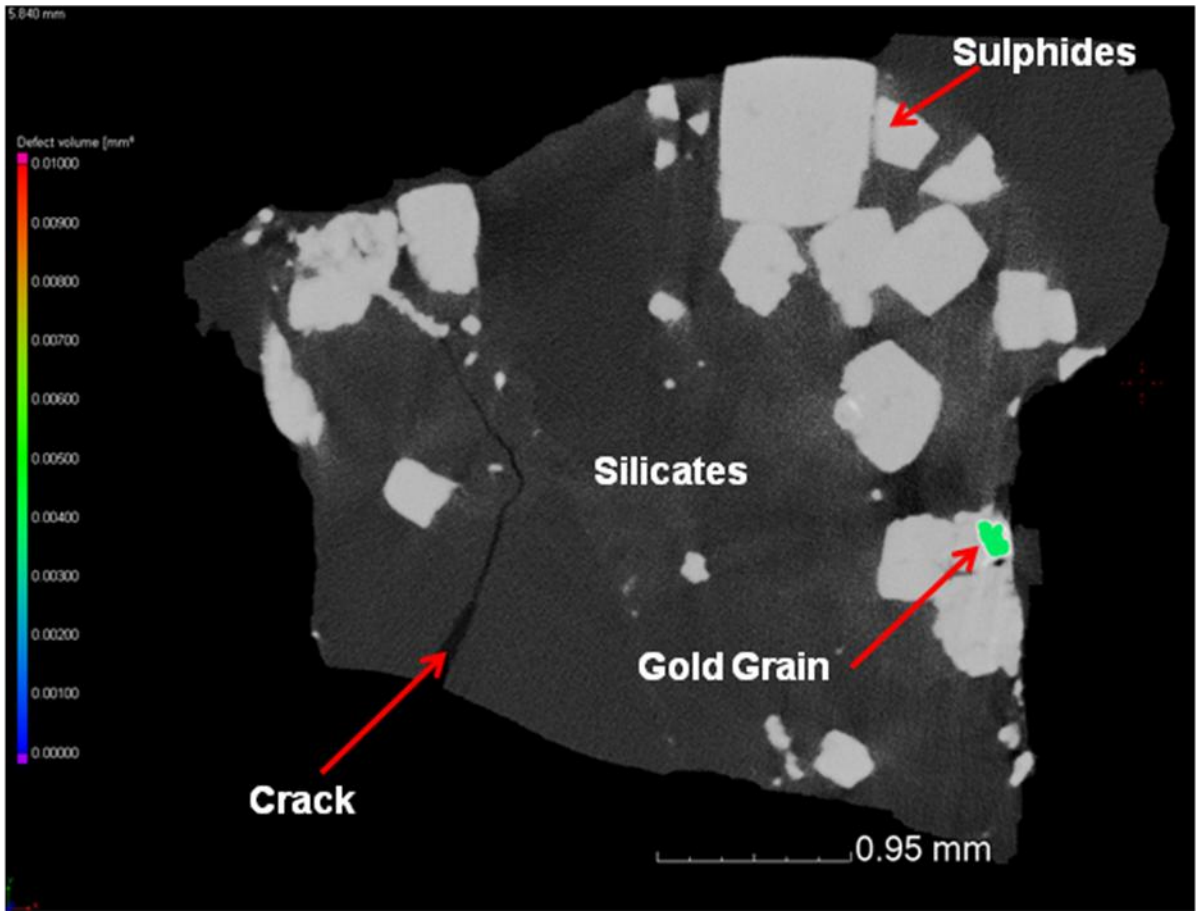

Figure 5-10: Visualisation of defect analysis on Witwatersrand gold ore particle map.

Figure 5-11 presents an example of the sequential gold visualisation and quantification using X-ray CT. The particle below contains 0.069 vol. % gold which is equivalent to a calculated grade of grade of 4900 g/t and this in a fact, a rather anomalous particle. It was also observed that it contains 650 gold grains of which 597 are associated with sulphides and 53 grains are associated with silicates. Gold association inspections were done manually since the VG studio software has no application to perform gold grain liberation characteristics. The sequential visualisation offers the opportunity to study gold morphology and associated minerals in 3D while virtually stripping the gangue minerals. Gold distribution is also easy to acquire through making the capping mineral transparent during 3D visualisation.

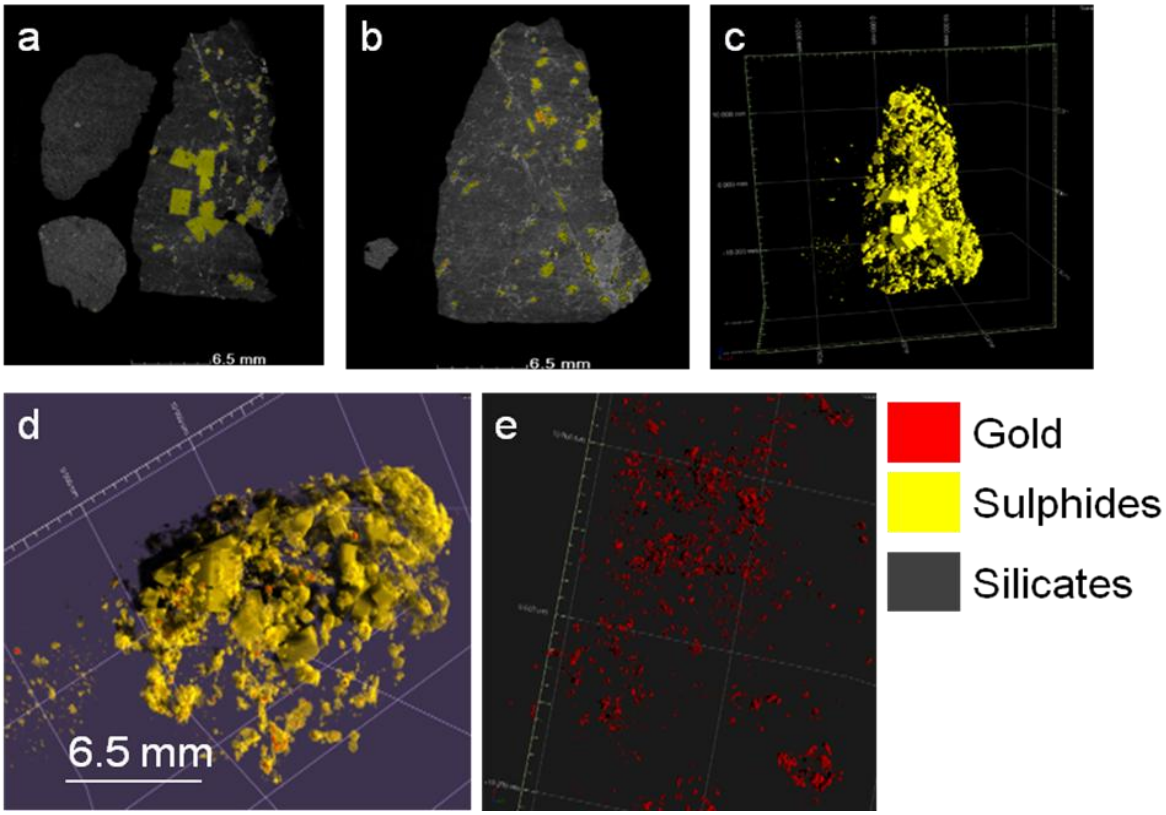

Figure 5-11: Ore characterisation using X-ray CT: a) 2D X-ray CT false colour image (grey represent silicates, golden yellow represent Fe sulphide bearing minerals and red represent gold); b) 3D image showing gold and its association with sulphide-bearing minerals; c) A 3D view of sulphide minerals; d) Rotated view of gold particles in partially coded transparent gangue minerals, and e) Rotated 3D distribution of gold particles (gangue minerals virtually stripped).

After obtaining the data from the defect and visual analysis, gold grain data was interpreted using various descriptive statistical graphs (the best fit model of distribution was applied) and compared with QEMSCAN data (Figure 5-12). Gold grain size in X-ray CT represents an equivalent sphere diameter which is measured similarly in QEMSCAN. The latter corresponds to the diameter of the maximum inscribed sphere calculated as the equivalent circular diameter. The X-ray CT gold diameter equivalent data shows a positively skewed pattern (lognormal distribution showing a high population of fine gold and less coarse gold population (Figure 5-12a). QEMSCAN gold grain size distribution data presented in Figure 5-12c showed the same lognormal distribution pattern; however, gold grain size was found to be much smaller due to resolution differences (X-ray CT voxel size of 17 µm and QEMSCAN pixel size of 1 µm). Considerably more gold grains were found using 3D X-ray CT (1000s on X-ray CT versus 100s on QEMSCAN and 10s on optical microscopy) providing good statistics since a large gold dataset is required to construct statistically representative conclusions. These large data sets are obtained within an hour using X-ray CT whereas

considerably more time is required in a QEMSCAN to obtain 100 grains. Figure 5-12b illustrates how gold grain shape was determined using X-ray CT data based on the sphericity of the gold grain. Sphericity of a grain is expressed as a value between 0 (flat object with no volume) and 1 (perfect sphere). This is the ratio between volume and surface area. Most of the gold grains are semi-rounded to rounded (sphericity >0.5) with minor occurrences of flaky gold grains (sphericity >0.5). The calculation of gold grain shape using the QEMSCAN (Figure 5-12d) shape factor confirmed that most of the gold is semi-rounded to rounded (shape factor of >12 to <16) with selective grains that are angular to flaky (shape factor of <18). This preliminary findings during development of the method proved that X-ray CT can be used to characterise the Witwatersrand gold ore, but several precautions should be taken with regard to the resolution.

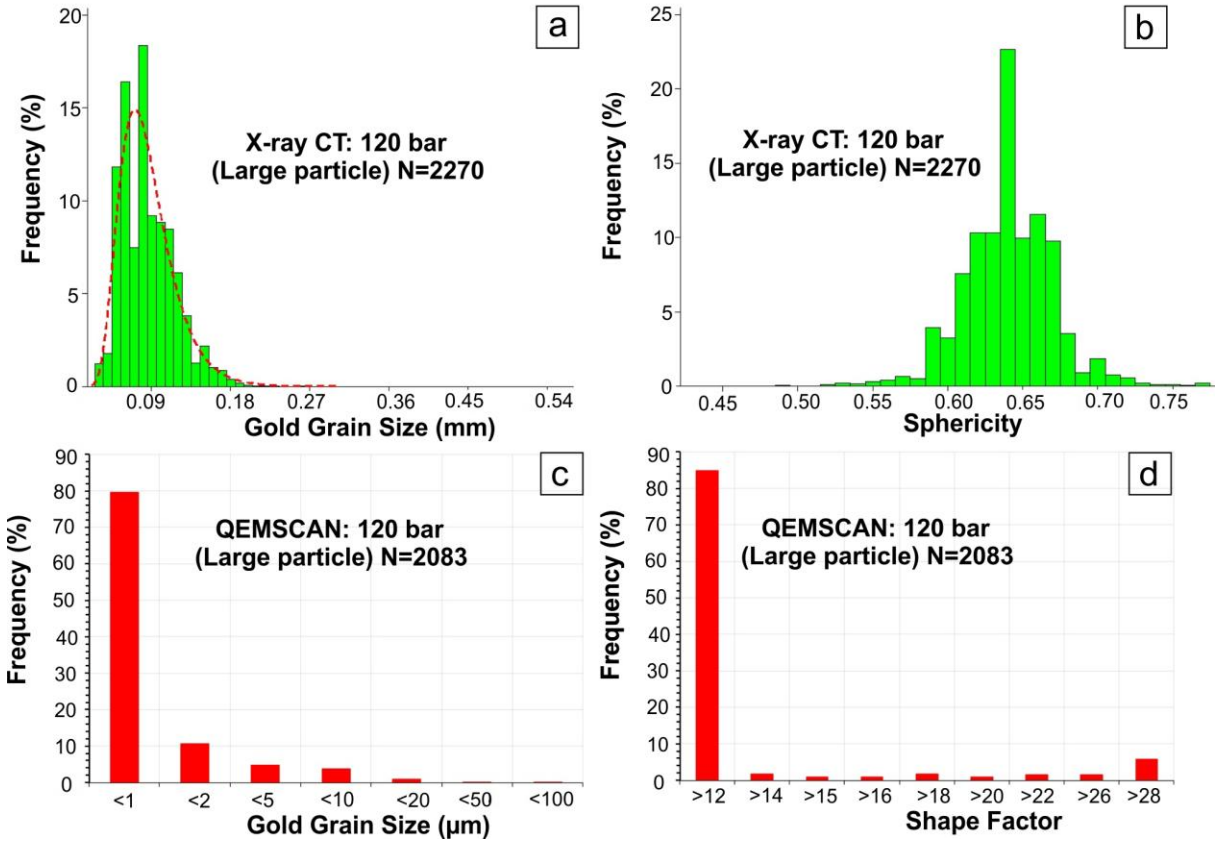

Figure 5-12: Gold grain size distribution and shape of 120 bar large particle: a) Gold grain size distribution verses frequency percentage obtained using X-ray CT; b) Gold grain sphericity determined using X-ray CT; c) Gold grain size distribution obtained using QEMSCAN; d) Gold grain shape factor determined by QEMSCAN.

5.6 ALTERNATIVE SOURCES OF TOMOGRAPHY: COLD NEUTRON TOMOGRAPHY

Witwatersrand gold ore particles were subjected to radiography (see Chapter 4 for experimental methods) using a cold neutron beam line. The aim of using neutron imaging was to explore the capabilities of the instrument, compared to standard X-ray CT. A 3D particle volume was produced using cold neutrons. Validation of the acquired neutron radiography results was done by comparing results with micro focus X-ray CT (Figure 5-12). Neutron radiography showed good gold contrast and attempted to map internal features of host minerals. However, low effective atomic number minerals such as silicates and sulphides were not clearly distinguishable. Micro focus X-ray CT results showed high resolution and clear distinction of various minerals phases whereas neutron radiography did not provide sufficient detail of the ore. An over-estimation of gold grain size was observed with high exaggeration by neutrons since they cover a wide part of the surrounding low density minerals (Figure 5-13).

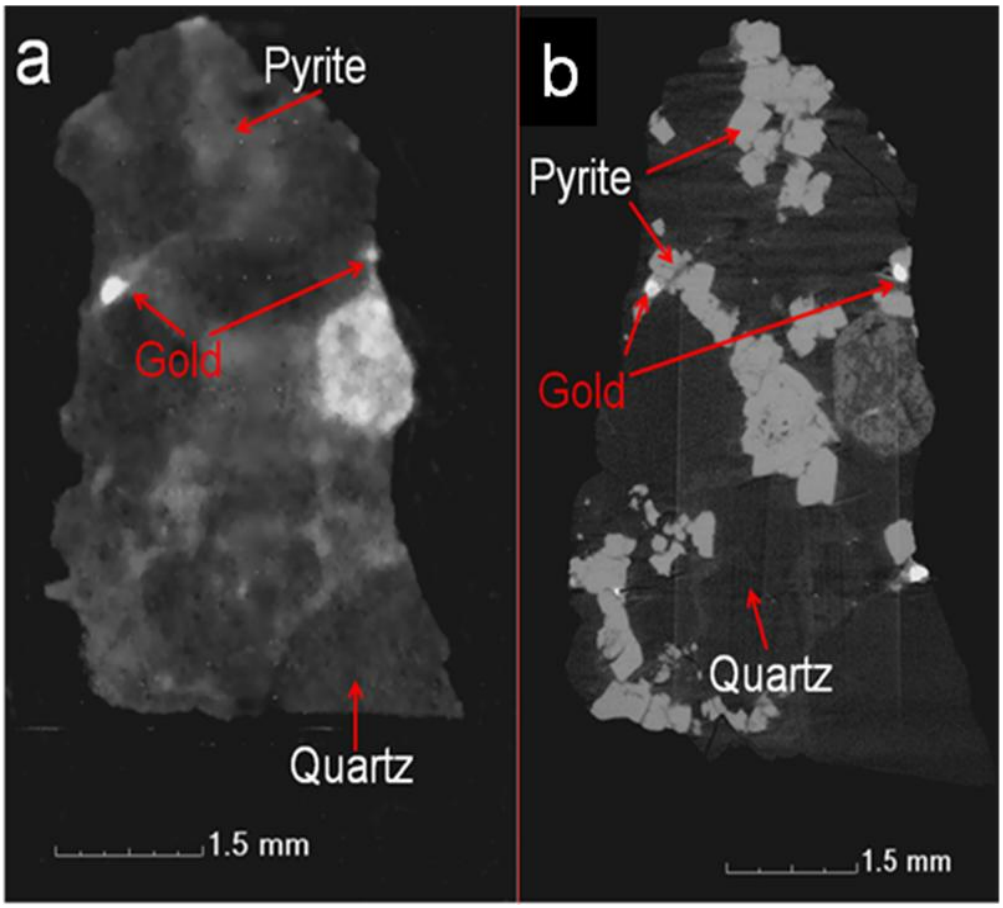

Figure 5-13: Correlation between 2D ICON and X-ray CT characterisation: (a) ICON tomography and (b) X-ray CT slice showing gold and host gangue minerals.

5.7 CHALLENGES ENCOUNTERED DURING DEVELOPMENT OF THE METHOD

The Witwatersrand gold ore contains more than five minerals of which each one of them has its own X-ray attenuation coefficient. This presents a challenge on mineral identification since the grey scale values of material are represented by continuous merged peaks. This is due to the nature of X-ray source (polychromatic X-ray source) used in this study. The grey value representing a mineral is a result of an averaged X-Ray spectrum. Due to the polychromatic X-ray source, quartz, chlorite and mica appear in one merged grey scale peak as fused material thus validation of data through the use of QEMSCAN was required. Resolution brought its own trials. At a resolution of 17 µm, gold finer than this voxel size was either not detected or the gold grain will get identified together with the host minerals changing its density. This results in overestimation of the gold grain sizes. Coarse gold grains usually occupy more than one voxel and these results in an omission of particle margins or overestimation of gold and host mineral surface area.

Figure 5-14 illustrates the concept of grain size overestimation using the partial volume effect. Each block is a pixel and the total pixel has a grey value range of 0 to 65535 in practice but smaller values were used in the illustration (20 to 50 grey values). Considering the tomography results for X-rays, higher density material (i.e. Au) will have more attenuation and thus a higher voxel value. If a gold particle is large and fills the total pixel in 2D of the detector, the total pixel (and thus total voxel in 3D) will take on the "*true*" grey value of the Au which is 50 in Figure 5-14. If a gold grain is ½ as large as a pixel and fills only that pixel thus partially, the pixel (and thus total voxel in 3D) will take on a lower value averaged with the surrounding mineral (grey value of 40 in the illustration). A dominant material in a voxel affected by the partial volume effect, resulting in overestimation of gold grain on blurred material edges, is given by the following simplified equation:

Au grey value=50

Au-1 grey value=40 (This is allocated as gold based on the weighting of the grey values and the below equation confirms the allocation of material name)

Silicates grey value=20

x (50) + (1-x) (20) = 40

50x+20-20x=40

30x=20

x=2/3

Therefore Au contributes 2/3 of the blurred edges while silicates contribute 1/3 thus the blurred edge will be considered as part of the gold grain resulting in exaggeration of the actual grain size.

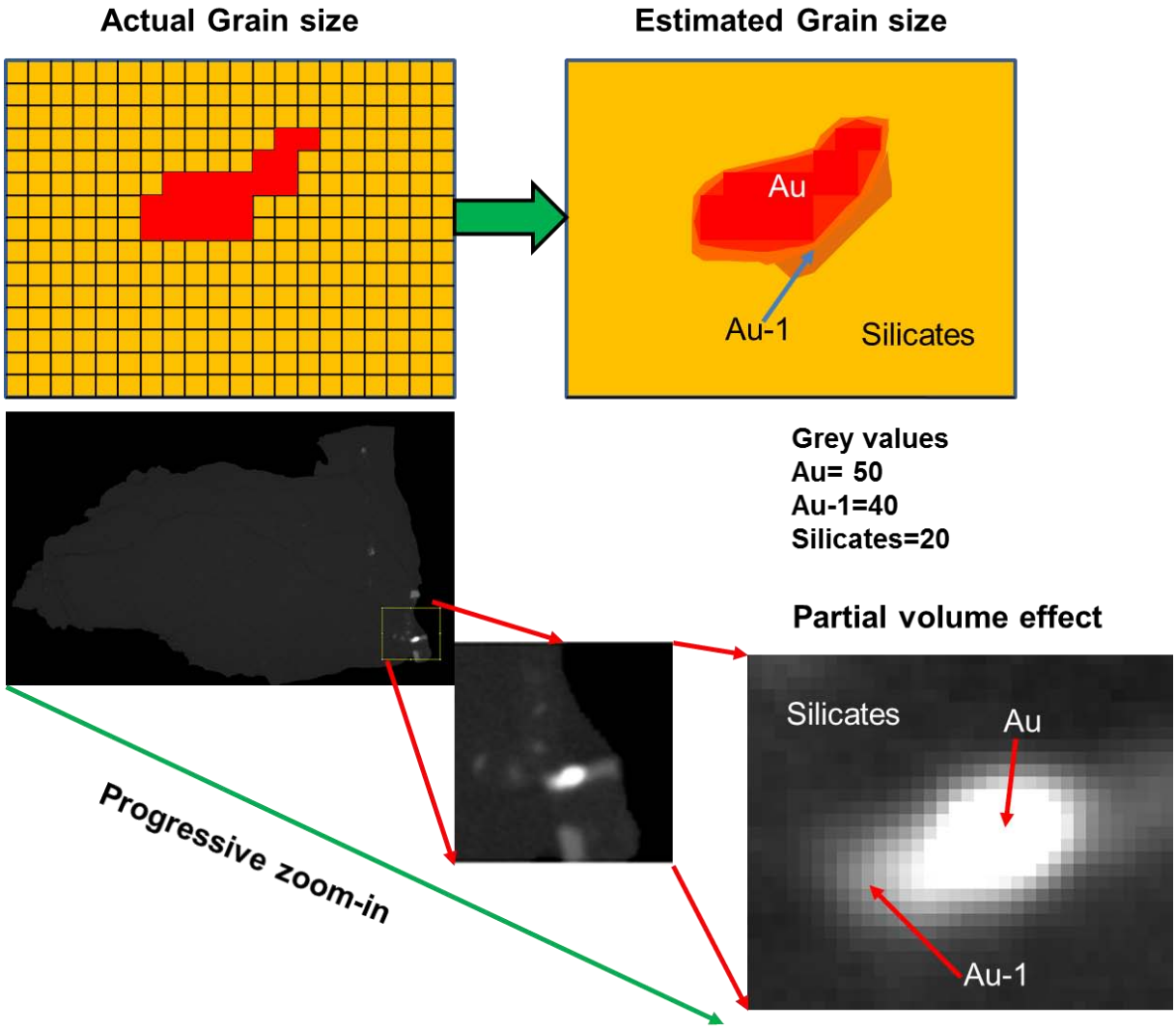

Figure 5-14: The concept of grain overestimation of X-ray CT data due to limited voxel size resulting in partial volume effect.

In order to resolve this, an attempt was made by scanning some of the gold grains with a Versa X-radial CT machine of which voxel sizes close to 4 µm were achieved thus solving some of mineral misidentification issues. A dual source X-ray CT machine was also used during experimental testing and validation of the scans as a means to resolve the gold-uraninite distinction. The dual energy approach showed a slight visible discrimination of these minerals, but since the sources were both polychromatic beams, no clear distinction was found. Solving challenges associated with gold liberation and accessibility was first attempted by navigating through individual slices tracking gold grains using *ImageJ* software. Gold grains were segmented in ImageJ based on grey values. A total number of gold grains present in a particle were quantified using ImageJ particle analyser functionality. This was followed by the visual inspections of gold grains that appear to be sitting on the surface or edges of other material. These grey zones were then filtered out and calculated as exposed grains. However, this only calculates the minimum grain exposure and does not provide the actual exposed grains. To obtain the locked grains, the exposed grains were subtracted from the total particle gold grains. This was a tedious manual process and an automated method was then tried.

The automated method involved writing an algorithm using the Matlab software and coding mineral phases. This was not successful due to limitations in voxel size and inclusion of host minerals as gold on the output of the algorithm due to partial volume effect. On the other hand, crack width measurements were difficult to quantify and to obtain good statistical representation. This is due to the fact that each and every crack had to be tracked from its point of origin in order to avoid measuring the same crack more than once. Cracks that are smaller than the voxel size of ~17 µm were below the detection limit; therefore it was assumed that not all cracks and pores were quantified. Therefore it was necessary to use defect analysis sphericity data in order to study the roundness of a 3-dimensional particles to compare the extent of cracks and pores. Besides these challenges, X-ray CT appears to offer state-of-the-art 3D characterisation of HPGR products for metallurgical test work.

CHAPTER 6: INVESTIGATION INTO THE POTENTIAL OF WITWATERSRAND GOLD ORE FOR HEAP LEACHING

6.1 INTRODUCTION

This chapter discusses results of investigations undertaken to evaluate the potential of the Witwatersrand gold ores for heap leaching. The effects of HPGR feed pressure, crack volume, width and distribution on comminution and mineralogy of the Witwatersrand gold ore are presented. These are seen as the key parameters in assessing the potential of this ore for heap leaching. Process mineralogy, together with X-ray tomography, might offer a hybrid opportunity for determining the mineralogy of Witwatersrand gold ore while investigating its potential for heap leaching. The aspects of mineralogy presented in this chapter are: ore bulk mineralogy, petrography, gold grain size distribution, liberation and association. In order to test the amenability of the ore to heap leaching, gold recovery results obtained from laboratory cyanide tests are presented.

6.2 COMMINUTION

6.2.1 HPGR specific energy and grinding force

HPGR tests were performed at three different pressure settings of 60, 90 and 120 bar, which correspond to the specific grinding forces of 1.90, 2.85 and 3.79 N/mm^2 respectively (Table 6-1). The specific energy for the comminution of this ore was calculated to be between 1.08 and 2.16 kWh/t. The grinding force is defined as the total hydraulic force exerted on the rolls divided by the projected area of the rolls and expressed in units of N/mm². The specific energy is the energy input, which is absorbed per ton of material and expressed in units of kWh/t. It is related to the functional specific grinding force (Daniel, 2007). During HPGR crushing, particle damage occurs by compression in a packed particle bed and micro-cracks are created on the particles. Maximum compression was obtained at 120 bar which exceeded the compressive strength of the feed material.

Table 6-1: Specific energy and grinding force at the different pressure of HPGR

Pressure (bar)	F(sp): Specific grinding Force (N/mm^2)	W (sp): Specific Energy (kWh/t)
60	1.90	1.08
90	2.85	1.62
120	3.79	2.16

6.2.2 Particle size distribution

The particle size distribution was determined in order to investigate the effects of HPGR on particle breakage. The particle size distributions from the HPGR test samples are illustrated in Figure 6-1. As expected, the product became progressively finer with an increase in the starting pressure. The duplicate test at 120 bar shows that the repeatability of the tests was good (Figure 6-1).

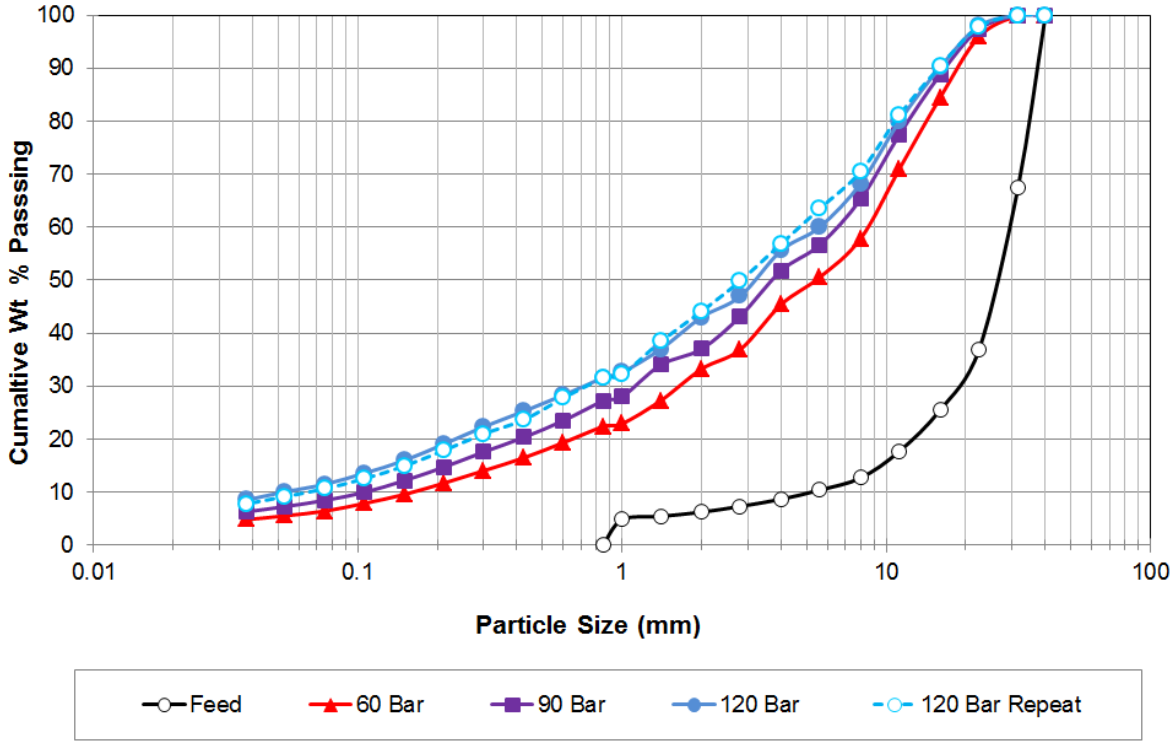

Figure 6-1: Cumulative particle size distribution of the Witwatersrand gold ore prepared by HPGR with different pressure settings.

6.2.3 Quantitative analysis of cracks

Selected particles from the three HPGR pressure settings were studied in detail using a combination of QEMSCAN and X-ray CT techniques to investigate and quantify the HPGR induced crack network (Chapter 5, section 5.5.3). Mapping of the particle crack density using X-ray CT showed a variation in crack distribution for the three HPGR pressures (Figure 6-2). Particles prepared at 60 bar HPGR pressure (Figure 6-2a and -b) have cracks with little interconnectivity. Extensive cracks crossing along grain boundaries are created in 90 bar HPGR pressure and consist of wide cracks with some connectivity (Figure 6-2c and -d). The networks of interlinked micro cracks created at 120 bar show the impact of the increased HPGR pressure on particle damage, but these observations will be further assessed in the leaching experiments section to see if it correlates with gold recovery (Figure 6-2e and -f).

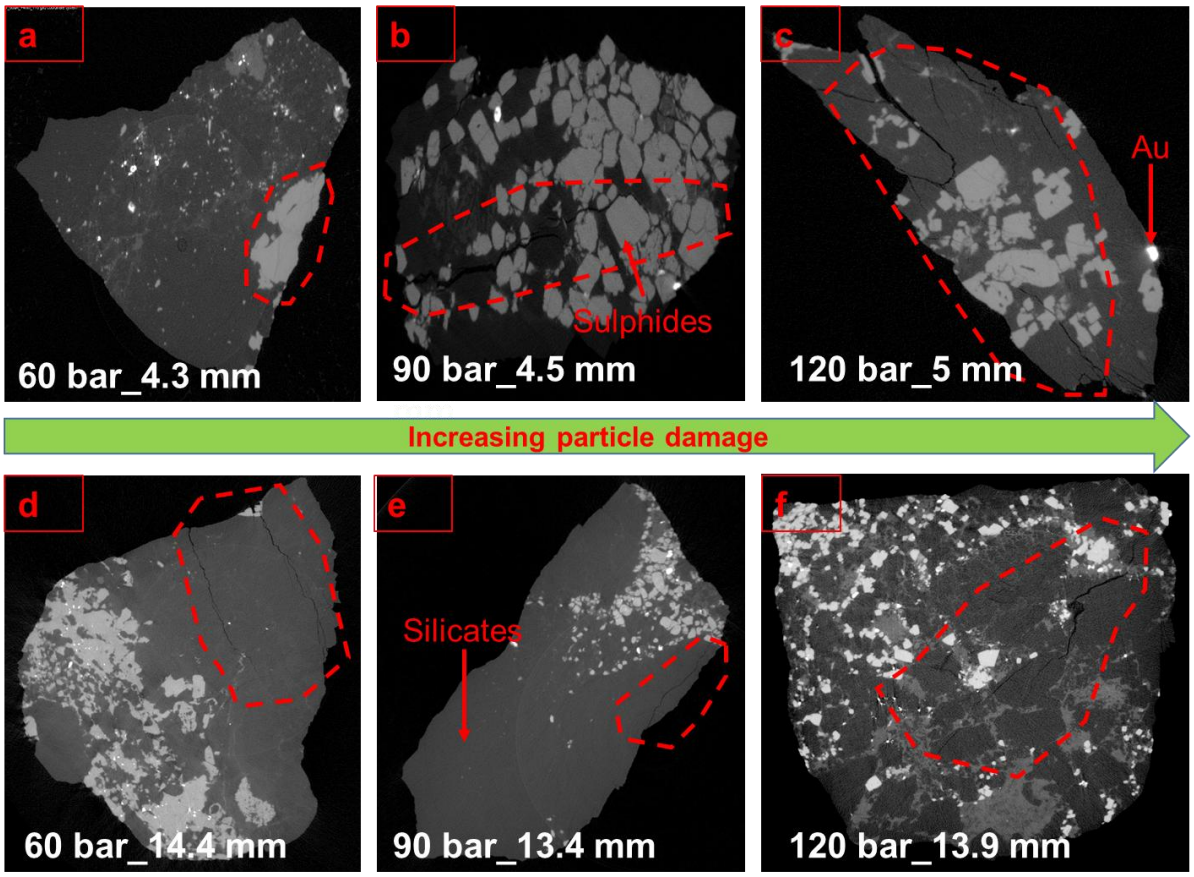

Figure 6-2: X-ray CT illustration of Witwatersrand ore HPGR-induced cracks: 4 to 6 mm represent small particles and 11 to 16 mm represent large particles (dotted line highlights some of the most pronounced cracks in particles)

Quantification of crack width was done using micro-focus X-ray CT (Figure 6-3). Small particles contain wider cracks (0.04-0.15 mm) when compared to large particles (0.02-0.03 mm). X-ray CT crack width analysis indicate slightly wider cracks in the samples prepared by the HPGR at the 90 bar pressure setting, suggesting that this may be close to the optimal pressure for processing this ore sample. HPGR pressure of 120 and 60 bar produced crack width with less clear differences, and this was observed in both the small and large particles.

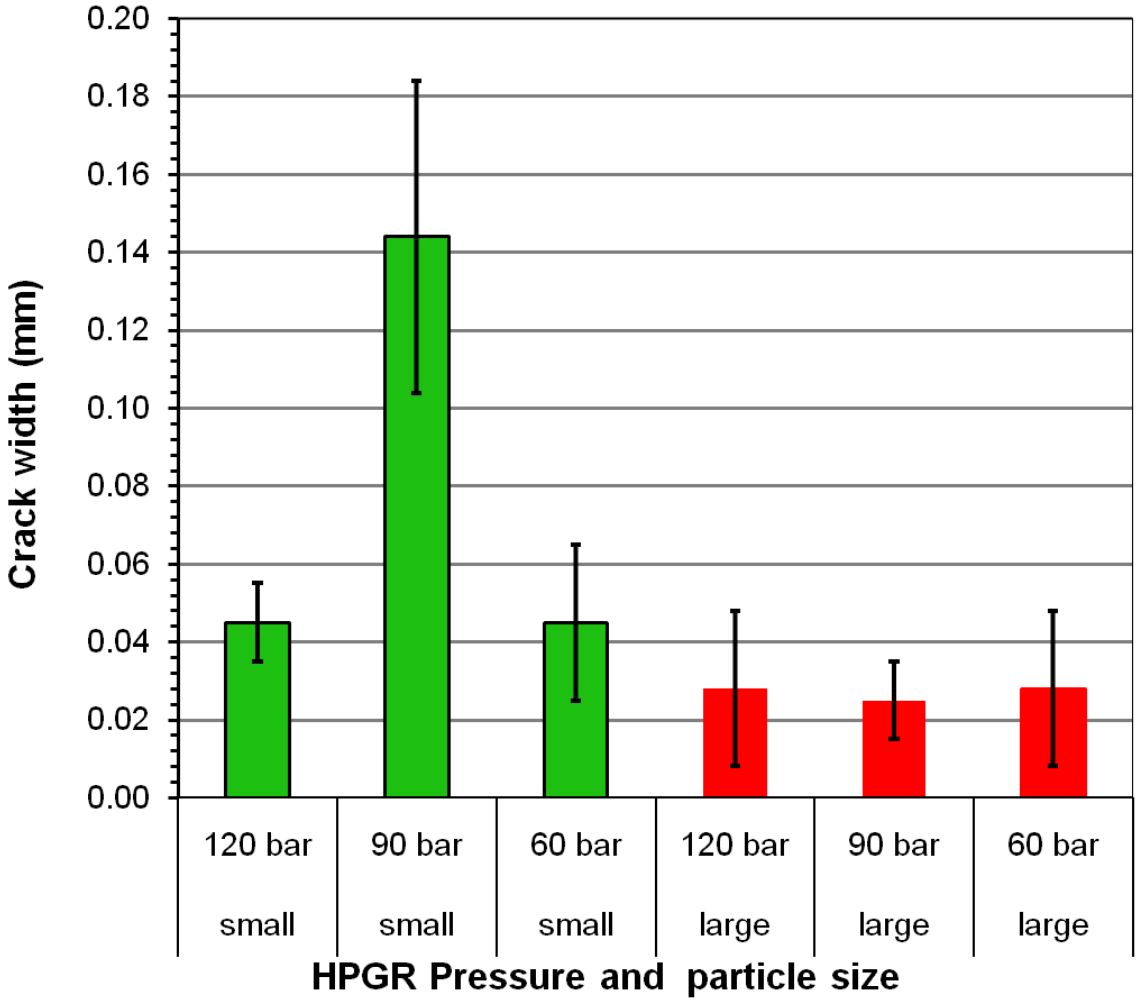

Figure 6-3: Quantification of crack network width using X-ray CT (green= small particles and red= large particles).

The results of both QEMSCAN and X-ray CT showed that more micro-cracks were present in the products obtained from the HPGR operated at the pressure setting of 90 bar (Figure 6-4). This suggests that for the HPGR device used in this work, the best pressure setting to produce particles with crack along grain boundaries and intermediate finer product is around 90 bar which is favourable for heap leaching whereas HPGR operated at pressure setting of 120 bar appeared to give higher finer product and preferential crack network propagation. The study by Ghorbani et al., (2011) also found that an HPGR pressure setting of around 90 bar is more effective in crack network generation, but no increase of product fineness was observed for the 120 bar operating pressure in the Gamsberg ore used in this study.

X-ray CT and QEMSCAN spatial surveys showed that the ore particles contain an HPGR induced fracture/crack network. The volume percentage cracks (Figure 6-4) produced by the HPGR (0.12 to 0.87 vol. %) were much lower compared to those on the Gamsberg ore (0.75

to 1.1 vol. %) studied by Ghorbani et al., (2011). These differences are primarily related to differences in hardness between the two ores. The study of Ghorbani et al., (2011) also showed the inability of the more traditional techniques (e.g. Mercury intrusion porosimetry and Physical gas adsorption) to measure the crack network produced by the HGPR. Minor differences in percentage cracks between QEMSCAN and X-ray CT are attributed to stereology (2D measurement for QEMSCAN, 3D measurement for X-ray CT), as well as differences in the numbers of particles analysed. Given the nature of the measurements and the size of the particles, only four particles were analysed per HPGR pressure and particle size using X-ray CT whereas almost 20 particles were analysed using QEMSCAN in this study.

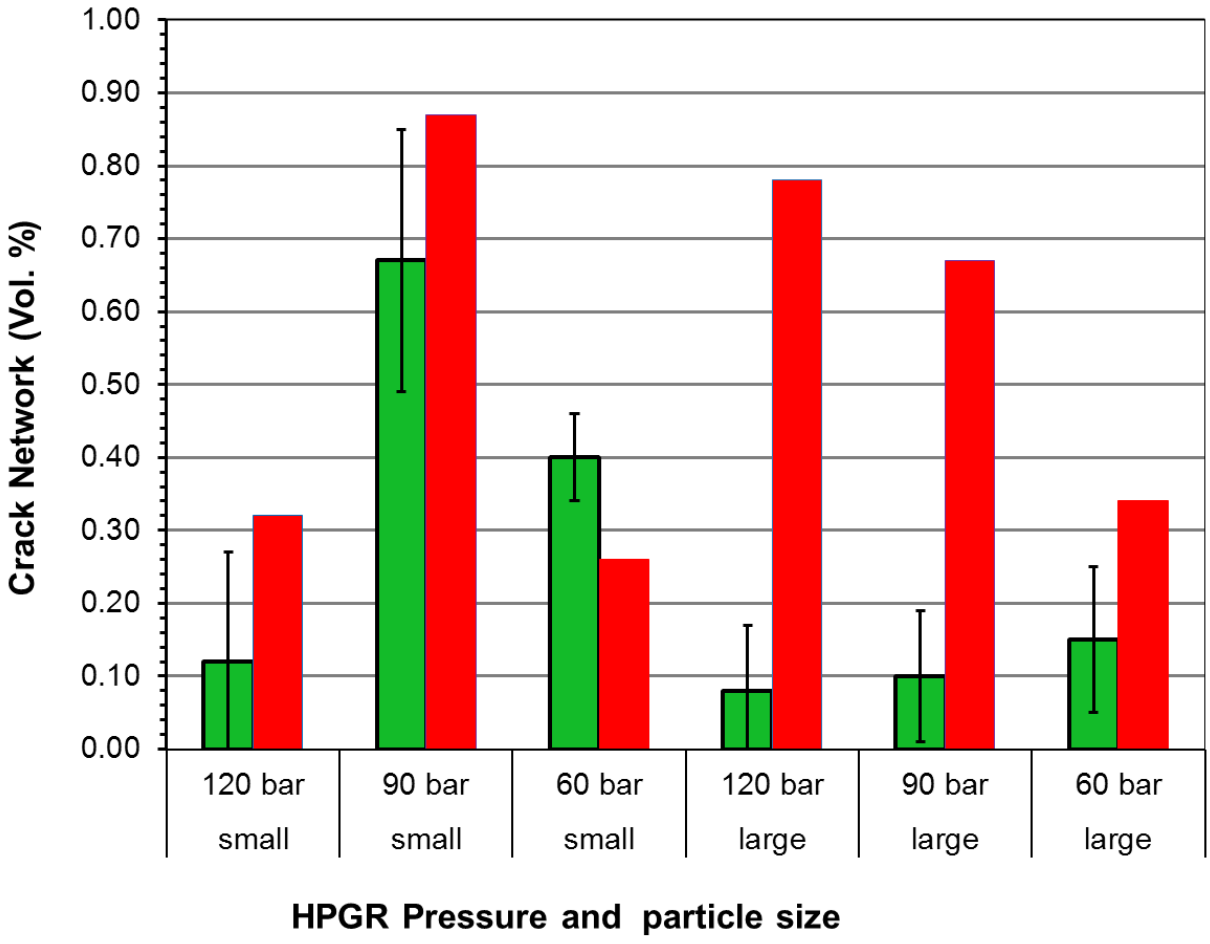

Figure 6-4: Quantification of HPGR induced cracks and ore porosity using X-ray CT (left green filled bar) and QEMSCAN (right red bar).

6.3 MINERALOGICAL CHARACTERISATION AND GOLD DEPORTMENT

6.3.1 Petrography of the Witwatersrand gold ore

The dominant reef type in this project is the VCR since it is the primary reef mined, whereas the ER is mined as a secondary reef at Harmony Gold. SEM based petrography is presented in Figure 6-5 and photomicrographs of the Witwatersrand gold ore obtained using optical microscopy are presented in Figure 6-7. Analysis done in this work was on a composite sample, except for samples in Figure 6-5, but based on the author's experience as a mine geologist and literature (Engelbrecht et al., 1986; Frimmel, 2008, 2005; Koglin et al., 2010), distinctions between VCR and ER could still be made. The composite ore is dominated by quartz, chlorite and mica. Significant amount of sulphides were observed (pyrite and pyrrhotite) with minute amounts of gold. No major feldspar component was observed during the petrographical investigations. The quartz clasts are bounded by sheet silicates such as chlorite and mica forming the ore matrix, resulting from the diagenesis and/or metamorphosis of clay.

Three main types of pyrite, namely porous pyrite, compact pyrite and euhedral (hydrothermal) pyrite were observed (Figure 6-6). Compact pyrite is rounded in shape with minor to no inclusions and is found in various grain sizes from 0.2 to 3 mm (Figure 6-5a and 6-7d). Compact pyrite is usually referred to as buckshot pyrite and it is detrital in origin due to the nature of sedimentary processes responsible for its transportation. The Witwatersrand Basin compact pyrite is believed to have developed its roundness by attrition during sediment transport (Figure 6-6a). Figure 6-6b and 6-7d shows rounded pyrite (compact) that has redeveloped some euhedral form morphology. Ramdohr (1958) described this type of redevelopment as due to the continuous growth of rounded pyrite within the conglomerate thus assuming the appearance of an authigenic crystal.

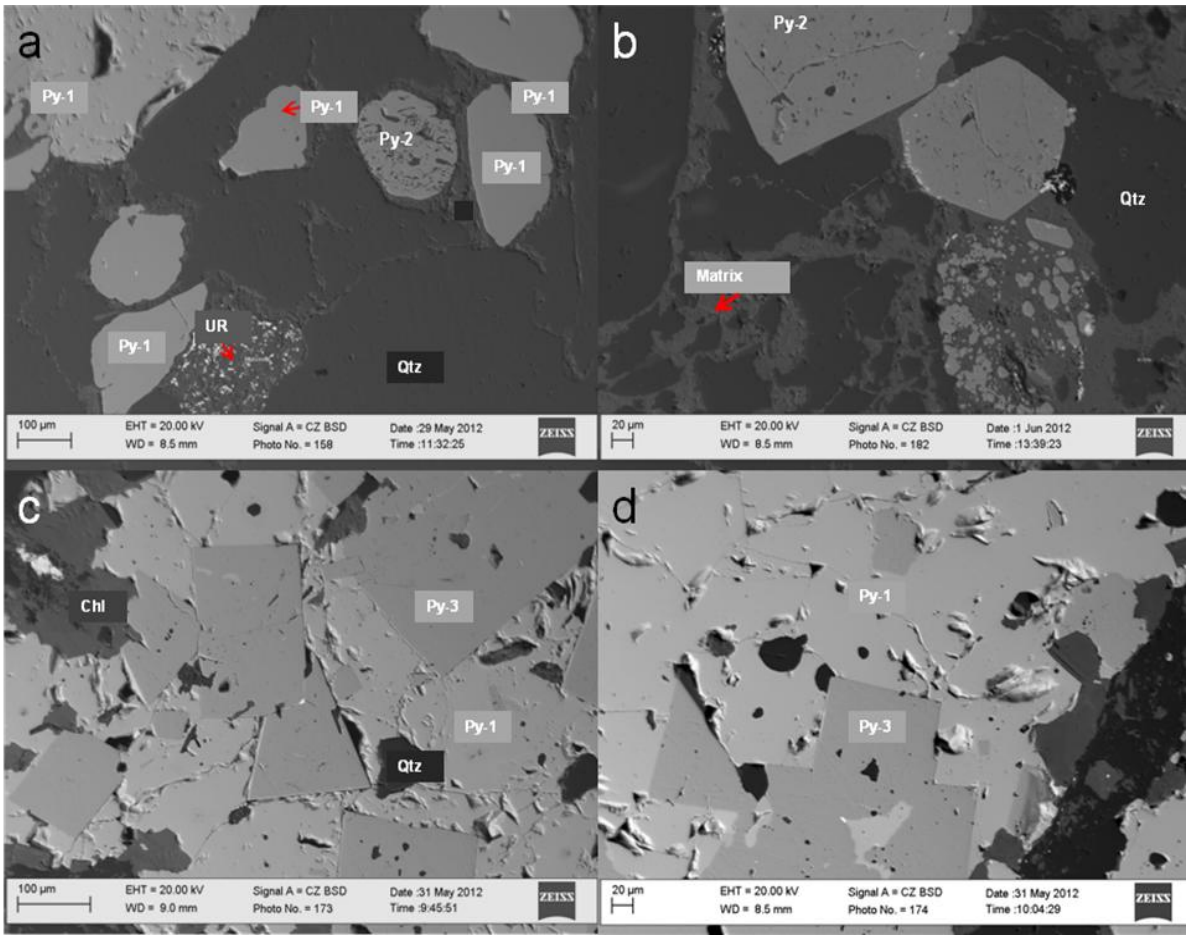

Figure 6-5: 2D SEM images illustrating the morphology of the three generations of pyrite: (a) VCR-semi rounded compact pyrite (Py-1) and porous pyrite (Py-2) associated with quartz (Qtz) and uraniferous minerals (UR); (b) VCR-porous pyrite filled with quartz inclusions surrounded by muscovite-chlorite matrix; (c) ER- euhedral pyrite (Py-3) interlocked with compact pyrite; (d) ER- euhedral pyrite associated with re-crystallised quartz and compact pyrite.

Porous pyrite, also known as concretionary pyrite, frequently occurs as rounded pyrite due to reworking that occurred as a result of remobilisation and occurs in grain sizes similar to compact pyrite (Figure 6-5b, 6-6b, and 6-7e). Concretionary pyrite (which is syn-sedimentary) consists of micro-inclusions hosting other sulphides and micas. Compact and porous pyrites observed in this study are syn-sedimentary. Most of these two pyrite generations in this study are from the VCR (Frimmel and Gartz, 1997; Gartz and Frimmel, 1999). Hydrothermal pyrite appears in both the VCR and the ER, though it is more dominant in the ER (Figure 6-5d and 6-6c). Hydrothermal pyrite was formed by mobilisation and re-crystallisation during metamorphism and can occur in various grain sizes. The most common form observed in this study is euhedral pyrite (Figure 6-5c and -d). Crystals of euhedral pyrite form wedge-like pyrite grains that cut through re-crystallised quartz and selected allogenic minerals.

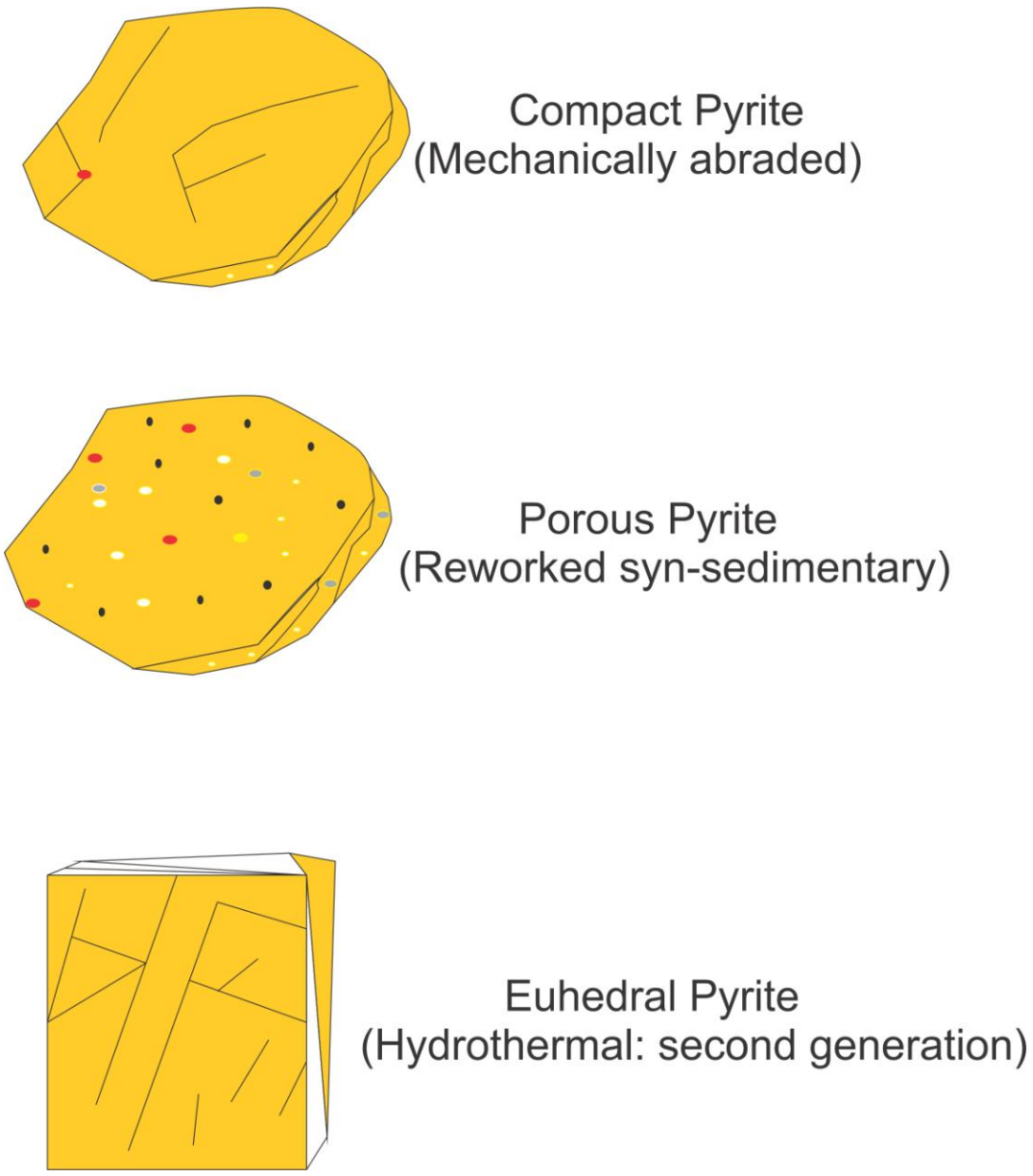

Figure 6-6: Schematic representations of three different generations of pyrite.

Particles derived from the VCR have a chlorite-muscovite matrix, pyrrhotite and are dominated by compact and porous pyrite (Figure 6-5a and -b). Particles derived from the Elsburg reefs are dominated by the presence of euhedral and compact pyrite (Figure 6-5c, d). Both the VCR and Elsburg reefs showed a variable degree of remobilisation/alteration. This alteration is evident in the form of re-crystallised quartz and various morphologies of sulphide-bearing minerals. Use of the magnetic colloid method on pyrrhotite indicates that the majority of the pyrrhotite present (>95 %) is non-magnetic. This is consistent with the study by de Villiers and Liles (2010), who reported non-magnetic pyrrhotite, with a 6C structure and formula $Fe_{11}S_{12}$ from one of the neighbouring gold mines in the study area (Mponeng gold mine, AngloGold Ashanti).

Figure 6-7a shows regular to irregular shaped coarse native gold grains associated with pyrrhotite and quartz. Quartz grains show pyrrhotisation as pyrrhotite precipitate at the edges of the quartz grains. Figure 6-7b shows a well-mineralised sample, characterised by coarse-to-fine gold with a flaky and semi-rounded shape. Gold mineralisation is concentrated within the sulphidic mineralisation zones (i.e. pyrrhotite and pyrite) and silicates. Gold in a poly-mineralic boundary of quartz and pyrrhotite was also found (see Figure 6-7c). Overall, in the Witwatersrand gold only minor electrum (alloy of Au with Ag-Hg) exists, which is confirmed by QEMSCAN. The distribution of different pyrite minerals and pyrrhotite in the Witwatersrand gold ore is given in Figure 6-7d-to-f.

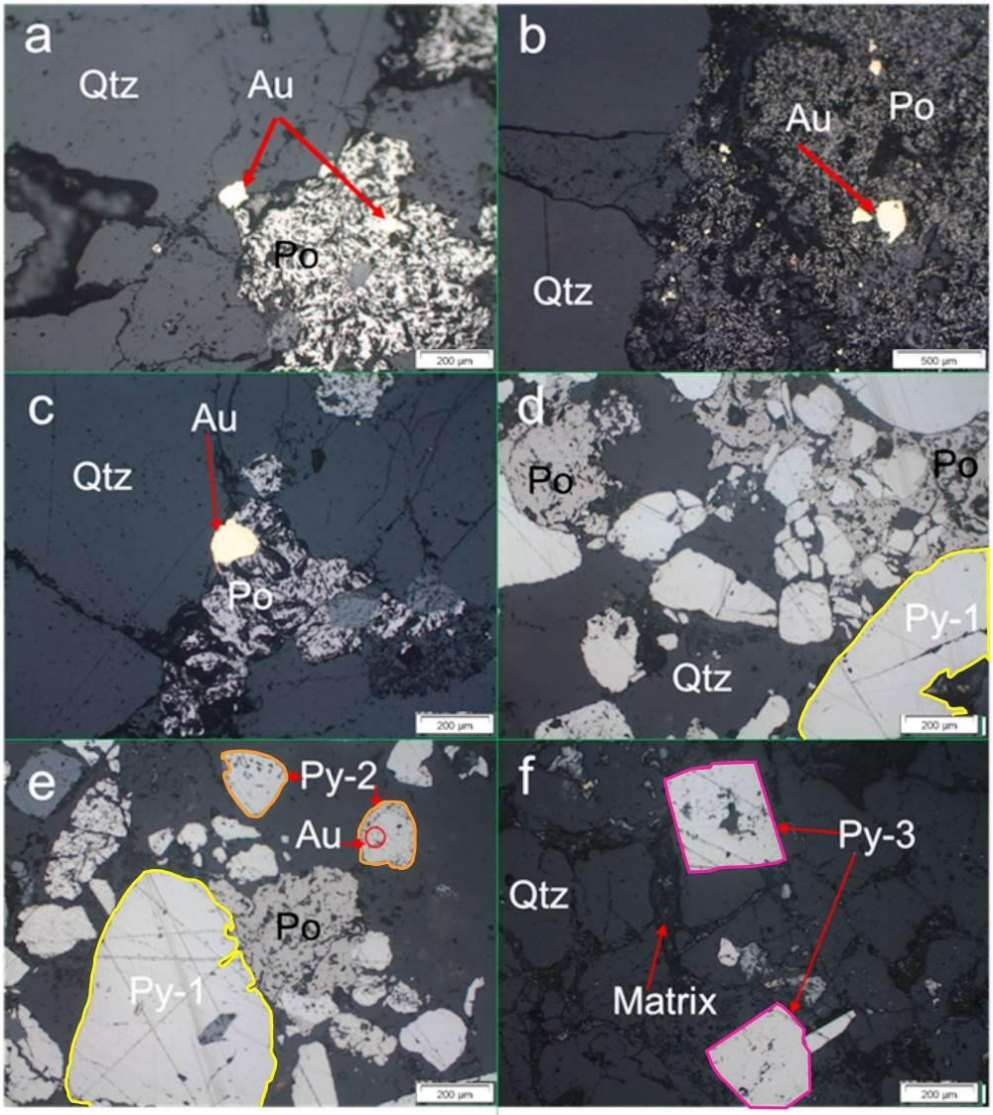

Figure 6-7: Reflected light photomicrographs of the Witwatersrand gold ore (a) Gold (Au) associated with quartz (Qtz) and Pyrrhotite (Po); (b) Coarse to fine gold particles associated with Pyrrhotite; (c) Coarse gold grain in poly-mineral boundary; (d) Pyrrhotite and compact pyrite (Py-1); (e) Semi-rounded porous pyrite (Py-2) filled with fine gold inclusions and compact pyrite surrounded by re-crystallised quartz; (f) Euhedral pyrite surrounded by quartz pebbles.

6.3.2 Gold grain size distribution and morphology

It is important to understand the variability of gold distribution in terms of size because of challenges associated with variability in gold grain size; especially in the Witwatersrand gold ores (see Chapter 2 for gold grain size and Chapter 3 for detailed review of the Witwatersrand gold province). In this study, ~100 gold grains were measured using the QEMSCAN trace mineral search for each sample (Figure 6-8). The gold grains identified were characterised using descriptive statistical methods.

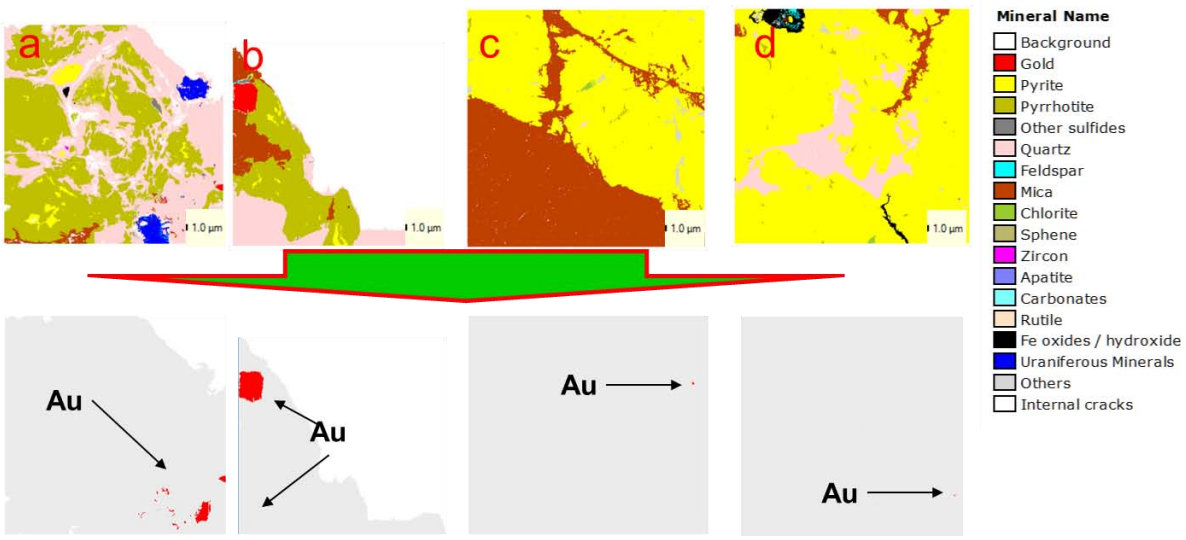

Figure 6-8: QEMSCAN trace mineral search showing particle mappings of gold.

Figure 6-9 presents the gold grain size distribution of the Witwatersrand gold ore. The distribution pattern from QEMSCAN forms a unimodal positively skewed pattern. Positively skewed distribution indicates a dominance of fine gold, with grain size of <50 µm for all samples investigated. Most of the gold grain size is between 1 and 10 µm (Figure 6-9a, -c and -e). It should be noted that the grain size distribution for gold does not reflect the particle-size distribution of the ore. Following different gold grain size classification methods (Wang and Poling, 1983; Stewart and Ramsay, 1993; Henney et al., 1995), it appears that the gold ores used in this study predominantly fall under the fine gold grain size scale.

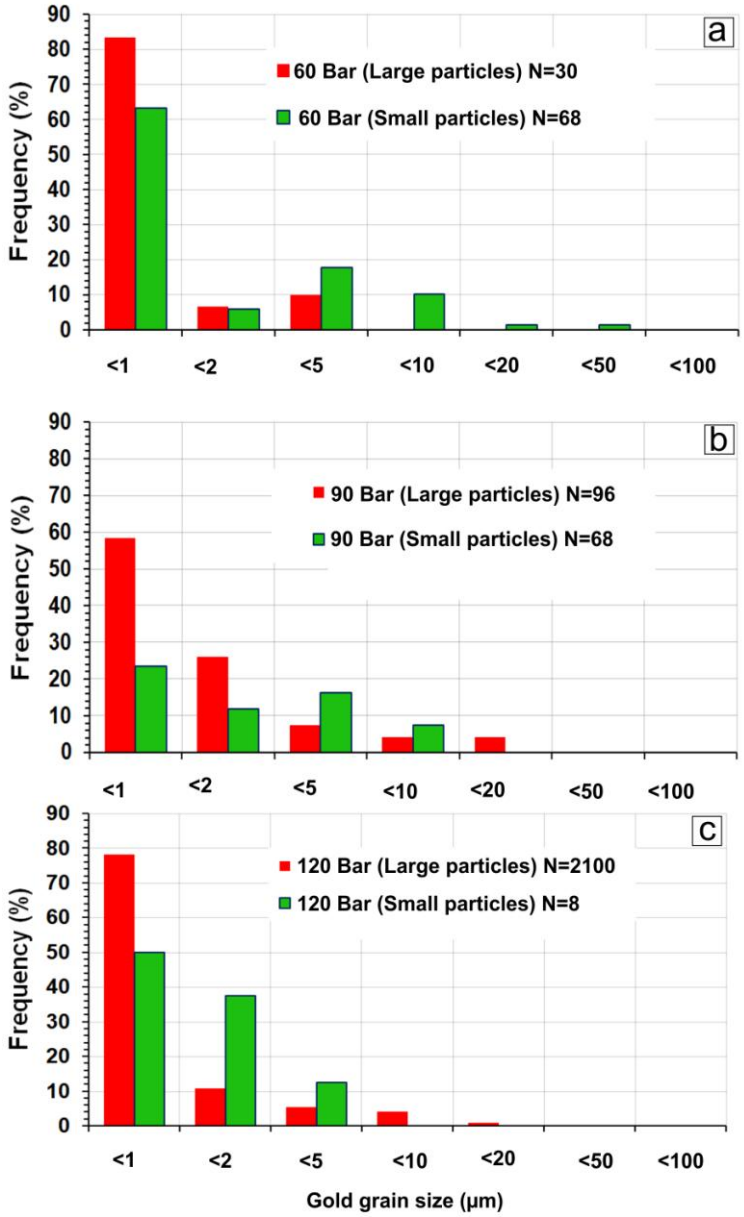

Figure 6-9: QEMSCAN gold grain size distribution against frequency

The morphology of gold grains varies within the samples analysed, and therefore a classification using QEMSCAN shape factor categories was developed (Figure 6-10b, -d and -f). Shape factor is indicative of the roundness of the particles based on its cross-section. The lower the shape factor number (i.e. the closer to 12), the rounder the grain becomes. In this study, it was calculated by perimeter^2/ area. For a perfect circle, the value will be 4π (about 12.6). However, in this study data that plots at a shape factor of 12 was considered to be in the region of terroidal (disc shape) and perfect circle shape. For a square, the value will be 16. An equilateral triangle has a value of about 20.8. It was observed using shape factor

analysis that gold occurs in shapes ranging from flaky, irregular and sub-rounded (Figure 6-10). Flaky gold grains are formed during fluvial transport and are particularly difficult to recover during tank leaching as a result of their different settling velocities (insufficient residence time to dissolve) but react more readily during heap leaching due to their surface area (Zhou et al., 2004). Sub-rounded to more round fossil placer gold grains (Figure 6-10) which are more dominant in the Witwatersrand gold ore, are much easier to leach since they have already been concentrated by hydraulic sorting during deposition and thus are considered as free milling gold.

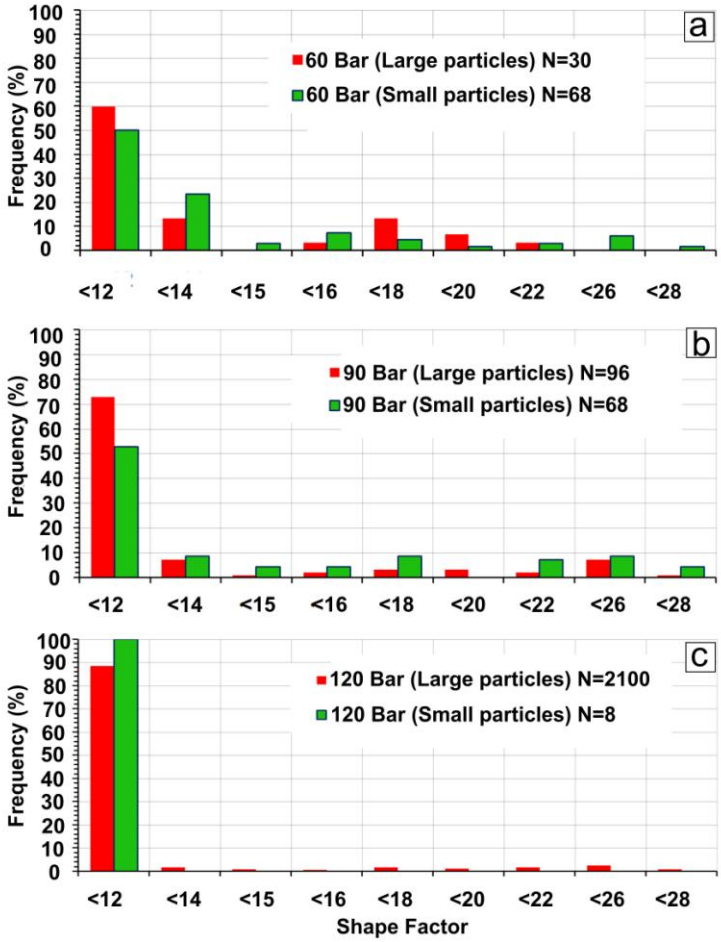

Figure 6-10: QEMSCAN gold morphology inspection using shape factor functionality.

Comparison of gold characteristics between X-ray CT and QEMSCAN shows that X-ray CT overestimates the gold grain size due to particle resolution issues (Chapter 5), therefore the grain size distribution acquired using X-ray CT will be used for the purpose of showing the nature of gold grain size distribution and estimated grain size. A total of over 1000 gold grains were identified using X-ray CT and a summary of their sizes and variations between

different particle size fractions and HPGR pressure are presented in Table 6-2. The ability of X-ray CT to provide large, statistically meaningful data sets of gold grain sizes provides a better confidence of the representation and interpretation, but only if the voxel size is sufficiently small. The gold grain size distribution against frequency percentage is given in Figures 6-11 and -13 whereas Figure 6-12 and -14 show sphericity against frequency percentage. A unimodal log-normal distribution was found in all HPGR prepared particles (large and small particles). This shows that even though X-ray CT over-estimates the gold grain size, the Witwatersrand gold is fine grained (<300 µm). A lack of a larger population of coarse gold limits the interpretation of possible nugget effects. Both the small and large sized particles show the dominance of round to subrounded gold grain with a minor amount of flaky to angular gold. Sphericity of the gold grains was also measured as a means to determine the morphology of the gold. Small particles show the majority of the population falling under low to moderate sphericity (Figure 12 and 14) and are sub-rounded to more round. A smaller population falls under the flaky to angular shape group (sphericity of 0-0.0.3). Large particles display a near well-formed bell shape distribution representing rounded gold grains with several outliers in the angular to flaky morphology. Table 6-2 represents gold grain descriptive statistics acquired using X-ray CT.

Table 6-2: Summary of gold grains size distribution (mm) statistics generated using X-ray CT.

Size Fraction	(N)	Mean (µm)	STDev	Median	Mode	Skewness	Kurtosis
60 Bar: large particles	1208	130	0.11	0.09	0.03	2.33	7.33
60 Bar: small particles	266	110	0.10	0.05	0.04	1.17	0.17
90 Bar: large particles	990	140	0.11	0.09	0.03	1.60	2.77
90 Bar: small particles	252	150	0.11	0.14	0.02	2.00	7.88
120 Bar: large particles	2270	130	0.09	0.10	0.05	0.06	6.22
120 Bar: small particles	637	40	0.06	0.02	0.01	2.49	6.04

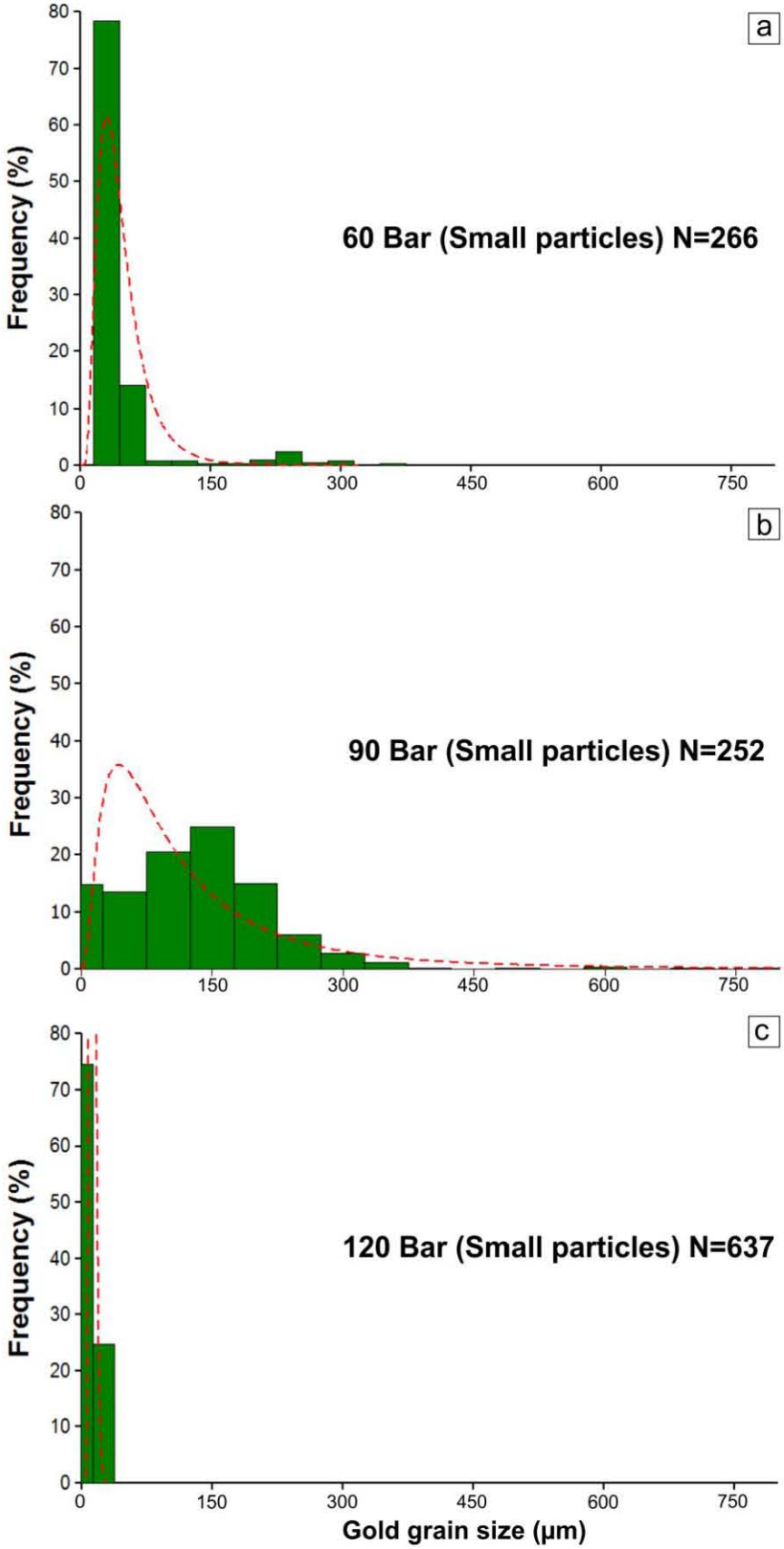

Figure 6-11: X-ray CT small particles gold grain size distribution against frequency percentage (the Gaussian dotted line fit represent the distribution trend.

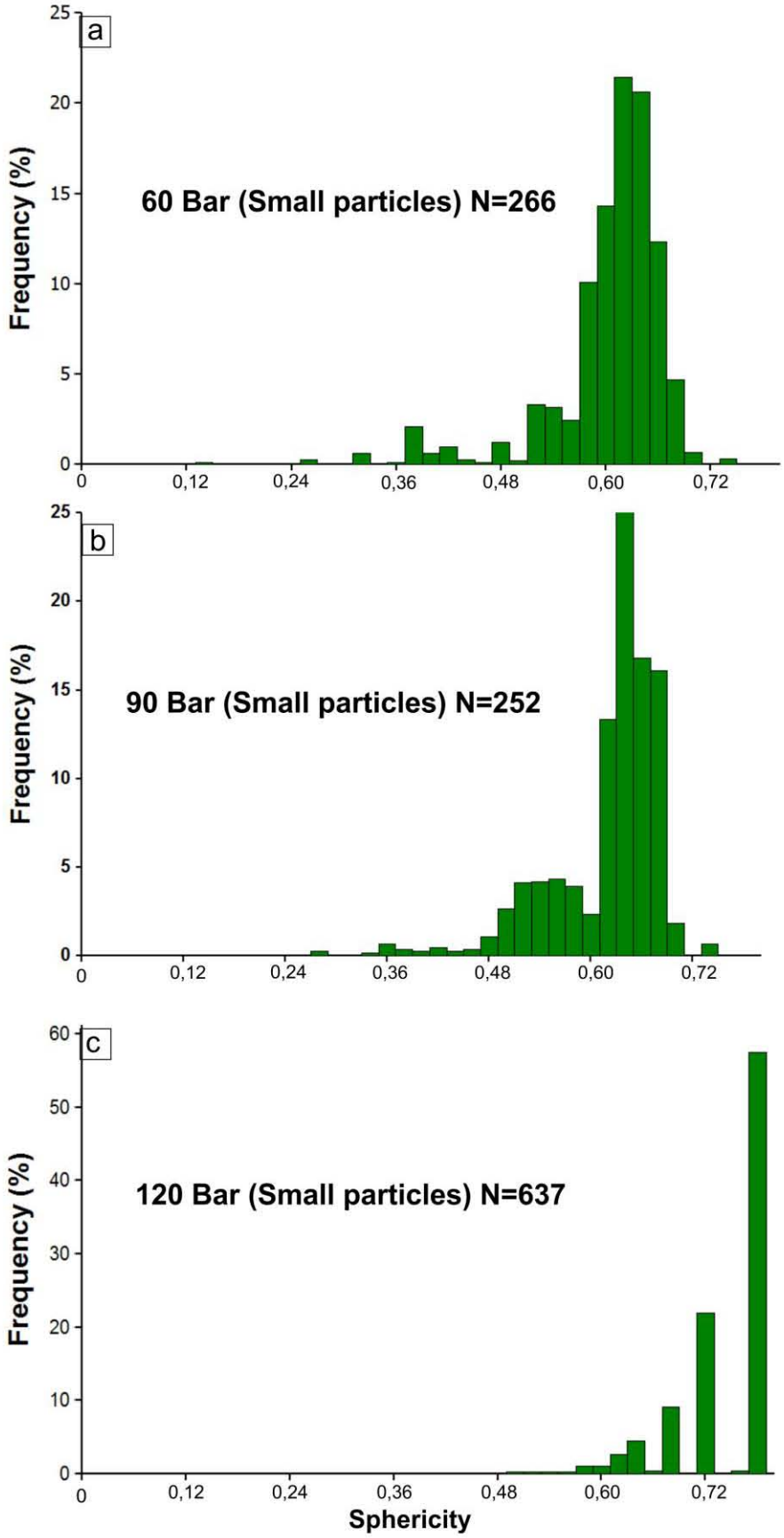

Figure 6-12: X-ray CT small particles gold sphericity distribution against frequency percentage.

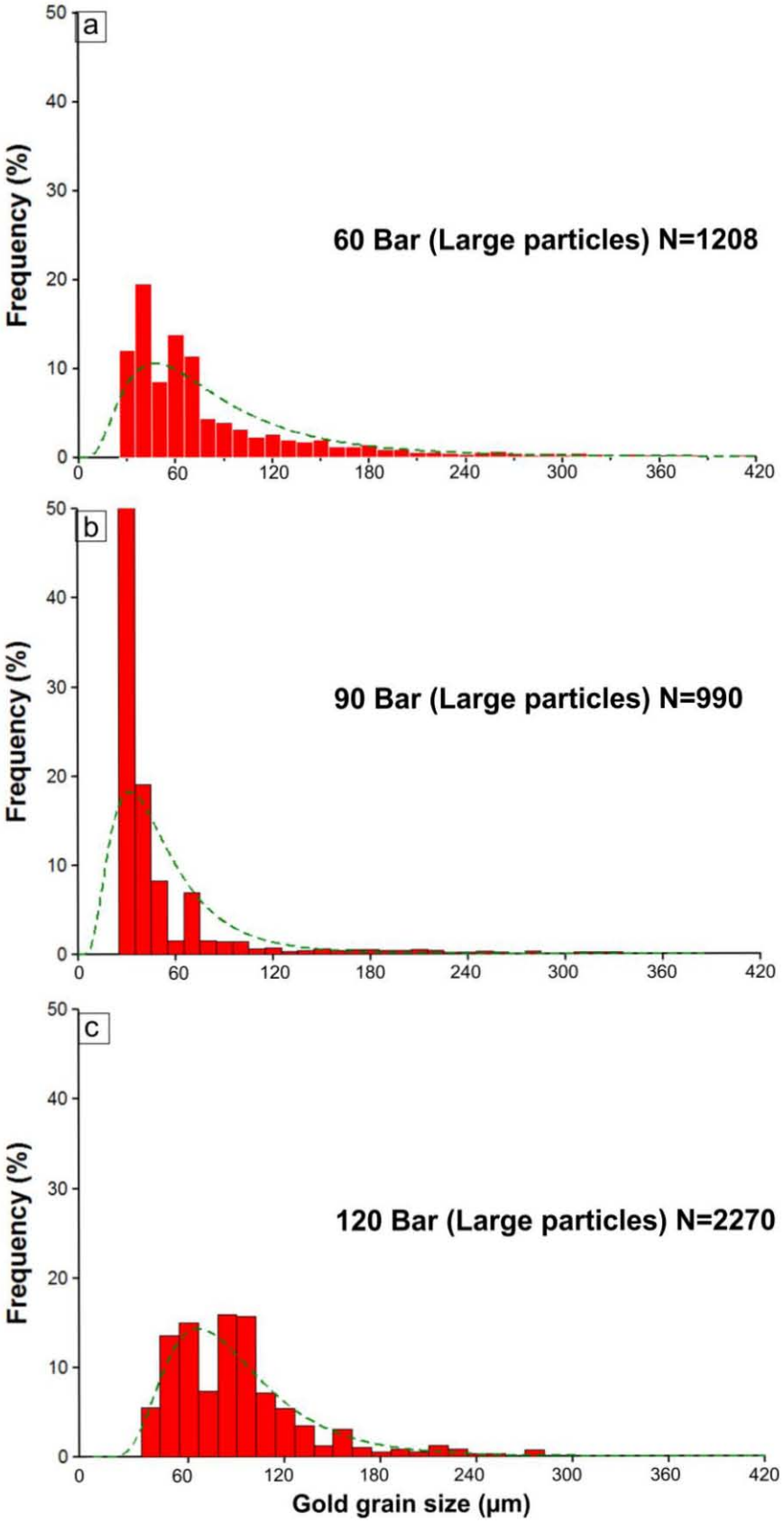

Figure 6-13: X-ray CT large particles gold grain size distribution against frequency percentage (the Gaussian fit represent the distribution trend).

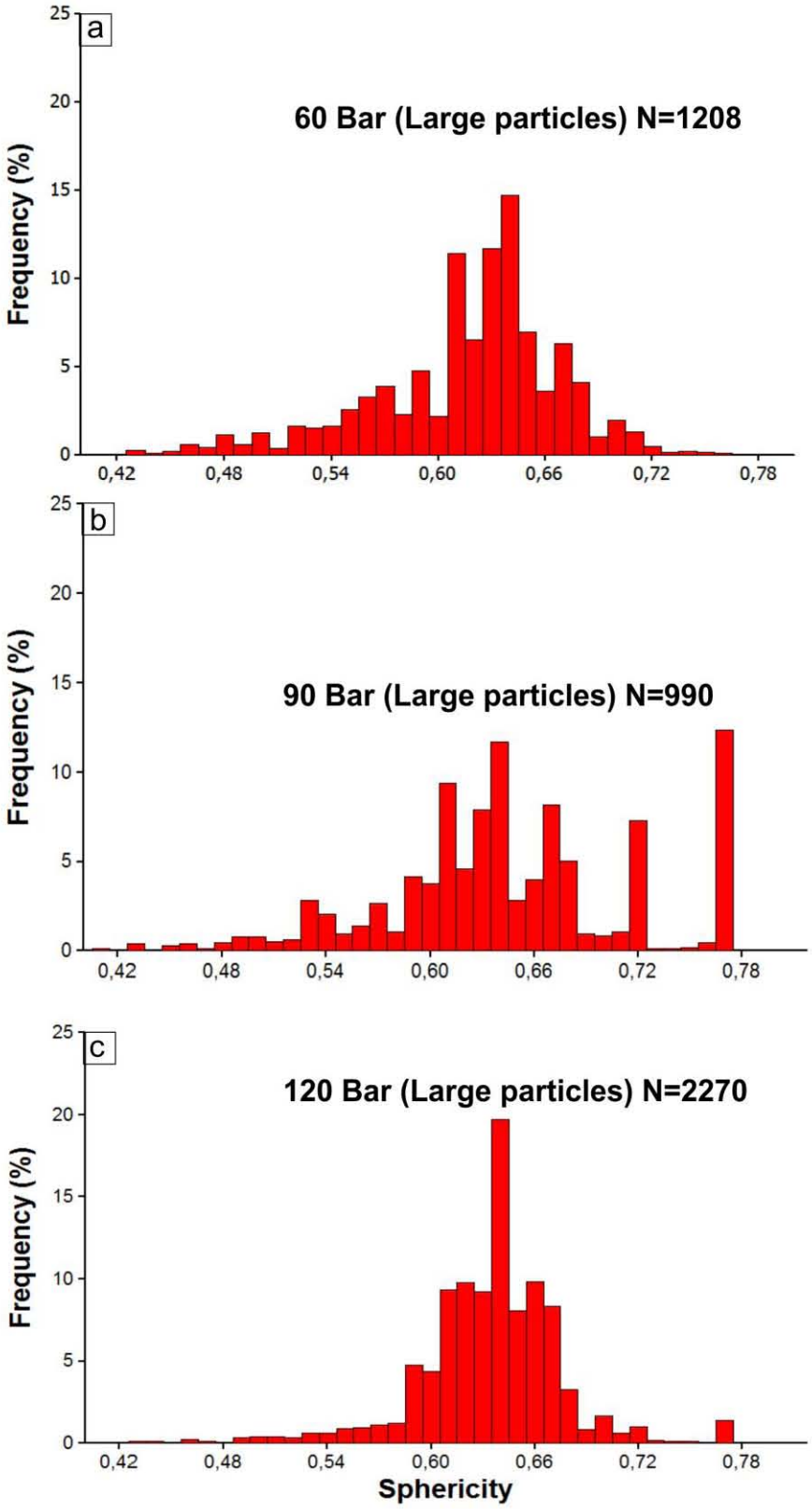

Figure 6-14: X-ray CT large particles gold sphericity distribution against frequency percentage.

6.3.3 Mineralogical association and gold liberation status

A thorough understanding of gold association with the host gangue minerals is also a key to potential heap leaching studies, as these minerals may have a deleterious effect during cyanidation. For this study, mineralogical association of gold with other minerals was quantified using QEMSCAN and X-ray CT based on area. Due to a wide spectrum of the minerals in the Witwatersrand and to simplify results, minerals have been reclassified based on their mineral groups. The majority of the gold shows a strong association with silicates, sulphides and oxide minerals (Figure 6-15). No significant association of gold with pyrophyllite and carbonaceous material (Corrans and Dunne, 1985; Cook, 1990) was noted. Free surface in this study refers to gold that is liberated or not locked in a specific host mineral. Only few grains (<10 % of the total population) of gold were found to be associated with free surface.

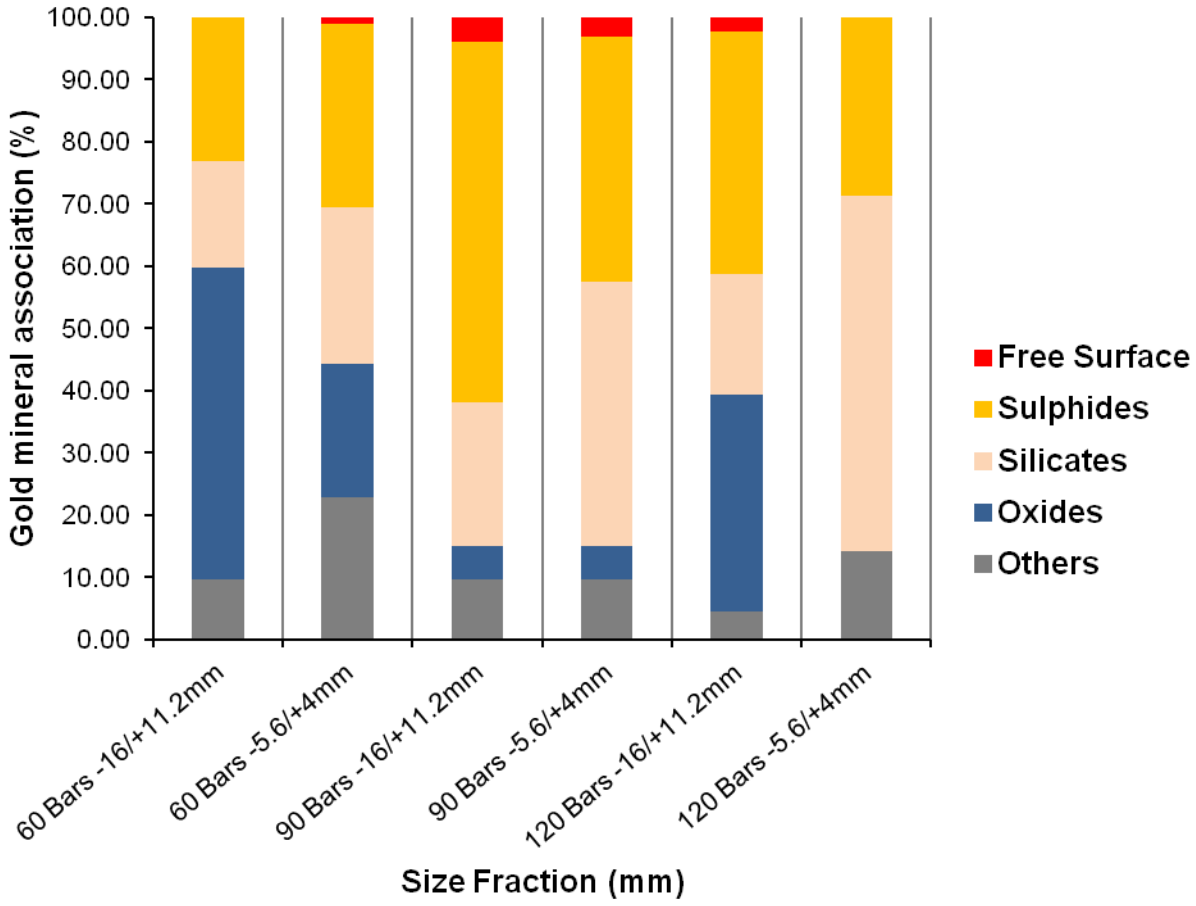

Figure 6-15: QEMSCAN mineralogical association of gold with gangue mineralogy

Liberation status of gold is one of the most significant parameters in gold cyanidation. Only partial exposure of gold grain is required for recovery by cyanidation to occur. The classification scheme was defined in this study for QEMSCAN gold liberation based on area and it is presented in Figure 6-16. This is a typical classification scheme used for this type of study (Coetzee et al., 2011; Lotter, 2011; Lotter et al., 2010).

Table 6-3: Description of liberation status classification scheme

Liberation status	Description
A	Exposed>70 %
B	Exposed <10 %
C	Locked in sulphides (>90 %)
D	Locked in silicate (>90 %)
E	Locked in oxide (>90 %)
F	Locked in carbonates (>90 %)
G	Locked on sulphide-silicate boundary
H	Locked on sulphide-oxide boundary
I	Locked on sulphide-carbonate boundary
J	Locked on silicate-oxide boundary
K	Locked on silicate-carbonate boundary
L	Locked on poly-mineral boundary

Results of liberation characteristics of the studied Witwatersrand ores shows that the major proportion of the gold is locked in sulphides, silicates and within poly-mineral boundaries (Figure 6-16). Less that 5 % of the gold grains are liberated with no clear distinctions of liberation between HPGR pressures. Small particles have slightly higher liberated gold grains as compared to the large particles. The 120 bar large particles contains a noticeable fraction of particles that are >70 % liberated, but the total number of gold grains (N) analysed is small to draw definitive conclusions.

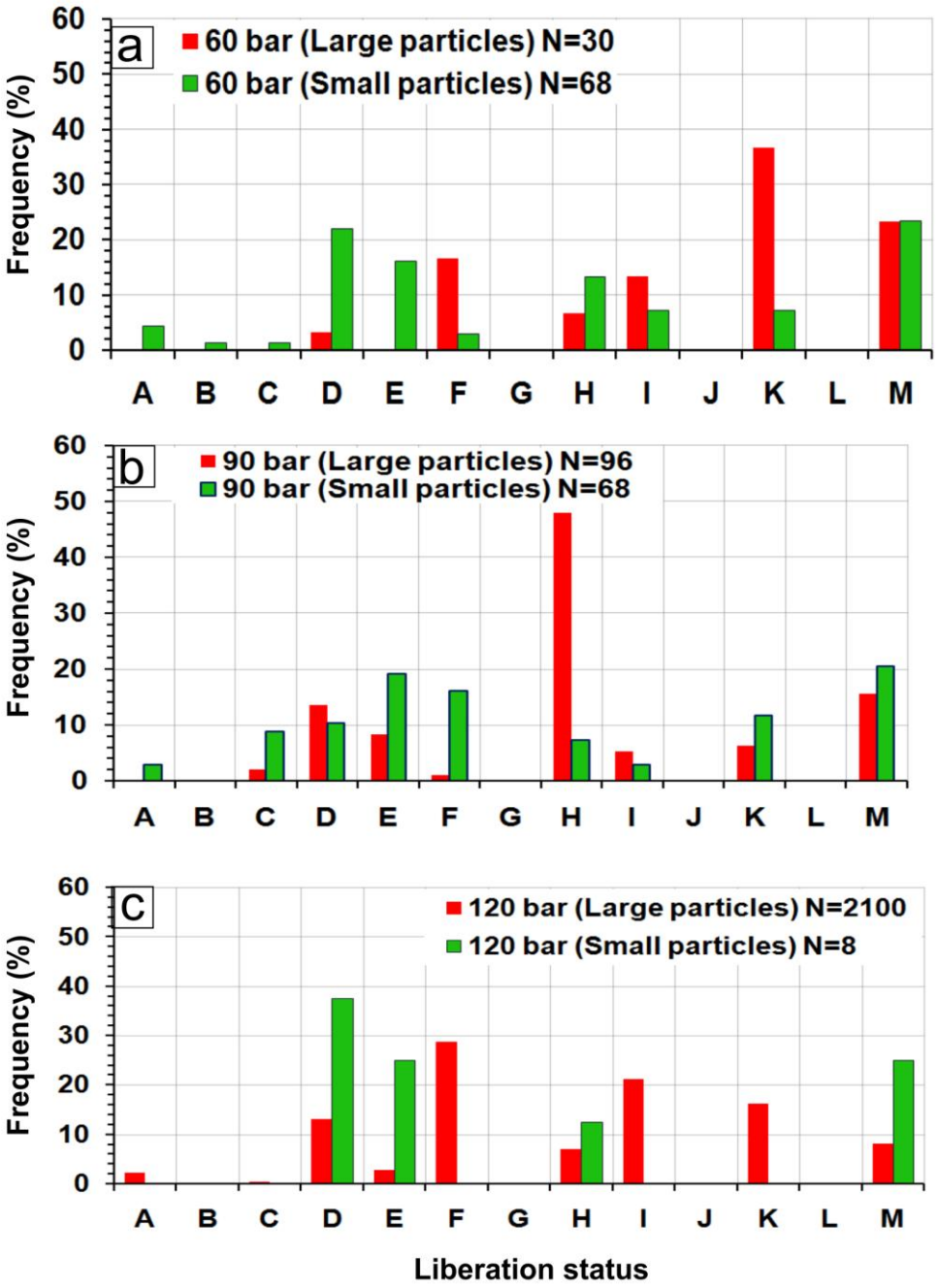

Figure 6-16: Liberation characteristics of the Witwatersrand gold ore (legend for liberation status can be found in Table 6-3).

A classification scheme was also defined for gold liberation in X-ray CT data. This scheme classifies gold into five different classes as a result of their comminution and their expected leaching behaviours using X-ray CT (Figure 6-17). Sulphides and silicates were found to be the main hosts of gold. Accessibility of this gold grain was promoted by the presence of HPGR-induced cracks and spatial distribution within the host minerals. Below are the five X-ray CT gold grain liberation classes:

a) Grains located at the surface of particles and exposed to the leach solution (for example, grain marked A);
b) Grains located close to the surface of particles which become exposed to the leach solutions only after other grains have reacted (for example, grain marked B);
c) Grains located inside the particles and not connected to the surface (for example, grain marked C);
d) Grains located inside the particles but connected to the surface via pores or cracks (detectable only in the particles crushed using HPGR) (for example, grains marked D) and;
e) Grains that are partially exposed which can be accessed by the leach solution (for example, grain marked E).

This classification was done manually and cannot be done quantitatively as yet, but automation would be ultimately a useful tool.

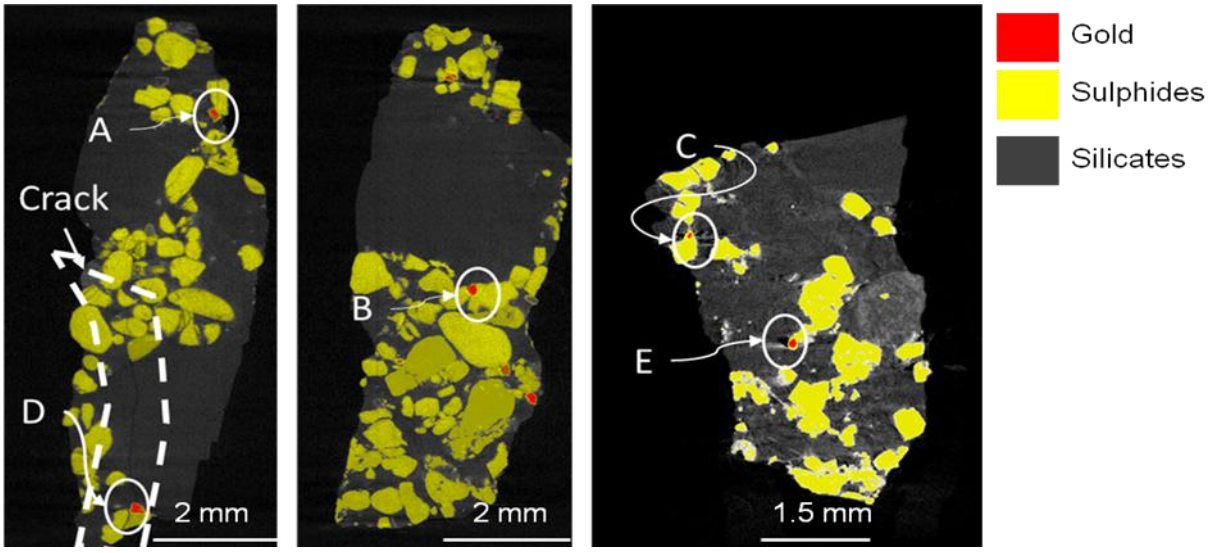

Figure 6-17: 2D X-ray CT false colour images illustrating the Witwatersrand gold ore based on comminution and their expected leaching behaviour.

6.3.4 Summary of gold deportment studies in the prediction of metallurgical behaviour

Ore characterisation forms the most critical part in understanding the deportment of gold and the prediction of metallurgical behaviour. In this study, some gold occurs in variable alloyed compositions (Au-Ag-Hg), implying that there is solid-solution reaction series (i.e. with Ag)

forming electrum; however, most of it is in metallic native state (pure gold). These findings are important since gold alloyed with other elements can be less soluble during cyanide leaching than native gold. The bulk composition of the Witwatersrand gold ore is dominated by insoluble minerals (quartz and phyllosilicates) but which can dissolve in certain alkaline conditions resulting in gold particles becoming coated which are difficult to leach. Certain gold grain characteristics influence the efficiency of particular gold recovery methods. The majority of the gold is sub-rounded with sporadic occurrences of flaky gold grains. This is good for heap leaching as long as the grains are not coated since there will be no selective grain leaching and no reduced gold grain size density along edges.

A statistically representative population of gold grains analysed in this study showed that most of the gold is fine grained (<50 µm) and this would have a negative effect on heap leaching if the gold grains are not exposed. The gold grain size distribution curve is positively skewed, forming a log-normal distribution, resulting in different geometric mean and mode. This means that the coarse grained gold sizes are rare or absent. The statistics are poor on grains in this range, limiting sufficient interpretation of coarse gold. This is usually a key problem with measuring gold grain size distributions.

The finer the gold the harder to liberate and thus the harder to get the crack network through. The exposure status of gold has metallurgical implications in terms of accessibility. Such size fractions are below conventional mill target of 80 % passing -75 µm and are unfavourable for coarse particle heap leaching. A minor percentage (<5 %) of exposed gold was found in this category but still not liberated, and this is important, since it allows the gauging of best crush size of the ore for heap leaching. Most of the gold grains are associated with sulphides and silicates and tend to be locked in grains of these minerals which are situated on poly-mineral boundary phases. Gold grains that are exposed to cyanide are expected to dissolve fully during cyanidation, but the challenge lies with locked and fine gold grains.

6.4 CYANIDE LEACHING EXPERIMENTS

The cyanide leaching experiments were designed to investigate the effect of particle size on gold recovery; leaching behaviour over time and to study the effect of HPGR feed preparation pressure using the methodology described in Chapter 4.

6.4.1 The pH behaviour

The pH behaviour of the gold leaching experiments was measured when collecting samples for gold recovery analysis in order to evaluate the potential interaction of minerals and cyanide. From the activation of the reactors at zero hours, the pH decreased for all HPGR pressures and size fractions (Figure 6-18). This continuous decrease in pH occurred until 220 hours with large particles crushed at 120 bar and 60 bar pH reaching below 9.8. During this period of decreasing pH, gold together with host minerals (i.e. silicates, oxides and sulphide minerals such, galena and non-magnetic pyrrhotite) are interpreted to have reacted or interacted with the cyanide solution (Figure 6-18). Oxidation of sulphide minerals, especially pyrite is rendered to be the main contributor to rapid decline in pH. No major differences in pH related to particle size and pressure setting was observed.

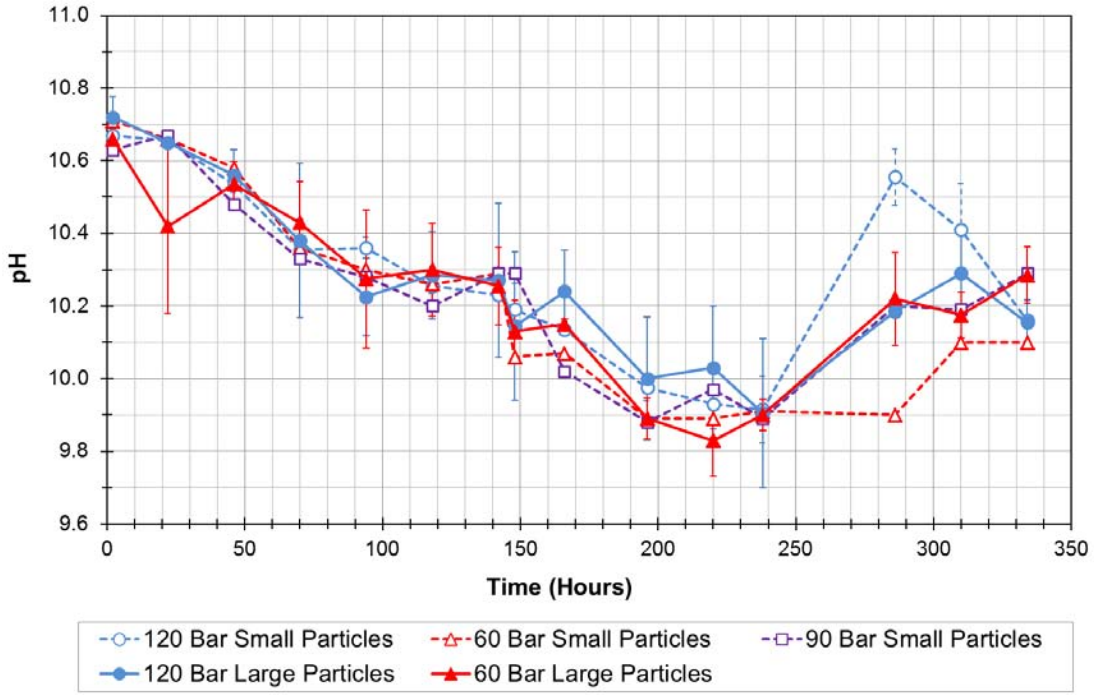

Figure 6-18: Change in pH over time for large particles (-16/+11.2 mm) and small particles (-5.6/+4 mm) from leaching experiments. Error bars represent the standard deviation of every sampling interval.

6.4.2 Gold extraction curves

Results of the gold extraction behaviour over time and effect of particle size for three HPGR pressure setting showing both small and large particles are presented in Figure 6-19. From the activation of the leach reactors, a slow leaching rate in all reactors and size fractions

extending over the first 22 hours was observed. The gold extraction trends show that the gold dissolution was affected by the presence of sulphide minerals which are known to retard the gold cyanidation process (Aghamirian and Yen, 2005; Deschênes et al., 2009). The studied gold ore has >4 wt. % sulphides and is dominated by less soluble minerals such as quartz. Porous and to some extent compact pyrite are expected to be the most active substrate for oxygen reduction due to their relatively high reactivity due to their morphology and surface area. Porous pyrite hosts the majority of the gold as micro-inclusions and thus makes the Witwatersrand gold amenable to cyanide leaching. Secondary/hydrothermal pyrite (euhedral pyrite) is deemed to be the least reactive. The reaction equations 6.1 to 6.4 explain the behaviour of pyrite in cyanide solution. The sulphide minerals interfere with gold dissolution, potentially explaining the intermediate levelling off of the leach curves during cyanidation. Oxidation of sulphide minerals such as pyrite during cyanidation results in the production of acid which explains the decline of the pH in Figure 6-18. The overall chalcopyrite reactions during cyanidation can be represented by the reaction equations 6.5 and 6.6. The oxidation of sulphur could therefore be associated with reduction of Cu (II) to Cu (I) in order to complex with cyanide. The reaction of pyrrhotite with cyanide is expressed in equation 6.7 and 6.8 (Deschênes et al., 2003). The dissolution of pyrrhotite in cyanide solution results in formation of ferro-cyanide ion and thiocyanate.

Pyrite reaction equations (Liu and Yen, 1995):

$$4FeS_2+8CN^-+3O_2+2H_2O\rightarrow 4FeOOH+8SCN^- \quad \text{Eq. (6.1)}$$

$$4FeS_2+7O_2+8OH^-\rightarrow 4FeOOH+4S_2O_3^{2-}+2H_2O \quad \text{Eq. (6.2)}$$

$$4FeS_2+11O_2+16OH^-\rightarrow 4FeOOH+8SO_3^{2-}+6H_2O \quad \text{Eq. (6.3)}$$

$$4FeS_2+15O_2+16OH^-\rightarrow 4FeOOH+8SO_4^{2-}+6H_2O \quad \text{Eq. (6.4)}$$

*Chalcopyrite reaction equation (*Dai and Jeffrey, 2006):

$$CuFeS_2+5CN^-+O_2+H_2O\rightarrow Cu(CN)_3^{2-}+FeOOH+2SCN^-+OH^- \quad \text{Eq. (6.5)}$$

$$CuFeS_2+3CN^-+2O_2+OH\text{-}\rightarrow Cu(CN)_3^{2-}+S_2O_3^{2-} \quad \text{Eq. (6.6)}$$

Pyrrhotite reaction equations (Deschênes et al., 2003):

$$Fe_{1-x}S+0.75yO_2+1.5yH_2O\rightarrow Fe_{1-x-y}S+yFe(OH)_3 \quad \text{Eq. (6.7)}$$

$$S^{2-}+CN^-\rightarrow CNS^-+2e \quad \text{Eq. (6.8)}$$

Where $Fe_{1-x}S$ illustrate the loss of iron and $Fe_{1-x-y}S$ represents the iron deficient surface layer. Sulphur in iron deficient sulphide surface layer may be leached according to equation 6.8.

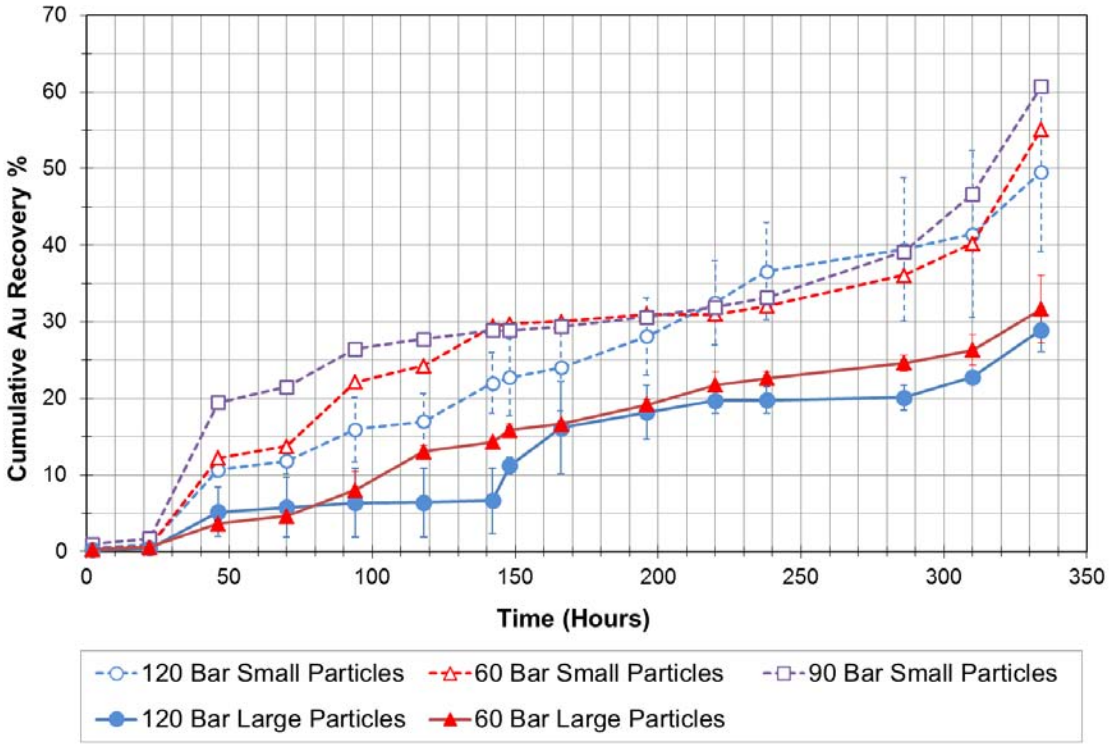

Figure 6-19: Cumulative gold recovery percentage verses time for large particles (-16/+11.2 mm) and small particles (-5.6/+4 mm) from leaching experiments. Error bars represent the standard deviation of every sampling interval.

The fact that the increase of pH coincides with an increase in gold leaching rate is an indication that the interference of that sulphide minerals reaction has come to an end. By the end of the leach cycle (termination of reactors), all leach reactors were showing similar trends of gold recovery with 90 bar HPGR small particles reaching just over 60 % cumulative recovery (Figure 6-19).

6.4.3 Crack density and mineral dissolution potential

Comminution plays a key role during mineral conversion since finely milled minerals react at a faster rate (i.e. can be processed in a tank leaching process) than coarsely crushed ore (which would require heap leaching) the dissolution of which is governed by diffusion through the particle matrix. There is a definite difference between large and small particles, and differences within a given size class (at different pressure settings) are more subtle. Particle mapping (section 6.3.3, Figure 6-17) showed that certain cracks lead to valuable mineral exposure promoting a leach solution diffusion pathway. In low-porosity rocks, such as the Witwatersrand gold ore, the solid/liquid contact is mainly a function of the particle size

of the material and is a major factor in determining the kinetics of the leaching reactions (Ghorbani et al., 2013). Leaching reagents are able to penetrate into micro-fissures and micro-pores of the rock mass where the crack density is sufficient, Figure 6-20 shows the crack network connecting internal grains, which is hence likely to promote reagent ingress.

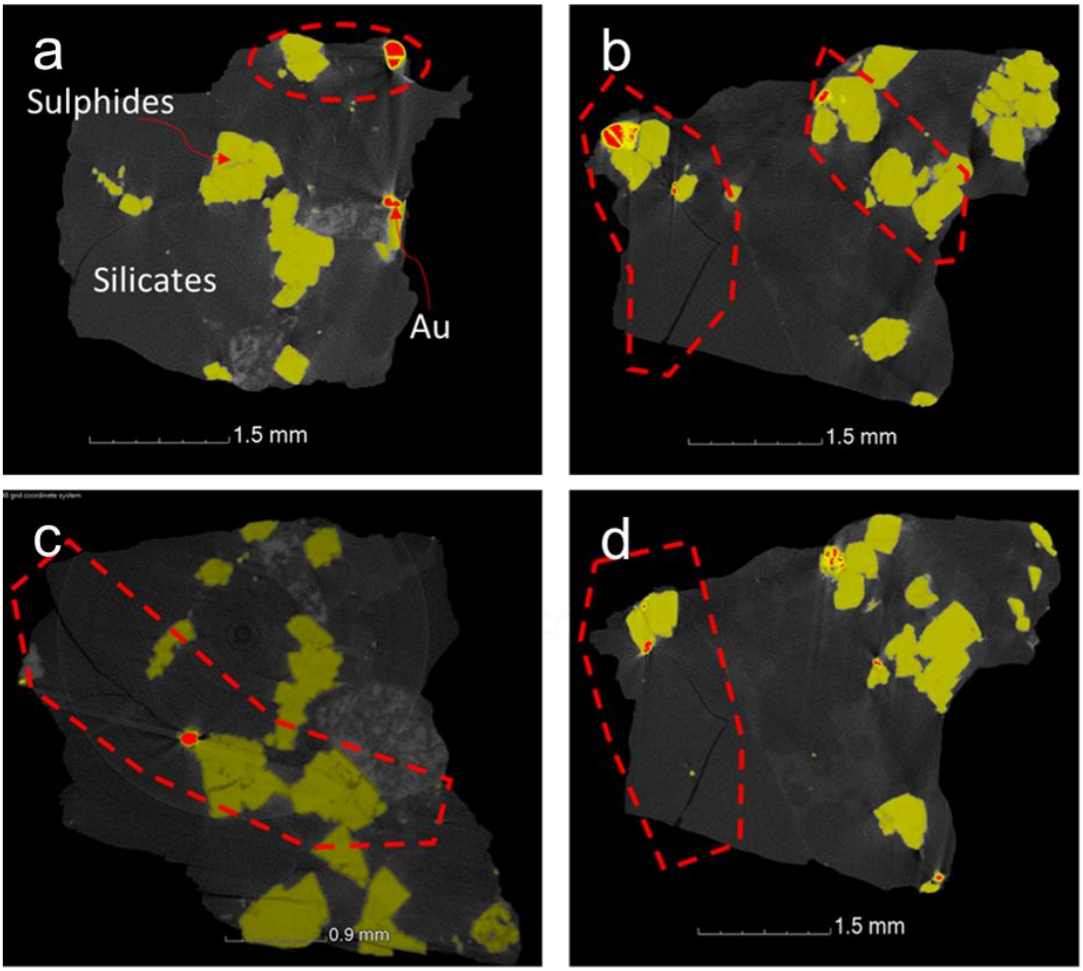

Figure 6-20: X-ray CT false colour images showing crack network distribution and exposure of valuable mineral.

6.4.4 Laboratory cyanide-leaching performance discussion

The results of the leaching experiments conducted using a dilute cyanide solution (200 ppm) showed better gold extraction for the small particles (> 50 % Au recovery) than the large particles (~ 30 % recovery) for all the different HPGR settings investigated. These findings concur with findings of both Ling et al., (1996), and Ghorbani et al., (2011), which showed better metal extraction on smaller-sized particles for Au and Zn respectively. Sulphide minerals form a major competitor of gold dissolution in cyanide with porous pyrite being

deemed the most reactive and euhedral pyrite the least reactive of the three main generations of pyrite observed in this study. The effects of pyrrhotite and chalcopyrite are expected to be minimal due to the morphological nature and concentration of these minerals in the Witwatersrand gold ore.

Leaching rates (approximately 7.2 % per day on small particles and ~3.7 % per day on large particles) are more distinct between 0 and <150 hours in all size fractions of the ore. This is due to the heterogeneous mineral constitution of the Witwatersrand gold ore, which results indifferent dissolution rates for the same ore. Ghorbani et al., (2013) also showed better metal extraction for particles prepared using HPGR compared with particles prepared using a cone crusher. Similarly, Tavares (2007) showed that the application of HPGR plays a major role in particle weakening and the induction of a micro crack network which has a positive impact in heap leaching.

The best results in terms of both gold recovery (60.7 % Au) and crack density (0.87 vol. % cracks as measured with QEMSCAN) were obtained on the small particles prepared at 90 bar HPGR feed pressure. This suggests that the optimum HPGR conditions for preparing the ore lie close to 90 bar. In terms of the overall performance of the cyanide leaching, the rate of Au extraction appeared to increase fairly rapidly, indicating that the columns were terminated before gold was fully exploited. Given that the gold extraction has not reached a plateau, there is a strong basis to indicate that, with additional leaching time, the final gold recovery would be considerably higher. Further work in this regard is recommended to determine how the final gold recovery, given additional leaching time, would be compare to standard gold recovery obtained in a conventional cyanide leach circuit of the same ore i.e. > 80-90 % recovery (Fivaz, 1988b).

CHAPTER 7: CONCLUDING DISCUSSION AND RECOMMENDATIONS FOR FUTURE WORK

7.1 CONCLUDING DISCUSSION

This study investigated the potential into the Witwatersrand gold ore for heap leaching using process mineralogy, X-ray CT and a series of laboratory scale column leach tests. The study investigated a ROM ore comprising the Ventersdorp contact- and Elsburg reefs sampled from Harmony gold mine near Carletonville, South Africa, that was prepared using the energy efficient high pressure grinding rolls for comminution. The following concluding discussion will revisit the key questions posed in Chapter 1:

The first key question aimed to determine *what information can be obtained on a Witwatersrand gold ore using micro-focus X-ray CT*. In this study, micro-focus X-ray CT provided valuable information throughout all stages of investigation into the potential for heap leaching of the Witwatersrand gold ore. This included detailed mapping and quantification of HPGR micro-cracks together with ore porosity, gold deportment and characterisation of the ore (section 5.5). X-ray CT's non-destructive ability also provided quantification of modal mineralogical compositions of the ore which can be used to assay the feed (section 5.5.2) and residues of tracked particles during leaching in future heap leaching studies. A large statistical dataset on gold (a total of 7993 gold grains were analysed in this study) and host (section 6.3.2) minerals were generated with minimum effort. The acquisition of total number of gold grains using X-ray CT was done in conjunction with QEMSCAN. Gold grain shape was measured and played a major role in understanding the effect of shape in process mineralogy. This information allowed the interpretation of the possible effects of gold grain size verses ore particle size and exposure in the leaching experiments. Certain X-ray CT and QEMSCAN datasets have limitations due to resolution differences, therefore meaningful conclusions were drawn where both instruments showed consistent evidence.

Most of the Witwatersrand gold ores have very low primary porosity due to metamorphism and other geological processes (Steven, 2009). Therefore, for effective gold cyanidation, a

crack network needs to be induced by means such as HPGR to ensure access of the lixiviant to the individual gold grains. The second key question aimed to determine *the effects of HPGR feed pressure, crack volume, crack width density and distribution on the comminution of the Witwatersrand gold ore*. All HPGR prepared particles were found to contain micro-cracks which are the key parameter for leach solution-particle interaction. However, cracks with <0.1 vol. % were not detected/measured due to resolution limitation in X-ray CT. A clear variation in crack volume and width (section 6.2.3) between small and large particles on three different HPGR pressure setting was observed, with small particles having more pronounced cracks (0.87 vol. % and 0.15 mm width) when compared to large particles. With a HPGR pressure of 90 bar, micro-cracks are extensive and connected, creating a good environment of solution flow. A more pronounced crack vol. % (i.e. 0.78 vol. %) was found in 120 bar large particles with a slightly lower crack width of 0.028 mm. Although a certain amount of fines is required in coarse particle heap leaching to maintain solution retention, possibly a bigger overall concern is that HPGR products are known to have high proportions of fine particles (e.g. Solomon et al., 2011), which could result in reduced heap permeability (section 2.4.2).

The Witwatersrand gold ore is heterogeneous, nevertheless much of it is dominated by silicates (i.e. quartz) and economic minerals such as gold occur in minute amounts when compared to the host minerals. *The third key question was aimed at determining the mineralogical features of the Witwatersrand gold ore affecting cyanide leaching, and heap leaching*. Typically, gold in Witwatersrand ores varies in size between 1 to 200 µm (section 6.3.2). The majority of the gold occurs as fine inclusions locked in host gangue minerals such as porous pyrite. Given the relatively coarse particle sizes used in this study (>4 mm), gold is mostly unliberated (<10 % of the total ore is liberated, section 6.3.3) compared to that which is typically used for gold tank leaching (P_{80} <75 µm). In the context of ore prepared using HPGR, un-liberated does not necessarily mean inaccessible (Figure 6-20) due to the presence of micro-cracks.

The Witwatersrand gold shows a strong association with the Fe-sulphides, particularly pyrite and pyrrhotite and this finding has been published (section 3.1.4) in several Witwatersrand mineralogical studies (Mngoma, 2012; Frimmel et al., 2005; Ramdohr, 1969). The presence of both pyrite (three generations, Figure 6-6) and pyrrhotite (mainly non-magnetic in the studied Witwatersrand gold ore) in this ore accounts for the slow initial extraction of gold (especially in the first 48 hours of leaching). During gold cyanidation, cyanide has to participate in the dissolution of the host mineral before it can penetrate the gold. Pyrrhotite is

most likely to be the stronger consumer of cyanide, given its greater reactivity relative to pyrite (Thomas et al., 2000; Deschênes et al., 2003). The presence of the non-magnetic, less reactive pyrrhotite as the dominant pyrrhotite phase is considered a positive feature in terms of a slightly lower consumption rate of available oxygen from the leach solution compared to if the more reactive magnetic phase dominated. Subsequently, pyrite would be the major cyanide consumer and, in this ore, the relative reactivity of pyrite is expected to be correlated with the type or pyrite present (porous / concretionary, compact and hydrothermal/ euhedral pyrite). The oxidation of pyrite during leaching depends on its concentration and distribution (Lui and Yen, 1995).

Porous pyrite is the most reactive form of pyrite (Figure 6-6) due to its high surface area and presence of micro-pores within its crystal structure, whereas compact pyrite is most likely to be the second most reactive as it has minor micro-pores and moderate surface area. Hydrothermal (euhedral pyrite) is the least reactive compared to porous and compact pyrite, as it was formed by mobilization and recrystallisation during metamorphism, thus leading to its single crystal structure. Petrographical studies (section 6.3.1) of the VCR showed that it is dominated by porous and compact pyrite (syn-sedimentary) which is most likely to react with cyanide during gold cyanidation, resulting in its excessive consumption of the cyanide solution and oxygen. The ER is enriched in hydrothermal euhedral pyrite which is likely to be less reactive.

The presence and interaction of multiple sulphide minerals in the Witwatersrand ore (pyrite, pyrrhotite, minor chalcopyrite and galena) will also contribute to retarding gold extraction through factors such as galvanic interactions (e.g. between pyrite and pyrrhotite), dissolution of transition metals, complex formation and consumption of free oxygen (Habashi, 1967; Lorenzen and van Deventer, 1992; Teague et al., 1999; Dai and Breuer, 2013). If these factors were to become excessively prohibitive to cyanidation, the possibility of ore pre-treatment with bio-oxidation or roasting (section 2.4) may need to be reviewed.

Sheet silicates such as chlorite, pyrophyllite (results from the diagenesis/ metamorphism of clay minerals) and even muscovite (a clay-forming mineral), which are present in Witwatersrand gold ores, may also affect the gold cyanidation process (section 2.3.1). Potentially deleterious minerals such as preg-robbers (for example, active carbon and pyrrhotite), environmentally undesirable elements (for example, arsenic and lead), and minerals that could potentially consume acid, alkali or oxygen should not be overlooked. Given the relatively low concentrations of these clay minerals present in the ore, they are

unlikely to have a major effect on gold cyanidation. The VCR and ER contain low concentration of carbonaceous material (section 5.2); however, certain gold ores in the Witwatersrand Basin, such as the CLR, contain significant concentrations of carbonaceous material, resulting in preg-robbing during gold cyanidation (Zhou et al., 2004).

The final key question was devoted to assessing *the potential for heap leaching of Witwatersrand gold ore*. Even though sufficient evidence to answer this question conclusively was not gathered in this study, the findings show promise for heap leaching of Witwatersrand gold ores, since the rate of gold recovery was still steadily increasing when the experiments were terminated. Particle size played an important role on gold extraction with differences between large and small particle in terms of cracks vol. % and gold extraction. Large particles show narrow crack width and crack-porosity volume except for 120 bar large particles, hence the diffusion path for cyanide solution is limited, resulting in large particles leaching more slowly. These findings agree with those of Ghorbani et al., (2011) which showed primarily that the cracks penetrated only to a certain depth, which was deep enough for small particles, but covered only a certain outer layer in larger particles. Small particles have wider cracks and higher crack volume, hence the diffusion path is sufficiently long to allow cyanide interaction with gold providing sufficient solution saturation, thus small particles leach faster when compared to large particles. The best gold extraction (~60 % recovery) was obtained for small particles (-5.6+4 mm) prepared using the HPGR at 90 bar feed pressure. Small particles prepared under these conditions had the greatest vol. % of cracks (0. 87 vol. %), and slightly wider cracks (> 0.03 mm) compared to large particles (-15.6+11.2 mm). For all samples investigated the initial gold extraction was slow due to the consumption of free cyanide by sulphide minerals such as pyrite and pyrrhotite, as well as chlorite and muscovite. VCR pyritic minerals were interpreted to be more reactive due to high surface area whereas the ER is dominated by less reactive pyritic minerals.

It has become critically important to investigate alternative methods to process low grade gold ores due to conventional cyanidation becoming increasingly uneconomic (section 1.1). The amenability of the Witwatersrand gold ore to the process of heap leaching offers new innovative mineral processing opportunities in the Witwatersrand Basin. This finding could yield great long-term benefits for South Africa's gold mining industry, following the progressive decline in gold grade and subsequent production rates. Preparation of the ore feed using HPGR offers the advantage of lower energy costs compared to comminution used in conventional cyanide leaching, as well as the formation of micro cracks that allow effective cyanide penetration. This study has demonstrated the value of a multi-disciplinary

approach in interpreting the potential of the Witwatersrand gold ore for heap leaching. The use of tools allowing the assessment of results in both 2D (optical microscopy, QEMSCAN) and 3D (X-ray CT, ICON) has been equally valuable.

7.2 RECOMMENDATIONS FOR FUTURE WORK

The present research has revealed that the investigation in the following areas may be beneficial:

I. Further study using micro-focus X-ray CT with better resolution to minimise the partial volume effect is recommended.
II. More customised tomography analysis software for process mineralogy application with the capability to provide eventual data integration with autoSEM data (i.e. QEMSCAN, MLA and TIMA), providing quantitative grain size distribution, liberation, association, linkages of grey levels to minerals is required.
III. Additional studies to determine the maximum amount of gold that can be recovered on the Witwatersrand gold ore prepared using HPGR and detailed assessment of ore variability is recommended.
IV. A study to analyse the leach residue, upscaling of the reactors, including mass balance using QEMSCAN and X-ray CT is suggested.
V. Further studies that include tracking of Fe and Cu ions during leaching, potentially toxic elements (example, As, U) in solution and also track where the gold particle is leached from is recommended.
VI. Unsaturated column leach trials of ore sample prepared for heap leaching is recommended

REFERENCES

Acevedo, F., 2002. Present and future of bioleaching in developing countriesle. Electron. J. Biotechnol. 52–56.

Afewu, K.I. and Lewis, G., 1998. Sampling of run-of-mine mill feed—A practical approach. SAIMM.

Aghamirian, M. M., 1997. Reactivity of sulfide minerals and its effect on gold dissolution and its electrochemical behaviour in cyanide solution. Queen's University, Canada. PhD thesis

Aghamirian, M.M. and Yen, W.T., 2005. Mechanisms of galvanic interactions between gold and sulfide minerals in cyanide solution. Miner. Eng. 18, 89–102.

Alacer Gold, 2011. Alacer gold announces smooth production ramp up at Çöpler. http://www.alacergold.com/files/asr_20110228a.pdf (accessed 4.11.13).

Andersen, J.C.Ø., Rollinson, G., Snook, B., Herrington, R. and Fairhurst, R., 2009. Use of QEMSCAN for the characterization of Ni-rich and Ni-poor goethite in laterite ores. Miner. Eng. 22, 1119–1129.

AngloGold, 2008. Review of operations: Progress on gold heap leaching projects. http://www.anglogold.com/subwebs/informationforinvestors/reports08/annualreport08/files/review_ml.pdf (accessed 4.11.13).

Armstrong, R.A., Compston, W., Retief, E.A., Williams, I.S. and Welke, H.., 1991. Zircon ion microprobe studies bearing on the age and evolution of the Witwatersrand triad. Precambrian Res. 53, 243–266.

Assibey-Bonsu, W., 1996. Summary of present knowledge on the representative sampling of ore in the mining industry. SAIMM.

ASTM, 1992. Standard Guide for Computed Tomography (CT) Imaging, in: Annual Book of ASTM Standards, S. 3 M.T.M. and A.P. (Ed.), ASTM Designation E 1441 - 92a. ASTM, Philadelphia, pp. 690–713.

Ayling, B., Rose, P., Petty, S., Zemach, E. and Drakos, P., 2012. QEMSCAN® (quantitative evaluation of minerals by scanning electron microscopy): Capability and application to fracture characterization in geothermal systems. Proceedings, Thirty-Seventh Work. Geotherm. Reserv. Eng. Stanford Univ. Stanford, California, January 30 - February. 1, 2012 SGP-TR-194.

Bartlett, H. and Viljoen, R., 2002. Variance relationships between the masses, grades and particle sizes for gold ores from the Witwatersrand. SAIMM. 491–500.

Barton, E.S. and Hallbauer, D.K., 1996. Trace-element and U-Pb isotope compositions of pyrite types in the Proterozoic Black Reef, Transvaal Sequence, South Africa: Implications on genesis and age. Chem. Geol. 133, 173–199.

Baum, W. and Ausburn, K., 2011. HPGR comminution for optimization of copper leaching. Miner. Metall. Process. 28, 77–81.

Becker, M., De Villiers, J. and Bradshaw, D., 2010. The flotation of magnetic and non-magnetic pyrrhotite from selected nickel ore deposits. Miner. Eng. 23, 1045–1052.

Belzile, N., Chen, Y.W., Cai, M.F. and Li, Y., 2004. A review on pyrrhotite oxidation. J. Geochem. Explor. 84, 65–76.

Benvie, B., 2007. Mineralogical imaging of kimberlites using SEM-based techniques. Miner. Eng. 20, 435–443.

Berger, M.J., Hubbell., J.H., Seltzer, S.M., Chang, J., Coursey, J.S., Sukumar, R., Zucker, D.S. and Olsen, K., 1998. XCOM: Photon cross sections database: NIST standard Reference Database 8. v. http//www.nist.gov/pml/data/xcom/index.cfm.

Bernstein, F., 1963. Particle Size and Mineralogical Effects in Mining Applications. Adv. X-ray Anal. 436–4456.

Boin, M. and Haibel, A., 2006. Compensation of ring artefacts in synchrotron tomographic images. Opt. Express 14, 12071–12075.

Boyle, R., 1987. Gold history and genesis of deposits. Van Nostrand, New York 200–233.

Bumby, A.J., Eriksson, P.G., Catuneanu, O., Nelson, D.R. and Rigby, M., 2012. Meso-Archaean and Palaeo-Proterozoic sedimentary sequence stratigraphy of the Kaapvaal craton. March. Pet. Geol. 33, 92–116.

Chaize, T., 2009. Gold Production in the World with special reference to south Africa. http://www.kitco.com/ind/Chaize/may192009.html (accessed 8.12.12).

Chamber of Mines of South Africa., 2012. Annual Report: Review of Gold mining bulletin. http://www.bullion.org.za/documents/AR_2012_web_Final.pdf (accessed 6.15.13).

Charland, A., Kormos, L.J., Whittaker, P.J., Arrué-Canales, C.A., Fragomeni, D., Lotter, N.O., Mackey, P. and Anes, J., 2006. A case study for the integrated use of automated mineralogy in plant optimisation: the Montcalm concentrator. In: Proc. Automated Mineralogy, MEI Conference, Brisbane, July 2006.

Cheney, E.., 1996. Sequence stratigraphy and plate tectonic significance of the Transvaal succession of southern Africa and its equivalent in Westerrn Australia. Precambrian Res. 79.

Chetty, D., Clark, W., Bushell, C., Nshimirimana, R. and De Beer, F., 2012. The Use of 3D X-ray computed tomography for gold Location in exploration drill cores. 10th international congress for applied mineralogy, Trondheim 2011.1–5.

Chryssoulis, S. and McMullen, J., 2005. Mineralogical investigation of gold ores. Dev. Miner. Process. Mike D. Adams 15, 21–71.

Coetzee, L.L., Theron, S.J., Martin, G.J., Van Der Merwe, J.D. and Stanek, T., 2011. Modern gold deportments and its application to industry. Miner. Eng. 24, 565–575.

Cook, N., 1990. Mineralogical examination of gold-bearing samples. CIM Bull. 83, 51–55.

Corrans, J. and Dunne, R.., 1985. Optimisation of recovery of gold and uranium from Witwatersrand residues. Mintek Rev. 2, 18–24.

Craig, J.R. and Vaughan, D.., 1981. Ore microscopy and ore petrography. John Wiley and Sons, New York.

Dai, X. and Breuer, P.L., 2013. Leaching and electrochemistry of gold, silver and gold–silver alloys in cyanide solutions: Effect of oxidant and lead(II) ions. Hydrometallurgy 133, 139–148.

Dai, X. and Jeffrey, M., 2006. The effect of sulfide minerals on the leaching of gold in aerated cyanide solutions. Hydrometallurgy 82, 118–231.

Daniel, M., 2007. Energy Efficient Mineral Liberation Using HPGR Technology. University of Queensland, Australia. PhD thesis.

Daniel, M.J and Morrell, S., 2004. HPGR model verification and scale-up. Miner. Eng. 17, 1149–1161.

De Villiers, J.P.R and Liles, D., 2010. The crystal-structure and vacancy distribution in 6C pyrrhotite. Am. Mineral. 95, 148–152.

De Wit, M.J., Roering, C., Hart, R.J., Armstrong, R.A., De Ronde, R.E.J., G., R.W.E., Tredoux, M., Perberdy, E. and Hart, R., 1992. Formation of an Archaean continent. Nature 357, 553–562.

Deschênes, G., Xia, C., Fulton, M., Cabri, L.J. and Price, J., 2009. Evaluation of leaching parameters for a refractory gold ore containing aurostibite and antimony minerals: Part I – Central zone. Miner. Eng. 22, 799–808.

Deschênes, G., Hall, D. and Fulton, M., 2003. Cyanidation of a pyrrhotite-bearing gold ore. Eur. J. Miner. Process. Environ. Prot. 3, 353–361.

Dhawan, N., Safarzadeh, M. and Miller, J., 2012. Recent advances in the application of X-ray computed tomography in the analysis of heap leaching systems. Miner. Eng. 75–86.

Dhawan, N., Safarzadeh, M.S., Miller, J.J.D., Moats, M.S., Rajamani, R.K. and Lin, C., 2012. Recent advances in the application of X-ray computed tomography in the analysis of heap leaching systems. Miner. Eng. 35, 75–86.

Dixon, D.G. and Petersen, J., 2003. Comprehensive modelling study of chalcocite column and heap bioleaching, in: Riveros, P.A., Dixon, D., Dreisinger, D., Menacho, J. (Ed.), Hydrometallurgy of Copper (Book 2). CIM, Montreal, Canada, pp. 493–516.

Doucouré, C.M., and de Wit, M., 2002. Temporal variation in the rigidity and mechanical behaviour of old continental lithosphere. South African J. Geol. 105, 39–50.

Dunne, R., Goulsbra, A. and Dunlop, I., 1996. High-pressure grinding rolls and the effect on liberation: comparative test results. Randol Gold Forum, pp. 49–54.

Eglington, B.M. and Armstrong, R., 2004. The Kaapvaal Craton and adjacent orogens, southern Africa: a geochronological database and overview of the geological development of the craton. South African J. Geol. 107, 13–32.

Els, B.G., 1987. The auriferous Middlevlei Reef depositional system, West Wits Line, Witwatersrand Supergroup. Rand Afrikaans University, South Africa. PhD thesis.

Engelbrecht, C., 2011. XRF analysis of Base Metals prepared by fused bead method. Witwatersrand.

Engelbrecht, C.J., Baumbach, G.W.S., Mathysen, J.L. and Fletcher, P., 1986. The West Wits Line. Anhaeusser, C.R., Maske, S. (Eds.), Miner. Depos. South. Africa, 1. Geol. Soc. South Africa 599–648.

Enzweiler, J. and Webb, P.C., 1996. Determination of Trace Elements in Silicate Rocks by X-ray Fluorescence Spectrometry on 1:5 Glass beads Discs: Comparison of Accuracy and Precision with Pressed Powder Pellet Analysis. Chem. Geol. 130, 195–202.

Eriksson, P.G. and Reczko, B.F., 1995. The sedimentary and tectonic setting of the Transvaal Supergroup floor rocks to the Bushveld Complex. J. African Earth Sci. 21, 487–504.

Eriksson, P.G., Condie, K.C., van der Westhuizen, W., van der Merwe, R, de B., H. and Nelson, D.., 2002. Late Archaean superplume events: a Kaapvaal-Pilbara perspective. J. Geodyn. 34, 207–247.

Eriksson, P.G., Schweitzer, J.K., Bosch, P.J.A., Schreiber, U.M., Van Deventer, J.L. and Hatton, C.., 1993. The Transvaal Sequence: an overview. J. African Earth Sci. 16, 25–51.

Esna-Ashari, and Kellerwessel, H., 1998. Roller press comminution improves heap leach recovery. andol Gold Meet. Scottsdale, AZ, Proc. 50–53.

Everard, A.D., 1988. Flat faulting in the Ventersdorp contact reef, sub-shaft area. Carletonville.

Fivaz, C., 1988. Presidential Address: How the MacArthur-Forrest cyanidation process ensured South Africa's golden future. J. South African Inst. Min. Metall. 88, 309–318.

Fragomeni, D., Yu, S., Anes, J., Edwards, T. and Scott, D., 2009. Advancing asset performance at the Montcalm operation. In: Proc. Canadian Mineral Processors, Ottawa, January 2009, Paper No. 12 205–219.

Francois-Bongarcon, D., 1993. The practice of the sampling theory of broken ores. CIM Bull. 86.

Francois-Bongarcon, D., 1995. Sampling in the mineral industry, theory and practice. Course presented in Johannesburg by the Mineral Resources Development Consultants, California, USA APR 1995.

Frimmel, H. and Müller, J., 2011. Estimates of Mineral Resource Availability–How Reliable Are They? Geodyn. 28, 39–62.

Frimmel, H.E., 2005. Archaean atmospheric evolution: evidence from the Witwatersrand gold fields, South Africa. Earth-Science Rev. 70, 1–46.

Frimmel, H.E., 2008. Earth's continental crustal gold endowment. Earth Planet. Sci. Lett. 267, 45–55.

Frimmel, H.E. and Gartz, V.H., 1997. Witwatersrand gold particle chemistry matches model of metamorphosed, hydrothermally altered placer deposits. Miner. Depos. 32, 523–530.

Frimmel, H.E., Zeh, A., Lehrmann, B., Hallbauer, D. and Frank, W., 2009. Geochemical and Geochronological Constraints on the Nature of the Immediate Basement next to the Mesoarchaean Auriferous Witwatersrand Basin , South Africa 50, 2187–2220.

Frimmel, H. E. and Minter, W.E.L., 2002. Recent developments concerning the geological history and genesis of the Witwatersrand gold deposits. Soc. Econ. Geol. Spec. Publ. 9, 17–45.

Frimmel, H. E, Groves, D. I, Kirk, J, Ruiz., J, Chelsey, J. and Minter, W.E.L., 2005. The formation and preservation of the Witwatersrand Goldfields, the world's largest gold Province. Econ. Geol. 100th Anniv. 769–797.

Gartz, V.H. and Frimmel, H., 1999. Complex metasomatism of an Archaean placer in the Witwatersrand Basin, South Africa: the Ventersdorp Contact Reef — a hydrothermal aquifer? Econ. Geol. 95, 689–706.

Ghorbani, Y., Becker, M., Mainza, A.N., Franzidis, J-P and Petersen, J., 2013. Investigation of the effect of mineralogy as rate-limiting factors in large particle leaching. Miner. Eng. 24, 1172–1184.

Ghorbani, Y., Becker, M., Petersen, J., Morar, S.H., Mainza, A. and Franzidis, J-P., 2011. Use of X-ray computed tomography to investigate crack distribution and mineral dissemination in sphalerite ore particles. Miner. Eng. 24, 1249–1257.

Ghorbani, Y., Mainza,. N., Petersen, J., Becker, M. and Franzidis, J-P., Kalala, J.T., 2013. Investigation of particles with high crack density produced by HPGR and its effect on the redistribution of the particle size fraction in heaps. Miner. Eng. 43-44, 44–51.

Ghorbani, Y, Becker, M, Mainza, A, Franzidis, J-P and Peterson, J., 2011. Large particle effects in chemical/biochemical heap leach processes. Miner. Eng. 24, 1172–1184.

Godel, B., 2013. High-Resolution X-Ray Computed Tomography and Its application to Ore Deposits: From Data Acquisition to Quantitative Three-Dimensional Measurements with Case Studies from Ni-Cu-PGE Deposits. Soc. Econ. Geol. 108, 2005–2019.

Godel, B. and Barnes, C.S.J., 2010. High-resolution X-ray computed tomography: A new technique to illuminate platinum ores 3–6.

Goodall, W.R., Scales, P.J., Butcher, A., Goodall, W.R., Scales, P.J. and Butcher, A.R., 2005. The use of QEMSCAN and diagnostic leaching in the characterisation of visible gold in complex ores. Miner. Eng. 18, 877–886.

Gottlieb, P., Wilkie, G., Sutherland, D. and Ho-Tun, E., 2000. Using quantitative electron microscopy for process mineralogy applications. J. Mineral. 52, 24–27.

Gu, Y., 2003. Automated scanning electron microscope based mineral liberation analysis. JOM 2, 33–41.

Guo, H., Deschênes, G., Pratt, A., Fulton, M. and Lastra, R., 2004. Leaching kinetics and mechanisms of surface reactions .1–8.

Gy, P., 1979. Sampling of Particulate Materials, Theory and Practice. Elsevier, Amsterdam.

Habashi, F., 1967. Kinetics and mechanism of gold and silver dissolution in cyanide solution, in: Montana Bureau of Mines and Geology Bulletin. Montana Bureau of Mines and Geology Bulletin, Butte, Montana, USA.

Hallbauer, D.K. and Joughin, N., 1972. An investigation into the distribution, size and shape of gold particles in some Witwatersrand reefs and their effects on sampling procedures. Chamb. mines 43.

Harmony gold., 2013. Kusasalethu mine . http://www.harmony.co.za/our-business/our-operations/kusasalethu (accessed 11.22.13).

Hartnady, C.J.H., 2009. South Africa's Gold Production and Reserves. S. Afr. J. Sci. 105, 328–329.

Hatton, C., 1995. Mantle plume origin for the Bushveld and Ventersdorp magmatic provinces. J. African Earth Sci. 21, 571–577.

Henney, P.J., Styles, M.T., Bland, D.J. and Wetton, P., 1995. Characterisation of gold from the Lubuk Mandi area, Terengganu, Malaysia. Br. Geol. Surv. Tech. Rep. WC/95/20, 26.

Hoffman, E.L., Clark, J.R. and Yeager, J., 1998. Gold Analysis – Fire Assaying and Alternative Methods. Explor. Min. Geol. 7, 155–160.

Hoffman, J.W. and De Beer, F., 2012. Characteristics of the micro-focus x-ray tomography facility (MIXRAD) at Necsa in South Africa, in: 18th World Conference on Nondestructive Testing, 16-20 April 2012. Durban, South Africa.

Hsih, C.S., Wen, S.B. and Kuan, C.C., 1995. An exposure model for valuable components in crushed particles. Int. J. Miner. Process. 43, 145–153.

Hunt, J., Berry, R. and Bradshaw, D., 2011. Characterising liberation and flotation potential using image analysis. Simulated fragmentation and small-scale flotation 5–7.

IAEA., 2013. IAEA TM on Regional RR Users' Networks (RRUNs): advances in neutron imaging, 26-29 Nov. 2012, Serpong, Jakarta, Indonesia. IAEA, Vienna, February. 2013.

ICMC., 2013. International cyanide management code for the gold mining industry. www.cyanidecode.org#sthash.VMpDRFmc.dpuf (accessed 1.25.14).

Lovea, M., Oaie, G., Ricman, C., Mateiasi, G., Neagu, M., Szobotka, S. and Duliu, O.G., 2009. Dual-energy X-ray computer axial tomography and digital radiography investigation of cores and other objects of geological interest. Eng. Geol. 103, 119–126.

Jansen, M. and Taylor, A., 2003. Overview of gangue mineralogy issues in oxide copper heap leaching, in: ALTA Conference, May 19-. 24. Perth, Australia, p. 32.

Jardine, M., 2013. Optimisations of CT Analysis for the Identification and Spatial Resolution of Platinum Group Minerals, Bushveld Complex. Stellenbosch University, South Africa. BSc. Hons. thesis.

Jolley, S.J., Freeman, S.R., Barnicoat, A. C., Phillips, G.M., Knipe, R.J., Pather, a., Fox, N.P.C., Strydom, D., Birch, M.T.G., Henderson, I.H.C. and Rowland, T.W., 2004. Structural controls on Witwatersrand gold mineralisation. J. Struct. Geol. 26, 1067–1086.

Juvonen, R., 1999. Analysis of Gold and the Platinum Group Elements in Geological Samples. Espoo Geol. Surv. Finl.

Kaestner, A.P., Hartmann, S., Kuhne, G., Frei, G. Grunzweig, C., Josic, L., Schmid., F. and Lehmann, E., 2011. The ICON beamline – a facility for cold neutron imaging at SINQ. Nucl. Instruments Methods Phys. Res. Sect. A 659, 387–393.

Ketcham, R. and Carlson, W.D., 2001. Acquisition, optimization and interpretation of X-ray computed tomographic imagery: applications to the geosciences. Comput. Geosci. 27, 381–400.

Kirk, J., Ruiz, J., Chesley, J., Titley, S. and Walshe, J., 2001. A detrital model for the origin of gold and sulfides in the Witwatersrand basin based on Re-Os isotopes. Geochim. Cosmochim. Acta 65, 2149–2159.

Kodali, P., Dhawan, N., Depci, T., Lin, C.L. and Miller, J., 2011. Particle damage and exposure analysis in HPGR crushing of selected copper ores for column leaching. Miner. Eng. 24, 1478–1487.

Koenig, R., 2006. Design selection for large-scale grinding operations-AG/SAG or HPGR?, in: Metallurgical plant design and operating strategies (MetPlant 2006). Perth, WA., 18–19.

Koglin, N., Zeh, A., Frimmel, H.E. and Gerdes, A., 2010. New constraints on the auriferous Witwatersrand sediment provenance from combined detrital zircon U–Pb and Lu–Hf isotope data for the Eldorado Reef (Central Rand Group, South Africa). Precambrian Res. 183, 817–824.

Kositcin, N. and Krapež, B., 2004. Relationship between detrital zircon age-spectra and the tectonic evolution of the Late Archaean Witwatersrand Basin, South Africa. Precambrian Res. 129, 141–168.

Kyle, J.R., Mote A.S. and Ketcham, R., 2008. High resolution X-ray computed tomography studies of Grasberg porphyry Cu-Au ores, Papua, Indonesia. Miner. Depos. 43, 519–523.

Leahy, M.J, Davidson, M.R. and Schwarz, M., 2007. A model for heap bioleaching of chalcocite with heat balance: mesophiles and moderate thermophiles. Hydrometallurgy 85, 24–39.

Lim, I.L., Voight, W. and Weller, K., 1996. Product size distribution and energy expenditure in grinding minerals and ores in high pressure rolls. Int. J. Miner. Process. 44-45, 539–559.

Lim, W.I.L., Campbell, J.J. and Tondo, L., 1997. The effect of rolls speed and rolls surface on high pressure grinding rolls performance. Miner. Eng. 10, 401–419.

Ling, P, Papangelakis, V. G, Argyropoulos, S. A. and Kondos, P.D., 1996. An improved rate equation for cyanidation of a gold ore. Can. Metall. Q. 35, 225–234.

Liu, G.Q. and Yen, W., 1995. Effects of sulfide minerals and dissolved oxygen on the gold and silver dissolution in cyanide solution. Miner. Eng. 8, 111–123.

Longley, R.J., Katsikaros, N. and Hillman, C., 2002. A New Age Gold Plant Flowsheet for the Treatment of High Grade Ores. AusIMM - Metall. Plant Des. Oper. Strateg. Conf. April.

Lorenzen, L and van Deventer, J.S.J., 1992. Electrochemical interactions between gold and its associated minerals during cyanidation. Hydrometallurgy 30, 177–194.

Lotter, N.O., 2011. Modern Process Mineralogy: An integrated multi-disciplined approach to flowsheeting. Miner. Eng. 24, 1229–1237.

Lotter, N.O., Di Feo, A., Kormos, L.J., Fragomeni, D. and Comeau, G., 2010. Design and measurement of small recovery gains – a case study at Raglan concentrator. Miner. Eng. 23, 567–577.

Lowe, D.R. and Byerly, G., 2007. An overview of the geology of the Barberton Greenstone Belt and vicinity: Implications for early crustal development. Van Kranendonk, M.J., Smithies, R.H. Bennett, V.C. (Eds). Earth's Oldest Rocks. Dev. Precambrian Geol. 15, 481-526. Elsevier, Amsterdam.

Mambane, P., 2009. The Elsburg Reef Subcrop. Kusasalethu Gold mine Intern. report, Harmon. Gold. 1–13.

Manzi, M.S.D., Hein, K., King, N., Durrheim, R.J., Manzi, M.S.D., Hein, K.A.A., King, N. and Durrheim, R., 2013. Neoarchaean tectonic history of the Witwatersrand Basin and Ventersdorp Supergroup: New constraints from high-resolution 3D seismic reflection data. Tectonophysics 590, 94–105.

Marsden, J and House, I., 2006. The Chemistry of Gold Extraction . Soc. Mining, Metall. Explor. http://books.google.co.za/ (accessed 1.12.13).

Marsden, J. O. and House, C.I., 1992. The Chemistry of Gold Extraction, 2nd ed. Littleton, CO: Society for Mining, Metallurgy and Exploration, Inc., Ellis Horwood, England.

McKay, N., Wilson, S. and Lacouture, B., 2007. Ore characterisation of the Aqqaluk deposit at Red Dog. In: Proc. Canadian Mineral Processors, Ottawa, January 23–25 5, 55–74.

McKibben, M.A., 2005. Gold and its chemical properties. Elsevier Science, Carlifonia, USA.

Miller, J., Lin, C., 2009. High Resolution X-ray Micro CT (HRXMT) - Advances in 3D Particle Characterization for Mineral Processing Operations. in Recent Advances in mineral Processing Plant Design, D. Malhotra, P.R. Taylor, E. Spiller, and M. LeVier, eds., SME, Littleton, Colorado, pp. 48-59., 12/2009.

Mining-technology., 2013. The top ten deepest mines in the world . 12 Sept. 2013. http://www.mining-technology.com/features/feature-top-ten-deepest-mines-world-south-africa/ (accessed 11.22.13).

Mngoma, L., 2012. A gold , uranium and thorium deportment analysis of Witwatersrand ore from cooke section , Rand Uranium RANDFONTEIN. University of Johannesburg.

Moreno, L, Martinez, J and Casas, J., 1999. Modelling of bioleaching copper sulphide ores in heaps or dumps. Process Met. 9, 443–453.

Morley, C., 2010. HPGR-FAQ. J. South. African Inst. Min. Metall. 110, 107–115.

Napier-Munn, T.J., Morrell, S., Morrison, R.D. and Kojovic, T., 1996. Mineral Comminution Circuits, Their Operation and Optimisation. Julius Kruttschnitt Mineral Research Centre. Indooroopilly, Aust. 413.

Ntsele, C. and Sauermann, G., 2007. HPGR technology – the heart and future of the diamond liberation processing. SAIMM.

Ogbonna, N., Petersen, J. and Laurie, H., 2006. An agglomerate scale model for the heap bioleaching of chalcocite. J. South African Inst. Min. Metall. 106, 433–442.

Oosthuyzen, E., 1985. Image analysis of gold-bearing ores and products. Mintek 50—International Conf. Miner. Sci. Technol. Counc. Miner. Technol.

Patzelt, N, Knecht, H. and Baum, W., 1995. Case made for high-pressure roll-grinding in gold plants. J. Min. Eng. 47, 524–529.

Petersen, J. and Dixon, D.G., 2007. Modelling zinc heap bioleaching. Hydrometallurgy 85, 127–143.

Ramdohr, P., 1957. Die Pronto Reaktion, Neues Jahrbuch fur Mineralogie. Monatshefte, Jahrgang 10, 217–222.

Ramdohr, P., 1958. New observations on the ores of Witwatersrand in South Africa and their genetic significance. Transvaal Geol. Soc. South Africa, Annex. 61, 1–50.

Ramdohr, P., 1969. The ore minerals and their overgrowths, 3rd ed. Pergamon Press, Oxford.

Rand, D.A., 1977. Oxygen reduction on sulphide minerais: Part II Comparison of activities of Vanous copper, iron, lead and nickel minera1 electrodes. J. Electroanal Chem 83, 19–32.

Robb, L.C. and Meyer, M., 1995. The Witwatersrand Basin, South Africa: geological framework and mineralization processes. Ore Geol. Rev. 10, 67–94.

Robert, F., Poulsen, K.H. and Dubé, B., 1997. Gold deposits and their geological classification, in: Gubins, A.G. (Ed.), Poceedings of Exploration'97: Fourth Decennial International Conference on Mineral Exploration. pp. 209–220.

Robertson, S., 2008. Progression of Metallurgical Testwork during Heap Leach Design. www.saimm.co.za/conferences/Hydro2009/Robertson.ppt (accessed 11.25.13).

Robertson, S.W., Vercuil, A., van Staden, P.J. and Craven, P., 2005. A Bacterial Heap Leaching Approach for the Treatment of Low Grade Primary Copper Sulphide Ore. 3rd S. African Conf. Base Met. Symp 471–484.

Roels, S. and Carmeliet, J., 2006. Analysis of moisture flow in porous materials using microfocus X-ray radiography. Int. J. Heat Mass Transf. 49, 4762–4772.

Rollinson, G.K., Andersen, J.C.Ø., Stickland, R.J., Boni, M. and Fairhurst, R., 2011. Characterisation of non-sulphide zinc deposits using QEMSCAN®. Miner. Eng. 24, 778–787.

Rosario, P., Hall, R., Grundy, M. and Klein, B., 2011. A preliminary investigation into the feasibility of a novel HPGR-based circuit for hard, weathered ores containing clayish material. Miner. Eng. 24, 290–302.

Rosario, P.P, Boyd, K. and Grundy, M., 2009. Recent trends in the design of comminution circuits for high tonnage hard rock mining., in: Recent Advances in Mineral Processing Plant Design. Society for Mining, Metallurgy, and Exploration, Inc. (SME), pp. 347–355.

Rose, P.A., 1983. Stratigraphy, lithology and sedimentology of the Elsburg reefs at Elandsrand gold mine. Carletonville.

Roufail, R., 2011. The effect of stirred mill operation on particle breakage mechanism and their morphological features. Dep. Min. Eng. Univ. Br. Columbia, Vancouver. PhD thesis.

Sánchez-Chacón, E. and Lapidus, G.T., 1997. Model for heap leaching of gold ores by cyanidation. Hydrometallurgy 44, 1–20.

Saramak, D. and Kleiv, R.A., 2013. The effect of feed moisture on the comminution efficiency of HPGR circuits. Miner. Eng. 43-44, 105–111.

Schaefer, B.F., Pearson, D.G., Rogers, N.W. and Barnicoat, A.C., 2010. Re–Os isotope and PGE constraints on the timing and origin of gold mineralisation in the Witwatersrand Basin. Chem. Geol. 276, 88–94.

Schmid, G. and Corain, B., 2003. Nanoparticulated Gold: Syntheses, Structures, Electronics, and Reactivities. Eur. J. Inorg. Chem. 2003, 3081–3098.

Schonert, K., 1988. first survey of grinding with high-pressure compression roller mills. Int. J. Miner. Process. 22, 401.

Silver, M., 1994. Target self-attenuation extension to the Desorby and Boyer thick-target bremsstrahlung spectrum. Med. Phys. 21, 577–579.

Solomon, N., Becker, M. and Mainza, A., 2011. Understanding the influence of HPGR on PGM flotation behavior using mineralogy. Miner. Eng. 24, 1370–1377.

Sowerby, B.D., Cutmore, N.G., Liu, Y., Peng, H., Tickner, J.R., Xie, Y. and Zong, C., 2009. Recent Developments in Fast Neutron Radiography for the Interrogation of Air Cargo Containers 4–8.

Stanford, W., 1987. Amax Sleeper mine exceeds expectations on all counts as low cost gold producers. Min. Eng. April 241–246.

Stephenson, I., 1997. The downstream effects of high pressure grinding rolls processing. Jul. Kruttschnitt Miner. Res. Center. University of Queensland, Australia. PhD thesis.

Steven, N., 2009. Potential in situ leach exploitation of back-filled Witwatersrand gold mines: parameters and flow-rate calculations from a Zambian Copperbelt analogue. SAIMM. 193–196.

Stewart, D.F. and Ramsay, P., 1993. Improving the simple sluice box. Int. J. Miner. Process. 39, 119–136.

Tavares, L., 2007. Particle weakening in high pressure roll grinding. Miner. Eng. 18, 651–657.

Teague, J., Van Deventer, J.S.J. and Swaminathan, C., 1999. A conceptual model for gold flotation. Miner. Eng. 12, 1001–1019.

Thiel, R. S. and Smith, M.E., 2003. State of the practice review of heap leach pad design issues. Proc. GRI-18, Las Vegas, Nevada, USA 22, 555–568.

Thomas J.E. and Smart R.S.C., 2000. Kinetic factors for oxidative and non-oxidative dissolution of iron sulfides. Miner. Eng. 13, 1149–1159.

Thompsen, L, Patzelt, N. and Knecht, J., 1996. High-pressure grinding for copper at three dimensional liberation analyses in the 21st century. Int. J. Mineral. 272–277.

Tinker, J., De Wit, M. and Grotzinger, J., 2002. Seismic Stratigraphic Constraints on NeoArchaean -Paleoproterozoic Evolution of the Western Margin of the Kaapvaal Craton, South Africa. South African J. Geol. 105, 107–134.

Trexler, D. T., Flynn, T. and Hendrix, J., 1987. Enhancement of Previous Metal Recovery by Geothermal Heat. Geotherm. Resour. Counc. Trans. 11, 15–21.

Trexler, D. T., Flynn, T. and Hendrix, J., 1990. Preliminary Results of Column Leach Experiments at Two Gold Mines Using Geothermal Fluids. Geotherm. Resour. Counc. Trans. 14, 351–358.

Triffett, B., Veloo, C., Adair, B.J.I. and Bradshaw, D., 2008. An investigation into the recovery of molybdenite in the Kennecott Utah Copper bulk flotation circuit. In: Minerals Engineering, "'Flotation 2007'". 832–840.

University of Texas Computed Tomography (UCTC)., 2013. About High-resolution X-ray CT . http://www.ctlab.geo.utexas.edu/overview (accessed 11.22.13).

Valery, W., Jankovic, A., Valle, R., Nozawa, E. and Duffy, K., 2010. Metso process technology and innovation – "Review and optimisation of the Yanacocha grinding circuit."

Van der Lee, J., 2008. Mining of valuable metals: In situ and heap leaching. Fontainebleau, France.

Vorster, B.J. and Flatman, S.R., 2001. Cyanide control in the metallurgical process of gold extraction in. SAIMM 359–366.

Wang, W and Poling, G.., 1983. Methods for recovering fine placer gold. CIM Bull. 76, 47–56.

Wang, Y and Forssberg, E., 2007. Enhancement of energy efficiency for mechanical production of fine and ultra-fine particles in comminution. China Particuology 5, 193–201.

Weiss, N., 1985. SME mineral processing handbook. New York Soc. Min. Eng. 2.

Weller, K.R., Campbell, J.J., Wilkie, G., Thornber, M.R., B., R. and Ellis, S., 1998. The Ores of the golden mile, Kalgoorlie: coherent metallurgical testwork from comminution, through flotation, roasting and leaching, to mineralogical determination of key mineral deportments using QEM*SEM. AusIMM 98—The Min. Cycle, Mt. ISA, AusIMM.

Wipf, E., 2005. Relating HPGR specific energy efficiency to work index. Perth, Australia.

Withjack, E., 1988. Computed tomography for rock-property determination and fluid-flow visualization. SPE Form. Eval. 3, 696–704.

Wong Wai, L.E. and Arun, M., 2009. Gold Extraction and Recovery Processes. Faculty of Engineering, National University of Singapore.

Zanbak, C., 2012. Heap leaching technique in mining with the context of best available techniques (BAT). euromines 1–33.

Zhou, J., Jago, B. and Martin, C., 2004. Establishing the process mineralogy of gold ores. SGS Miner. Tech. Bull. 2004-03 1–16.

APPENDICES

Appendix I: Chemical assay of different HPGR pressure setting and size fractions (mm) using XRF (%).

	60 Bar -1.0	60 Bar +4	60 Bar +11.2	90 Bar -1.0	90 Bar +4	90 Bar +11.2	120 Bar -1.0	120 Bar +4	120 Bar +11.2
SiO2	82.32	80.49	79.74	83.27	81.11	79.11	83.50	80.08	79.34
TiO2	0.37	0.45	0.46	0.34	0.43	0.53	0.33	0.49	0.43
Al2O3	7.06	7.64	7.69	7.22	8.08	8.24	7.15	7.99	8.60
Fe2O3	3.95	4.59	5.17	3.51	4.43	4.51	3.49	4.67	4.77
MnO	0.04	0.04	0.04	0.03	0.04	0.05	0.03	0.04	0.04
MgO	0.79	1.13	1.04	0.82	1.03	1.34	0.66	1.38	1.02
CaO	0.60	1.01	0.72	0.57	0.63	1.27	0.57	0.77	0.59
Na2O	0.57	0.61	0.31	0.36	0.33	0.35	0.35	0.39	0.38
K2O	1.44	1.52	1.64	1.47	1.61	1.52	1.49	1.56	1.69
P2O5	0.06	0.07	0.07	0.05	0.06	0.08	0.06	0.07	0.06
SO3	0.10	0.29	0.07	0.09	0.08	0.13	0.13	0.15	0.10
Cr2O3	0.04	0.04	0.05	0.03	0.04	0.03	0.04	0.04	0.05
NiO	0.01	0.01	0.02	0.01	0.01	0.01	0.01	0.01	0.01
H2O-	0.11	0.04	0.05	0.03	0.03	0.03	0.00	0.00	0.02
LOI	1.83	1.98	2.41	1.79	1.93	1.88	1.76	1.85	2.41
Total	99.28	99.92	99.48	99.61	99.85	99.09	99.58	99.50	99.52

Appendix II: Size by size bulk mineralogy obtained using QEMSCAN in wt. %

Mineral	Combined	-150/+106 µm	-106/+75 µm	-75/+38 µm	-38/+0 µm
Pyrite	2.2	2.8	1.9	2.4	2.0
Pyrrhotite	2.5	1.8	2.2	2.9	2.7
Other sulphides	0.2	0.1	0.2	0.3	0.3
Carbonates	0.5	0.4	0.4	0.6	0.6
Quartz	71.1	78.7	81.2	79.1	64.5
Feldspar	3.2	3.2	2.7	3.0	3.3
Mica	12.3	6.5	6.1	5.3	17.1
Chlorite	5.0	3.9	3.2	3.9	6.1
Sphene	0.9	1.0	0.8	1.0	0.8
Fe-oxides / hydroxides	1.6	1.6	1.3	1.3	1.8
Others	0.6	0.2	0.3	0.3	0.9

Appendix III: Witwatersrand gold ore Sulphur concentration

HPGR Product	Method	Mass	Sulphur (%)	Sulphur (ppm)
90 bar+4 mm	GS 905-5 (5.14 %)	0.18	0.92	9231
60 bar-1 mm	GS 905-5 (5.14 %)	0.19	1.47	14681
120 bar+11.2 mm	GS 905-5 (5.14 %)	0.20	1.88	18849
60 bar+11.2 mm	GS 905-5 (5.14 %)	0.21	2.40	23977
120 bar rpt+11.2 mm	GS 905-5 (5.14 %)	0.21	0.47	4727
120 bar rpt-1 mm	GS 905-5 (5.14 %)	0.20	1.62	16221
120 bar rpt+4 mm	GS 905-5 (5.14 %)	0.20	0.69	6944
120 bar+4 mm	GS 905-5 (5.14 %)	0.20	0.76	7633
90 bar+11.2 mm	GS 905-5 (5.14 %)	0.21	0.23	2280
60 bar+4 mm	GS 905-5 (5.14 %)	0.21	1.85	18464
90 bar-1 mm	GS 905-5 (5.14 %)	0.20	8.38	8380
120 bar-1 mm	GS 905-5 (5.14 %)	0.21	0.89	8866

Appendix IV: Photographs of hand specimens obtained from underground channel mapping and sampling

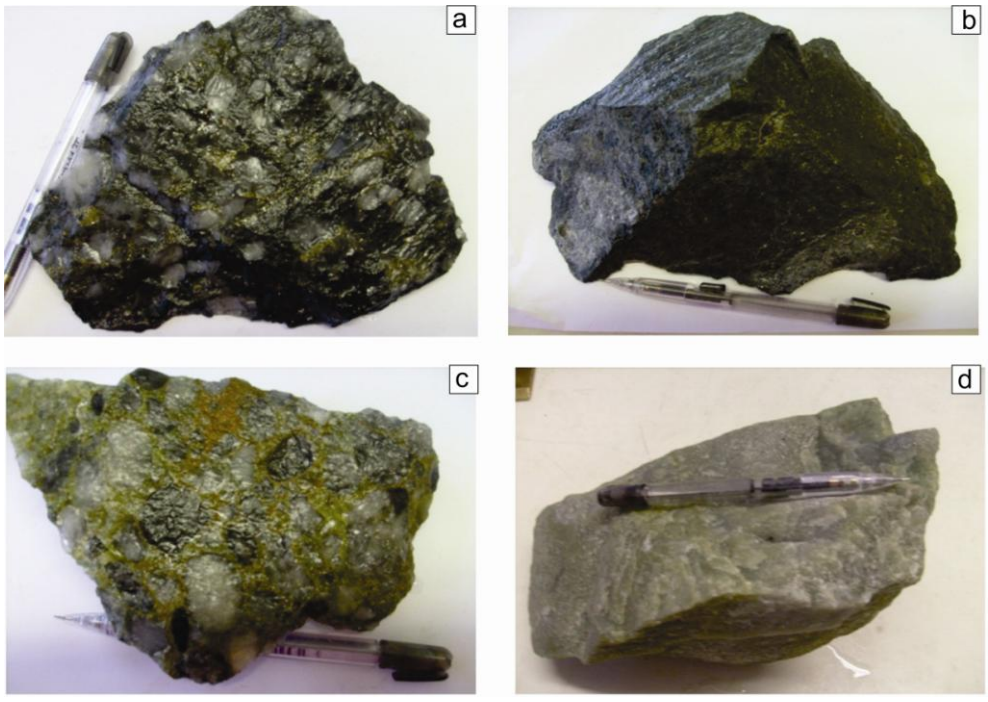

a) The VCR terrace-complex 5: Matrix supported quartz pebble conglomerate; b) The VCR hanging wall metabasalt with amygdales; c) The ER: Reworked matrix supported conglomerate; and d) Fine to medium grained footwall quartzite.

Appendix V: The VCR and ER Channel sampling gold distribution

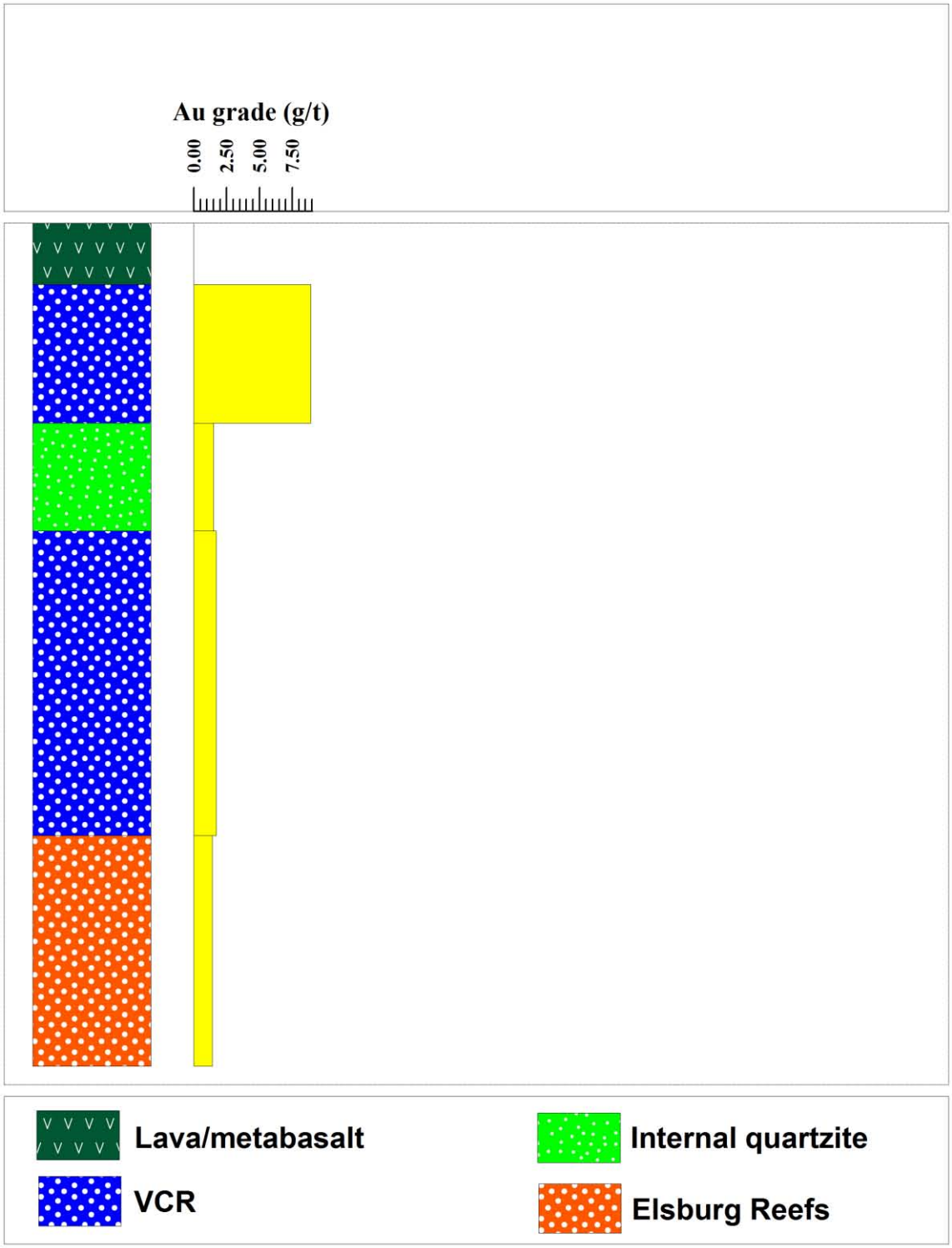

Appendix VI: Overview of different litho-facies uranium distribution trends

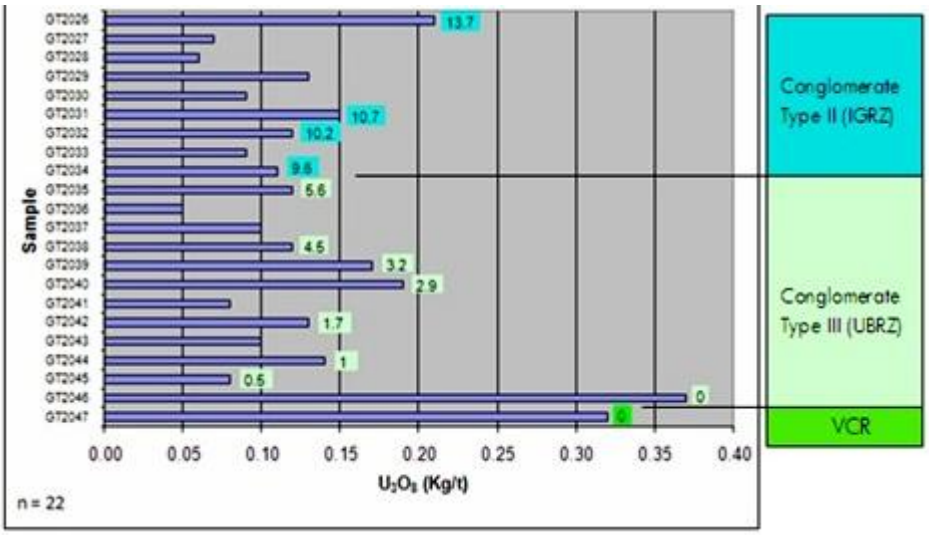

Appendix VII: Overview of different litho-facies gold distribution trends

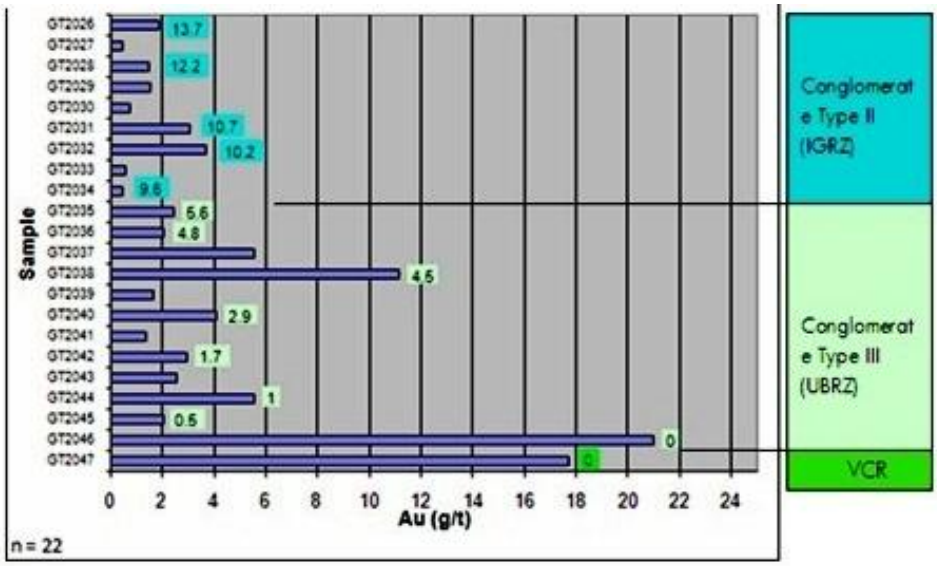

Appendix VIII: HPGR prepared Witwatersrand gold ore

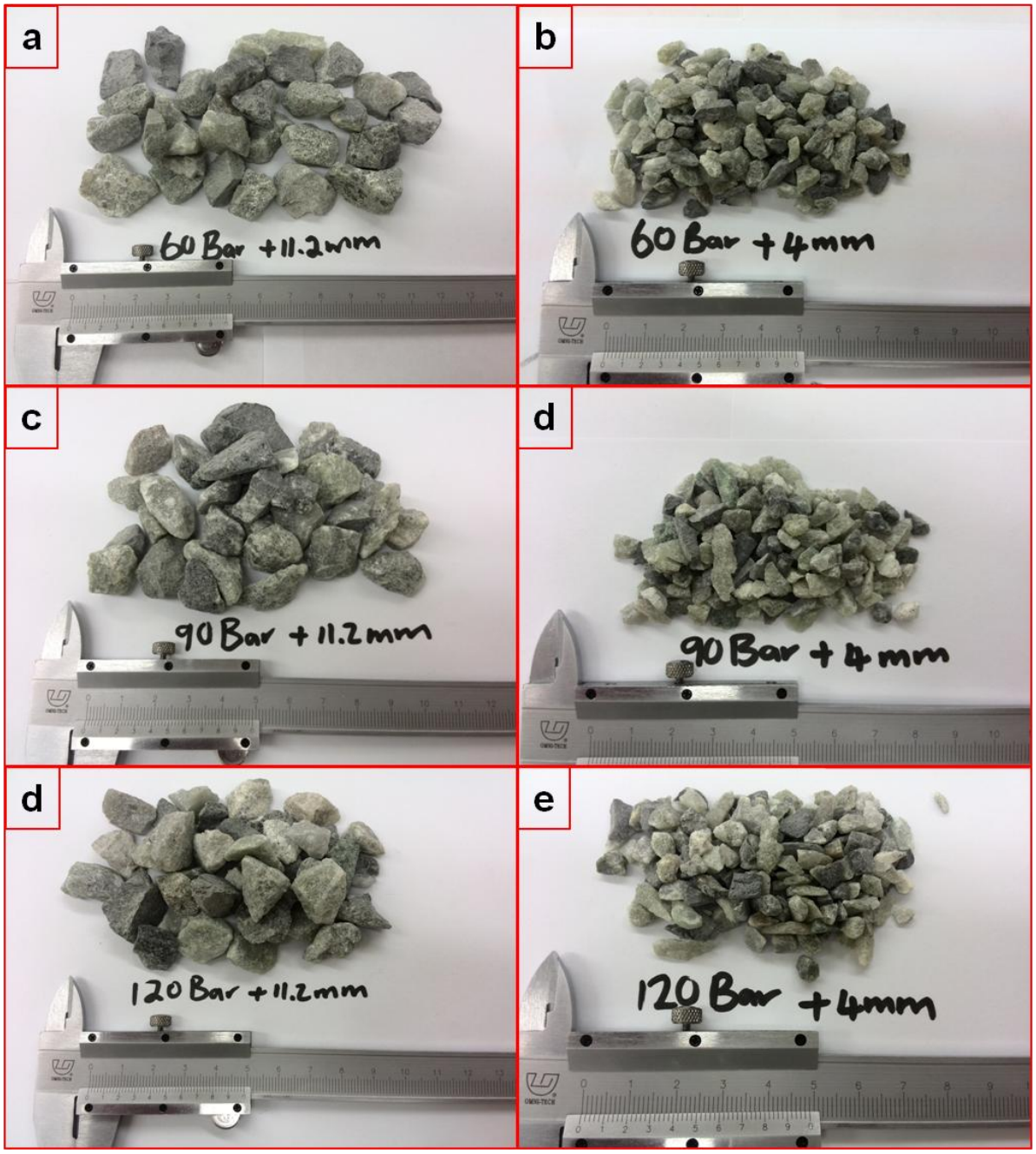

a) 60 Bar large particles; b) 60 Bar small particles; c) 90 Bar large particles; d) 90 Bar small particles; e) 120 Bar Large particles; and f) 120 bar small particles.

Appendix IX: QEMSCAN field images

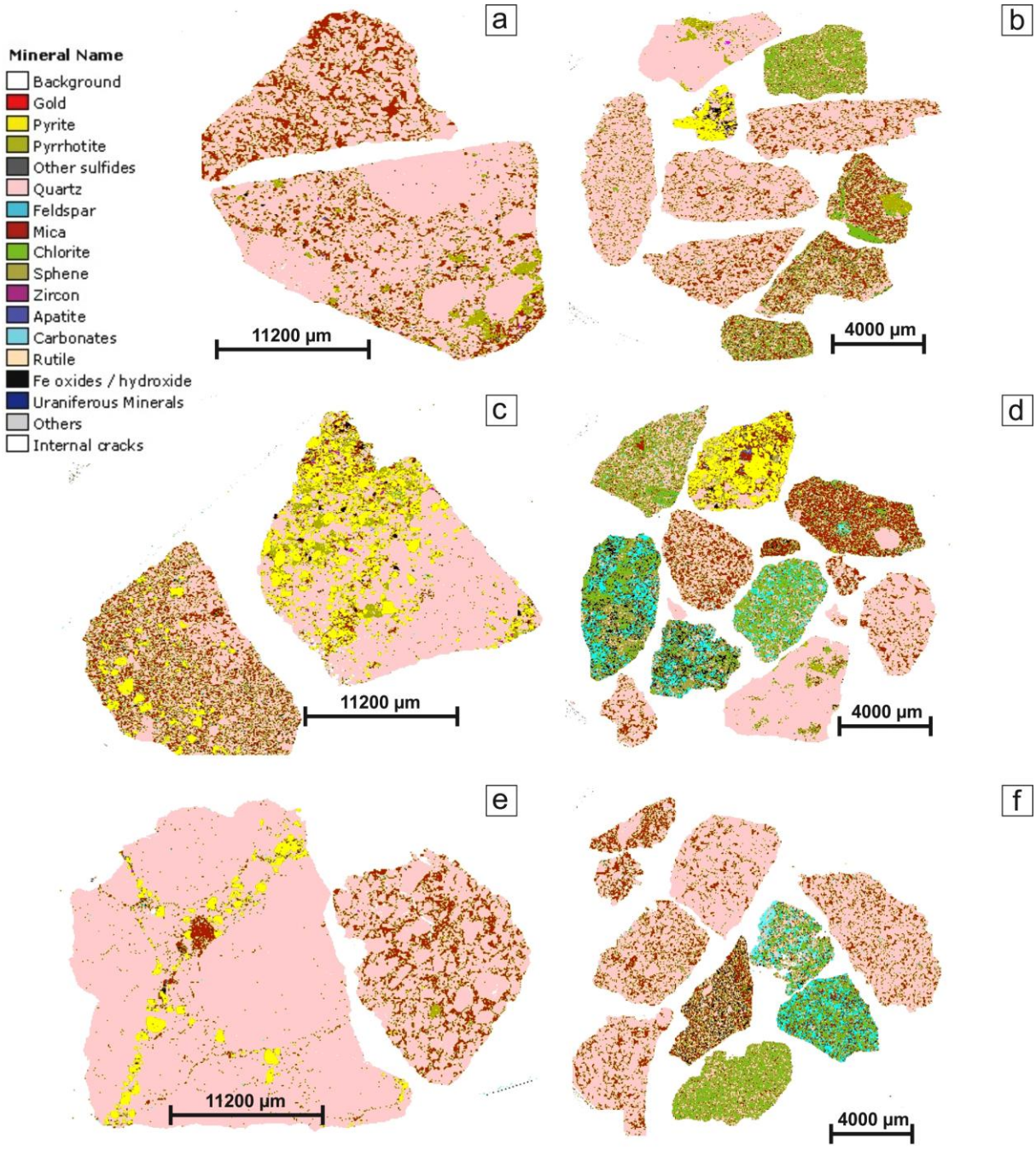

b) 60 Bar large particles; b) 60 Bar small particles; c) 90 Bar large particles; d) 90 Bar small particles; e) 120 Bar Large particles; and f) 120 bar small particles.

Appendix X: Selected QEMSCAN trace mineral search

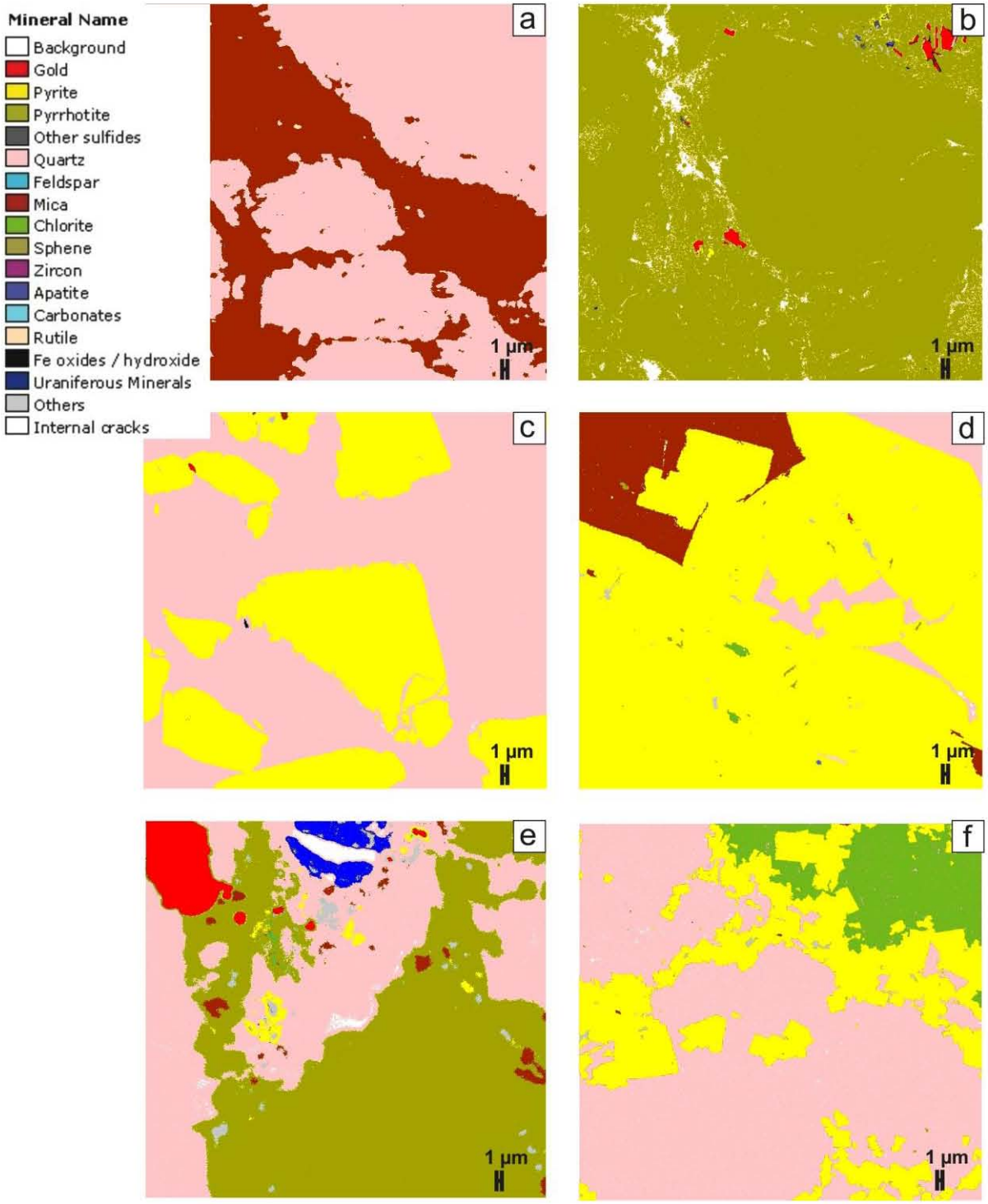

a) 60 Bar large particles; b) 60 Bar small particles; c) 90 Bar large particles; d) 90 Bar small particles; e) 120 Bar Large particles; and f) 120 bar small particles.

Appendix XI: X-ray CT 3D gold distribution and image classification

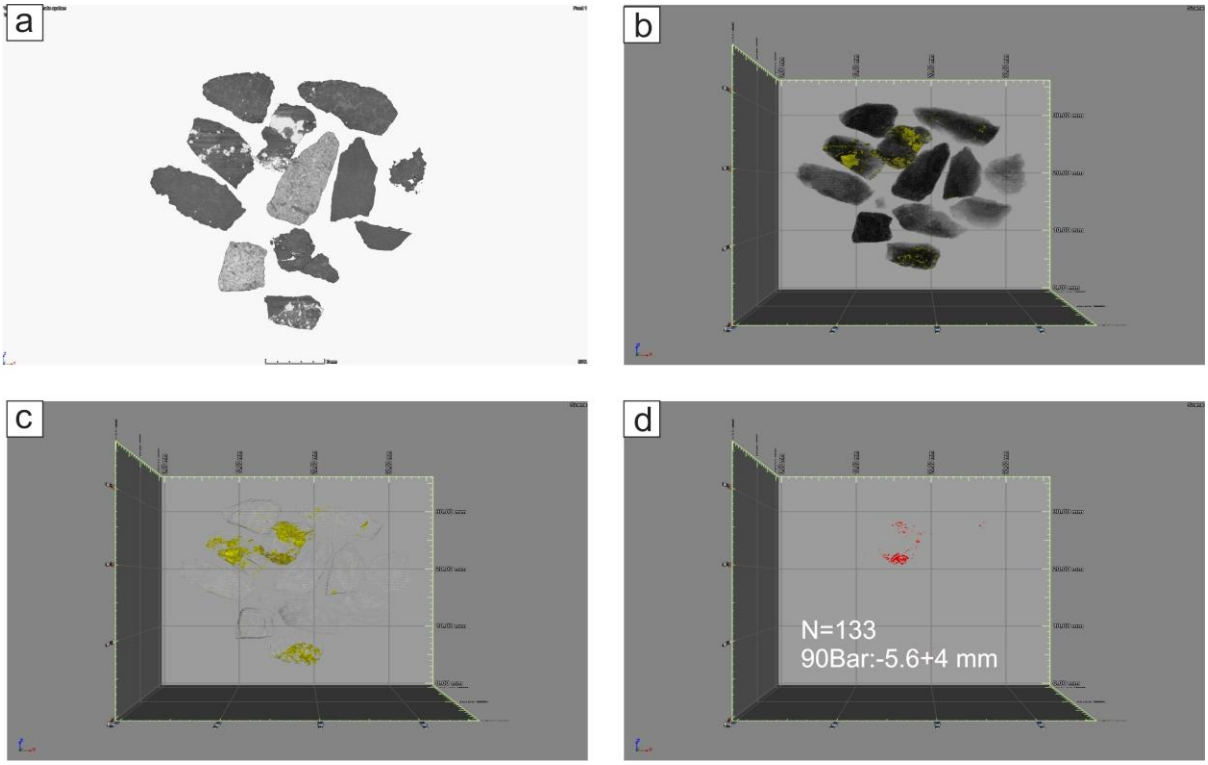

90 Bar small particle gold distribution: a) grey scale image; b) false colour image (yellow=sulphides; red= gold; grey= silicates); c) Transparent view of silicates in order to create a clear view of sulphides; and d) Gold distribution.

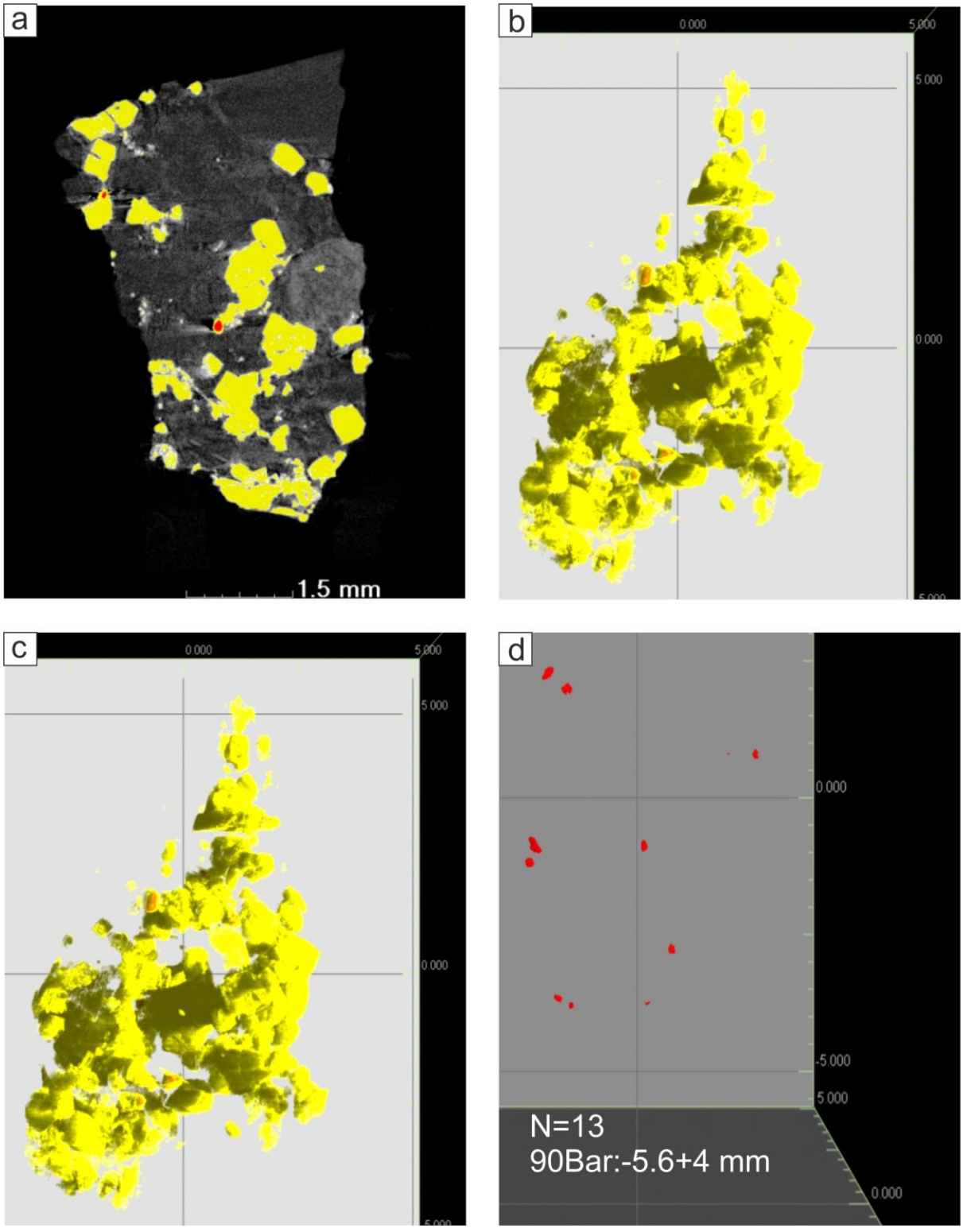

90 Bar small particle gold distribution: a) false colour image (yellow=sulphides; red= gold; grey= silicates); b and c) Transparent view of silicates in order to create a clear view of sulphides; and d) Gold distribution.

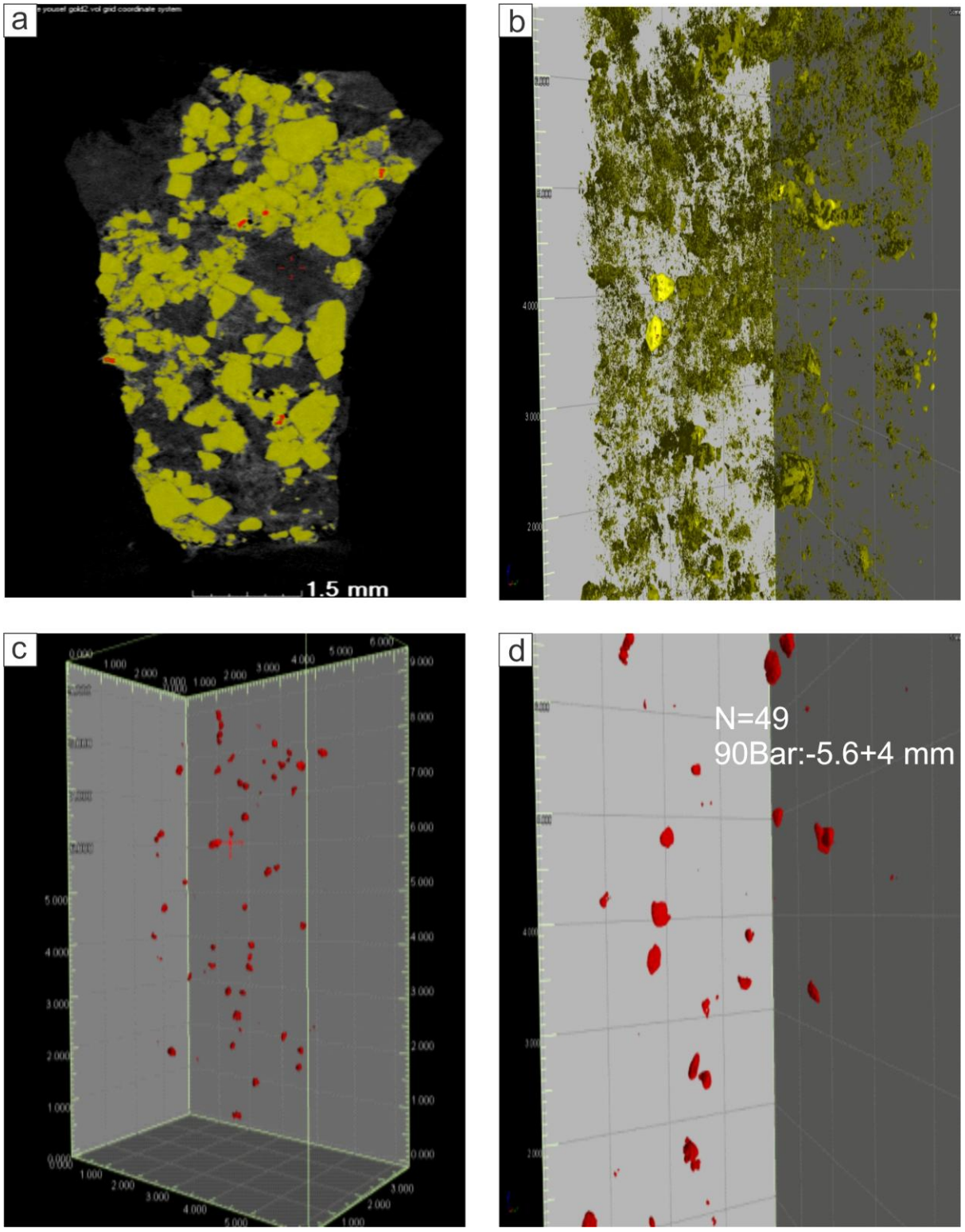

90 Bar small particle gold distribution: a) false colour image (yellow=sulphides; red= gold; grey= silicates); b) Transparent view of silicates in order to create a clear view of sulphides; c and d) Gold distribution and morphology.

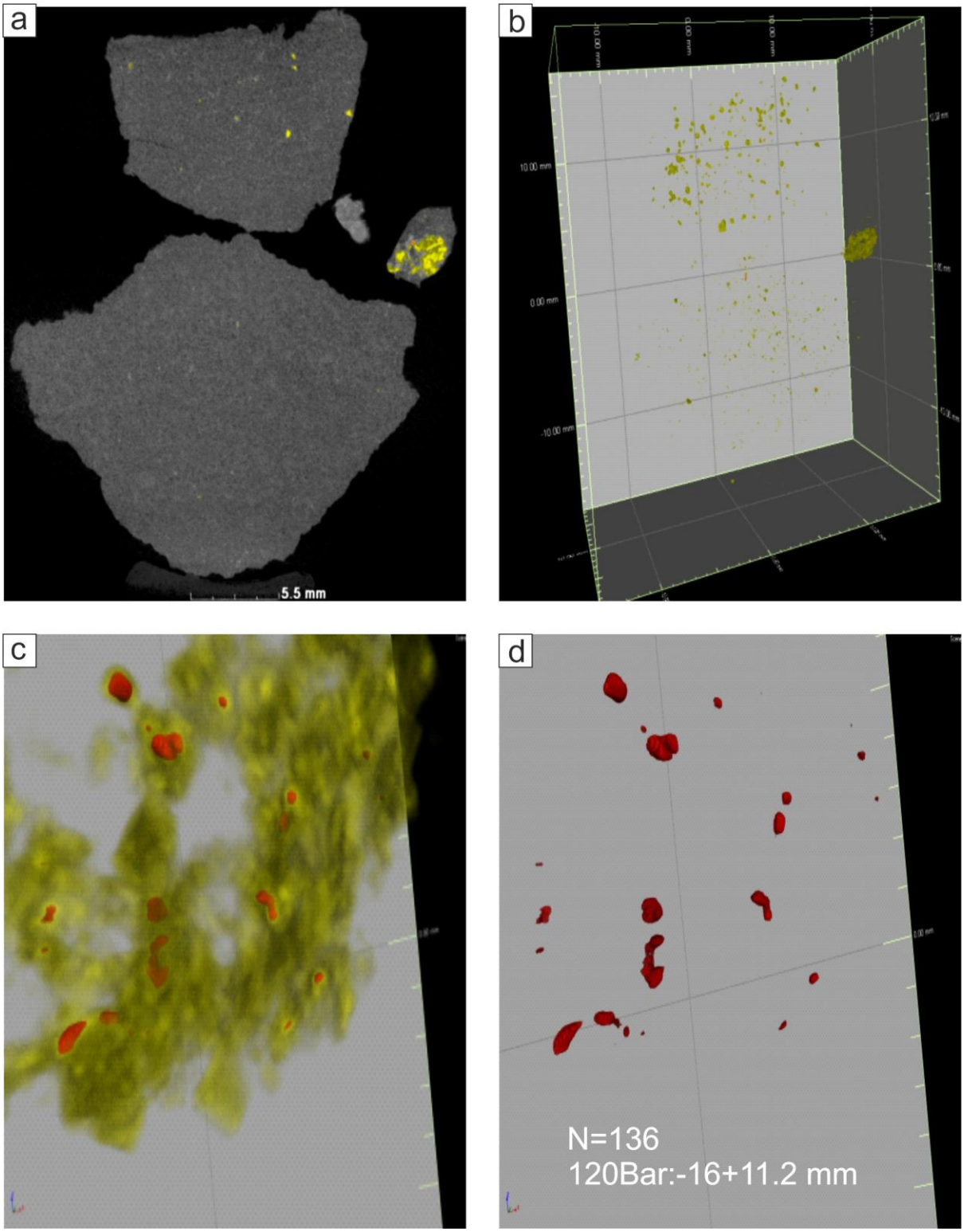

120 Bar large particle gold distribution: a) false colour image (yellow=sulphides; red= gold; grey= silicates); b) Transparent view of silicates in order to create a clear view of sulphides; c) Transparent view of sulphides in order to create a clear view of gold; and d) Gold distribution and morphology.

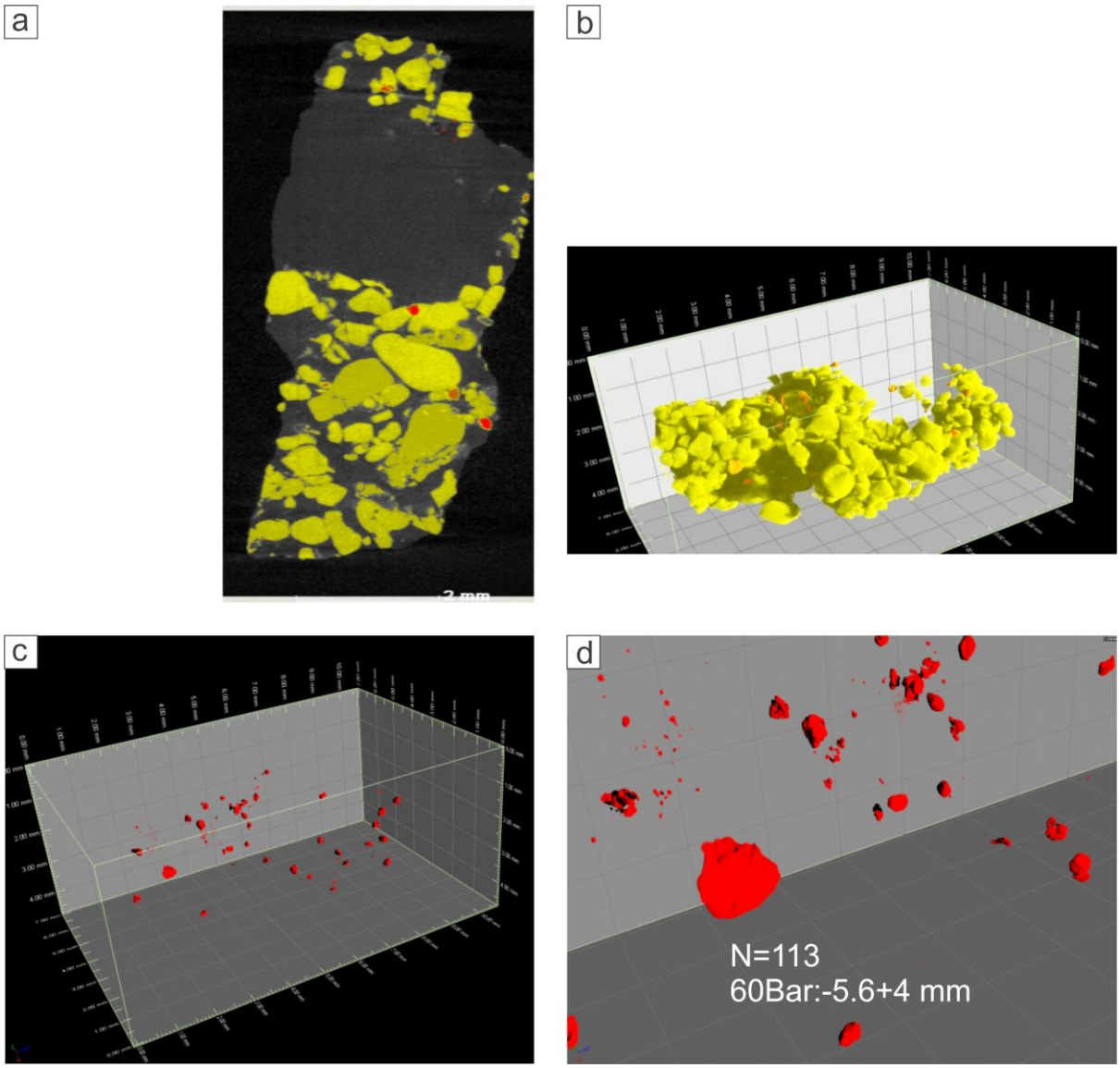

60 Bar small particle gold distribution: a) false colour image (yellow=sulphides; red= gold; grey= silicates); b) Transparent view of silicates in order to create a clear view of sulphides; c and d) Gold distribution and morphology.

Appendix XII: Laboratory leaching experiments procedure

i. Introduction

Cyanide (CN) is a single carbon atom with a triple bond to a nitrogen atom that is useful in extracting gold (Au) from the ore through a process called “gold cyanidation” or “the cyanide process”. Cyanide is universally used because of its relatively low cost and great effectiveness for gold dissolution. While cyanide is both economical and effective; the use and transportation poses a significant environmental as well as human risks due to its toxicity. Despite the toxic nature of cyanide all hydrometallurgical operations take place in open reactor vessels (open heaps, tanks and vats), with the exception of pressure cyanidation. This indicates as to how well cyanide risk management has developed over time. The question now remains to demonstrate how well cyanide risk management techniques employed in industry and specialist laboratories.

ii. Risk management

There are risks associated with the use of cyanide; therefore, this section purposes to outline these risks which the individuals working with it may be subjected to. The safety measures that were taken when using cyanide are outlined.

iii. Health risks

Cyanide compounds are classified as toxic and hazardous substances that can lead to fatality when exposed to sufficiently high doses. Cyanide is a fast-acting poison capable of killing a person within minutes when ingested in high volumes. Oxygen is prevented from being used by the cells, causing tissue hypoxia and cyanosis, as a result, the respiratory system fails to feed the cells with oxygen and if left untreated can cause a fast, deep breathing followed by convulsions, loss of consciousness and suffocation. Humans are exposed to cyanide through the skin, by inhalation and ingestion. The symptoms for cyanide poisoning include dizziness, numbness, headache, rapid pulse, nausea, reddened skin, and bloodshot eyes. Prolonged exposure results in vomiting, laboured breathing, followed by unconsciousness; cessation of breathing, rapid weak heart beat and death. Severe exposure by inhalation can cause immediate unconsciousness.

I**nhalation**: Hydrogen Cyanide (HCN) gas is the most toxic form of cyanide. The inhaled threshold limit for HCN is 4.7 ppm. After several hours, respiratory distress may be experienced when the concentrations of 20 to 40 ppm of HCN is present in the air and is

inhaled. Exposure to 50 ppm causes disturbances within an hour and 100 ppm is dangerous for exposures of 30 to 60 minutes and 300 can be rapidly fatal. Death occurs in minutes at HCN concentrations above approximately 250 ppm in air.

Skin Absorption: Normal skin absorbs HCN slowly, but nonetheless 2 % HCN in air may cause poisoning in 3 minutes, 1 % is dangerous in 10 minutes and 0.0 5 % may produce symptoms after 30 minutes.

Ingestion: Lethal dosage to humans by ingestion ranges from 50 to 200 mg (1 to 3 mg of free cyanide per kg body mass) for free cyanide.

The experiments in this study used 250 m*l* of sodium cyanide solution at concentration of 0.5 M. This means there was the following amount of cyanide for reaction:

$$0.00407Mx7lx49.09 = 1.3986g$$

Looking at the reaction between cyanide and acid to produce HCN:

$CN^- + H+ \rightarrow HCN$

This represents a 1 to 1 molar ratio; hence from 1.3986 g of sodium cyanide, the following amount of HCN will be evolved:

$$\frac{1.3986x27.03}{49.09} = 0.7701g$$

This amounts to 770 mg of HCN in a 7 *l* column. Taking the immediate area of exposure to the investigator as 1 m3; this amounts to a concentration of 770 mg/ 1000 *l* or 0.7701 ppm. This figure is below the maximum average safe exposure limit, and can only reach this level if all the cyanide is converted i.e. this is the maximum concentration it can reach.

iv. Risk containment measures

The Investigator: Gloves, eye goggles, half mask (protection against vapour, gas and dust particles) and a lab coat was employed when handling the salts and solutions. All handing of salts and solutions took place in the fume hood; this included all experimental procedures-preparation and standardisation of solutions, leaching, sampling, filtering, and transferring waste solutions to 25 *l* disposal containers. Containers containing solutions or salts were kept closed when not in use. The 25 *l* disposal containers were additionally kept in a heavy duty plastic bag as secondary containment. All glassware was rinsed with EDTA and a bicarbonate solution to remove any metal ions and acidic residues before using them for the

cyanide solutions. All solutions were prepared using a buffered water recipe obtained from Mintek's Cyanide Research Centre. A cyanide anti-dote kit was kept within reach

Individuals sharing the work space: All students and staff working in the vicinity were informed before working with the cyanide and briefed on the warning signs and first aid measures for dealing with cyanide exposure. The salts were kept in the laboratory safe where access is restricted. Periodic material balances were carried out on the salts, accounting for what has been used and what remains. All stored containers having cyanide solutions were clearly labelled showing the contents, concentration and warning of the hazard. A Materials Safety Data Sheet (MSDS) and warning labels were put up in the area where the experimental work is being conducted. The lab coat used by the investigator was being hung in the lab coat wardrobe in a heavy duty plastic bag.

v. First Aid measures

Eye Contact: Immediately flush eyes with plenty of water for at least 15 minutes. Cold water may be used. Get medical attention immediately.

Skin Contact: Immediately flush skin with plenty of water for at least 15 minutes while removing contaminated clothing and shoes. Cover the irritated skin with an emollient or apply cold water. Wash clothing before reuse. Thoroughly clean shoes before reuse. Get medical attention immediately.

Serious Skin Contact: Wash with a disinfectant soap and cover the contaminated skin with an anti-bacterial cream. Seek immediate medical attention.

Inhalation: If inhaled but victim is conscious and speaking, with a gas mask and goggles on, remove victim to fresh air. If the victim is unconscious but breathing, break an ampul of amyl nitrite in a cloth and hold it under the victim's nose for 15 s. Repeat five or six times. Use a fresh ampul every 3 min. Continue until the victim regains consciousness. Amyl nitrite is a powerful cardiac stimulant and should not be used more than necessary. If the patient is not breathing, apply artificial respiration; this can best be done using an oxygen resuscitator. The amyl nitrite antidote should also be administered during resuscitation. Get medical attention.

Ingestion and Serious Inhalation: If swallowed, do not induce vomiting unless directed to do so by medical personnel. Never give anything by mouth to an unconscious person. Loosen tight clothing such as a collar, tie, belt or waistband. Get medical attention

immediately. A suggested procedure for physicians or nurses is intravenous administration of 0.3 g (10 m*l* of a 3 % solution) of sodium nitrite at the rate of 2.5 m*l*/min followed by 12.5 g (50 m*l* of a 25 % solution) of sodium thiosulfate at the same rate. Watch the patient for 24 to 48 h, especially in cases of ingestion or skin absorption. If symptoms reappear, repeat the injections in half the original amounts. These solutions should be kept readily available. In some cases, first aid personnel have been trained to use the intravenous medication subject to government regulations.

vi. Handling and storage

All salt containers were locked away in the safe away from heat and sources of ignition. Container will be kept in well ventilated storage where temperature will not exceed 24^{o}C. All empty salt containers were kept in the safe until they can be passed on the Enviroserv for disposal. Not water will be added to these containers.

vii. Fire risks

Sodium cyanide may be combustible at high temperatures but is flammable in the presence of acids and moisture. It is not known whether there is a risk of explosion in the incidence of mechanical impact or static discharge. But regardless all the above situations will be avoided in storing and handling the salts and solutions. It must be noted that a fire resulting from the salt is dangerous on contact with acids, acid fumes, water or steam as it results in the immediate formation of toxic and flammable vapours of hydrogen cyanide gas and sodium oxide. When the salt is heated it will thermally decompose and emit fumes of hydrogen cyanide and oxides of nitrogen. Small fires can be contained using a dry chemical powder or sand and larger ones using a water spray or foam. If out of control the Fire alarm will be activated and the Emergency number will be dialled.

viii. Accidental release

All salt handling and solution preparations proceeded on a large plastic tray so that in the case of a spill, the salt or solution was transferred from the tray back into the container or disposal container rather than being cleaned from the floor or bench. In case of a solution spill on the floor the area was demarcated with coloured tape or a sign. The solution was mopped up and transferred to assigned container for disposal. The cleaning aids such as the

mop, dust pan and bucket was dedicated, labelled, and isolated for cyanide use. This was communicated to the rest of the laboratory users.

ix. Reactivity and stability risk

Violent reactions occur in contact with fluorine gas, magnesium, nitrates and nitric acid. The hazard of producing toxic and flammable vapours of hydrogen cyanide and sodium oxide come with the contact of cyanide and acids, acid fumes, water, steam; strong oxidisers such as acids, acid salts, chlorates, nitrates and carbon dioxide gas in ordinary air. These compounds will not be allowed to contact the salts or solutions. By far the biggest risk to this project is the formation of hydrogen cyanide gas as a result of any sudden pH change. This was approached through careful pH management. As stated earlier the solutions was prepared using a buffered water recipe obtained from Mintek's Cyanide Research Centre; the glassware was rinsed with EDTA and a bicarbonate solution before use, and all preparations proceeded in the fume cupboard. The experiments were not run concurrently with the low pH experiments in the Iron and sulphur laboratory. Rather a schedule was worked out to allow the cyanide experiments to run without interference. During this period no acids or oxidisers were found in the fume hood.

The experiments conducted for this first phase were for a total duration of 24 hours for which the investigator was present at specific time intervals. Samples were withdrawn at regular intervals allowing for constant pH monitoring. Any drop in pH towards 9.6 was countered with the addition of 6 M Sodium hydroxide solution. The flask was blocked with a stopper, the stopper had a connecting tube which ran and immersed in 2 blocked flasks, in series, containing a solution of hydrogen peroxide with some copper to catalyse the destruction of any hydrogen cyanide gas that may form (conversion to the less toxic cyanate compound).

$$HCN + H_2O_2 \rightarrow HOCN + H_2O$$

To prevent the possibility of any stray reactions in the 25 *L* disposal containers; the containers were rinsed with EDTA and bicarbonate solutions to remove metal ions and any acids and then rinsed with deionised water and allowed to stand and dry before being used to store the waste cyanide solutions. On completion of an experiment, glassware and other equipment were decontaminated by soaking them in a 0.00407M hydrogen peroxide solution for 1 hour. Other equipment such as mops, clothes, paper towels used for cleaning up spills

were stored in heavy duty plastic bags and handed over to Envirotech for disposal. All waste from experimental work (including solutions and solid waste) was handed over to Envirotech for disposal.

x. Preparation of 0.00407 M sodium cyanide solution

For the preparation of a 7 *l* solution of concentration 0.00407 M the following mass of sodium cyanide salt was weighed out into the reactor vessel:

Sodium cyanide molecular weight: 49.01 g/mole

$$mass = 7Lx0.00407Mx49.01 = 1.3963g$$

Buffered water was prepared by dissolving 18.64g Na_2CO_3 and 2.032g $NaHCO_3$ in 7 L of deionised water. The pH of water was measured to ensure it is in the region of 11. The buffered water was added to the cyanide salt in a fume hood ensuring all PPE is being worn. The pH of solution was measured and if it is below 10, it was adjusted with 6 M NaOH solution.

Appendix XIII: Laboratory leaching Results

1. Results from solution preparations

Container number	Vol (*l*)	NaCO3(g)	NaHCO3(g)	NaCN(g)	pH	T(^{o}C)
1	20	93	10.18	4.08	10.72	22
2	25	120.46	19.19	5.12	10.74	21.5
3	25	121.06	20.86	5.09	10.7	21
4	25	123.48	22.24	5.07	10.66	22.7
5	25	121.8	23.04	5.11	10.64	22.3
6	25	120.38	20.04	5.04	10.6	23.9
7	25	129.3	18	5.09	10.78	22
8	25	143	15	5.1	10.72	21.9

2. Results of gold extraction from leaching experiments

Time (Hour)	Reactor # 1A 120bar -16+11.2mm	Reactor # 2A 120bar -5.6+4mm	Reactor # 3A 60bar -16+11.2mm	Reactor # 4A 60bar -5.6+4mm	Reactor # 5A 90bar -5.6+4mm	Reactor # 6B 120bar -16+11.2mm	Reactor # 7B 120bar -5.6+4mm	Reactor # 8B 60bar -16+11.2mm
2	0	0	0	0	1	0	1	0
22	0	1	1	1	2	0	1	0
46	7	11	4	12	19	3	10	3
70	9	13	5	14	22	3	11	4
94	10	19	10	22	26	3	13	6
118	10	20	13	24	28	3	14	14
142	10	25	14	29	29	4	19	15
148	10	26	15	30	29	12	19	16
166	12	28	17	30	29	20	20	17
196	16	32	19	31	31	21	25	20
220	19	36	20	31	32	21	29	23
238	19	41	22	32	33	21	32	23
286	19	46	25	36	39	21	33	24
310	22	49	28	40	47	23	34	25
334	31	57	35	55	61	27	42	29

Appendix XIV: Harmony Gold: Kusasalethu mine recovery grade and tons milled

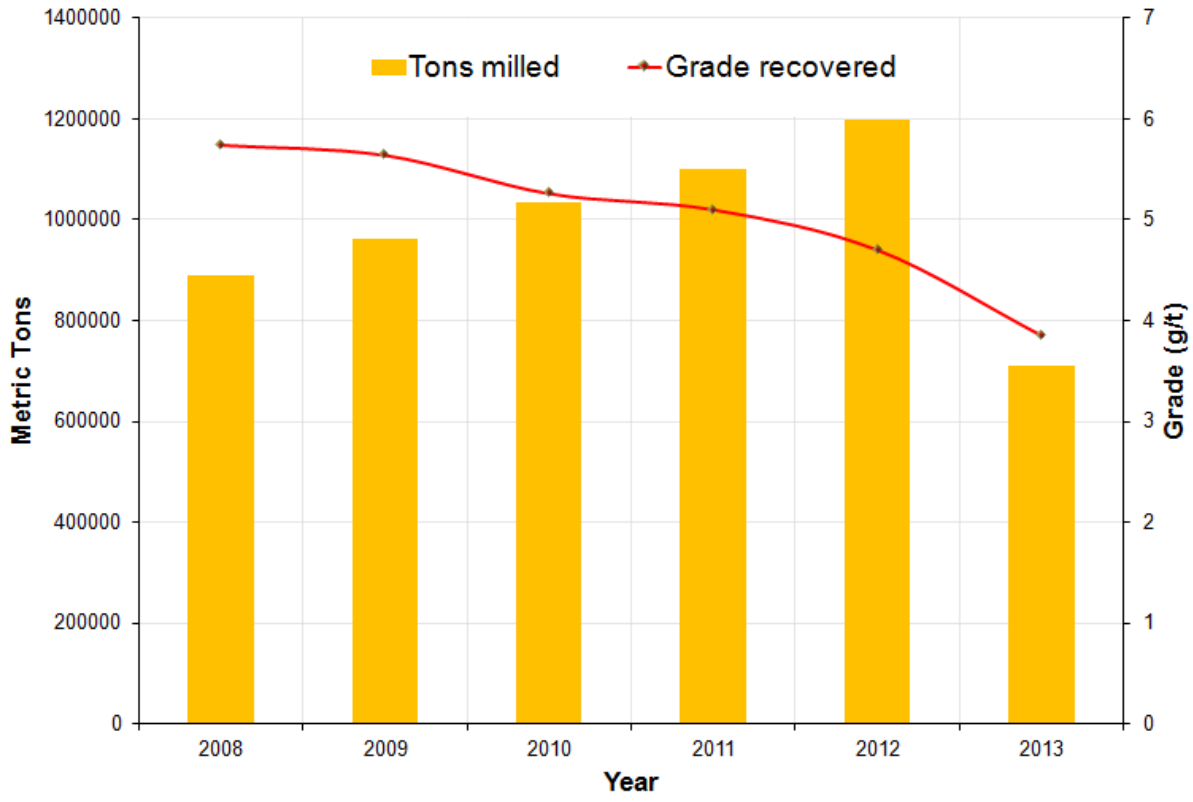

Illustration of the progressive decline in gold grade and fluctuations in metric tons milled due to problems related to electricity and labour unrest with special reference to Kusasalethu gold mine.

Appendix XV: Harmony Gold: Kusasalethu mine operating cost per kg and gold production per annum

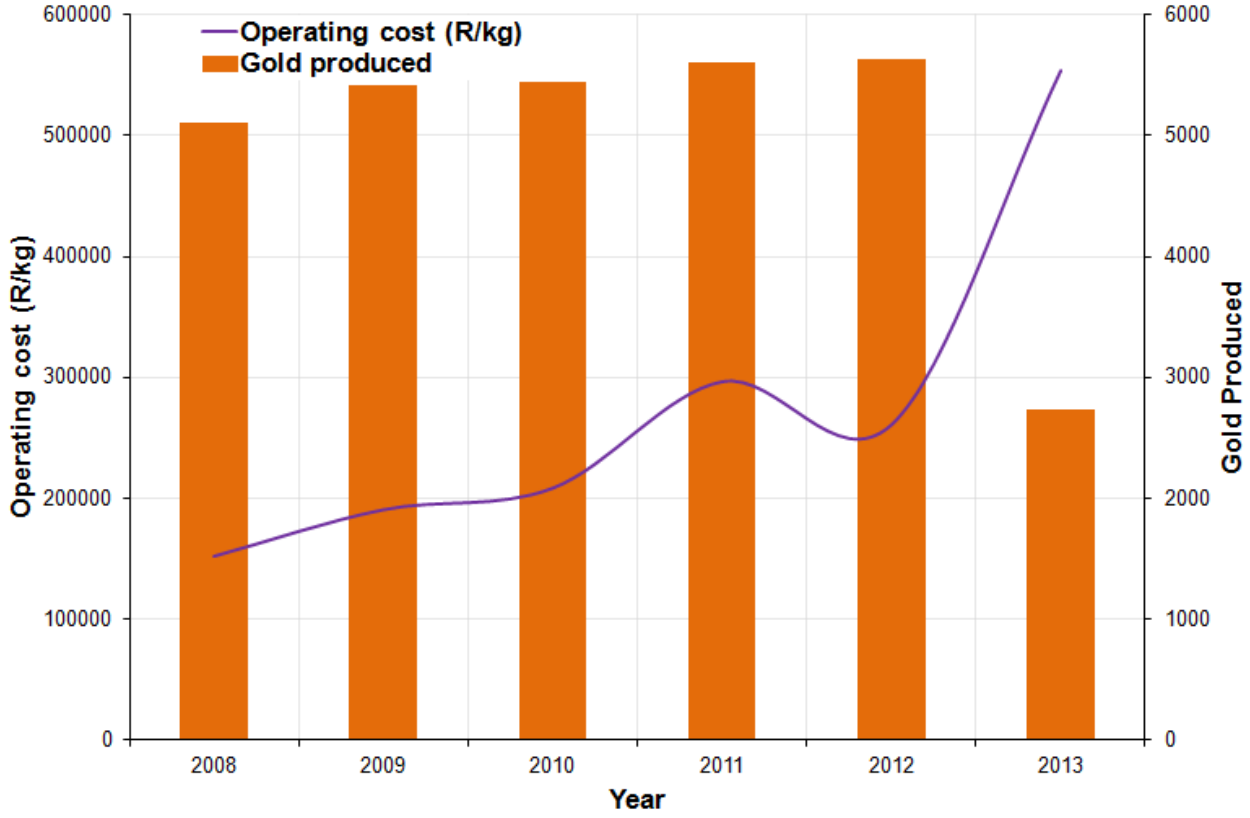

Indication of increased cost of gold production per kg and the significant decline in gold production due to safety issues (increase mining depth and seismic activities), labour unrest, milling cost and high energy usage.